The Pennsylvania State University

The Graduate School

THERMAL CHARACTERIZATION OF MODERN MICROSYSTEM TECHNOLOGIES FROM MATERIALS TO DEVICES

A Dissertation in

Mechanical Engineering

by

Yiwen Song

Submitted in Partial Fulfillment
of the Requirements
for the Degree of

Doctor of Philosophy

August 2024

The dissertation of Yiwen Song was reviewed and approved by the following:

Sukwon Choi
Associate Professor of Mechanical Engineering
Dissertation Co-Advisor
Chair of Committee

Susan Trolier-McKinstry
Evan Pugh University Professor and Flaschen Professor of Ceramic Science and Engineering and Electrical Engineering
Dissertation Co-Advisor

Wooram Lee
Associate Professor of Electrical Engineering

Md Amanul Haque
Professor of Mechanical Engineering

Robert Kunz
Professor and Associate Head for Graduate Program

ABSTRACT

Recent technological advancements, including fifth-generation (5G) mobile networks, electrified transportation systems, and artificial intelligence, are fundamentally improving human lifestyles. These modern technologies have been made possible by tremendous efforts in the research and development of functional materials. The ongoing drive for system-level improvements in size, weight, and power (SWaP) of modern electronics establishes the need for new materials with enhanced properties. However, even when a material demonstrates potential due to its superior properties, numerous obstacles must be overcome to meet the performance, reliability, and manufacturing requirements necessary for commercialization. As thermal challenges are becoming increasingly common and severe in emerging microsystems, electro-thermal co-design for material development becomes indispensable.

In this dissertation, frequency-domain thermoreflectance (FDTR), time-domain thermoreflectance (TDTR), and steady-state thermoreflectance (SSTR) were used to study and understand the fundamental thermophysical properties of emerging material systems for power electronics (β-Ga_2O_3 and $(Al_xGa_{1-x})_2O_3$) and microelectromechanical systems (AlN, $Al_{1-x}Sc_xN$, and $Pb(Zr_xTi_{1-x})O_3$). Device modeling was performed using the measured thermal properties to evaluate the cooling requirements and design thermal management solutions.

1. **Study of next generation β-Ga_2O_3 power electronics:**

β-Ga_2O_3 and β-$(Al_xGa_{1-x})_2O_3$ heteroepitaxial thin films were characterized. The measured thermal conductivities (6.3 - 9.4 W m^{-1} K^{-1}) of the sub-micron thick β-Ga_2O_3 thin films were relatively low as compared to the intrinsic bulk value (10.9 – 27 W m^{-1} K^{-1}). The measured thermal conductivities were compared with calculated values from a Debye-Callaway model incorporating phononic parameters derived from first-principles calculations. Results suggest that the reduction in the thin film thermal conductivity is primarily attributed to the increased phonon-boundary

scattering rate when the film thickness reduced. They were found to be a strong function of not only the layer thickness but also the film quality, resulting from growth on substrates with different offcut angles. Growth of β-Ga_2O_3 films on 6° offcut sapphire substrates was found to result in higher crystallinity and thermal conductivity relative to films grown on on-axis c-plane sapphire. However, the β-Ga_2O_3 films grown on 6° offcut sapphire exhibit a lower thermal boundary conductance at the β-Ga_2O_3/sapphire heterointerface. In addition, the thermal conductivity of $(\bar{2}01)$-oriented β-$(Al_xGa_{1-x})_2O_3$ thin films with x ranging from 2% to 43% were characterized. Because of phonon-alloy disorder scattering, the β-$(Al_xGa_{1-x})_2O_3$ films exhibit lower thermal conductivities (2.8-4.7 W/m·K) than β-Ga_2O_3 thin films. The dominance of alloy disorder scattering in β-$(Al_xGa_{1-x})_2O_3$ is further supported by the weak temperature dependence of the thermal conductivity. This work provides fundamental insight into the physical mechanisms that govern phonon transport within heteroepitaxially grown β-phase Ga_2O_3 and $(Al_xGa_{1-x})_2O_3$ thin films and lays the groundwork for the thermal modeling and design of β-Ga_2O_3 electronic and optoelectronic devices.

Due to the low intrinsic thermal conductivity of β-Ga_2O_3, overheating has been identified as a major bottleneck to the commercialization of β-Ga_2O_3 device technologies. In response to this, a novel β-Ga_2O_3/4H-SiC composite wafer with high heat transfer performance and an epi-ready surface finish has been developed using a fusion bonding method. Phonon transport across the β-Ga_2O_3/4H-SiC interface has been studied using FDTR and a differential SSTR approach. Scanning transmission electron microscopy (STEM) analysis suggests that phonon transport across the β-Ga_2O_3/4H-SiC interface is dominated by the thermal resistance of the SiN_x bonding layer and an unintentionally formed SiO_x interlayer. Extrinsic effects that impact the thermal conductivity of the 6.5 μm thick Ga_2O_3 layer were studied via TDTR. Thermal simulation was performed to estimate the improvement of the thermal performance of a hypothetical single-finger Ga_2O_3 metal-semiconductor field-effect transistor (MESFET) fabricated on the composite substrate. This novel power transistor topology was calculated to result in a ~4.3× reduction in the junction-to-package device thermal resistance. These innovations in device-level thermal management suggest improved exploitation of the promise of the ultra-wide bandgap material, which will lead to significant improvements in the power density and efficiency of power electronics over current state-of-the-art commercial devices.

Following the success of fabricating the β-Ga_2O_3/4H-SiC composite wafer using a fusion-bonding method, a low temperature ($\leq$ 600°C) device processing scheme was developed to fabricate MOSFETs on the composite wafer. The low temperature grown epitaxial β-Ga_2O_3 devices delivered high thermal performance (56% reduction in channel temperature) and a power figure of merit of ~300 MW/cm^2, which is the highest among heterogeneously integrated β-Ga_2O_3 devices reported to date. Simulations calibrated based on thermal characterization results of the β-Ga_2O_3-on-SiC MOSFET reveal that a β-Ga_2O_3/diamond composite wafer with a reduced β-Ga_2O_3 thickness (~1 μm) and thinner bonding interlayer (<10 nm) can reduce the device thermal resistance to a level lower than today's GaN-on-SiC power switches.

2. **Study of piezoelectric micro-electro-mechanical systems (MEMS) resonators:**

Thermophysical property measurements were performed on AlN and $Al_{1-x}Sc_xN$, materials that are used in radio frequency (RF) filters for wireless communication applications. Different AlN growth methods and conditions lead to different film microstructures. Phonon scattering mechanisms that impact the cross-plane (κ_z; along the *c*-axis) and in-plane (κ_r; parallel to the *c*-plane) thermal conductivities of AlN thin films prepared by various synthesis techniques were investigated. In contrast to bulk single crystal AlN, which has an isotropic thermal conductivity of ~330 W/mK, a strong anisotropy in the thermal conductivity was observed in thin films. The κ_z values show a strong film thickness dependence due to phonon-boundary scattering. Electron microscopy reveals the presence of grain boundaries and dislocations that limit the κ_r. For instance, oriented films prepared by reactive sputtering possess lateral crystalline grains with a size ranging from 20 to 40 nm that significantly lower the κ_r to ~30 W/mK. Simulation results suggest that the self-heating in AlN film bulk acoustic resonators can limit the power handling capability of RF filters. A device employing an oriented film as the active piezoelectric layer shows a ~2.5× higher device peak temperature as compared to a device based on a higher thermal conductivity epitaxial film.

$Al_{1-x}Sc_xN$ based (RF) MEMS are replacing AlN-based devices because of their higher achievable bandwidths, suitable for 5G mobile networks. However, overheating of $Al_{1-x}Sc_xN$ film bulk acoustic resonators (FBARs) used in RF MEMS filters limits the power handling capability. Therefore, the phone's ability to operate in an increasingly congested RF environment while maintaining its maximum data transmission rate is limited as well. In this dissertation, the ramifications of tailoring of the piezoelectric response and microstructure of $Al_{1-x}Sc_xN$ films on thermal transport have been studied. The thermal conductivity of $Al_{1-x}Sc_xN$ films ($3 – 8\ \mathrm{W\,m^{-1}\,K^{-1}}$) grown by reactive sputter deposition was found to be orders of magnitude lower than that for *c*-axis textured AlN films ($18 – 59\ \mathrm{W\,m^{-1}\,K^{-1}}$) due to alloying effects. The film thickness-dependence of the thermal conductivity suggests that higher frequency FBAR structures may suffer from limited power handling due to exacerbated overheating concerns. The reduction of the abnormally oriented grain (AOG) density was found to have a modest effect on the measured thermal conductivity. However, the use of low AOG density films results in lower insertion loss and thus less power dissipated within the resonator, which will lead to an overall enhancement of the device thermal performance.

3. **Study of piezoelectric MEMS actuators:**

The self-heating of lead zirconate titanate (PZT) thin films on Si and glass and a film released from a substrate were investigated to understand the effect of substrates on the device temperature rise. Nano-particle assisted Raman thermometry was employed to quantify the operational temperature rise of these PZT actuators. The results were validated using a finite element thermal model, where the volumetric heat generation was experimentally determined from the hysteresis loss. While the volumetric heat generation of the PZT films on different substrates were similar, the PZT films on Si substrate shows minimal temperature rise due to the effective heat dissipation through the high thermal conductivity substrate. The temperature rise of a released structure was 6.8× higher than that of a film on the glass substrates due to the absence of vertical heat dissipation. Experimental and modeling results show that a thin layer of residual Si remaining after substrate etching plays a crucial role in mitigating the effect of device self-heating. The outcomes of this study suggest that high thermal conductivity passive-elastic layers can be used as an effective thermal management solution for PZT-based MEMS actuators.

4. Conclusion:

The results presented in this dissertation contribute to the thermal property database of emerging functional materials and offer valuable insights into the thermal management of microsystems based on these materials. The demonstrated electro-thermal co-design process, that involves thermophysical property measurement, electro-thermal device modeling, device thermal imaging, and device-level thermal management, will support the continuous development and improvement of modern microsystems.

TABLE OF CONTENTS

LIST OF FIGURES

LIST OF TABLES

NOMENCLATURE

a	Lattice constant in a-direction
a_{eff}	Debye lattice constant
α	Thermal diffusivity
b	Burger vector
C	Stiffness constant
C_v	Volumetric heat capacity
d	Piezoelectric modulus
D	Density of states
E	Electric field
E_C	Breakdown field
E_G	Bandgap energy
e	Piezoelectric stress constant
f	Frequency
f_{mod}	modulation frequency
f_{BE}	Bose-Einstein distribution function
F_o	Fourier number
G	thermal boundary conductance
γ	Correction factor for SSTR; Grüneisen parameters
Γ	Impurity scattering variable for mass and ionic radii differences
I_D	Drain current

κ, κ_z, κ_r	Thermal conductivity, cross-plane thermal conductivity, in-plane thermal conductivity
k_B	Boltzmann constant
k_t^2	Electro-mechanical coupling factor
L_{GD}	Gate to drain distance
λ	Wavelength
M	Number of modes
μ	Mobility
NA	Numerical aperture
N	Avogadro's number
P	Power; peak position; polarization
Q	Heat flux
$\hbar$	Reduced Planck's constant
Θ	Debye temperature; angle of incidence
Θ, ω, χ	XRD angles
θ, θ_{ext}	Phase, external phase
θ	Angular frequency
ρ_e, ρ_s	Edge dislocation density, screw dislocation density
r_0	Pump radius
R	Reflectivity
$R_{on\text{-}sp}$	Specific ON resistance
S_x	Sensitivity of parameter x

t	Time
t_{d}; τ_{delay}	Delay time
τ	Scattering rate
$\tau_{1,2}$	Transmission coefficient from the medium 1 to 2
τ_{laser}	Laser pulse width
τ_{on}	Device pulse width
T, T_{ss}	Temperature, steady-state temperature
v	Phonon group velocity
V	Photodetector voltage; volume
V_{BR}	Breakdown voltage
V_{in}	In-phase voltage
V_{DS}	Drain voltage
V_{GS}	Gate voltage
V_{out}	Out-of-phase voltage
v_{s}	Saturated electron velocity
ω	Angular frequency
Z	Acoustic impedance; number of molecules per unit cell

PREFACE

There is a feeling of satisfaction after solving a problem. Since I was young, I’ve enjoyed various engineering projects, and what stands out most in my memory aren't the final products, but the joy of overcoming problems along the way. Mechanical engineering became the natural choice for my undergraduate major. Mechanical engineering has such a broad scope that we learn everything from fluid, vibration, to heat transfer. Entering my junior year, I was uncertain about my career path. To explore my options, I reached out to professors in various fields to discuss potential research opportunities and discovered there are so many real-life problems and challenges that need to be solved. Dr. Choi’s project in thermal characterization sparked my interest particularly (maybe I was interested in heat transfer already, as I used to build models on a steak and study how to cook it perfectly). As I started working on the project and eventually joined the group as a PhD student, I found myself enjoying research a lot. Although the devices we research may still be distant from commercialization, our work addresses incremental challenges and contributes to the evolution of future technologies. To me, this is the most satisfying part of being a researcher.

The research presented in this dissertation was executed under the advisement of Dr. Sukwon Choi in the Department of Mechanical Engineering at The Pennsylvania State University (University Park, PA) and Dr. Susan Trolier-McKinstry in the Department of Materials Science and Engineering at The Pennsylvania State University (University Park, PA). Chapters 3, 4, and 5 present studies from peer-reviewed journal publications.

Chapter 3.1, titled “Thermal Property Measurement,” is based on peer-reviewed journal publication in the American Chemical Society Applied Materials and Interfaces. This work was performed in collaboration with Praneeth Ranga, Yingying Zhang, Zixuan Feng, Hsien-Lien Huang, Marco D. Santia, Stefan C. Badescu, C. Ulises Gonzalez-Valle, Carlos Perez, Kevin Ferri, Robert M. Lavelle, David W. Snyder, Brianna A. Klein, Julia Deitz, Albert G. Baca, Jon-Paul Maria, Bladimir Ramos-Alvarado, Jinwoo Hwang, Hongping Zhao, Xiaojia Wang, Sriram Krishnamoorthy, Brian M. Foley, and Sukwon Choi* (* indicating the corresponding author). The author of this dissertation conducted thermal characterization using TDTR and FDTR, performed data analysis, and wrote the manuscript.

Chapter 3.2, titled "Thermal Management and Interface Phonon Transport," is based on peer-reviewed journal publication in the American Chemical Society Applied Materials and Interfaces. This work was performed in collaboration with Daniel Shoemaker, Jacob H. Leach, Craig McGray, Hsien-Lien Huang, Arkka Bhattacharyya, Yingying Zhang, C. Ulises Gonzalez-Valle, Tina Hess, Sarit Zhukovsky, Kevin Ferri, Robert M. Lavelle, Carlos Perez, David W. Snyder, Jon-Paul Maria, Bladimir Ramos-Alvarado, Xiaojia Wang, Sriram Krishnamoorthy, Jinwoo Hwang, Brian M. Foley, and Sukwon Choi*. The author of this dissertation developed the differential SSTR method utilized in this work and conducted thermal characterization and analysis using FDTR, TDTR, and SSTR.

Chapter 3.3, titled "Device-level Thermal Management," is based on peer-reviewed journal publication in the American Chemical Society Applied Materials and Interfaces. This work was performed in collaboration with Arkka Bhattacharyya, Anwarul Karim, Daniel Shoemaker, Hsien-Lien Huang, Saurav Roy, Craig McGray, Jacob H. Leach, Jinwoo Hwang, Sriram Krishnamoorthy*, and Sukwon Choi*. The author of this dissertation is a co-first author of this work, alongside Arkka Bhattacharyya. The author of this dissertation conducted thermophysical property measurement, device self-heating measurement, and led the writing of the manuscript.

Chapter 4.1, titled "Growth-Microstructure-Thermal Property Relations in AlN Thin Films," is based on the peer-reviewed journal publication in the Journal of Applied Physics. This work was performed in collaboration with Chi Zhang, James Spencer Lundh, Hsien-Lien Huang, Yue Zheng, Yingying Zhang, Mingyo Park, Timothy Mirabito, Rossiny Beaucejour, Chris Chae, Nathaniel McIlwaine, Giovanni Esteves, Thomas E Beechem, Craig Moe, Rytis Dargis, Jeremy Jones, Jacob H Leach, Robert M Lavelle, David W Snyder, Jon-Paul Maria, Roy H Olsson, Joan M Redwing, Azadeh Ansari, Jinwoo Hwang, Xiaojia Wang, Brian M Foley, Susan E Trolier-McKinstry, Sukwon Choi*. The author of this dissertation conducted thermophysical property measurements using TDTR, FDTR, and SSTR, performed material characterization with Raman, SEM, and XRD, conducted analytical modeling for AlN thermal conductivity, and performed FEA COMSOL 3D modeling.

Chapter 4.2, titled “Thermal Conductivity of Aluminum Scandium Nitride for 5G Mobile Applications and Beyond,” is based on the peer-reviewed journal publication in the American Chemical Society Applied Materials and Interfaces. This work was performed in collaboration with Carlos Perez, Giovanni Esteves, James Spencer Lundh, Christopher B Saltonstall, Thomas E Beechem, Jung In Yang, Kevin Ferri, Joseph E Brown, Zichen Tang, Jon-Paul Maria, David W Snyder, Roy H Olsson III, Benjamin A Griffin, Susan E Trolier-McKinstry, Brian M Foley, Sukwon Choi*. The author of this dissertation performed thermophysical property characterization with FDTR and TDTR and led the writing of the manuscript.

Chapter 5, titled “Substrate Dependence of the Self-heating in Lead Zirconate Titanate (PZT) MEMS Actuators,” is based on the peer-reviewed journal publication in the Journal of Applied Physics. This work was performed in collaboration with Kyuhwe Kang, Pannawit Tipsawat, Christopher Y. Cheng, Wanlin Zhu, Michael LaBella, Sukwon Choi*, Susan E. Trolier-McKinstry*. The author of this dissertation performed electrical characterization, thermal measurement with Raman thermometry, and FEA COMSOL modeling.

This dissertation includes work forming parts of the following peer-reviewed journal and conference publications:

- **Yiwen Song,** Praneeth Ranga, Yingying Zhang, Zixuan Feng, Hsien-Lien Huang, Marco D. Santia, Stefan C. Badescu, C. Ulises Gonzalez-Valle, Carlos Perez, Kevin

Ferri, Robert M. Lavelle, David W. Snyder, Brianna A. Klein, Julia Deitz, Albert G. Baca, Jon-Paul Maria, Bladimir Ramos-Alvarado, Jinwoo Hwang, Hongping Zhao, Xiaojia Wang, Sriram Krishnamoorthy, Brian M. Foley, and Sukwon Choi, Thermal Conductivity of β-Phase Ga_2O_3 and $(Al_xGa_{1-x})_2O_3$ Heteroepitaxial Thin Films, ACS Applied Materials & Interfaces, 2021, 13 (32), 38477-38490, DOI: 10.1021/acsami.1c08506

- **Yiwen Song**, Daniel Shoemaker, Jacob H. Leach, Craig McGray, Hsien-Lien Huang, Arkka Bhattacharyya, Yingying Zhang, C. Ulises Gonzalez-Valle, Tina Hess, Sarit Zhukovsky, Kevin Ferri, Robert M. Lavelle, Carlos Perez, David W. Snyder, Jon-Paul Maria, Bladimir Ramos-Alvarado, Xiaojia Wang, Sriram Krishnamoorthy, Jinwoo Hwang, Brian M. Foley, and Sukwon Choi, Ga_2O_3-on-SiC Composite Wafer for Thermal Management of Ultrawide Bandgap Electronics, ACS Applied Materials & Interfaces, 2021, 13 (34), 40817-40829, DOI: 10.1021/acsami.1c09736
- **Yiwen Song**#, Arkka Bhattacharyya#, Anwarul Karim, Daniel Shoemaker, Hsien-Lien Huang, Saurav Roy, Craig McGray, Jacob H. Leach, Jinwoo Hwang, Sriram Krishnamoorthy, and Sukwon Choi, Ultra-Wide Band Gap Ga_2O_3-on-SiC MOSFETs**,** ACS Applied Materials & Interfaces, 2023, 15 (5), 7137-7147**,** DOI: 10.1021/acsami.2c21048 **#Authors contributed equally.**
- **Yiwen Song**, Chi Zhang, James Spencer Lundh, Hsien-Lien Huang, Yue Zheng, Yingying Zhang, Mingyo Park, Timothy Mirabito, Rossiny Beaucejour, Chris Chae, Nathaniel McIlwaine, Giovanni Esteves, Thomas E. Beechem, Craig Moe, Rytis Dargis, Jeremy Jones, Jacob H. Leach, Robert M. Lavelle, David W. Snyder, Jon-Paul Maria, Roy H. Olsson, Joan M. Redwing, Azadeh Ansari, Jinwoo Hwang, Xiaojia Wang, Brian M. Foley, Susan E. Trolier-McKinstry, Sukwon Choi, Growth-

microstructure-thermal property relations in AlN thin films. J. Appl. Phys. 7 November 2022; 132 (17): 175108. https://doi.org/10.1063/5.0106916

- **Yiwen Song**[#], Carlos Perez[#], Giovanni Esteves, James Spencer Lundh, Christopher B. Saltonstall, Thomas E. Beechem, Jung In Yang, Kevin Ferri, Joseph E. Brown, Zichen Tang, Jon-Paul Maria, David W. Snyder, Roy H. Olsson III, Benjamin A. Griffin, Susan E. Trolier-McKinstry, Brian M. Foley, and Sukwon Choi, Thermal Conductivity of Aluminum Scandium Nitride for 5G Mobile Applications and Beyond, ACS Applied Materials & Interfaces, 2021, 13 (16), 19031-19041, DOI: 10.1021/acsami.1c02912 [#]**Authors contributed equally.**
- **Yiwen Song**, Kyuhwe Kang, Pannawit Tipsawat, Christopher Y. Cheng, Wanlin Zhu, Michael LaBella, Sukwon Choi, Susan E. Trolier-McKinstry; Substrate dependence of the self-heating in lead zirconate titanate (PZT) MEMS actuators. J. Appl. Phys. 28 April 2024; 135 (16): 164107. https://doi.org/10.1063/5.0204385
- Daniel C. Shoemaker, **Yiwen Song**, Kyuhwe Kang, Michael L. Schuette, James S. Tweedie, Scott T. Sheppard, Nathaniel S. McIlwaine, Jon-Paul Maria, and Sukwon Choi, Implications of Interfacial Thermal Transport on the Self-Heating of GaN-on-SiC High Electron Mobility Transistors, IEEE Transactions on Electron Devices, vol. 70, no. 10, pp. 5036-5043, Oct. 2023, doi: 10.1109/TED.2023.3303125.

ACKNOWLEDGMENTS

First, I will offer my sincere gratitude to my PhD advisors, Dr. Sukwon Choi and Dr. Susan Trolier-McKinstry. I joined Dr. Choi's research group as an undergraduate student in 2018. Being an undergrad in mechanical engineering learning mainly large systems, I was completely new to the world of nanoscale electronics. Dr. Sukwon Choi patiently provided me guidance, so I understood the importance of the work and acquired knowledge and skills to conduct the research. While pointing me in the right direction with his expertise and experience, he was always open to discussions and supportive of my ideas. Not every graduate student has the opportunity to collaborate directly with experts from outside their home department. Being co-advised by Dr. Susan Trolier-McKinstry was one of the most valuable experiences I had during my graduate study. Her passion for education and meticulous approach to science were truly inspiring. Over the years, thanks to the selfless guidance of my advisors, I was able develop into a more proficient researcher. I aim to apply the knowledge, passion, and engineering skills I've gained from them to drive technological advancements in my future career.

I would sincerely thank my co-workers in the ET-lab (Daniel Shoemaker, James Spencer Lundh, Bikramjit Chatterjee, Anwarul Karim, Kyuhwe Kang, Seokjun Kim, and Husam Walwil). With our lab location being next to so many downtown restaurants, we essentially had lunch together every day for many years; this group felt like a family. On the technical side, I genuinely appreciate the tremendous effort put in by my seniors, James Spencer and Bikram, to train me on all the lab equipment during my undergraduate years. I recognize that it was no easy task. I would like to give a special honorable mention to Daniel Shoemaker, who joined the group alongside me as an undergrad. Daniel not only assisted me on numerous research projects, working late nights even on Christmas Eve to troubleshoot measurement issues, but he also offered immense support in various aspects of life. From enjoying each other's jokes to helping me fix my car and move to a new apartment and hosting regular dinner parties together, Daniel has been an invaluable friend to me. I extend my gratitude to the members of the STM group. The weekly seminars significantly improved not only my presentation skills but also my ability to ask questions effectively.

I would like to acknowledge Dr. Brian Foley for building the FDTR and TDTR system at Penn State and sharing his expertise with me on these techniques. I would like to acknowledge my gratitude to faculty members who generously shared their time, knowledge, and resources with me – Dr. Aman Haque, Dr. Fan He, Dr. Bill Mahoney, Dr. Wooram Lee, Dr. Bangzhi Liu, Dr. Suzanne Mohney, Dr. Jon-Paul Maria, Dr. Joan Redwing, Dr. Nichole Wonderling. Your patient guidance in my unfamiliar areas significantly contributed to my success throughout my years of research.

I extend my gratitude to all our collaborators. The work presented in this dissertation would not have been possible without your invaluable support. The fruitful discussions we engaged in were instrumental in my growth as a researcher. Your diverse expertise opened alternative avenues of thinking and presented new possibilities. Specifically, I would like to recognize Arkka Bhattacharyya, Azadeh Ansari, Christopher B Saltonstall, Craig McGray, Hsien-Lien Huang, Hongping Zhao, Jacob H. Leach, James S Tweedie, Jinwoo Hwang, Michael Schuette, Mohamadali Malakoutian, Nathaniel McIlwaine, Pannawit Tipsawat, Praneeth Ranga, Robert M Lavelle, Samuel Graham, Samuel Kim, Scott T Sheppard, Srabanti Chowdhury, Sriram Krishnamoorthy, Thomas E Beechem, Timothy Mirabito, Xiaojia Wang. For my fellow students, I wish you all a fruitful career, making a significant impact with your expertise. To our industrial and academic collaborators, I extend my wish for the continued success of our collaboration.

I extend my heartfelt thanks to all my friends for the enjoyable moments and shared laughter during my studies. Additionally, I appreciate the members of the Penn State Pokémon Society for traveling to various cities to compete in video game and trading card game tournaments together. I am deeply grateful for the emotional support provided by my two corgis, Colin and

Angela. Their presence not only brings joy but also encourages and helps me to be a more responsible person.

Lastly, I want to extend my sincere gratitude to my mother, Xiaoming Hu, and my father, Zhouhu Song. Their unwavering love and support throughout my entire life have played a pivotal role in shaping the person I am today. Not only did they provide financial support throughout my education, but they also consistently supported my decisions and acknowledged my achievements.

Acknowledgment of Federal Funding

The work in this dissertation was supported by the following funding agencies:

- National Science Foundation, as part of the Center for Dielectrics and Piezoelectrics under grant nos. IIP-1361571, IIP-1361503, IIP-1841453, and IIP-1841466;
- Air Force Office of Scientific Research (AFOSR) Young Investigator Program (grant no. FA9550-17-1-0141, Program Officers: Dr. Brett Pokines and Dr. Michael Kendra, also monitored by Dr. Kenneth Goretta);
- The Penn State Materials for Enhancing Energy and Environmental Stewardship Seed Grant Program;
- National Science Foundation (CBET-1934482, Program Director:Dr. Ying Sun).

This dissertation describes objective technical results and analysis. Any subjective views or opinions that might be expressed in this dissertation do not necessarily represent the views of the funding agencies or the United States Government.

Chapter 1

Introduction

The rapid advancements in technology are driving the performance limits beyond that of silicon-based electronic devices. During the past decade, there has been a notable shift in power electronics from junction engineering of Si to material/device engineering of alternative materials, such as silicon carbide (SiC) and gallium nitride (GaN). These new wide bandgap (WBG) semiconductor devices have entered the market and experienced significant growth.[1] New materials are being actively explored to meet the increasingly demanding technological requirements across various industries, ranging from the massive electrification of vehicles to the enhancement of RF communication. Finding a suitable new material is often challenging, since this requires not only intrinsic material properties that enable new functionalities but also cost-effective manufacturing and integration into current technologies to facilitate commercialization. Significant research efforts are required for the development of devices based on a new material system. Such challenges include manufacturing high-quality wafers/substrates, doping, junction design, and thermal management. This thesis primarily addresses the challenges associated with device-level thermal management. Comprehensive thermal characterization was performed at both material- and device-levels for $Ga_2O_3/(Al_xGa_{1-x})_2O_3$ power electronics. Fundamental phonon transport mechanisms were investigated for AlN and $Al_{1-x}Sc_xN$ for RF microelectromechanical systems (MEMS). Additionally, the self-heating behavior of lead zirconate titanate (PZT) MEMS actuators was investigated.

1.1 Ultra-wide Bandgap Power Electronics

1.1.1 Overview of β-Ga_2O_3

The β-gallium oxide (β-Ga_2O_3) material system holds great promise in improving the electrical performance and cost-effectiveness of next-generation power electronics due to its ultra-wide bandgap of ~4.8 eV[2,3] and the availability of high-quality single-crystal bulk substrates. The suitability of Ga_2O_3 for high-power applications is evident from the significant improvement in Baliga's figure of merit (BFOM)[4], which evaluates the performance of power switching semiconductor devices. For instance the BFOM of β-Ga_2O_3 is four times higher than that of GaN.[4] The Johnson's figure of merit (JFOM), which represents the power-frequency product for RF applications, suggests that β-Ga_2O_3 has great potential for RF applications given that its JFOM is 3 times higher than that of GaN.[5] A comparison of the material properties is given in **Table 1.1**. Moreover, β-$(Al_xGa_{1-x})_2O_3$ alloys enable bandgap engineering up to 8.8 eV[6] for deep-ultraviolet (DUV) optoelectronic applications. β-Ga_2O_3 electronics benefit from the availability of high-quality single-crystal β-Ga_2O_3 substrates grown via low-cost melt growth techniques such as Czochralski[7,8], floating-zone[9], and edge defined film-fed growth (EFG) method[10]. Homoepitaxial growth of β-Ga_2O_3 has been demonstrated with halide vapor phase epitaxy (HVPE)[11], metalorganic vapor-phase epitaxy (MOVPE)[12], molecular-beam epitaxy (MBE)[13], and low pressure chemical vapor deposition (LPCVD)[14]. Additionally, heteroepitaxy of β-Ga_2O_3 on foreign substrates like sapphire[15–17], Si[18], GaAs[19,20], SiC[21], and MgO[22,23] has been achieved using various growth methods including MBE[18], MOVPE[19,24], HVPE[25], pulsed laser deposition (PLD)[26], and LPCVD[27,28].

Doping strategies have been developed to enhance optical and electrical properties for β-Ga_2O_3. Several approaches have been demonstrated including Si[29,30], Sn[31,32], Mg[33,34] and N[35] doping. Notably, Si is commonly used for n-type doping in β-Ga_2O_3 to enhance carrier concentration and conductivity in the doped material.

Table 1.1: Properties for Conventional, WBG, and UWBG materials.[36–41]

	Conventional	WBG		UWBG		
	Si	SiC	GaN	AlN	β-Ga_2O_3	Diamond
Bandgap (eV)	1.1	3.3	3.4	6.2	4.9	5.5
Relative dielectric constant	11.8	9.7	9	8.5	10	5.5
Breakdown field (MV/cm)	0.3	2.5	3.3	15	8	10
Majority carrier mobility [channel] (cm^2/Vs)	1400	1000	1350 [2000]	300	250 [150]	4500 [300]
Carrier saturation velocity (cm/s)	1×10^7	2×10^7	2.5×10^7	1.3×10^7	1.1×10^7	1×10^7
Thermal Conductivity (W/mK)	150	490	130	340	11-27	2400
Normalized BFOM	1	340	870	15000	2870 [1720]	55500 [3700]
Normalized JFOM	1	17	28	67	29	33

1.1.2 Ga_2O_3 Based Devices

Recent advancements in material growth and doping techniques enabled the development of β-Ga_2O_3 electronics, particularly in the fabrication of metal semiconductor field effect transistor (MESFET)[42,43] and modulation doped field effect transistors (MODFETs).[44,45] Although β-Ga_2O_3 exhibits a low intrinsic carrier density, precise n-type doping has been demonstrated to achieve carrier densities within the range of 10^{15}-10^{19} cm^{-3}, facilitating their use as channel layers with electron mobilities typically ranging from 150-200 cm^2/Vs.[42,46,47] Low-resistance ohmic contacts also play a crucial role in the performance of β-Ga_2O_3-based MESFETs to achieve high current densities and minimize conduction losses.[42] Typically, heavily-doped n^+ regrown source and drain contacts are used to achieve low contact resistance as show in the schematic in **Figure 1.1 (a)**.[42] *Bhattacharyya et al.* has demonstrated β-Ga_2O_3 MESFETs with a maximum ON current of 130 mA/mm[42] and breakdown voltage of 4.4 kV[48], showing promise for low to medium voltage power-device applications. Additionally, *Xia et al.* achieved a maximum ON current of 260 mA/mm and a cut-off frequency of 27 GHz in their β-Ga_2O_3 MESFET, indicating potential for RF and millimeter-wave device applications.[49]

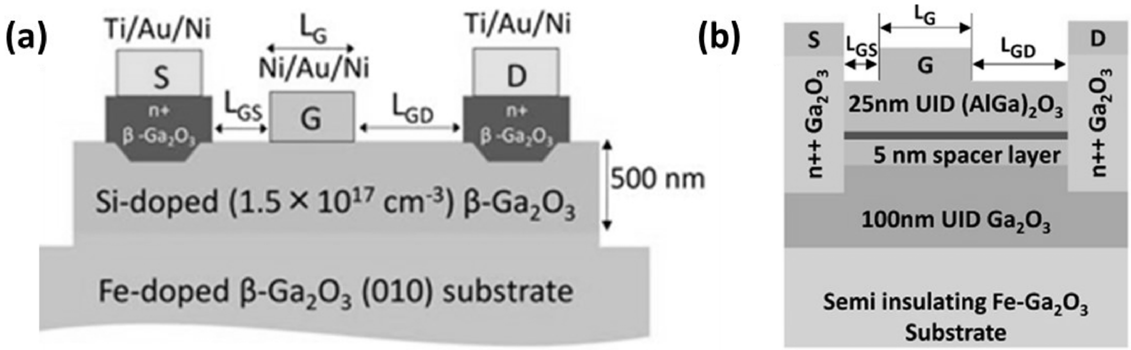

Figure 1.1: (a) Epitaxial structure of β-Ga_2O_3 MESFET. Figure adopted from *Bhattacharyya et al.*[42] (b) Epitaxial structure of an β-$(Al_{0.19}Ga_{0.81})_2O_3/Ga_2O_3$ MODFET. Figure adopted from *Bikramjit et al.* [44]

While the carrier mobility reduces with increased doping concentration due to electron-impurity scattering, the intrinsic low bulk mobility of β-Ga_2O_3 can be alleviated by using Si δ-modulation-doped epitaxial β-$(Al_xGa_{1-x})_2O_3/Ga_2O_3$ heterostructures to realize two-dimensional electron gas (2DEG).[50] A typical structure for β-$(Al_xGa_{1-x})_2O_3/Ga_2O_3$ modulation-doped field effect transistors (MODFET) is show in **Figure 1.1 (b)**.[44] An β-$(Al_xGa_{1-x})_2O_3/Ga_2O_3$ epitaxial stack consisted of a 100 nm unintentionally-doped (UID) β-Ga_2O_3 buffer layer and a 30 nm β-$(Al_xGa_{1-x})_2O_3$ layer with δ-doping in this layer. The 5 nm β-$(Al_xGa_{1-x})_2O_3$ space was used to improve the modulation doping efficiency. A 2DEG density of ~10^{12} cm^{-2} and room temperature mobility around 180 cm^2/Vs has been demonstrated.[45] While still in early development, optimization of transport and resistance properties in β-Ga_2O_3 heterojunction devices holds promise for improving power-switching performance.[45,50]

1.2 Piezoelectric Materials for Microelectromechanical Systems

Piezoelectric microelectromechanical systems (piezoMEMS) are finding application in diverse areas including filters, sensors, actuators, and energy harvesting. In this dissertation, AlN/$Al_{1-x}Sc_xN$ and lead zirconate titanate (PZT) material systems were studied.

1.2.1 Overview of AlN and $Al_{1-x}Sc_xN$

Aluminum nitride (AlN) is an ultra-wide bandgap (~6.2eV) semiconductor with notable piezoelectric properties, suitable for applications in multiple areas including optoelectronics, power electronics, and electro-acoustics. For examples, AlN-based deep ultraviolet (DUV) LEDs enable emission at 210 nm, extendable up to 400 nm through alloying with Ga, which is of interest for water purification and UV sensor applications.[51] In terms of power electronics, AlN's direct bandgap of around 6.2 eV results in a high breakdown field exceeding 10 MV/cm. Accordingly, the Baliga figure of merit (BFOM) of AlN is an order of magnitude greater than that of GaN.[52] Notably, a variety of AlN-based MEMS such as surface acoustic wave (SAW) devices,[53] flexural plate wave (FPW) sensors,[54] micromachined ultrasonic transducers (pMUTs)[55], and contour mode resonators (CMRs)[56] have been commercialized. During the 4G communication era, AlN-based film bulk acoustic resonators (FBAR) achieved great commercial success due to their high quality factor ($Q > 2000$) at frequencies surpassing 2 GHz and their compatibility with the complementary metal oxide semiconductor (CMOS) process.[57]

Doping AlN with Sc to form $Al_{1-x}Sc_xN$ can significantly enhance the electromechanical coupling coefficient (k_t^2) for FBAR resonators.[58] $Al_{1-x}Sc_xN$ addresses the intrinsic limitations of AlN, enabling operation at higher frequencies (>3 GHz) and wider bandwidths (>500 MHz), extending its applicability to the fifth-generation (5G) communication systems. A more detailed literature survey for AlN and $Al_{1-x}Sc_xN$ is provided in chapters 4.1.1 and 4.2.1, respectively.

1.2.3 Overview of PZT

The piezoelectric devices market is valued at $32.7 billion[59] in 2023 and is consistently growing at around 10% per annum. This sustained growth is due in part to ongoing innovation in PZT devices.[60] In recent years, PZT thin films have seen extensive exploration for piezoelectric MEMS (piezoMEMS) applications. Thin film PZT-based devices are commonly used in energy harvesters,[61] low loss resonators,[62] and high-performance actuators,[63] sensors,[64] and transducers.[65] Typically, achieving the desired perovskite crystals requires processing temperatures beyond 600˚C; however, ongoing efforts toward low-temperature processing (<500˚C) have the potential to expand the compatibility of PZT thin films with semiconductors and flexible electronics.[66]

1.3 Thermal Considerations Associated with Emerging Microsystems

Wide-bandgap (WBG) semiconductors such as silicon carbide (SiC) and gallium nitride (GaN) have been successfully commercialized over the past decade for their suitability in high-power applications. However, their theoretical performance limits based on the superior electronic properties have yet to be fully realized.[67] When operating a transistor under high-power and high-frequency conditions, excessive waste heat leads to significant self-heating in the channel region, resulting in degradation of the performance and lifetime (for instance, the device mean-time-to-failure exponentially decays with increasing channel temperature).[68] Although the theoretical power limit for GaN is projected to exceed 90 W/mm, today's commercial GaN devices typically operate at around 5 W/mm of output power density to maintain acceptable temperatures for reliable operation.[69] Several government sponsored programs have aimed to provide thermal management solutions to realize higher power density of GaN-based technologies.[70–72]

While emerging ultra-wide-bandgap (UWBG) materials such as β-Ga_2O_3 and β-$(Al_xGa_{1-x})_2O_3$ show great promise for their excellent electronic properties, their figure of merits is often evaluated without any thermal considerations. The continuous drive for devices with smaller size and higher performance exacerbates self-heating issues. However, thermal management is currently recognized as one of the most critical technical challenges to the commercialization of β-Ga_2O_3 electronics due to the Ga_2O_3's inherently low thermal conductivity.[47] A comprehensive understanding of thermal transport mechanisms from material level to device level is necessary to design thermal management solutions. The thermal conductivity of crystalline solids often decreases at elevated temperatures, reduced thickness, and high impurity concentrations, which exacerbates self-heating issues in practical devices. Device modeling to assess thermal performance relies heavily on measured thermal property data. This dissertation focuses on thermal property characterization to address the current lack of a thermal property database for emerging materials, including β-Ga_2O_3.

Since β-Ga_2O_3 UWBG devices are intended to offer higher power handling capabilities (10 W/mm) than current wide-bandgap WBG technologies, overcoming thermal limitations is essential to realize this potential. Following the evolution of GaN-on-SiC[73-75] and GaN-on-diamond[76–78] technologies, *Chatterjee et al.* demonstrated that integration with high thermal conductivity substrates could serve as an effective thermal management solution for Ga_2O_3 MOSFETs.[38] Reducing the thermal boundary resistance (TBR) across the heterointerface is crucial for enhancing the heat removal. As a result, considerable efforts have been directed towards characterizing and minimizing TBR in GaN-based technologies.[74,79,80] Characterizing the TBR in β-Ga_2O_3-based systems poses a challenge with traditional techniques like TDTR, primarily due to the dominant sensitivity of the low thermal conductivity Ga_2O_3 layer. Therefore, a differential SSTR measurement technique was developed to characterize the TBR within a β-Ga_2O_3-on-SiC composite wafer. β-Ga_2O_3 MOSFETs were fabricated on this composite wafer, and comprehensive characterization and evaluation of their electrical and thermal performance are presented in this dissertation.

While AlN is an established material with thermal properties that are well-understood, its diverse applications require different material growth methods, resulting in different film microstructures. Variations in the impurity concentration, grain size, thickness, dislocation density, and stress can lead to deviations in thermal conductivity from its intrinsic value.[81] Utilizing incorrect thermal conductivity values can result in inaccurate estimation of the device performance and reliability. This dissertation investigates the relationship between the microstructure and the thermal conductivity of AlN thin films grown using different methods and discusses how these variations affect device performance.

Similar to the situation with UWBG materials, doping scandium into AlN presents a promising opportunity for 5G communication applications due to the resulting superior electro-mechanical properties; however, thermal challenges must be overcome to realize its full potential. Alloying typically leads to a drastic reduction in the thermal conductivity by orders of magnitude compared to the base materials, exacerbating the self-heating in $Al_{1-x}Sc_xN$-based FBARs at the high operational frequencies of the 5G mobile network.[82] Thermal property data for $Al_{1-x}Sc_xN$ were lacking in the literature. To understand the fundamental thermal transport mechanisms in $Al_{1-x}Sc_xN$, this dissertation investigated the impacts of the alloy composition, film thickness, ambient temperature, and grain structures on its thermal conductivity. The outcome of this work offers significant insights into the electro-thermo-mechanical co-design considerations for 5G RF acoustic filters.

Heat generation in PZT ferroelectrics primarily arises from hysteresis loss induced by domain wall motion. The self-heating of PZT-based actuators has been demonstrated to increase with higher operational frequency, voltage amplitude, and slew rate.[83] Moreover, when operated at high frequencies, closely positioned actuator arrays can exacerbate overheating. It has been reported that the temperature of an industrial thin film PZT-based inkjet die can exceed 100°C when all actuators are operated simultaneously.[84] PZT actuators are typically intentionally limited to self-heating up to 20°C above the ambient temperature to prevent changes in the domain structure.[85] Therefore, thermal management in PZT-based microsystems should not be overlooked. Since the thermal conductivity of PZT thin films (1.45-1.8 W/mK) has been previously reported,[86,87] device level thermal characterization and analysis were the focus in this study.

1.4 Outline of Study

This dissertation presents comprehensive thermal characterization of the material systems mentioned above, involving the measurement of thermophysical properties at the material level and conducting temperature measurements and modeling at the device level. This approach enables understanding of the heat generation mechanisms, identification of thermal bottlenecks, and assessment of the effectiveness of thermal management solutions.

Since the thermophysical property measurement is a major focus of this dissertation, Chapter 2 explains the FDTR, TDTR, and SSTR techniques. Among these techniques, SSTR is a relatively new one established in 2019 and is not widely reported in the literature; therefore, Chapter 2.1 provides a more detailed description of the system and its limitations. FDTR and TDTR are relatively well-established and have been used extensively in literature. As such, Chapter 2.2 and 2.3 provides a brief introduction to the fundamentals of these techniques while emphasizing the author's perspective on factors that are less commonly discussed in the literature. Measurement sensitivity analysis and the transducer thickness characterization are also discussed in Chapter 2.

Chapter 3 demonstrates the thermal analysis of β-Ga_2O_3 based systems. Section 3.1 focuses on material-level characterization of β-Ga_2O_3 and β-$(Al_xGa_{1-x})_2O_3$ films. The thickness-, crystallinity-, and doping-dependence of their thermal conductivities were studied. In Section 3.2, a β-Ga_2O_3-on-SiC composite wafer is introduced as a potential thermal management solution. The section provides a detailed investigation of the thermal properties of the composite wafer and evaluates its device cooling effectiveness via modeling. In Section 3.3, β-Ga_2O_3 MOSFETs were fabricated on the composite wafer. Their thermal performance was evaluated experimentally under both steady-state and transient conditions. Modeling was utilized to identify potential improvements, and an optimized design was suggested based on the findings.

In Section 4.1, the microstructure and thermal conductivity of AlN thin films synthesized by different growth techniques are presented. A thermal conductivity model is developed to qualitatively analyze the influence of dislocation density and impurities on the phonon transport in AlN. A 3D finite-element thermal model was constructed for an FBAR to assess the practical implications of different growth methods on the device thermal performance. Section 4.2 presents a thorough thermal characterization of $Al_{1-x}Sc_xN$. The impacts of Sc composition, film thickness, ambient temperature, and grain structures on its thermal conductivity are examined. A virtual crystal approximation (VCA) model for $Al_{1-x}Sc_xN$ is used to validate the experimental observations. This chapter provides insights into phonon scattering mechanisms and offers fundamental knowledge associated with the electro-thermal co-design of 5G $Al_{1-x}Sc_xN$-based RF acoustic filters.

Chapter 5 presents the impact of the substrate material on the self-heating of PZT thin film-based MEMS. Experimental findings and modeling data indicate potential thermal management solutions for PZT MEMS through the choice of the passive elastic layer.

To conclude the dissertation, Chapter 6 presents a summary of the reported findings and key contributions. In addition, a proposed future work section describes preliminary data and possible approaches to experimentally study the self-heating in AlN and $Al_{1-x}Sc_xN$-based FBARs.

Chapter References

[1] M. Baldini, Z. Galazka, and G. Wagner, “Recent progress in the growth of β-Ga_2O_3 for power electronics applications,” Mater. Sci. Semicond. Process. **78**(October 2017), 132–146 (2018).

[2] H.H. Tippins, “Optical absorption and photoconductivity in the band edge of beta-Ga_2O_3,” Phys. Rev. **140**(1A), A316–A319 (1965).

[3] B.J. Baliga, “Power semiconductor device figure of merit for high-frequency applications,” IEEE Electron Device Lett. **10**(10), 455–457 (1989).

[4] S.J. Pearton, J. Yang, P.H. Cary, F. Ren, J. Kim, M.J. Tadjer, and M.A. Mastro, “A review of Ga_2O_3 materials, processing, and devices,” Appl. Phys. Rev. **5**(1), 11301 (2018).

[5] H. Peelaers, J.B. Varley, J.S. Speck, and C.G. Van de Walle, “Structural and electronic properties of Ga_2O_3-Al_2O_3 alloys,” Appl. Phys. Lett. **112**(24), 242101 (2018).

[6] Y. Tomm, P. Reiche, D. Klimm, and T. Fukuda, “Czochralski grown β-Ga_2O_3 crystals,” J. Cryst. Growth **220**(4), 510–514 (2000).

[7] Z. Galazka, K. Irmscher, R. Uecker, R. Bertram, M. Pietsch, A. Kwasniewski, M. Naumann, T. Schulz, R. Schewski, D. Klimm, and M. Bickermann, “On the bulk β-Ga_2O_3 single crystals grown by the Czochralski method,” J. Cryst. Growth **404**, 184–191 (2014).

[8] E.G. Villora, K. Shimamura, Y. Yoshikawa, K. Aoki, and N. Ichinose, “Large-size β-Ga_2O_3 single crystals and wafers,” J. Cryst. Growth **270**(3–4), 420–426 (2004).

[9] Hideo Aida and Kengo Nishiguchi and Hidetoshi Takeda and Natsuko Aota and Kazuhiko Sunakawa and Yoichi Yaguchi, “Growth of β-Ga_2O_3 single crystals by the edge-defined,

film fed growth method," Jpn. J. Appl. Phys. **47**(11R), 8506 (2008).

[10] J.H. Leach, K. Udwary, J. Rumsey, G. Dodson, H. Splawn, and K.R. Evans, "Halide vapor phase epitaxial growth of β-Ga_2O_3 and α-Ga_2O_3 films," APL Mater. **7**(2), 22504 (2018).

[11] G. Wagner, M. Baldini, D. Gogova, M. Schmidbauer, R. Schewski, M. Albrecht, Z. Galazka, D. Klimm, and R. Fornari, "Homoepitaxial growth of β-Ga_2O_3 layers by metal-organic vapor phase epitaxy," Phys. Status Solidi **211**(1), 27–33 (2014).

[12] H. Okumura, M. Kita, K. Sasaki, A. Kuramata, M. Higashiwaki, and J.S. Speck, "Systematic investigation of the growth rate of β-Ga_2O_3(010) by plasma-assisted molecular beam epitaxy," Appl. Phys. Express **7**(9), 95501 (2014).

[13] S. Rafique, L. Han, M.J. Tadjer, J.A. Freitas, N.A. Mahadik, and H. Zhao, "Homoepitaxial growth of β-Ga_2O_3 thin films by low pressure chemical vapor deposition," Appl. Phys. Lett. **108**(18), 182105 (2016).

[14] S. Rafique, L. Han, and H. Zhao, "Synthesis of wide bandgap Ga_2O_3 (Eg ~ 4.6–4.7 eV) thin films on sapphire by low pressure chemical vapor deposition," Phys. Status Solidi **213**(4), 1002–1009 (2016).

[15] Y. Yao, S. Okur, L.A.M. Lyle, G.S. Tompa, T. Salagaj, N. Sbrockey, R.F. Davis, and L.M. Porter, "Growth and characterization of α-, β-, and ϵ-phases of Ga_2O_3 using MOCVD and HVPE techniques," Mater. Res. Lett. **6**(5), 268–275 (2018).

[16] Z. Feng, A.F.M.M. Anhar Uddin Bhuiyan, M.R. Karim, and H. Zhao, "MOCVD homoepitaxy of Si-doped (010) β-Ga_2O_3 thin films with superior transport properties," Appl. Phys. Lett. **114**(25), 250601 (2019).

[17] T. Hadamek, A.B. Posadas, F. Al-Quaiti, D.J. Smith, M.R. McCartney, and A.A. Demkov, "β-Ga_2O_3 on Si (001) grown by plasma-assisted MBE with γ-Al_2O_3 (111) buffer layer: Structural characterization," AIP Adv. **11**(4), 45209 (2021).

[18] V. Gottschalch, K. Mergenthaler, G. Wagner, J. Bauer, H. Paetzelt, C. Sturm, and U. Teschner, "Growth of β-Ga_2O_3 on Al_2O_3 and GaAs using metal-organic vapor-phase epitaxy," Phys. Status Solidi **206**(2), 243–249 (2009).

[19] Y. Chen, H. Liang, X. Xia, R. shen, Y. Liu, Y. Luo, and G. Du, "Effect of growth pressure on the characteristics of β-Ga_2O_3 films grown on GaAs (100) substrates by MOCVD method," Appl. Surf. Sci. **325**, 258–261 (2015).

[20] N. Nepal, D.S. Katzer, B.P. Downey, V.D. Wheeler, L.O. Nyakiti, D.F. Storm, M.T. Hardy, J.A. Freitas, E.N. Jin, D. Vaca, L. Yates, S. Graham, S. Kumar, and D.J. Meyer, "Heteroepitaxial growth of β-Ga_2O_3 films on SiC via molecular beam epitaxy," J. Vac. Sci. Technol. A **38**(6), 63406 (2020).

[21] N. Matsuo, N. Doko, Y. Yasukawa, H. Saito, and S. Yuasa, "Epitaxial growth of MgO/Ga_2O_3 heterostructure and its band alignment studied by X-ray photoemission spectroscopy," Jpn. J. Appl. Phys. **57**(7), 70304 (2018).

[22] W. Mi, J. Ma, Z. Zhu, C. Luan, Y. Lv, and H. Xiao, "Epitaxial growth of Ga_2O_3 thin films on MgO (110) substrate by metal–organic chemical vapor deposition," J. Cryst. Growth **354**(1), 93–97 (2012).

[23] Q. Cao, L. He, H. Xiao, X. Feng, Y. Lv, and J. Ma, "β-Ga_2O_3 epitaxial films deposited on epi-GaN/sapphire (0001) substrates by MOCVD," Mater. Sci. Semicond. Process. **77**, 58–63 (2018).

[24] H. Murakami, K. Nomura, K. Goto, K. Sasaki, K. Kawara, Q.T. Thieu, R. Togashi, Y. Kumagai, M. Higashiwaki, A. Kuramata, S. Yamakoshi, B. Monemar, and A. Koukitu, "Homoepitaxial growth of β-Ga_2O_3layers by halide vapor phase epitaxy," Appl. Phys. Express **8**(1), 15503 (2014).

[25] H. Yang, Y. Qian, C. Zhang, D.-S. Wuu, D.N. Talwar, H.-H. Lin, J.-F. Lee, L. Wan, K. He, and

Z.C. Feng, “Surface/structural characteristics and band alignments of thin Ga_2O_3 films grown on sapphire by pulse laser deposition,” Appl. Surf. Sci. **479**, 1246–1253 (2019).

[26] S. Rafique, L. Han, A.T. Neal, S. Mou, J. Boeckl, and H. Zhao, “Towards high-mobility heteroepitaxial β-Ga_2O_3 on sapphire − dependence on the substrate off-axis angle,” Phys. Status Solidi **215**(2), 1700467 (2018).

[27] S. Rafique, L. Han, and H. Zhao, “Synthesis of wide bandgap Ga_2O_3 (Eg ~ 4.6-4.7 eV) thin films on sapphire by low pressure chemical vapor deposition,” Phys. Status Solidi Appl. Mater. Sci. **213**(4), 1002–1009 (2016).

[28] S. Rafique, M.R. Karim, J.M. Johnson, J. Hwang, and H. Zhao, “LPCVD homoepitaxy of Si doped β-Ga_2O_3 thin films on (010) and (001) substrates,” Appl. Phys. Lett. **112**(5), 52104 (2018).

[29] K. Goto, K. Konishi, H. Murakami, Y. Kumagai, B. Monemar, M. Higashiwaki, A. Kuramata, and S. Yamakoshi, “Halide vapor phase epitaxy of Si doped β-Ga_2O_3 and its electrical properties,” Thin Solid Films **666**, 182–184 (2018).

[30] A.Y. Polyakov, N.B. Smirnov, I. V Shchemerov, D. Gogova, S.A. Tarelkin, and S.J. Pearton, “Compensation and persistent photocapacitance in homoepitaxial Sn-doped β-Ga_2O_3,” J. Appl. Phys. **123**(11), 115702 (2018).

[31] N. Suzuki, S. Ohira, M. Tanaka, T. Sugawara, K. Nakajima, and T. Shishido, “Fabrication and characterization of transparent conductive Sn-doped β-Ga_2O_3 single crystal,” Phys. Status Solidi C **4**(7), 2310–2313 (2007).

[32] M.H. Wong, C.-H. Lin, A. Kuramata, S. Yamakoshi, H. Murakami, Y. Kumagai, and M. Higashiwaki, “Acceptor doping of β-Ga_2O_3 by Mg and N ion implantations,” Appl. Phys. Lett. **113**(10), 102103 (2018).

[33] Z. Feng, A.F.M.A.U. Bhuiyan, N.K. Kalarickal, S. Rajan, and H. Zhao, “Mg acceptor doping in

MOCVD (010) β-Ga_2O_3," Appl. Phys. Lett. **117**(22), 222106 (2020).

[34] L. Dong, R. Jia, C. Li, B. Xin, and Y. Zhang, "Ab initio study of N-doped β-Ga_2O_3 with intrinsic defects: the structural, electronic and optical properties," J. Alloys Compd. **712**, 379–385 (2017).

[35] Y. Sasama, K. Komatsu, S. Moriyama, M. Imura, T. Teraji, K. Watanabe, T. Taniguchi, T. Uchihashi, and Y. Takahide, "High-mobility diamond field effect transistor with a monocrystalline h-BN gate dielectric," APL Mater. **6**(11), 111105 (2018).

[36] G. Jessen, K. Chabak, A. Green, N. Moser, J. McCandless, K. Leedy, A. Crespo, and S. Tetlak, "Gallium oxide technologies and applications," in *2017 IEEE Compd. Semicond. Integr. Circuit Symp.*, (2017), pp. 1–4.

[37] B. Chatterjee, K. Zeng, C.D. Nordquist, U. Singisetti, and S. Choi, "Device-level thermal management of gallium oxide field-effect transistors," IEEE Trans. Components, Packag. Manuf. Technol. **9**(12), 2352–2365 (2019).

[38] H. Ahmad, J. Lindemuth, Z. Engel, C.M. Matthews, T.M. McCrone, and W.A. Doolittle, "Substantial p-type conductivity of AlN achieved via beryllium doping," Adv. Mater. **33**(42), 2104497 (2021).

[39] Y. Taniyasu, M. Kasu, and T. Makimoto, "Electrical conduction properties of n-type Si-doped AlN with high electron mobility (>100$cm^2V^{-1}s^{-1}$)," Appl. Phys. Lett. **85**(20), 4672–4674 (2004).

[40] S.K. O'Leary, B.E. Foutz, M.S. Shur, and L.F. Eastman, "Steady-state and transient electron transport within the III-V nitride semiconductors, GaN, AlN, and InN: A Review," J. Mater. Sci. Mater. Electron. **17**(2), 87–126 (2006).

[41] A. Bhattacharyya, S. Roy, P. Ranga, D. Shoemaker, Y. Song, J.S. Lundh, S. Choi, and S. Krishnamoorthy, "130 mA mm−1 β-Ga_2O_3 metal semiconductor field effect transistor

with low-temperature metalorganic vapor phase epitaxy-regrown ohmic contacts," Appl. Phys. Express **14**(7), 76502 (2021).

[42] Z. Xia, C. Joishi, S. Krishnamoorthy, S. Bajaj, Y. Zhang, M. Brenner, S. Lodha, and S. Rajan, "Delta doped β-Ga_2O_3 field effect transistors with regrown ohmic contacts," IEEE Electron Device Lett. **39**(4), 568–571 (2018).

[43] B. Chatterjee, Y. Song, J.S.J.S. Lundh, Y. Zhang, Z. Xia, Z. Islam, J. Leach, C. McGray, P. Ranga, S. Krishnamoorthy, A. Haque, S. Rajan, and S. Choi, "Electro-thermal co-design of β-$(AlxGa1\text{-}x)_2O_3/Ga_2O_3$ modulation doped field effect transistors," Appl. Phys. Lett. **117**(15), 153501 (2020).

[44] R. Singh, T.R. Lenka, D.K. Panda, R.T. Velpula, B. Jain, H.Q.T. Bui, and H.P.T. Nguyen, "The dawn of Ga_2O_3 HEMTs for high power electronics - A review," Mater. Sci. Semicond. Process. **119**, 105216 (2020).

[45] M. Higashiwaki, K. Sasaki, A. Kuramata, T. Masui, and S. Yamakoshi, "Gallium oxide (Ga_2O_3) metal-semiconductor field-effect transistors on single-crystal β-Ga_2O_3 (010) substrates," Appl. Phys. Lett. **100**(1), 013504 (2012).

[46] M. Higashiwaki, "β-Gallium oxide devices: progress and outlook," Phys. Status Solidi – Rapid Res. Lett. **15**(11), 2100357 (2021).

[47] A. Bhattacharyya, S. Sharma, F. Alema, P. Ranga, S. Roy, C. Peterson, G. Seryogin, A. Osinsky, U. Singisetti, and S. Krishnamoorthy, "4.4 kV β-Ga_2O_3 MESFETs with power figure of merit exceeding 100 MW cm^{-2}," Appl. Phys. Express **15**(6), 61001 (2022).

[48] Z. Xia, H. Xue, C. Joishi, J. Mcglone, N.K. Kalarickal, S.H. Sohel, M. Brenner, A. Arehart, S. Ringel, S. Lodha, W. Lu, and S. Rajan, "beta-Ga_2O_3 delta-doped field-effect transistors with current gain cutoff frequency of 27 GHz," IEEE Electron Device Lett. **40**(7), 1052–1055 (2019).

[49] S. Krishnamoorthy, Z. Xia, C. Joishi, Y. Zhang, J. McGlone, J. Johnson, M. Brenner, A.R. Arehart, J. Hwang, S. Lodha, and S. Rajan, "Modulation-doped β-$(Al_{0.2}Ga_{0.8})_2O_3/Ga_2O_3$ field-effect transistor," Appl. Phys. Lett. **111**(2), 23502 (2017).

[50] Y. Taniyasu, M. Kasu, and T. Makimoto, "An aluminium nitride light-emitting diode with a wavelength of 210 nanometres," Nature **441**(7091), 325–328 (2006).

[51] J.Y. Tsao, S. Chowdhury, M.A. Hollis, D. Jena, N.M. Johnson, K.A. Jones, R.J. Kaplar, S. Rajan, C.G. Van de Walle, E. Bellotti, C.L. Chua, R. Collazo, M.E. Coltrin, J.A. Cooper, K.R. Evans, S. Graham, T.A. Grotjohn, E.R. Heller, M. Higashiwaki, M.S. Islam, P.W. Juodawlkis, M.A. Khan, A.D. Koehler, J.H. Leach, U.K. Mishra, R.J. Nemanich, R.C.N. Pilawa-Podgurski, J.B. Shealy, Z. Sitar, M.J. Tadjer, A.F. Witulski, M. Wraback, and J.A. Simmons, "Ultrawide-bandgap semiconductors: Research opportunities and challenges," Adv. Electron. Mater. **4**(1), 1600501 (2018).

[52] C. Li, X. Liu, L. Shu, and Y. Li, "AlN-based surface acoustic wave resonators for temperature sensing applications," Mater. Express **5**(4), 367–370 (2015).

[53] M. Reusch, K. Holc, L. Kirste, P. Katus, L. Reindl, O. Ambacher, and V. Lebedev, "Piezoelectric AlN films for fpw sensors with improved device performance," Procedia Eng. **168**, 1040–1043 (2016).

[54] J. Jung, W. Lee, W. Kang, E. Shin, J. Ryu, and H. Choi, "Review of piezoelectric micromachined ultrasonic transducers and their applications," J. Micromechanics Microengineering **27**(11), (2017).

[55] G. Piazza, P.J. Stephanou, and A.P. Pisano, "Piezoelectric aluminum nitride vibrating contour-mode MEMS resonators," J. Microelectromechanical Syst. **15**(6), 1406–1418 (2006).

[56] K. Yang, C. He, J. Fang, X. Cui, H. Sun, Y. Yang, and C. Zuo, "Advanced RF filters for wireless communications," Chip **2**(4), 100058 (2023).

[57] A. Zukauskaite, G. Wingqvist, J. Palisaitis, J. Jensen, P.O.Å. Persson, R. Matloub, P. Muralt, Y.

Kim, J. Birch, and L. Hultman, “Microstructure and dielectric properties of piezoelectric magnetron sputtered w-$Sc_xAl_{1-x}N$ thin films,” J. Appl. Phys. **111**(9), 93527 (2012).

[58]“Piezoelectric devices market by product, element, application and region - global forecast to 2028,” MarketsandMarkets, (2023).

[59] A.J. Bell, T.P. Comyn, and T.J. Stevenson, “Expanding the application space for piezoelectric materials,” APL Mater. **9**(1), 10901 (2021).

[60] J.C. Park, J.Y. Park, and Y.-P. Lee, “Modeling and characterization of piezoelectric d_{33}-mode MEMS energy harvester,” J. Microelectromechanical Syst. **19**(5), 1215–1222 (2010).

[61] S.S. Bedair, J.S. Pulskamp, R.G. Polcawich, D. Judy, A. Gillon, S. Bhave, and B. Morgan, “Low loss micromachined lead zirconate titanate, contour mode resonator with 50Ω termination,” in *2012 IEEE 25th Int. Conf. Micro Electro Mech. Syst.*, (2012), pp. 708–712.

[62] E. Hong, S. Trolier-McKinstry, R.L. Smith, S. V Krishnaswamy, and C.B. Freidhoff, “Design of MEMS PZT circular diaphragm actuators to generate large deflections,” J. Microelectromechanical Syst. **15**(4), 832–839 (2006).

[63] B. Chen, H. Li, W. Tian, and C. Zhou, “PZT based piezoelectric sensor for structural monitoring,” J. Electron. Mater. **48**(5), 2916–2923 (2019).

[64] P. Tipsawat, S.J. Ilham, J.I. Yang, Z. Kashani, M. Kiani, and S. Trolier-Mckinstry, “32 element piezoelectric micromachined ultrasound transducer (PMUT) phased array for neuromodulation,” IEEE Open J. Ultrason. Ferroelectr. Freq. Control **2**, 184–193 (2022).

[65] L. Song, S. Glinsek, and E. Defay, “Toward low-temperature processing of lead zirconate titanate thin films: Advances, strategies, and applications,” Appl. Phys. Rev. **8**(4), 41315 (2021).

[66] F. Roccaforte, P. Fiorenza, G. Greco, R. Lo Nigro, F. Giannazzo, F. Iucolano, and M. Saggio, “Emerging trends in wide band gap semiconductors (SiC and GaN) technology for power devices,” Microelectron. Eng. **187–188**, 66–77 (2018).

[67] B. Chatterjee, C. Dundar, T.E. Beechem, E. Heller, D. Kendig, H. Kim, N. Donmezer, and S.

Choi, “Nanoscale electro-thermal interactions in AlGaN/GaN high electron mobility transistors,” J. Appl. Phys. **127**(4), 44502 (2020).

[68] A. Bar-Cohen, J.J. Maurer, and D.H. Altman, “Embedded cooling for wide bandgap power amplifiers: A Review,” J. Electron. Packag. **141**(4), (2019).

[69] A. Bar-cohen, J.J. Maurer, and A. Sivananthan, “Near-junction microfluidic thermal management of RF power amplifiers,” 2015 IEEE Int. Conf. Microwaves, Commun. Antennas Electron. Syst. (November), 2–4 (2015).

[70] A. Bar-Cohen, J.D. Albrecht, and J.J. Maurer, “Near-junction thermal management for wide bandgap devices,” Tech. Dig. - IEEE Compd. Semicond. Integr. Circuit Symp. CSIC, 1–5 (2011).

[71] M. Tyhach, D. Altman, S. Bernstein, R. Korenstein, J. Cho, K.E. Goodson, D. Francis, F. Faili, F. Ejeckam, S. Kim, and S. Graham, “S2-T3: Next generation gallium nitride HEMTs enabled by diamond substrates,” in *2014 Lester Eastman Conf. High Perform. Devices*, (2014), pp. 1–4.

[72] D.-Y. Chen, A. Malmros, M. Thorsell, H. Hjelmgren, O. Kordina, J.-T. Chen, and N. Rorsman, “Microwave performance of ‘buffer-free’ GaN-on-SiC high electron mobility transistors,” IEEE Electron Device Lett. **41**(6), 828–831 (2020).

[73] M. Malakoutian, D.E. Field, N.J. Hines, S. Pasayat, S. Graham, M. Kuball, and S. Chowdhury, “Record-low thermal boundary resistance between diamond and GaN-on-SiC for enabling radiofrequency device cooling,” ACS Appl. Mater. Interfaces **13**(50), 60553–60560 (2021).

[74] R.S. Pengelly, S.M. Wood, J.W. Milligan, S.T. Sheppard, and W.L. Pribble, “A review of GaN on SiC high electron-mobility power transistors and MMICs,” IEEE Trans. Microw. Theory Tech. **60**(6), 1764–1783 (2012).

[75] X. Gu, C. Lee, J. Xie, E. Beam, M. Becker, T.A. Grotjohn, J. Anaya, M. Kuball, and W.R. Road,

"GaN-on-diamond with ultra-low thermal barrier resistance," Def. Tech. Inf. Cent. (March 2016), 405–408 (2016).

[76] P.C. Chao, K. Chu, J. Diaz, C. Creamer, S. Sweetland, R. Kallaher, C. McGray, G.D. Via, J. Blevins, D.C. Dumka, C. Lee, H.Q. Tserng, P. Saunier, and M. Kumar, "GaN-on-diamond HEMTs with 11W/mm output power at 10GHz," MRS Adv. **1**(02), 147–155 (2016).

[77] Y. Gu, Y. Zhang, B. Hua, X. Ni, Q. Fan, and X. Gu, "Interface engineering enabling next generation GaN-on-diamond power devices," J. Electron. Mater. **50**(8), 4239–4249 (2021).

[78] H. Sun, R.B. Simon, J.W. Pomeroy, D. Francis, F. Faili, D.J. Twitchen, and M. Kuball, "Reducing GaN-on-diamond interfacial thermal resistance for high power transistor applications," Appl. Phys. Lett. **106**(11), (2015).

[79] J. Cho, K.K. Chu, P.C. Chao, C. McGray, M. Asheghi, and K.E. Goodson, "Thermal conduction normal to thin silicon nitride films on diamond and GaN," Thermomechanical Phenom. Electron. Syst. -Proceedings Intersoc. Conf., 1186–1191 (2014).

[80] A. V Inyushkin, A.N. Taldenkov, D.A. Chernodubov, E.N. Mokhov, S.S. Nagalyuk, V.G. Ralchenko, and A.A. Khomich, "On the thermal conductivity of single crystal AlN," J. Appl. Phys. **127**(20), 205109 (2020).

[81] Y. Zheng, M. Park, A. Ansari, C. Yuan, and S. Graham, "Self-heating and quality factor: Thermal challenges in aluminum scandium nitride bulk acoustic wave resonators," in *2021 21st Int. Conf. Solid-State Sensors, Actuators Microsystems*, (2021), pp. 321–324.

[82] J.S. Lundh, W. Zhu, Y. Song, S.W. Ko, C. Fragkiadakis, P. Mardilovich, S. Trolier-McKinstry, and S. Choi, "Local measurements of domain wall-induced self-heating in released $PbZr_{0.52}Ti_{0.48}O_3$ films," J. Appl. Phys. **128**(21), 214102 (2020).

[83] C. Fragkiadakis, S. Sivaramakrishnan, T. Schmitz-Kempen, P. Mardilovich, and S. Trolier-McKinstry, "Heat generation in PZT MEMS actuator arrays," Appl. Phys. Lett. **121**(16), 162906 (2022).

[84] K. Uchino, J.H. Zheng, Y.H. Chen, X.H. Du, J. Ryu, Y. Gao, S. Ural, S. Priya, and S. Hirose, "Loss mechanisms and high power piezoelectrics," J. Mater. Sci. **41**(1), 217–228 (2006).

[85] B.M. Foley, E.A. Paisley, C. DiAntonio, T. Chavez, M. Blea-Kirby, G. Brennecka, J.T. Gaskins, J.F. Ihlefeld, and P.E. Hopkins, "Phonon scattering mechanisms dictating the thermal conductivity of lead zirconate titanate ($PbZr_{1-x}Ti_xO_3$) thin films across the compositional phase diagram," J. Appl. Phys. **121**(20), 205104 (2017).

[86] R. Varghese, H. Harikrishna, S.T. Huxtable, W.T.J. Reynolds, and S. Priya, "Effect of crystallinity on thermal transport in textured lead zirconate titanate thin films," ACS Appl. Mater. Interfaces **6**(9), 6748–6756 (2014).

Chapter 2

Thermal and Material Characterization Methods

Optical based pump-probe techniques including time-domain thermoreflectance (TDTR), frequency-domain thermoreflectance (FDTR), and steady-state thermoreflectance (SSTR) serve a pivotal rule in characterizing the thermal properties of materials. TDTR and FDTR measure a material's thermal properties by recording the phase lag in temperature response due to the material's finite thermal diffusivity.[1,2] SSTR measures the material's thermal conductivity by comparing the magnitude of the temperature to a reference sample with known thermal conductivity at a given heat flux. In this chapter, the experimental setup and the methodology adopted for data analysis are described.

2.1 Steady-state Thermoreflectance (SSTR)

2.1.1 Operating principle and Instrumentation Setup

SSTR was first demonstrated by Braun *et. al.* in 2019.[3] It is an optical pump/probe based technique based on Fourier's law of heat transfer. The technique operates on the premise that, under steady-state, semi-infinite conditions, and with the same heat flux, a material with low thermal conductivity experiences a greater temperature rise compared to a material with high thermal conductivity. The time required for a material to reach the steady-state temperature depends on the thermal diffusivity and the pump laser radius. Braun *et. al.* used a nondimensional Fourier number, $Fo = \alpha t/r_0^2$, where α is the material thermal diffusivity, t is the time, and r_0 is the pump radius, to determine the required time for any material to reach steady-state, as shown in **Figure 2.1**.[3] When targeting the time to reach 95% of the steady-state temperature with a 5 μm radius pump size, Si and sapphire - two commonly used reference samples for thermal conductivity measurement - would require approximately ~1×10^{-5} s and ~8×10^{-5} s, respectively. It should be noted that the thermal time constant varies for unique material and spot size combinations, and it is crucial to verify that the selected frequency is sufficiently low for the specific application. With reduced frequency, 1/f noise will eventually limit the signal-to-noise ratio; however, with the setup described below, using a balanced photodetector and a lock-in amplifier, signal extraction was possible at the relevant frequencies in this work.

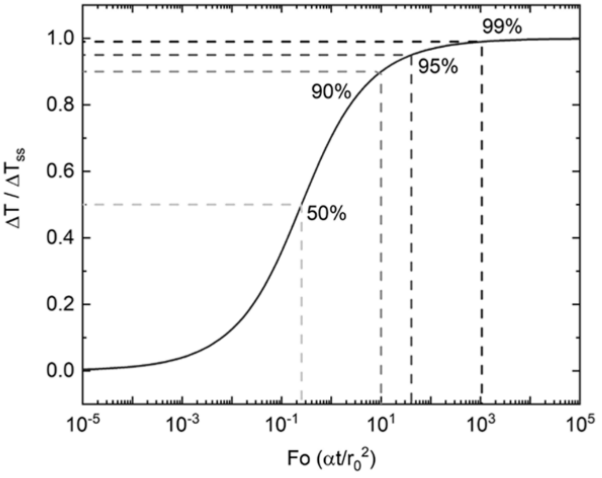

Figure 2.1: $\Delta T/\Delta TSS$ vs. Fourier number, where ΔT is the time-dependent surface temperature rise and ΔT_{SS} is the surface temperature rise under a steady state. Figure adopted from *Braun et al.*[3]

A schematic representing the interaction of the signals is shown in **Figure 2.2**. The pump laser is modulated with a square wave to induce a periodic heat flux (ΔP). The modulation frequency, typically around 150 Hz, leads to a heating time significantly longer than the required thermal time constant. This ensures that the internal temperature of the material reaches a steady state under heating/cooling conditions. The periodic change in temperature, ΔT, leads to a proportional change in transducer reflectivity, due to the thermoreflectance response.[4,5] The difference between the "cold" and "hot" reflectivity values is denoted by ΔR. This reflectivity change is quantified by measuring the reflected probe laser intensity with a balanced photodetector. A lock-in detection scheme is used to capture the small change in the thermoreflectance signal. The signal from the balanced photodetector is represented as ΔV/V, where V is the reference reflected probe intensity for the "cold" state, and ΔV is the change in the reflected probe intensity between the "cold" and "hot" states.

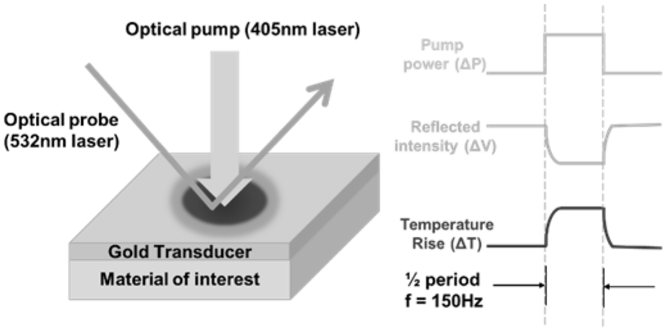

Figure 2.2: Operating principle of steady-state thermoreflectance (SSTR). The pump and probe are aligned co-axially in the actual setup. The reflectance of gold at 532 nm decreases with increasing temperature; therefore, ΔV drops at the higher temperature.

The change of transducer reflectivity, ΔR, is linearly proportional to the change in temperature, ΔT. Since the temperature is also a linear function of heat flux because of steady-state heating, the aforementioned variables can be related by[3]:

$$\frac{\Delta V}{V} \propto \frac{\Delta R}{R} \propto \Delta T \propto \Delta P \tag{2.1}$$

By re-arranging terms in equation (1):

$$\frac{\Delta V}{V\Delta P} = \gamma \left(\frac{\Delta T(\kappa)}{\Delta|Q|}\right) \tag{2.2}$$

where Δ|Q| is the heat flux used in the model, ΔT(κ) is the modeled temperature rise as a function of material thermal conductivity κ, and γ is a correction factor that includes the thermoreflectance coefficient and the absorption factor of the transducer. The left side of equation (2.2) is obtained by performing linear regression on the experimentally obtained ΔV/V and ΔP data. A given heat flux would induce a larger temperature rise for low thermal conductivity materials. γ can be found by relating this slope to a thermal model based on Fourier's law. Note that Δ|Q| used in the model can be an arbitrary value because the proportionality is captured in the γ. By depositing the same transducer on a calibration sample with a well-known thermal conductivity (e.g., silicon = 145 W/mK and/or sapphire = 40 W/mK), the γ value can be extracted and used to fit the thermal conductivity of the materials to be analyzed.

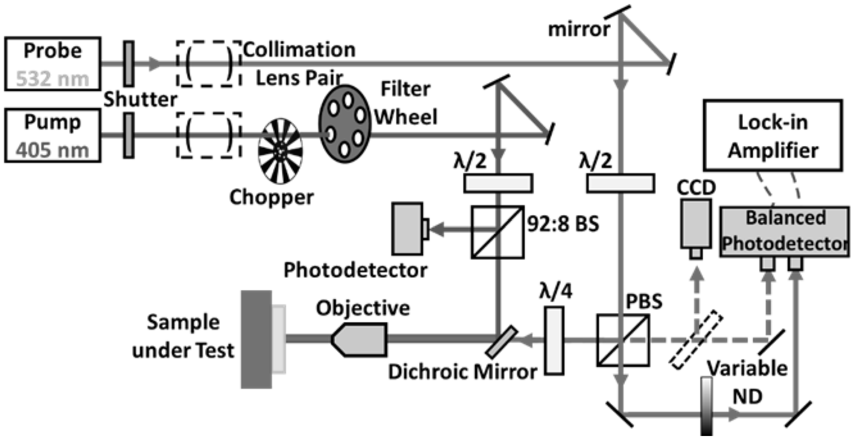

Figure 2.3. Schematic of the SSTR setup. The solid blue line is the path from the 405 nm pump laser. The solid green line is the probe path from the 532 nm probe laser. The dashed green line is the reflected probe path.

A schematic of the SSTR is shown in **Figure 2.3**. The probe laser (COHERENT OBIS 532) travels through a collimation lens pair and a half waveplate (λ/2) and is split into two paths with a polarized beam splitter (PBS). One probe path passes through the quarter waveplate (λ/4) and dichroic mirror, which transmits 532 nm and reflects 405 nm light, and is focused on the sample. The other path passes through a variable neutral density filter (variable ND) and focuses on the balanced photodetector (Thorlabs PDB425A - AC) as the reference signal to eliminate background noise in the reflected probe signal. The pump laser (COHERENT OBIS 405) travels through a collimation lens pair and was modulated at 150 Hz with a mechanical chopper (Thorlabs MC20000B). A motorized filter wheel (Thorlabs FW212CNEB) loaded with ND filters at different levels was used to sweep the pump laser power. After the half waveplate (λ/2), the pump is split into two paths with a 92% transmission/8% reflection beam splitter (92:8 BS). The 92% transmitted path is reflected by a dichroic mirror to align with the probe spot on the sample, and the 8% reflected path is collected by a photodetector as the ΔP signal. The reflected probe beam from the sample surface contains information about the temperature change (ΔT) at the pump modulation frequency. This signal is collected by the balanced photodetector, where ΔV is extracted using lock-in detection and V is the background intensity.

2.1.2 Additional Remarks and Insights

SSTR is based on Fourier's model that does not require knowledge for the volumetric heat capacity. This enables the accurate assessment of thermal conductivity without assumptions for the heat capacity. SSTR uses a simpler setup compared to FDTR and TDTR, which will be discussed in the following sections, primarily due to the lower frequency utilized. While using a lock-in amplifier and balanced photodetectors significantly improves the pump-probe alignment and signal-to-noise ratio, a more economical setup implementing an oscilloscope and a single photodetector can achieve comparable measurements. SSTR can achieve large thermal penetration depth that enables thermal characterization on some buried layers.[6,7] SSTR can achieve a substantial thermal penetration depth, allowing for thermal characterization of buried layers. This penetration depth is typically close to the pump radius; whereas the penetration depth of FDTR and TDTR is strongly dependent on the material properties and modulation frequency, typically < 1 μm.[8]

However, it is important to exercise caution when using large pump sizes, as the thermal time constant increases quadratically with the radius.[3]

The main disadvantage of SSTR lies in the requirement for calibration samples which is not adequately discussed in the literature. One fundamental assumption for SSTR is that the correction factor, γ, is universal between the measured sample and the calibration sample; however, this assumption may not hold true due to differences in surface morphology between samples. Even when the transducer is deposited on all samples in the same deposition batch, a rougher sample surface can lead to the transducer having lower reflectivity and higher absorption. Due to the convolution of actual absorption and the thermoreflectance coefficient within γ, it is challenging to accurately account for differences in transducers. Experimentally, a typical 8% difference in the γ was noticed between commercial-grade Si (145 W/mK) and sapphire (40 W/mK). In practice, an average γ for Si and sapphire was used, and the uncertainty is calculated for the result.

The requirement for calibration samples also introduces substantial uncertainties into the final fitting of the thermal properties due to error propagation. The error sources that need to be considered include the uncertainty in the assumed thermal conductivities for the calibration samples (10%), the γ (8%), the accuracy of the linear regression fitting on the experimental data, the laser spot size (5%), the thermal boundary conductance (TBC) between transducer and material (10%), the spot-to-spot variation of the sample (typically measured at 3 different spots on each sample, 5%), the thickness of the transducer (2%), and the layer thicknesses and TBC between layers for multi-layer material stacks. Due to the multitude of error sources and their individual sensitivities, a Monte Carlo approach is best suited for studying the uncertainties. In a Monte Carlo approach, each parameter is defined within a mean value and an error range, and a random value is generated based on a Gaussian distribution within that range. These randomly generated parameters are then used to fit for thermal properties. By repeating this process enough times, the fitted values will converge to a Gaussian distribution. In the studies presented in this thesis, a typical uncertainty level of >30% is observed for SSTR measurements on multi-layer material stacks, whereas the typical error for bulk materials measured by SSTR is around ~10-15%.[3] Depending on the sensitivity of the thermal property of interest, the error may not converge through Monte Carlo simulations. In such cases, additional validation may be necessary using other characterization techniques such as FDTR, TDTR, and finite element modeling. The limitations of SSTR will be further demonstrated in Chapter 3 on characterization of a Ga_2O_3-on-SiC material stack.

2.2 Time-domain Thermoreflectance (TDTR)

2.2.1 Operating Principle and Instrumentation Setup

TDTR has been widely adopted for measuring the thermal properties of thin films,[9] bulk materials,[10] nanostructures,[11,12] and thermal interfaces.[13,14] The operation principle of TDTR is readily available in the literature. David G. Cahill laid the mathematical foundation for analyzing TDTR data by solving the heat conduction equation in the frequency domain and radial coordination, representing the Gaussian-shaped laser-induced heating on a semi-infinite surface.[15] Puqing Jiang *et. al.* provided a detailed description of the theory and experimentation setup for TDTR.[16] Adaptations and different system configurations have been demonstrated in the literature to address diverse characterization needs. Below, the operational principles are briefly discussed and the instrumentation of the TDTR system at Penn State is detailed.

TDTR measures the transient thermal response of a material under pulsed laser heating. A train of picosecond (10^{-12} s) or femtosecond (10^{-15} s) laser pulses (pump) arrives at the sample surface at a frequency of 76 MHz, inducing periodic instantaneous heating that subsequently cools down between each pulse (time interval ~1.3×10^{-8} s). The probe laser, pulsed at the same frequency as the pump, arrives at the sample surface after the pump laser with a controllable delay time. This delay is achieved via a mechanical stage that adjusts the distance the probe pulse travels before it reaches the sample surface. The probe can therefore map the cooling response within the delay range, typically ~3000 ps. A schematic is shown in **Figure 2.4 (a)** to demonstrate this process.

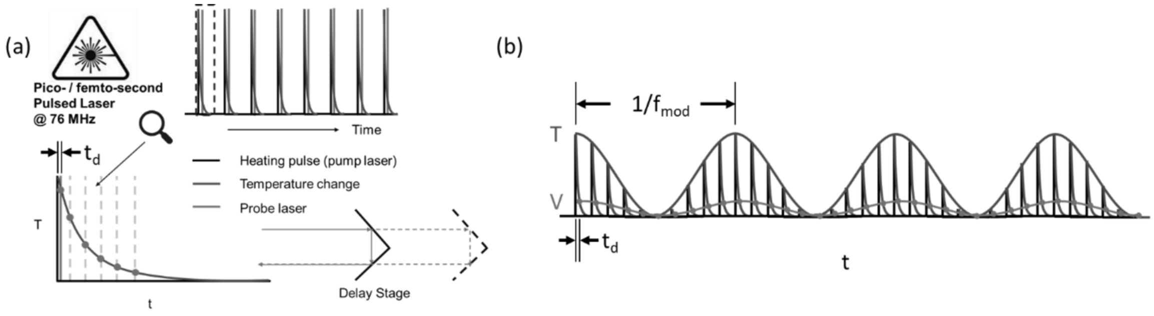

Figure 2.4: Schematic of the pump and probe pulse use on TDTR. (a) without modulation, (b) with pump modulation at frequency = f_{mod}, where T is the temperature at the sample surface and V is the measured photodetector voltage.

However, precise measurement of small temperature fluctuations is challenging. Therefore, an additional modulation is introduced to the pump laser to enable lock-in detection of small signals carried by the probe, which drastically improves the signal-to-noise ratio. As illustrated in **Figure 2.4 (b)**, the probe signal will carry the same frequency of f_{mod} but lag behind the pump. The lock-in amplifier outputs the detected probe signal at the reference frequency as in-phase (V_{in}) and out-of-phase (V_{out}) components. The magnitude of V_{in} corresponds to the surface temperature. The decay rate of V_{in} with respect to the delay time corresponds to the cooling rate of the sample, which can be used to extract thermal diffusivity.[15,16] In practice, the ratio of $-V_{in}/V_{out}$ is used to extract material thermal properties because it provides an easy way to correct for non-idealities, such as changes in the probe spot size at different delay times due to the change in optical path length.[17]

It should be noted that external phase shifts in cables, optics, and electronics must be accounted for during data extraction when performing FDTR and TDTR measurements. While the phase calibration procedure for TDTR is typically straightforward and often only briefly mentioned in the literature,[16] a more detailed outline of the procedure is described here. For TDTR, the external phase can be eliminated because, in an ideal scenario, the probe should be in phase with the pump at zero delay time. Therefore, the external phase (θ_{ext}) can be calculated as:

$$\theta_{ext} = -tan^{-1}\left(\frac{\Delta V_{out}(0)}{\Delta V_{in}(0)}\right) \tag{2.3}$$

where $\Delta V_{in}(0)$ and $\Delta V_{out}(0)$ can be extracted from the jump at $t_d = 0$, as illustrated in **Figure 2.5 (a). Figure 2.5 (b)** graphically illustrates that $V_{in}(0)$ and $V_{out}(0)$ result in the angle θ which needs to be corrected in order for the signal to be completely in-phase. Note that in a real scenario, $\Delta V_{out}(0) \neq V_{out}(0)$ because the pulsed pump laser induces a small background temperature rise, resulting in a non-zero out-of-phase signal. Since θ_{ext} should be constant throughout the measurement, the measured V_{in} and V_{out} data can be corrected by a rotation of axis calculation:

$$V_{in}' = V_{in}\cos(\theta_{ext}) - V_{out}\sin(\theta_{ext}) \tag{2.4}$$

$$V_{out}' = V_{out}\cos(\theta_{ext}) + V_{in}\sin(\theta_{ext}) \tag{2.5}$$

where V_{in}' and V_{out}' represent the corrected in-phase and out-of-phase component of the signal, respectively. **Figure 2.5 (b)** shows a graphic representation of the phase correction.

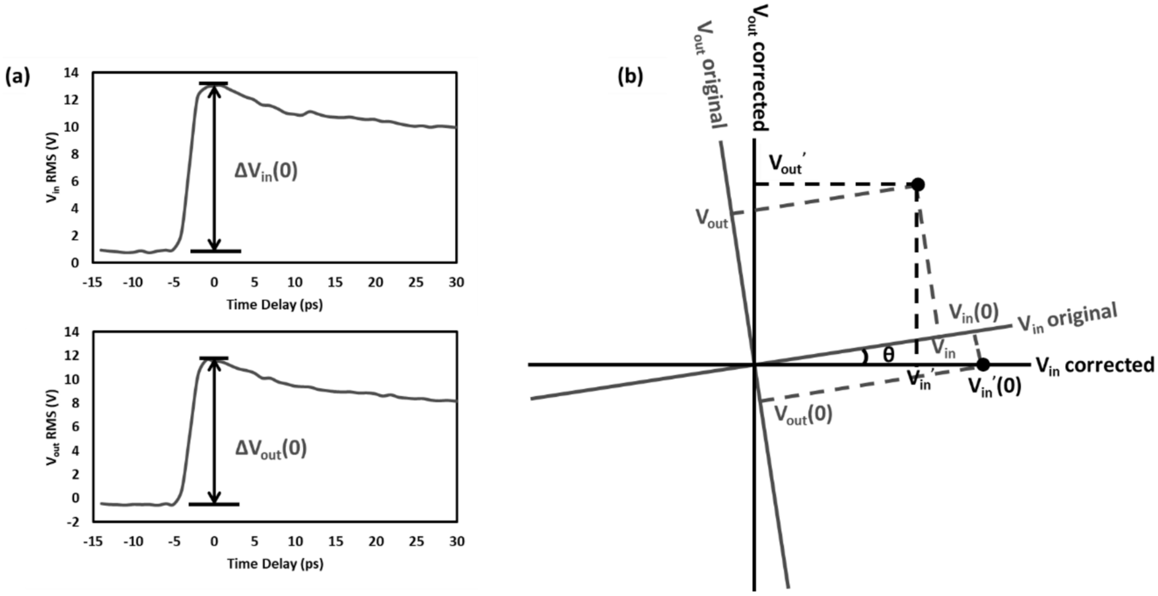

Figure 2.5: (a) The V_{in} and V_{out} components at zero delay time; V_{out} results from the external phase since the thermal response at $t_d = 0$ must be in-phase with the modulation. (b) Schematic of phase correction for TDTR data. In this schematic, it is assumed that $\Delta V_{out}(0) = V_{out}(0)$ for simplicity.

Eliminating the pump signal at the photodetector is crucial to prevent interference with lock-in detection. This is particularly important due to the small thermoreflectance coefficient (~1×10^{-4}) of transducers, which results in the probe signal carrying the thermal response being significantly weaker compared to the modulated pump signal. Multiple methods can be used to separate the probe and pump signal collected by the photodetector. Using the same wavelength pump and probe is possible by spatially separating them and blocking the pump at the detector.[18] Such an approach often involves implementing a secondary modulation with a mechanical chopper on the probe signal. This enables lock-in detection on the probe signal exclusively, as even a small amount of leaked pump signal can disrupt the measurement.[16] Spectral separation of pump and probe is another commonly used method. The 'two-tints' approach involves separating the pump and probe wavelengths by a small amount (~7 nm) using sharp-edged filters. This method is described in detail in the literature.[19] The Penn State setup implements a 'two-color' setup that incorporates a Bismuth Borate (BiB_3O_6) crystal, which uses second harmonic generation to halve the wavelength of the source laser (probe: 1028 nm) to 514 nm for use as the pump laser. While the spectrum separation makes it easy to filter out the pump signal for data acquisition, the pump power is greatly limited due to the finite conversion efficiency (<60%) and the damage threshold of the BiB_3O_6 crystal.

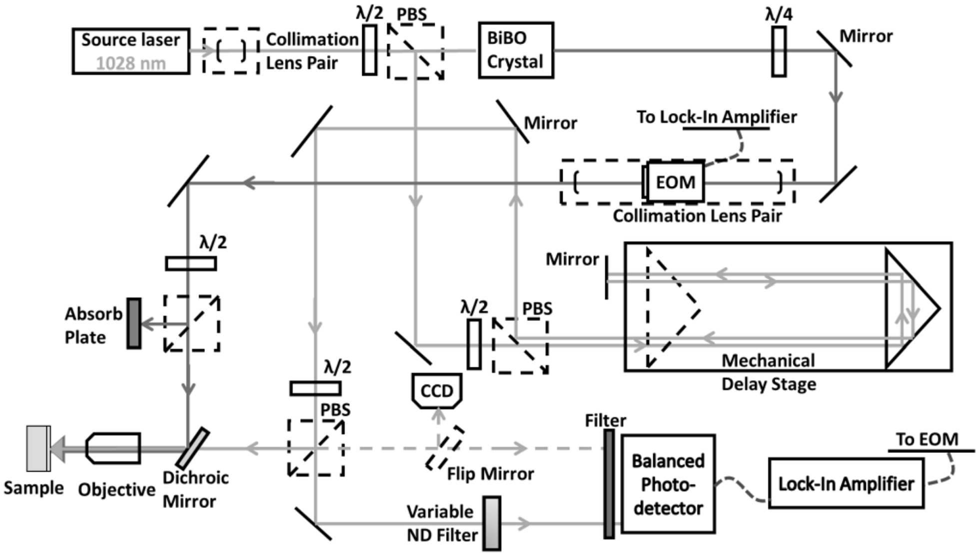

Figure 2.6: Schematic of the TDTR setup. The solid pink line is the probe path that originated from the 1028 nm source laser. The solid green line is the pump path from the BiB_3O_6 crystal that doubles the frequency of the source laser and converts it to 514 nm. The dashed pink line is the reflected probe path from the sample.

A schematic of the TDTR setup is shown in **Figure 2.6**. In the TDTR configuration, the source laser is a pulsed laser (Flint FL2-12 by Light Conversion) emitting light at a wavelength of 1028 nm, with a repetition rate of 76 MHz and a pulse width of approximately 100 fs. The source laser passes through a PBS and splits into two paths – one as a pump and one as a probe. The pump path passes through a BiB_3O_6 crystal (1030/515nm) and doubles in frequency, changing the laser's wavelength to 514 nm. The pump beam is amplitude-modulated via an electro-optical modulator (EOM, THORLABS EO-AM-NR-C4) to establish periodic heating. A collimation lens pair is used to assist beam alignment within the EOM. Subsequently, the pump laser passes through a half waveplate and PBS pair for intensity adjustment. A long-pass dichroic mirror reflects the pump laser onto the sample through an objective lens. The probe beam travels through a half waveplate and PBS pair before entering the mechanical delay stage (Newport Delay Line Stage with 225 mm travel). A mirror positioned at the exit end of the delay stage reflects the beam back into the delay stage. In the schematic shown in **Figure 2.6**, the two passes are artificially offset for demonstration clarity. This dual pass delay configuration effectively doubles the traveling distance of the light; a maximum delay time of 3000 ps can be achieved. After the probe exits the second pass, it is reflected by the PBS and passes through a half waveplate and PBS pair for intensity adjustment. The transmitted path goes through a variable ND filter and focuses on the balanced photodetector (Thorlabs PDB425A - AC) as the reference signal to eliminate background noise in the reflected probe signal. The reflected path transmits through the long-pass dichroic mirror and focuses on the sample surface using an objective lens. After reflecting from the sample surface, the probe beam carries the thermal response at the modulation frequency and is collected by the balanced photodetector. To prevent any pump signal from leaking through the dichroic mirror, a filter is positioned in front of the balanced photodetector. The signals collected by the balanced photodetector are processed by the lock-in amplifier (Zurich Instrument HF2LI) and a custom LabVIEW VI is used to collect data.

2.2.2 Additional Remarks and Insights

Given that the TDTR utilizes a 1028 nm laser as a probe, the beam is difficult to observe with the naked eye. However, it is crucial to align the post-sample beam based on the probe instead of the pump. Even though a visible portion of pump can leak through the dichroic mirror, it is not necessarily aligned with the probe. In fact, it is desirable for the pump to deviate from the probe post-sample to avoid the pump going into the photodetector and interfering with the lock-in detection. Special alignment tools, such as IR viewing cards and targets designed for the probe beam, are available on site to aid in tracking the probe during alignment.

High noise levels in the data are often observed during TDTR measurements, as illustrated by the low pump power data in **Figure 2.7**. These noise levels should be promptly observed during data acquisition and corrected to ensure accurate data. Common reasons for such noisy data include poor pump/probe alignment, low signal to noise ratio caused by insufficient pump or probe power, or a rough sample surface. As shown in **Figure 2.7**, increasing the pump power resulted in a significant decrease in noise level for the same sample. The required pump power depends on the thermal resistance of the material under test. A practical guideline for selecting the correct pump/probe power combination is to begin with approximately 1 mW of probe power and adjust the pump power until the phase and amplitude of the lock-in signal remain stable after proper alignment. It is suggested to use the minimal pump power required to achieve stable signal conditions, as further increases in power may not improve signal stability and could lead to unnecessary sample heating.

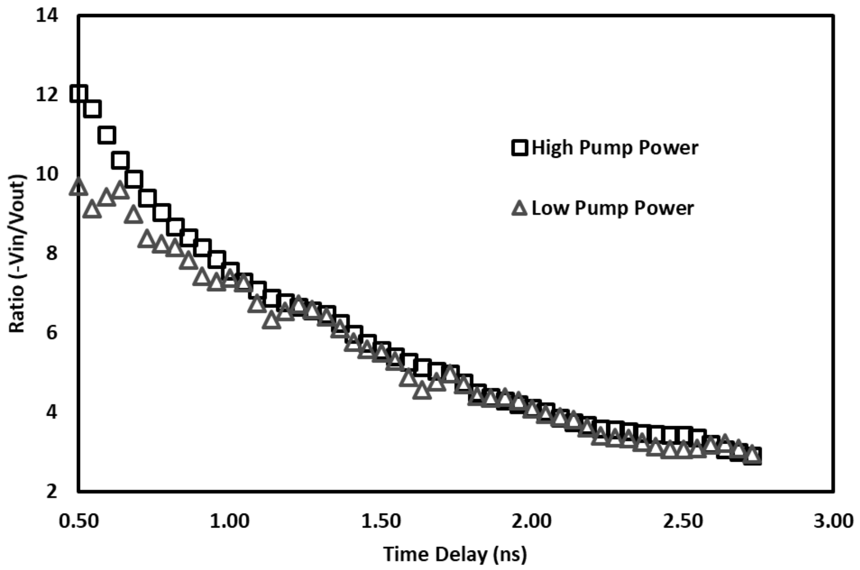

Figure 2.7: Comparison between a noisy data set and a good data set. The only difference between the two data sets was that a higher pump power was used in the good data set.

Moreover, TDTR is a highly customizable system. Although not implemented in the current Penn State setup, it is possible to add optical components to enable beam-offset[20] or elliptical beam[21] measurement that improves sensitivity to the in-plane thermal properties as a future upgrade. For example, to enable beam-offset, the pump needs to be precisely steered by the dichroic mirror. A piezoelectric gimbal mount (THORLABS PGM1SE) can be added to achieve this purpose.

2.3 Frequency-domain Thermoreflectance (FDTR)

2.3.1 Operating Principle and Instrumentation Setup

FDTR was first demonstrated by Aaron J. Schmidt *et al.* [1,22] and Jia Yang's thesis provides detailed instrumentation, data acquisition, and signal processing for the FDTR.[23] This thesis focuses on the system at Penn State and the procedure specific to this system.

FDTR is similar to TDTR in many aspects. They are both based on the transient temperature response of the material when a modulated heat source is provided by the pump laser. The probe signal reflected from the sample carries the same modulation frequency as the pump, allowing its amplitude (V_{in} and V_{out}) and phase (θ) to be measured by a lock-in amplifier. Instead of mapping the cooling rate in time space, FDTR measures the phase delay in the thermal response as a function of heat source (pump) modulation frequency. Thermal properties including a materials' thermal diffusivities and the boundary conductance between layers can be extracted.

A schematic of the FDTR is shown in **Figure 2.8**. FDTR systems share the same basic setup as SSTR and can be easily reconfigured into either system with simple modifications. The probe laser (COHERENT OBIS 532) travels through a collimation lens pair and a half waveplate ($\lambda/2$) and is split into two paths with the second polarized beam splitter (PBS). One probe path passes through the quarter waveplate ($\lambda/4$) and dichroic mirror, and it is focused on the sample; the other path passes through a variable neutral density filter (variable ND) and focuses on the balanced photodetector (Thorlabs PDB425A - AC) as the reference signal to eliminate background noise in the reflected probe signal. The pump laser (COHERENT OBIS 405) travels through a collimation lens pair and is digitally modulated with the lock-in amplifier (Zurich Instrument HF2LI). The pump is reflected by a dichroic mirror (Thorlabs DMLP490R) to align with the probe spot on the sample. The reflected probe beam from the sample surface contains information about the thermal response at the pump modulation frequency and is collected by the balanced photodetector. A 405 nm filter positioned in front of the balanced photodetector serves to block the pump signal leaking through the dichroic mirror; this is essential to prevent interference with lock-in detection, as the modulation frequency would also be present in the leaked light. This filter can be removed for phase calibration purposes.

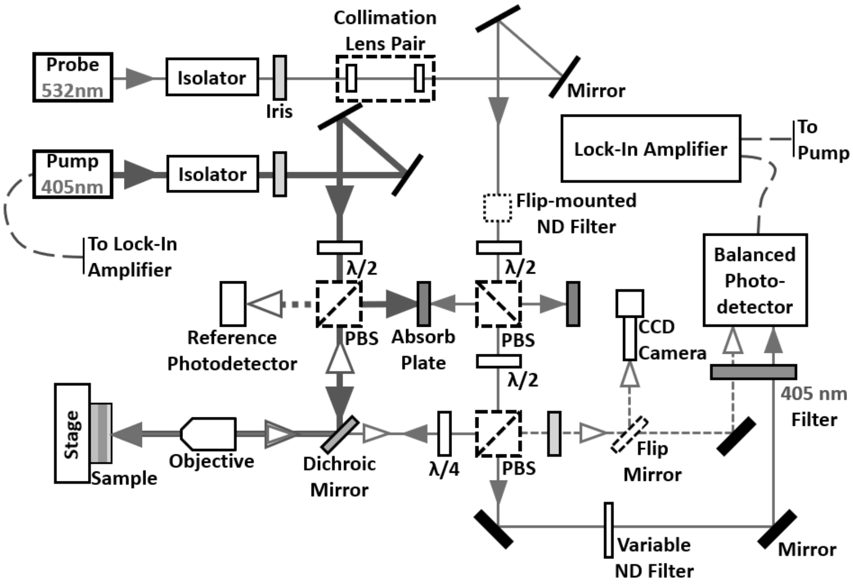

Figure 2.8: Schematic of the FDTR setup. The solid blue line is the pump path that originated from the 405 nm pump laser. The solid green line is the probe path that originated from the 532 nm probe laser. The dashed green line is the reflected probe path. The path length in this schematic is not true to scale.

To obtain the true thermal phase, the external phase (θ_{ext}) must be removed from the signal recorded by the lock-in amplifier. A popular method for phase correction involves redirecting a small amount of the pump beam into the photodetector to separately collect the phase delay between when the modulation is sent and when the signal is recorded.[2] If the optical path length between the redirected pump and the probe is matched, they should experience the same phase. This phase can then be subtracted from the measured probe phase to obtain the true thermal phase. Internally, we refer to this method as “path calibration”. In the Penn State FDTR setup, a different method, “leak calibration” is used. Due to the dichroic mirror's 0.18% transmission (Thorlabs’ data sheet) at a wavelength of 405 nm, enough pump can leak through it to reach the photodetector and create a strong lock-in signal. The 405 nm filter in front of the balanced photodetector blocks this part of the pump during measurement to eliminate interference. However, it can be removed to collect the phase in the pump for calibration purposes. “Leak calibration” requires matching pump and probe path lengths, which necessitates rigorous beam alignment to ensure that the lasers are centered along the path. As shown in **Figure 2.9**, the two calibration methods show good agreement, with a maximum 0.5-degree difference observed around 5 MHz. Although small, this difference resulted in fitted values for the Si thermal conductivity of 139.3 ± 9.3 W/mK and 130.7 ± 9.6 W/mK with the 'leak' and 'path' calibration methods, respectively. The small difference in phase between the two methods is believed to be caused by the pump and probe traveling through different optics in the “path calibration” setup, which involves additional mirrors and translation stages for the pump. In comparison, the pump and probe share much of the optics in the “leak calibration”. Due to this reason, “leak calibration” is preferred and is used throughout the studies presented in this thesis.

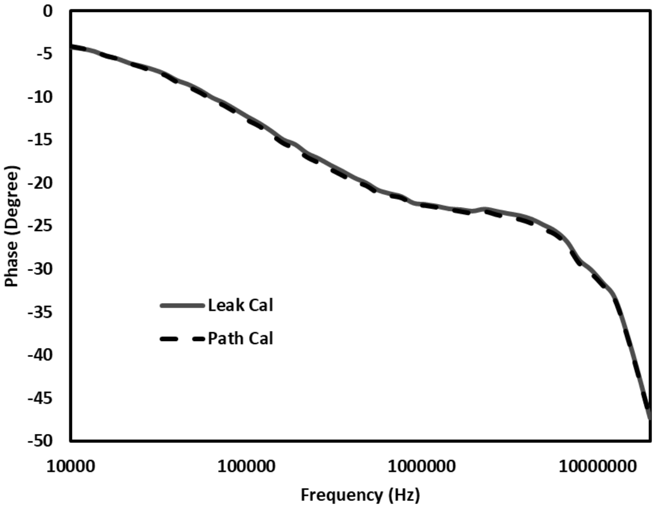

Figure 2.9: comparison between path calibration and leak calibration on a Si reference sample.

2.3.2 Additional Remarks and Insights

Although FDTR and TDTR are interchangeable in many scenarios, one key difference is that FDTR does not have a fixed thermal penetration depth during the sweep. Due to the large frequency range used to sweep FDTR, the thermal penetration depth can range from a few microns to over a hundred microns depending on the material. This introduces difficulties in measuring the thermal conductivity of inhomogeneous layers. For example, it is common for a film to exhibit lower crystal quality or smaller grain sizes at the nucleation side, leading to lower thermal conductivity closer to the interface. While TDTR can utilize different modulation frequencies to investigate thermal conductivity variation across the film thickness, as illustrated in this polycrystalline diamond case,[24] FDTR is fundamentally limited in its ability to perform similar studies. During this study, difficulties were encountered when attempting to use FDTR to investigate the effect of irradiation on a material's thermal conductivity due to the gradient in particle density along the thickness of the film.

It should be noted, however, that while varying penetration depth is unavoidable for a FDTR measurement, fitting over a segment of the frequency range is a good way to maximize sensitivity to specific parameters while minimizing unwanted contributions. The user should ensure enough data points are acquired to perform the least square fitting in any frequency range. After fitting a parameter within its most sensitive range, it is essential to verify its value by fitting it across the entire frequency range.

2.4 Sensitivity Analysis

The sensitivity (S_x) of a thermal model to a parameter x is quantified as the change of thermal response with a ±10% change in that thermal property value.

For TDTR[18]:

$$S_x = \frac{x}{-\frac{V_{in}}{V_{out}}} \frac{\partial - \frac{V_{in}}{V_{out}}}{\partial x} \tag{2.6}$$

For FDTR[1]:

$$S_x = \frac{\partial \theta}{d \ln(x)} \tag{2.7}$$

For SSTR[3]:

$$S_x = \frac{\Delta T_{1.1x}(r) - \Delta T_{0.9x}(r)}{\Delta T_x(r)} \tag{2.8}$$

where T is the calculated temperature and r is the effective radius defined as $r = \sqrt{r_{pump}^2 + r_{probe}^2}$. The additional division term in the SSTR sensitivity normalizes the magnitude of temperature rise between different samples to allow fair comparison.

Typically, a sensitivity greater than 0.1 is required for fitting that parameter. The unique sensitivity of these three techniques to each parameter allows for their collaborative use in extracting properties that may be challenging to determine with a single technique. The advantages of using all three capabilities are demonstrated in the later chapters of the thesis.

It is crucial to note that sensitivities are calculated based on assumed parameter values. If significant differences between assumed and fitted values arise during the fitting process, it is important to update the assumed values and recalculate the sensitivities accordingly. This is illustrated in a study on thermal boundary conductance (TBC) between GaN and SiC.[25] Initially assuming a TBC of 200 MW/m^{2}K, a sensitivity greater than 0.1 was observed, as shown in **Figure 2.10** TBC$_{GaN/SiC}$ (200 MW/m^{2}K). However, subsequent fitting suggested that the TBC would exceed 300 MW/m^{2}K, causing the sensitivity to drop below 0.1, as shown in **Figure 2.10** TBC$_{GaN/SiC}$ (300 MW/m^{2}K). Consequently, the accurate value cannot be determined.

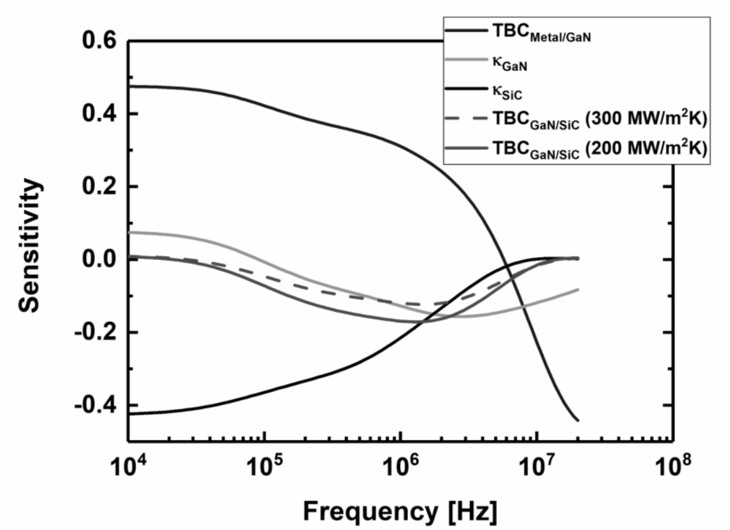

Figure 2.10: Sensitivity plot for a GaN film on SiC measured by FDTR. In the legend, κ_{GaN} is the thermal conductivity of GaN. κ_{SiC} is the thermal conductivity of SiC. TBC is the thermal boundary conductance.

2.5 Supporting Characterization Techniques

2.5.1 Laser Spot Size Characterization

Accurate pump and probe size are critical for all three thermoreflectance techniques. To measure the $1/e^2$ radius of the laser spot, a beam profiler (Thorlabs BP209-VIS) is used. The knife edge mode is suitable for measuring beams from 2.5 μm to 20 μm in diameter. Users should follow the Thorlabs manual when performing beam characterization.

2.5.2 Transducer Thickness Measurement

The transducer thickness is a highly sensitive parameter in the model. A ±2 nm variation on an 80 nm transducer can yield approximately a 7% error in fitted thermal properties. Therefore, ensuring precise measurement of the transducer thickness is important for accurate analysis. A Si and a sapphire piece are added to each transducer deposition batch as witness samples. Multiple techniques were used during the study to characterize the film thickness.

X-Ray Reflectivity (XRR) can accurately extract the thickness and density of the transducer on top of a Si or sapphire substrate. It is nondestructive and measures a large area (~10 mm × 10 mm) for good spatial averaging. However, it is worth noting that the instrument at Penn State Material Research Institute (Malvern Panalytical - MRD) is often configured for X-Ray Diffraction (XRD), requiring an appointment in advance or additional training to reconfigure the system. Alignment and acquisition would take a total usage time averaging ~ 1 hour for each thickness measurement.

A cross-sectional scanning electron microscope (SEM) was also used. The high contrast between the metal transducer and substrate allowed accurate thickness measurement. An advantage of SEM is its capability to visually assess the quality of the transducer, including uniformity and roughness. Multiple locations should be scanned for averaging to get an accurate result.

Profilometry (Tencor P16+) is an easy method to characterize the transducer thickness. During deposition, Kapton tapes can be used to mask a thin strip of transducer on the witness samples, and the step height of the transducer can be measured with a fast scan of ~30 seconds. When conducting profilometry, it is important to consider the curvature and roughness of the substrate; it has been observed that the sapphire witness sample is better suited for this purpose. It is also important to avoid reading data from the edge where the Kapton tape was lifted off.

Pico-second acoustic measurement is a built-in capability of the TDTR which allows for the extraction of the transducer thickness based on the time it takes for the acoustic wave to reach the interface, reflect back, and be detected. The accuracy of pico-second acoustic measurement relies on the speed of sound in the transducer, which is typically consistent if the transducer has full density and good smoothness.

A comprehensive study was performed using different techniques to measure the thickness of a same transducer. Good agreements were observed with ~ ±2 nm variation. This ±2 nm should be considered in the error analysis as the uncertainty in the transducer. Profilometry is often the preferred method due to its simplicity and efficiency.

Chapter References

[1] A.J. Schmidt, R. Cheaito, and M. Chiesa, "A frequency-domain thermoreflectance method for the characterization of thermal properties," Rev. Sci. Instrum. **80**(9), 94901 (2009).

[2] J. Yang, C. Maragliano, and A.J. Schmidt, "Thermal property microscopy with frequency domain thermoreflectance," Rev. Sci. Instrum. **84**(10), 104904 (2013).

[3] J.L. Braun, D.H. Olson, J.T. Gaskins, P.E. Hopkins, D.H. Olson, and J.T. Gaskins, "A steady-state thermoreflectance method to measure thermal conductivity," Rev. Sci. Instrum. **90**(2), 24905 (2019).

[4] Y. Wang, J.Y. Park, Y.K. Koh, and D.G. Cahill, "Thermoreflectance of metal transducers for time-domain thermoreflectance," J. Appl. Phys. **108**(4), 43507 (2010).

[5] R.B. Wilson, B.A. Apgar, L.W. Martin, and D.G. Cahill, "Thermoreflectance of metal transducers for optical pump-probe studies of thermal properties," Opt. Express **20**(27), 2267–2269 (2012).

[6] Z. Cheng, F. Mu, X. Ji, T. You, W. Xu, T. Suga, X. Ou, D.G. Cahill, and S. Graham, "Thermal visualization of buried interfaces enabled by ratio signal and steady-state heating of time-domain thermoreflectance," ACS Appl. Mater. Interfaces **13**(27), 31843–31851 (2021).

[7] M.S. Bin Hoque, Y.R. Koh, K. Aryana, E.R. Hoglund, J.L. Braun, D.H. Olson, J.T. Gaskins, H. Ahmad, M.M.M. Elahi, J.K. Hite, Z.C. Leseman, W.A. Doolittle, and P.E. Hopkins, "Thermal conductivity measurements of sub-surface buried substrates by steady-state thermoreflectance," Rev. Sci. Instrum. **92**(6), 64906 (2021).

[8] J.L. Braun, and P.E. Hopkins, "Upper limit to the thermal penetration depth during modulated heating of multilayer thin films with pulsed and continuous wave lasers: A numerical study," J. Appl. Phys. **121**(17), 1–13 (2017).

[9] J. Cho, "Thermal properties of anisotropic and/or inhomogeneous suspended thin films assessed

via dual-side time-domain thermoreflectance: a numerical study," Nanoscale Microscale Thermophys. Eng. **22**(1), 6–20 (2018).

[10] P. Jiang, X. Qian, R. Yang, and L. Lindsay, "Anisotropic thermal transport in bulk hexagonal boron nitride," Phys. Rev. Mater. **2**(6), 64005 (2018).

[11] Z. Cheng, N. Tanen, C. Chang, J. Shi, J. McCandless, D. Muller, D. Jena, H.G. Xing, and S. Graham, "Significantly reduced thermal conductivity in β-$(Al_{0.1}Ga_{0.9})_2O_3/Ga_2O_3$ superlattices," Appl. Phys. Lett. **115**(9), 92105 (2019).

[12] M.N. Luckyanova, J.A. Johnson, A.A. Maznev, J. Garg, A. Jandl, M.T. Bulsara, E.A. Fitzgerald, K.A. Nelson, and G. Chen, "Anisotropy of the thermal conductivity in gaas/alas superlattices," Nano Lett. **13**(9), 3973–3977 (2013).

[13] Z. Cheng, F. Mu, L. Yates, T. Suga, and S. Graham, "Interfacial thermal conductance across room-temperature-bonded GaN/diamond interfaces for GaN-on-diamond devices," ACS Appl. Mater. Interfaces **12**(7), 8376–8384 (2020).

[14] J. Cho, Z. Li, E. Bozorg-Grayeli, T. Kodama, D. Francis, F. Ejeckam, F. Faili, M. Asheghi, and K.E. Goodson, "Improved thermal interfaces of gan–diamond composite substrates for HEMT applications," IEEE Trans. Components, Packag. Manuf. Technol. **3**(1), 79–85 (2013).

[15] D.G. Cahill, "Analysis of heat flow in layered structures for time-domain thermoreflectance," Rev. Sci. Instrum. **75**(12), 5119–5122 (2004).

[16] P. Jiang, X. Qian, and R. Yang, "Tutorial: Time-domain thermoreflectance (TDTR) for thermal property characterization of bulk and thin film materials," J. Appl. Phys. **124**(16), 161103 (2018).

[17] D.G. Cahill, K. Goodson, and A. Majumdar, "Thermometry and thermal transport in micro/nanoscale solid-state devices and structures," J. Heat Transfer **124**(2), 223–241 (2001).

[18] P. Jiang, X. Qian, and R. Yang, "Time-domain thermoreflectance (TDTR) measurements of anisotropic thermal conductivity using a variable spot size approach," Rev. Sci. Instrum. **88**(7), 74901 (2017).

[19] K. Kang, Y.K. Koh, C. Chiritescu, X. Zheng, and D.G. Cahill, "Two-tint pump-probe measurements using a femtosecond laser oscillator and sharp-edged optical filters," Rev. Sci. Instrum. **79**(11), 114901 (2008).

[20] J.P. Feser, and D.G. Cahill, "Probing anisotropic heat transport using time-domain thermoreflectance with offset laser spots," Rev. Sci. Instrum. **83**(10), 104901 (2012).

[21] P. Jiang, X. Qian, and R. Yang, "A new elliptical-beam method based on time-domain thermoreflectance (TDTR) to measure the in-plane anisotropic thermal conductivity and its comparison with the beam-offset method," Rev. Sci. Instrum. **89**(9), 94902 (2018).

[22] A.J. Schmidt, R. Cheaito, and M. Chiesa, "Characterization of thin metal films via frequency-domain thermoreflectance," J. Appl. Phys. **107**(2), 24908 (2010).

[23] J. Yang, "Thermal property measurement with frequency domain thermoreflectance," Thesis, Boston University, (2016). pp. 7-27

[24] A. Sood, J. Cho, K.D. Hobart, T.I. Feygelson, B.B. Pate, M. Asheghi, D.G. Cahill, and K.E. Goodson, "Anisotropic and inhomogeneous thermal conduction in suspended thin-film polycrystalline diamond," J. Appl. Phys. **119**(17), 175103 (2016).

[25] D.C. Shoemaker, Y. Song, K. Kang, M.L. Schuette, J.S. Tweedie, S.T. Sheppard, N.S. McIlwaine, J.-P. Maria, and S. Choi, "implications of interfacial thermal transport on the self-heating of GaN-on-SiC high electron mobility transistors," IEEE Trans. Electron Devices **70**(10), 5036–5043 (2023).

Chapter 3

UWBG Ga_2O_3 Electronics

3.1 Thermal property measurement

3.1.1 Introduction

β-phase gallium oxide (β-Ga_2O_3) is an emerging ultra-wide bandgap (UWBG) semiconductor which promises improvements in the performance and manufacturing cost of deep-ultraviolet (DUV) solar blind photodetectors[1] and power electronic devices[2]. The ultra-wide bandgap of β-Ga_2O_3 (E_G~4.8 eV[3]) renders the material transparent from visible to ultraviolet (UV) wavelengths. Moreover, alloying with Al_2O_3, i.e., forming a β-phase solid solution $(Al_xGa_{1-x})_2O_3$ (where x is the Al composition), allows bandgap engineering which makes the material suitable for DUV optoelectronic applications.[4] The large bandgap energy also translates into a high critical electric field of ~8 MV/cm,[2] which gives promise to the development of compact power switches with kV-class breakdown voltages that are superior to wide bandgap semiconductor devices based on GaN and SiC. Another attractive attribute of β-Ga_2O_3 is that low cost substrates with high crystalline quality can be manufactured using melt-growth techniques, similar to the case of silicon wafers.[2]

Extensive efforts are being made on the heteroepitaxy of β-phase Ga_2O_3 and $(Al_xGa_{1-x})_2O_3$ films on non-native substrates to realize β-Ga_2O_3-on-sapphire DUV detectors with backside illumination capabilities and also heterojunction devices such as β-$(Al_xGa_{1-x})_2O_3/Ga_2O_3$ modulation-doped field effect transistors (MODFETs)[5]. Heteroepitaxy of β-Ga_2O_3 on high thermal conductivity substrates is also drawing significant attention as a potential solution for device overheating[6–9], stemming from the poor intrinsic thermal conductivity of bulk β-Ga_2O_3 (10.9-27 W/m·K[10,11]). Among diverse growth techniques, metalorganic vapor phase epitaxy (MOVPE) and low-pressure chemical vapor deposition (LPCVD) provide means to produce homogeneous, large-area, and optoelectronic/electronic-grade β-Ga_2O_3 and β-$(Al_xGa_{1-x})_2O_3$ epitaxial layers.

The key advantages of MOVPE growth of β-phase Ga_2O_3 and $(Al_xGa_{1-x})_2O_3$ films include the high growth rate (~10 μm/hr)[12], large growth process window[13], ability to handle large-area wafers, and low density of electronic defects[14]. N-type conductivity has been achieved for a wide range of carrier densities ($10^{16} – 10^{20}$ cm^{-3}) using Si as a dopant[15]. In addition, films with mobility values close to the theoretical limit of ~200 cm^2/Vs have been realized.[15] These are the highest mobility values reported so far for doped and undoped β-Ga_2O_3. By using N_2O as an oxygen precursor, the background doping in the films can be reduced to ~10^{14} cm^{-3}.[16] By reducing the acceptor densities to $2 \times 10^{13}cm^{-3}$, a record high low temperature hall mobility of 23,000 cm^2/Vs has been achieved.[17] The combination of high room temperature and low temperature mobilities confirm the high-quality of MOVPE-grown β-Ga_2O_3 thin films. In addition, significant progress has been made in the growth of (010) oriented β-$(Al_xGa_{1-x})_2O_3$[18–20]. N-type doping was realized for a wide range of Si doping for Al compositions up to x=0.33.[18,19] The Al composition can be further increased to x~0.5 by growing on (-201) and (100) bulk substrates.[21,22]

Low pressure chemical vapor deposition (LPCVD) is a scalable and low-cost film growth technique that has been demonstrated to produce high-quality β-Ga_2O_3 with a wide range of growth rates (~0.5-10 μm/h). High purity metallic gallium and oxygen are used as precursors. Argon is used as the carrier gas. Both homo- and heteroepitaxy of β-Ga_2O_3 with controllable n-type doping have been demonstrated by LPCVD.[23–26] ($\bar{2}01$)-oriented β-Ga_2O_3 films grown on c-plane sapphire substrates were shown to exhibit a relatively high dislocation density due to the large lattice mismatch.[23,24,27] However, it was demonstrated that the β-Ga_2O_3 crystalline quality and electronic transport properties can be significantly improved by growing on vicinal sapphire substrates, i.e., off-axis towards <11-20>.[23] The in-plane rotational domains were significantly suppressed via the use of off-axis sapphire substrates. Growth parameters of LPCVD β-Ga_2O_3 including growth temperature, chamber pressure, substrate preparation, and precursor flow rates have been comprehensively studied.[28,29]

Monoclinic β-Ga_2O_3 exhibits a relatively low and anisotropic thermal conductivity. For example, the [010] direction shows a bulk thermal conductivity of 21.5-27.0 W/m·K, which is about two times higher than that along the [100] direction (9.5-16.3 W/m·K).[10,11,30] The thermal conductivity along the direction perpendicular to the $(\bar{2}01)$ plane, which is most relevant to the current study, was reported to be 13.2-14.9 W/m·K.[10,11,30] As compared to bulk substrates, there are phonon scattering mechanisms that become prominent in thin films. First, when the thickness of a crystalline solid becomes comparable to the phonon mean free paths, incoherent phonon-boundary scattering reduces the thermal conductivity.[31,32] **Figure 3.1** shows the thermal conductivity accumulation function of bulk β-Ga_2O_3 in the direction perpendicular to the $(\bar{2}01)$ plane, obtained from first principles calculation. The calculation results indicate the contribution of the acoustic phonon branches (that are the dominant heat carriers) to the bulk thermal conductivity; it was shown that low-frequency optical phonon modes with non-negligible group velocities would also contribute to the bulk thermal conductivity of β-Ga_2O_3.[33] Results indicate that the intrinsic mean free path of the acoustic phonons of β-Ga_2O_3 ranges from several nm to ~1 μm.[30] Therefore, β-Ga_2O_3 films with a thickness on the order of (and less than) ~1 μm would exhibit a strong film thickness dependence for their thermal conductivities. Second, the β-Ga_2O_3 films formed via heteroepitaxy typically possess higher concentrations of point and extended defects (including dislocations and rotational grains), as compared to melt-grown bulk substrates. Therefore, the thermal conductivity of heteroepitaxial β-Ga_2O_3 thin films can be considerably lower than that of a bulk substrate due to phonon-defect and phonon-grain boundary scattering effects.[31,32] The impact of Ga and O vacancies on the suppression of the thermal conductivity of β-Ga_2O_3 has been studied via first-principles density functional theory (DFT) calculation.[33] A weak doping dependence (phonon-impurity scattering) of the thermal conductivity of bulk substrates has been experimentally demonstrated.[10] To this end, experimental studies on how the crystallinity of β-Ga_2O_3 thin films (along with the film thickness) impacts the thermal conductivity have yet to be reported.

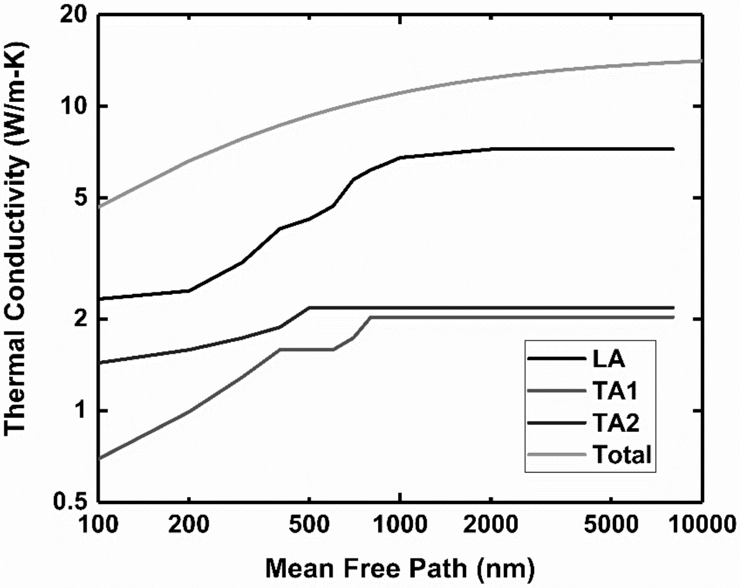

Figure 3.1: The thermal conductivity accumulation function for the acoustic branches of bulk β-Ga_2O_3 in the direction perpendicular to the ($\bar{2}01$) plane (at room temperature), derived from first principles calculations[30]. LA and TA are the abbreviations for longitudinal acoustic and transverse acoustic, respectively. The total thermal conductivity is obtained from the Debye-Callaway model[11]. Details can be found in the THEORETICAL CALCULATIONS section.

The film size effect on the thermal conductivity of polycrystalline Ga_2O_3 thin films grown via open atmosphere annealing of a GaN surface has been reported;[34] the measured thermal conductivities of films with a thickness range from 12.5 nm to 895 nm increased from 0.34 W/mK to 8.85 W/mK. Polycrystalline Ga_2O_3 thin films grown onto single crystalline diamond substrates via atomic layer deposition (ALD) were shown to exhibit a very low thermal conductivity of 1.5-1.76 W/mK for film thicknesses range of 28-115 nm.[35] This was found to be caused by the nanocrystalline nature of the films with an average grain size of 10-20 nm. It should be noted that the materials used in the aforementioned studies are polycrystalline, and do not meet requirements (e.g., electronic transport characteristics) for optoelectronic/electronic-grade materials.

The film thickness dependence of the thermal conductivity of single crystalline β-Ga_2O_3 has been studied using (100)-oriented films prepared via mechanical exfoliation from a bulk substrate.[36] The thermal conductivity in the [100] direction was shown to increase from 4.7 to 11.5 W/m·K when the film thickness increased from 206 to 768 nm, approaching the bulk value of 13 W/m·K. Similarly, the thermal conductivity of a 427-nm-thick (100)-oriented β-Ga_2O_3 exfoliated film transferred onto diamond was shown to exhibit a thermal conductivity of 8.4 W/m·K, which is 35% lower than that of a bulk crystal.[37] Exfoliated films offer an opportunity to exclusively study the phonon-boundary scattering effects (i.e., the film thickness dependence of the β-Ga_2O_3 thermal conductivity), due to their high crystal quality. However, mechanical exfoliation and transfer of Ga_2O_3 are not scalable approaches for the mass production of commercial devices. Thermal transport across ($\bar{2}01$)-oriented β-Ga_2O_3 thin films heterogeneously integrated with 4H-SiC substrates via ion-cutting and surface activation bonding techniques has been demonstrated.[38] The thermal conductivity of unintentionally doped (245 nm thick; 5.35 W/m·K) and Sn-doped (255 nm thick; 2.53 W/m·K) ($\bar{2}01$)-oriented β-Ga_2O_3 epitaxial films grown on sapphire via pulsed laser deposition (PLD) has been studied.[39] PLD is a popular film growth technique in laboratory research settings because thin films with high crystal quality can be produced. Historically, the high cost, low throughput, and very limited area of uniform deposition are major limitations of PLD for mass production of devices. Wafer-level mass production was only recently (2024) introduced by Lam's research with their PLD system (Pulsus^{TM}). On the other hand, MOVPE and LPCVD methods offer scalable precision growth capabilities that are necessary to construct electronic and photonic devices. For this reason, MOVPE and LPCVD have attracted much attention in both fundamental and industrial perspectives. However, the resulting thermal conductivity of β-Ga_2O_3 thin films heteroepitaxially grown via MOVPE and LPCVD remain unexplored.

In addition, the thermal conductivity data of β-$(Al_xGa_{1-x})_2O_3$, which is a solid solution of monoclinic β-Ga_2O_3 and corundum α-Al_2O_3, are scarce in the open literature. Only one data point at x=0.18 has been reported to date[6] while this information is critical for the electro-thermal co-design of β-Ga_2O_3 based electronic devices. For example, in a β-Ga_2O_3 modulation-doped field-effect transistor (MODFET)[5], a β-$(Al_xGa_{1-x})_2O_3/Ga_2O_3$ heterostructure is formed to create a two-dimensional electron gas (2DEG)[40] with electron mobility (potentially greater than 500 $cm^2/V\cdot s$[41]) higher than that for bulk β-Ga_2O_3 (<100 $cm^2/V\cdot s$[2]). High-power β-Ga_2O_3 electronics are known to suffer from overheating due to the extremely high operational heat flux and the poor thermal conductivity of the base material.[6–9] Flip-chip heterointegration has been proposed to be a viable solution to overcome the intense device self-heating in β-$(Al_xGa_{1-x})_2O_3/Ga_2O_3$ MODFETs.[6,7] For this device configuration, the thermal resistance associated with the β-$(Al_xGa_{1-x})_2O_3$ barrier layer must be understood to optimize the thermal design.

In this work, the cross-plane thermal conductivities of MOVPE and LPCVD grown β-phase Ga_2O_3 and $(Al_xGa_{1-x})_2O_3$ heteroepitaxial thin films have been measured using time-domain thermoreflectance (TDTR). The crystal quality of the films, resulting from growth on on-axis/off-axis c-plane sapphire substrates, was evaluated via X-ray diffraction and Raman spectroscopy. The measured data were compared with the Debye-Callaway model predictions to elucidate the fractional contributions of film thickness and the crystallinity to the reduction of the thermal conductivity of the thin films as compared to the intrinsic bulk value. Interfacial thermal transport was studied via frequency-domain thermoreflectance (FDTR) measurements and scanning transmission electron microscopy (STEM).

3.1.2 Results and Discussion

Unintentionally doped (UID) β-Ga_2O_3 thin films with a large film thickness range of 160-4350 nm were heteroepitaxially grown on sapphire substrates with chemical and crystallographic compatibility, via LPCVD and MOVPE. Growth was performed on *c*-plane sapphire substrates with off-axis angles of 0° and 6° toward <$11\bar{2}0$>. This is because β-Ga_2O_3 films grown via halide vapor phase epitaxy (HVPE)[42] and LPCVD[23] on 6° off-angled *c*-plane sapphire substrates were shown to possess improved crystallinity, mainly because of the promotion of step flow growth and enhancement in the in-plane orientation. Details of the MOVPE and LPCVD growth procedures can be found in the EXPERIMENTAL METHODS section.

Representative top-side 50k× scanning electron microscopy (SEM) images of the MOVPE and LPCVD grown films are shown in **Figure 3.2**. The LPCVD films grown on sapphire substrates with 0° off-axis angle show pseudo hexagonal rotational domains (**Figure 3.2 (d)**). In contrast, improvement in the surface morphology is observed in the films grown on 6° off-cut substrates as evidenced by the domains aligned along the direction of the off-cut (**Figure 3.2 (e)**). MOVPE-grown films also show an improvement in the surface morphology; however, in a less pronounced manner (**Figure 3.2 (b)** and **(c)**). For comparison, SEM was also performed on a 650 μm thick commercial Fe-doped ($\bar{2}01$)-oriented bulk substrate (**Figure 3.2 (a)**).

Cross-sectional 20k× SEM images were taken on all samples to determine the β-Ga_2O_3 layer thickness (**Figure 3.2 (f)-(i)**). The average thicknesses of the β-Ga_2O_3 layers were calculated from six locations across each sample. The thickness of the Au metal transducers deposited on all samples for the TDTR measurements was measured to be 81.3±2 nm for all samples. These results were confirmed through both cross-sectional SEM and X-Ray reflectometry (XRR) analyses.

FDTR and TDTR measurements require a smooth sample surface to acquire reliable data.[31] Typically, a root-mean-square (RMS) surface roughness less than ~30 nm is necessary. The atomic force microscopy (AFM) image of a representative sample (LPCVD-grown β-Ga_2O_3 on 6° offcut sapphire; **Figure 3.2 (j)**) shows an RMS surface roughness of 14 nm. Only samples with an RMS surface roughness comparable to this sample, that would exhibit a similar reflected signal strength, were included in this study.

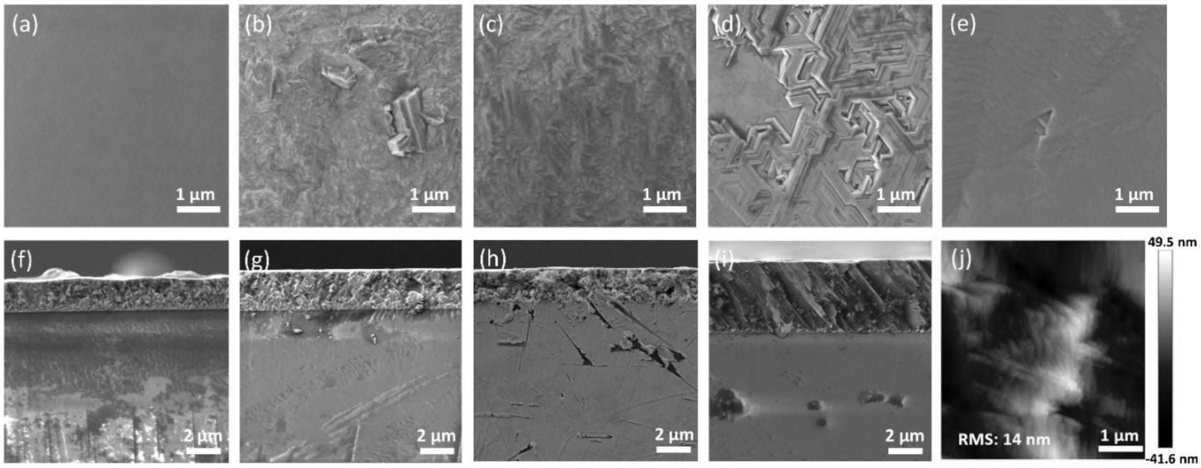

Figure 3.2: Representative top-view 50k× SEM images of (a) a commercial bulk substrate, MOVPE-grown films on (b) an on-axis c-plane sapphire substrate and (c) 6°off-cut sapphire substrate. LPCVD-grown films on (d) 0° and (e) 6°off-cut substrates. Also shown are cross-sectional 20k× SEM images of (f) MOVPE-grown films on 0° and (g) 6°off-cut sapphire substrates, (h) LPCVD-grown films on 0° and (i) 6°off-cut substrates. (j) AFM image and RMS surface roughness of an LPCVD-grown β-Ga_2O_3 film on a 6° offcut substrate.

X-ray diffraction (XRD) 2θ scans for the Fe-doped commercial substrate as well as the MOVPE- and LPCVD-grown samples are shown in **Figure 3.3**. XRD 2θ scans for the bulk substrate shows the $(\bar{2}01)$ orientation of the β-Ga_2O_3 material, as expected, with minor out-of-plane reflections (observable only on a logarithmic scale). The 2θ scans of the MOVPE and LPCVD-grown films reveal their $(\bar{2}01)$ orientation accompanied by the (0006) sapphire substrate peak.

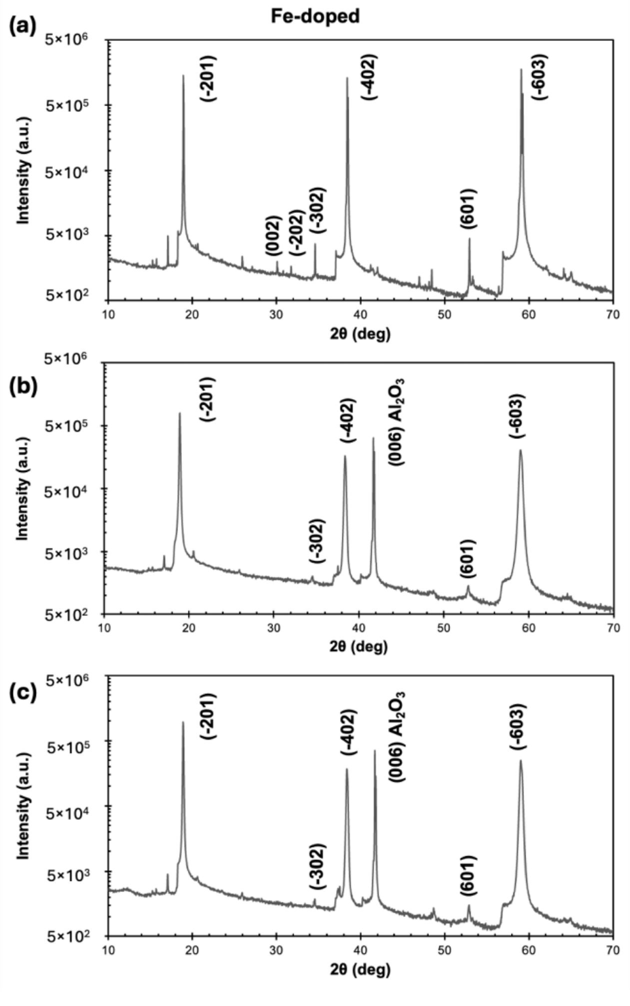

Figure 3.3: Representative XRD 2θ scans of (a) the $(\bar{2}01)$-orientated β-Ga_2O_3 substrate, (b) a MOVPE-grown film on a sapphire substrate, and (c) a LPCVD-grown film on a sapphire substrate.

In addition to determining the phase and orientation, the crystalline quality of the β-Ga_2O_3 films was evaluated by XRD rocking curve measurements. **Figure 3.4** shows the XRD rocking curves of symmetric ($\bar{4}02$) reflection peaks of the β-Ga_2O_3 films and the bulk substrate. The XRD rocking curve ω scan of the commercial substrate (**Figure 3.4 (a)**) shows a sharp narrow peak with a full-width-at-half-maximum (FWHM) of 0.018° (64.8 arcsec). The FWHM of the XRD rocking curves of the films grown on 6° off-cut substrates (while being significantly broader than the FWHM of the bulk β-Ga_2O_3) consistently exhibited lower values than those grown on 0° off-cut substrates, which could indicate lower screw and edge dislocation density.[43,44]

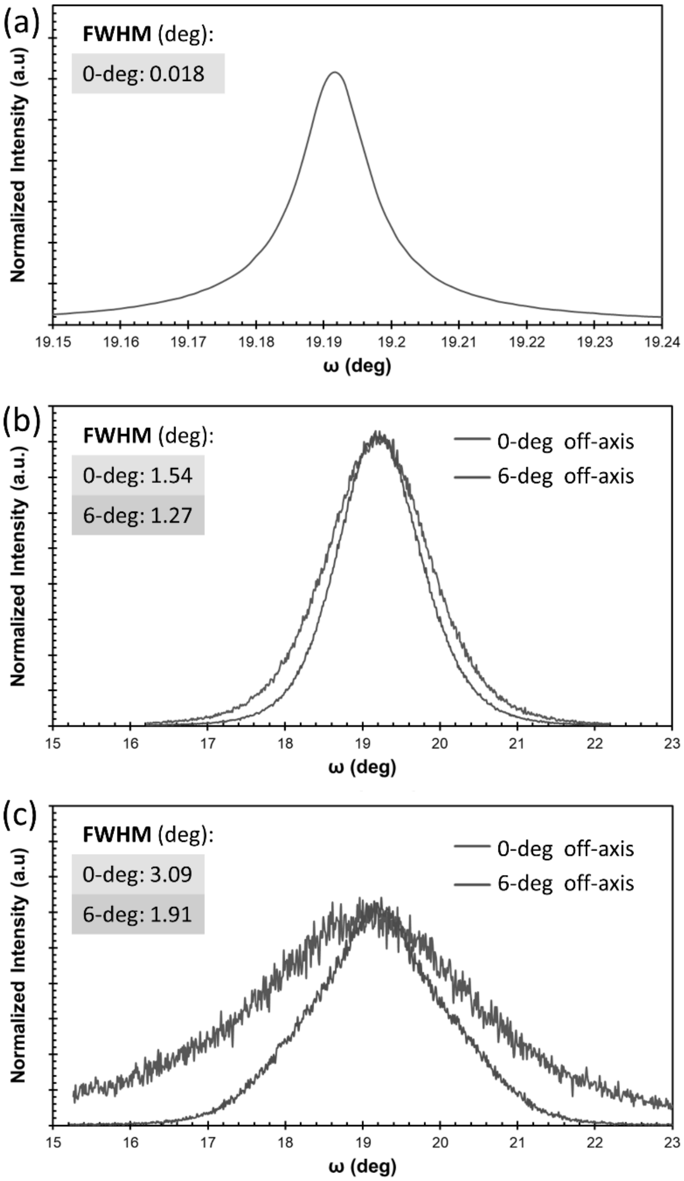

Figure 3.4: Representative XRD rocking curves, i.e., the symmetric ($\bar{4}02$) reflection peaks of (a) the (-201) oriented β-Ga_2O_3 bulk substrate, (b) on-axis vs. 6°off-axis MOVPE grown films, and (c) on-axis vs. 6°off-axis LPCVD grown films.

Additional qualitative assessment of the crystal quality of the films was made by performing Raman spectroscopy measurements. To assess the crystalline quality of the β-Ga_2O_3 thin films, the FWHM of the $A_g^{(3)}$ Raman peak[45] near 199.7 cm^{-1} was analyzed and compared to the linewidth of the $A_g^{(3)}$ peak of the bulk substrate (**Figure 3.5 (a)**). According to the energy-time uncertainty relation, as the crystalline quality increases, the linewidth of the phonon mode will decrease because the phonon lifetime increases.[46] For the Fe-doped bulk sample, an average FWHM of 1.62 cm^{-1} was calculated. As shown in **Figure 3.5 (b)**, The MOVPE 6° off-axis samples exhibited narrower FWHM values than on-axis grown samples, suggesting superior crystalline quality. Similar observations were found in the LPCVD-grown films, i.e., the 6° off-axis grown films exhibit narrower $A_g^{(3)}$ Raman peaks, as compared to the on-axis grown films, indicating better crystallinity **(Figure 3.5 (c))**. The Raman measurement results are consistent with the FWHM analysis performed via XRD rocking curve measurements.

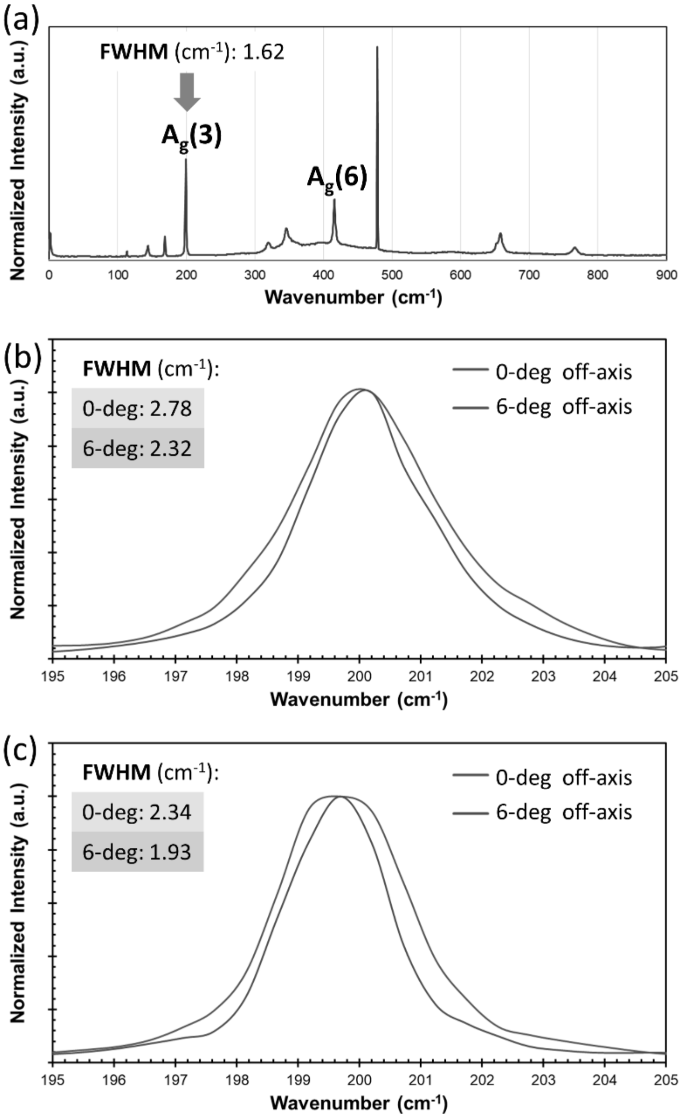

Figure 3.5: (a) Raman spectrum of the ($\bar{2}01$)-orientated β-Ga_2O_3 substrate. (b) Representative FWHM comparison of the Raman $A_g^{(3)}$ mode for on-axis vs. 6°off-axis MOVPE grown films. (c) A similar comparison for representative LPCVD grown films.

Cross-plane thermal conductivity measurements of ($\bar{2}01$)-oriented MOVPE and LPCVD grown β-Ga_2O_3 films, with a thickness range of 164 – 4,350 nm, were performed using time-domain thermoreflectance (TDTR)[47]. Half of the samples were grown on off-axis *c*-plane sapphire substrates and the rest were grown on sapphire substrates with an off-axis angle of 6° toward <$11\bar{2}0$>, as labeled in **Figure 3.6**. For this thickness range, TDTR measurement results show a noticeable thickness dependence of the thermal conductivity of the β-Ga_2O_3 films; specifically, the thermal conductivity reaches the bulk value for a film thickness of 4,350 nm and monotonically reduces with decreasing thickness. The measurement results in **Figure 3.6** indicate that phonons with mean free paths on the order of ~1 μm carry a significant fraction of the heat in this crystalline system, which is consistent with first principles calculation results shown in **Figure 3.1**. As the thickness of the films drops below ~1 μm, these phonons begin to scatter at the boundaries[31,32], leading to a continuing reduction in the thermal conductivity as the thickness decreases further. Cheng et al.[38] has reported the thermal conductivity of ($\bar{2}01$)-oriented thin films prepared via ion-cutting, and the data for high temperature annealed films relieved from the implantation-induced strain are included in **Figure 3.6**. Likewise, a strong film thickness dependence of the thermal conductivity of β-Ga_2O_3 at room temperature for the [100] direction has been reported in literature.[36,37]

The film thickness is a main design parameter to achieve the desired thermal performance of β-Ga_2O_3 electronic devices integrated with high thermal conductivity substrates.[6,7] Therefore, the results in **Figure 3.6** suggest that device engineers should account for the film thickness effect on the thermal conductivity of β-Ga_2O_3 when creating device thermal models to be used for design optimization. **Figure 3.6** also plots the thin film thermal conductivities of β-Ga_2O_3 obtained from Debye-Callaway model predictions (dashed lines). Based on the Debye-Callaway model, the phonon-boundary scattering rate is dominant over impurity and Umklapp scattering rates, leading to the increasing trend of thermal conductivity versus film thickness. As can be seen from **Figure**

3.6, both model predictions and measurement data capture the overall increasing trend of the thin film thermal conductivity when the film thickness increases; however, the predicted values are higher than those obtained from measurements for films with thicknesses ranging from 180 to 2500 nm. The discrepancies can be attributed to the crystallinity quality of the epitaxial films, which is not comparable to that of pure single crystals as assumed in the model predictions. The size effect of the β-Ga_2O_3 thermal conductivity is more notable for (100)-oriented films exfoliated from a single crystal β-Ga_2O_3 wafer due to the consistency in the crystalline quality of the films.[36]

The β-Ga_2O_3 films MOVPE-grown over 6° off-axis substrates exhibit a 10-30% higher thermal conductivity as compared to the films grown on on-axis *c*-plane sapphire substrates with comparable thickness. This aligns with the SEM, XRD, and Raman characterization results, showing improvement in the surface morphology and crystal quality for films grown on sapphire substrates with a 6° off-cut angle for both MOVPE and LPCVD-grown β-Ga_2O_3 thin films. It should be noted that the atomic steps provided by the off-cut substrates regulate the nucleation of the growth, which improves the crystalline quality and eliminates pseudo-hexagonal domains. Moreover, the off-cut surface steps terminate the interface defects more effectively due to the dislocation propagating at an angle to the growth direction.[23]

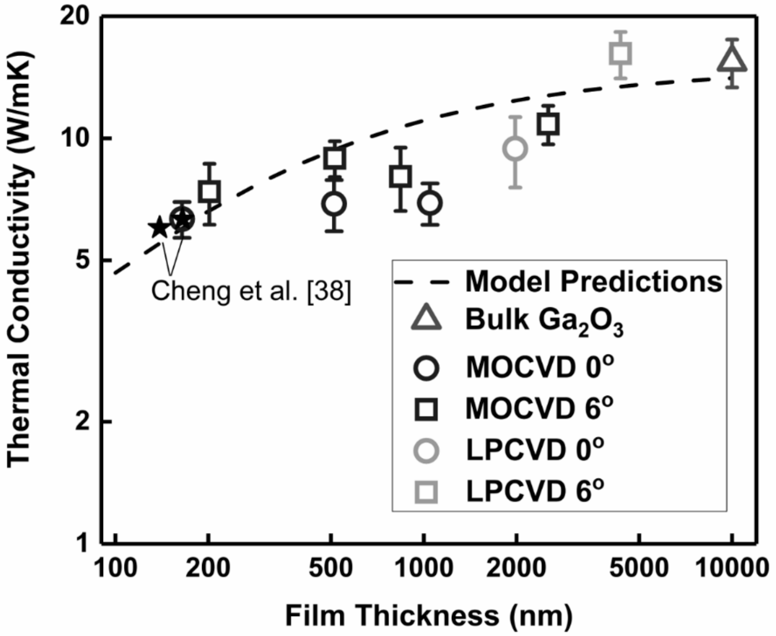

Figure 3.6: The measured cross-plane thermal conductivities of the ($\bar{2}01$)-oriented β-Ga_2O_3 thin films and the bulk substrate. Predictive modeling results that estimate the thickness dependence of the β-Ga_2O_3 thermal conductivity in a direction perpendicular to the ($\bar{2}01$) plane are shown for comparison. Also shown are two data points for ($\bar{2}01$)-orientated thin films prepared via ion-cutting from Cheng et al.[38]

Heteroepitaxy of β-Ga_2O_3 on high thermal conductivity substrates is a potential thermal management solution for β-Ga_2O_3 based devices; therefore, understanding thermal transport across the β-Ga_2O_3/substrate interface is important. Frequency-domain thermoreflectance (FDTR)[48] was used to measure the thermal boundary conductance (TBC) at the β-Ga_2O_3/sapphire interface of the heteroepitaxial films. The interface TBC measurements were performed on a 164 nm thick MOVPE-grown β-Ga_2O_3 film on c-plane sapphire and a 202 nm thick MOVPE-grown β-Ga_2O_3 layer on off-cut sapphire. These samples offered higher measurement sensitivity to the TBC as compared to the thicker films. FDTR was used for TBC measurement because TDTR would not offer sufficient measurement sensitivity to this parameter due to the shallower probing depth, owing to the higher pump modulation frequency. The cross-plane thermal conductivity of the films was treated as a known parameter based on the TDTR measurement results listed in **Figure 3.6**. For comparison, the TBC at the $(\bar{2}01)$ β-Ga_2O_3/sapphire substrate interfaces were calculated using the acoustic mismatch model (AMM) and diffusive mismatch model (DMM). The AMM and DMM_1 were calculated following the implementation presented by Bellis et al.[49] As shown in **Figure 3.7**, the β-Ga_2O_3 grown on the c-plane sapphire substrate has a higher TBC than the β-Ga_2O_3 grown on the sapphire substrate with an off-axis angle. It is important to note that even for the thinnest film (164 nm thick), FDTR does not offer high enough measurement sensitivity to quantify the TBC with low uncertainty. Nevertheless, the results still provide a qualitative assessment of the relative magnitude of the TBCs associated with the heterointerfaces of β-Ga_2O_3 films grown on *c*-plane and offcut sapphire substrates. The upper range of the TBC for the β-Ga_2O_3 film grown on *c*-plane sapphire is difficult to determine because FDTR loses sensitivity to the TBC when its value is high; therefore, its upper bound was chosen to be the AMM predicted value. Also shown in **Figure 3.7** is the DMM result calculated by Cheng et al.[38] for the TBC between $(\bar{2}01)$ β-Ga_2O_3 and c-plane sapphire (listed as DMM_2). Their model is based on the Landauer formula accounting for temperature-dependent phonon properties. The measured TBC results indicate that while growing β-Ga_2O_3 on a substrate with an offcut angle improves the crystalline quality due to the promoted step flow growth and dislocation termination,[23] the interfacial phonon transport is restricted as compared to films grown on on-axis *c*-plane sapphire.

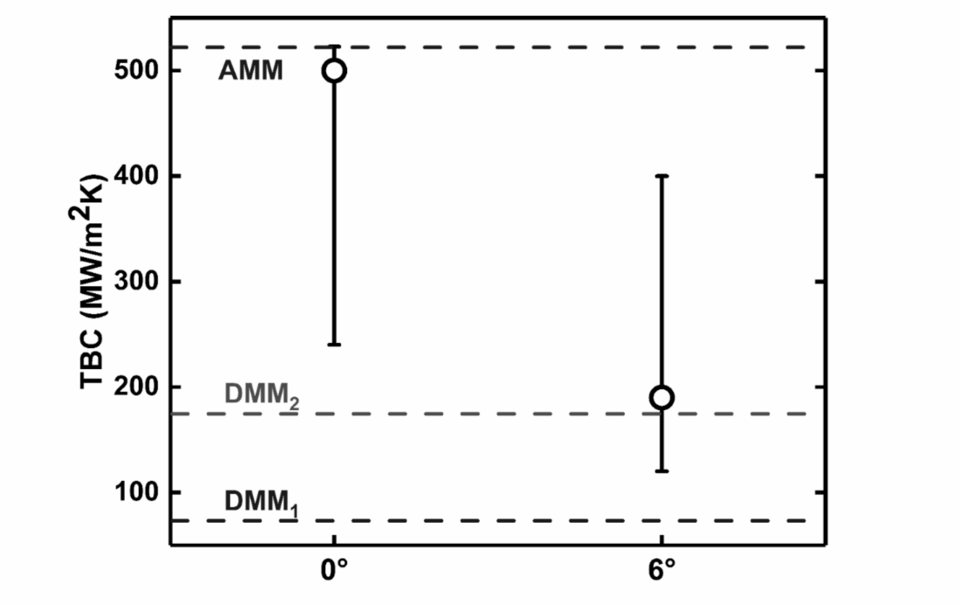

Figure 3.7: The measured thermal boundary conductance of β-Ga_2O_3 grown on 0° and 6° off-axis c-plane sapphire substrates (open circles with error bars). Due to the lack of sensitivity, the upper limit for the 6° sample cannot be experimentally determined; therefore, it is artificially bounded by the AMM predictions. The AMM and DMM_1 are calculated following the methodology presented by Bellis et al.[49] The DMM_2 was adopted from Cheng et al.[38]

The structural quality of the film interfaces between the β-Ga_2O_3 and both the on-axis and 6° off-axis substrates were investigated using cross-sectional scanning transmission electron microscopy (STEM) imaging. The representative images from both samples are shown in **Figure 3.8**. The images indicate that the interface of the on-axis grown sample (**Figure 3.8 (a)**) shows a smooth interface with a low density of structural defects. On the other hand, the 6° off-axis grown sample (**Figure 3.8 (b)**) shows a relatively higher degree of defects at the interface with more structural distortion and apparent strain field around the defective regions. The defective interface likely impedes the heat flow, which leads to the lower TBC measured from the 6° off-axis grown samples (**Figure 3.7**).

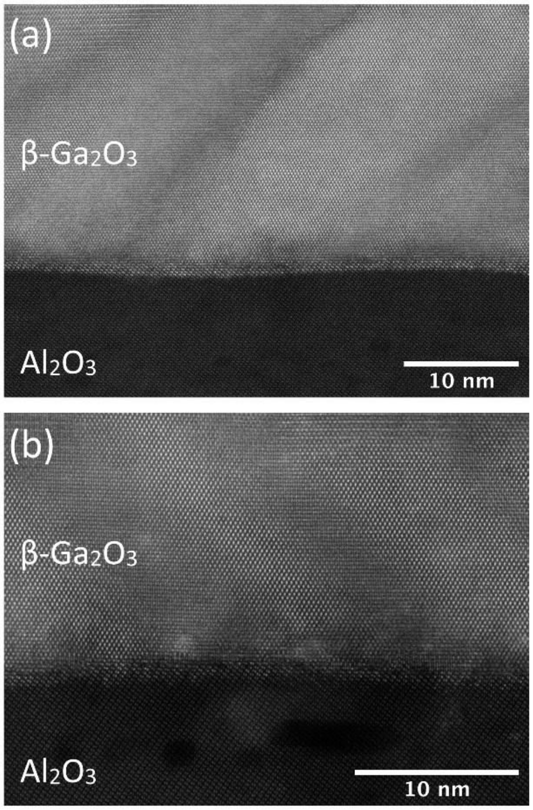

Figure 3.8: Atomic scale STEM images of β-Ga_2O_3 films grown on (a) 0° and (b) 6° off-axis *c*-plane sapphire substrates. The contrast lines at ~45° are dislocations along the (100) and (001) planes.

TDTR measurements were performed on MOVPE-grown $(\bar{2}01)$-oriented β-$(Al_xGa_{1-x})_2O_3$ films with various Al compositions (x = 0.08 – 0.43). The thickness of the films ranged 184 – 752 nm, where the films with lower x were thicker. For example, the thicknesses of the x=0.08, 0.27, and 0.43 films were 752 nm, 505 nm, and 184 nm, respectively. The measured cross-plane thermal conductivities for films with different Al compositions (x) are summarized in **Figure 3.9**. The thermal conductivity of the β-$(Al_xGa_{1-x})_2O_3$ films ranged 2.8 – 5.6 W/m·K, which is ~50% lower than those for β-Ga_2O_3 films of similar thickness. This large discrepancy between the thermal conductivity of β-Ga_2O_3 and β-$(Al_xGa_{1-x})_2O_3$ films is mainly attributed to phonon-alloy disorder scattering[50], which is known to severely restrict the mean free path of phonons. Similarly, the thermal conductivity of $Al_xGa_{1-x}N$ was reported to be an order of magnitude lower than those for the constituent base crystals, GaN and AlN.[51] While the β-Ga_2O_3 films exhibited a strong thickness dependence of their thermal conductivities, the β-$(Al_xGa_{1-x})_2O_3$ thermal conductivity values are relatively invariant with respect to the film thickness. This may indicate vibrational modes with considerably shorter mean free paths than β-Ga_2O_3 dominate thermal transport within the alloy.[52]

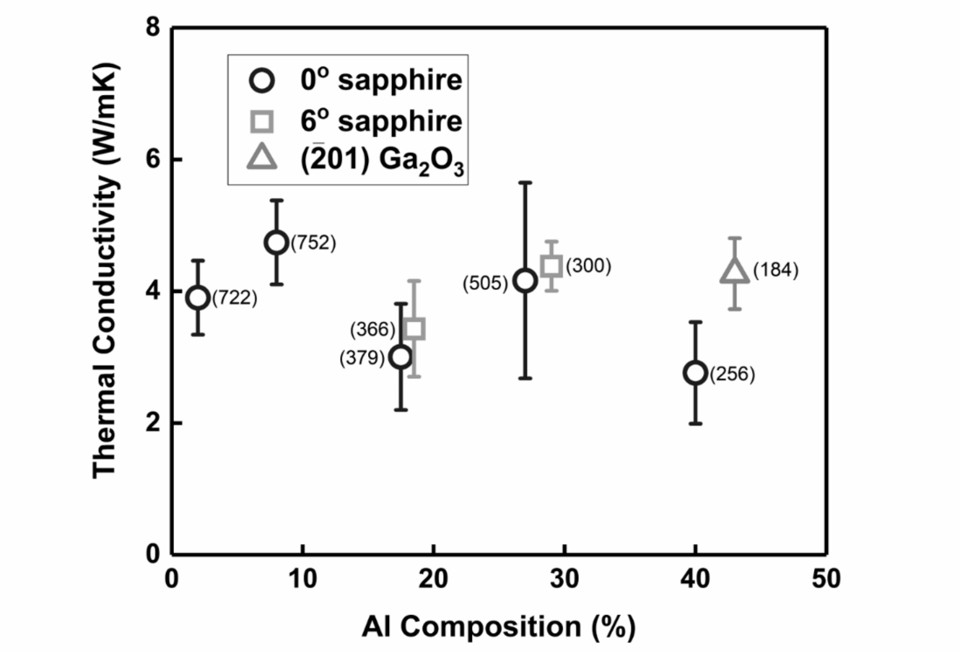

Figure 3.9: The compositional dependence of the thermal conductivity of β-$(Al_xGa_{1-x})_2O_3$ thin films. The numbers in the parentheses are the corresponding β-$(Al_xGa_{1-x})_2O_3$ film thicknesses in nanometers. The 366 nm and the 379 nm films have identical Al compositions of 18%; however, their Al compositions have been offset for an illustrative purpose.

Temperature-dependent thermal conductivity measurements were performed on β-Ga_2O_3 (521 nm) and β-$(Al_{0.27}Ga_{0.73})_2O_3$ (505 nm) films with a similar thickness using TDTR from room temperature up to 600 ˚C (**Figure 3.10**). As the temperature increases, the thermal conductivity of the β-Ga_2O_3 film monotonically decreases due to the increased Umklapp scattering rate; the temperature-dependent thermal conductivity of bulk β-Ga_2O_3 shows a similar trend as has been reported in the literature[53]. In contrast, the thermal conductivity of the β-$(Al_{0.27}Ga_{0.73})_2O_3$ film is relatively invariant across this temperature range. A similar trend was previously observed in solid solutions $Al_{1-x}Ga_xN$[51] and $Al_xSc_{1-x}N$[54]. The tested temperature range reaches up to the Debye temperatures of the two constitutive materials (α-Al_2O_3[55] and β-Ga_2O_3[56]). The relatively constant thermal conductivity of β-$(Al_xGa_{1-x})_2O_3$ within this temperature range suggests that phonon-phonon scattering is not the dominant scattering mechanism, in contrast to the case of β-Ga_2O_3. Instead, phonon-alloy disorder scattering dominates the thermal conductivity of the β-$(Al_xGa_{1-x})_2O_3$ solid solution. It is interesting to note that the temperature-dependent thermal conductivity of β-$(Al_xGa_{1-x})_2O_3/Ga_2O_3$ superlattices has also been reported[53]; the thermal conductivity increases with temperature up to 380K, due to phonon-structural imperfection scattering effects associated with the large number of boundaries. It is imperative to understand the dominant phonon scattering mechanisms associated with different β-Ga_2O_3 and β-$(Al_xGa_{1-x})_2O_3$ material platforms to understand the self-heating behavior of devices based on them.

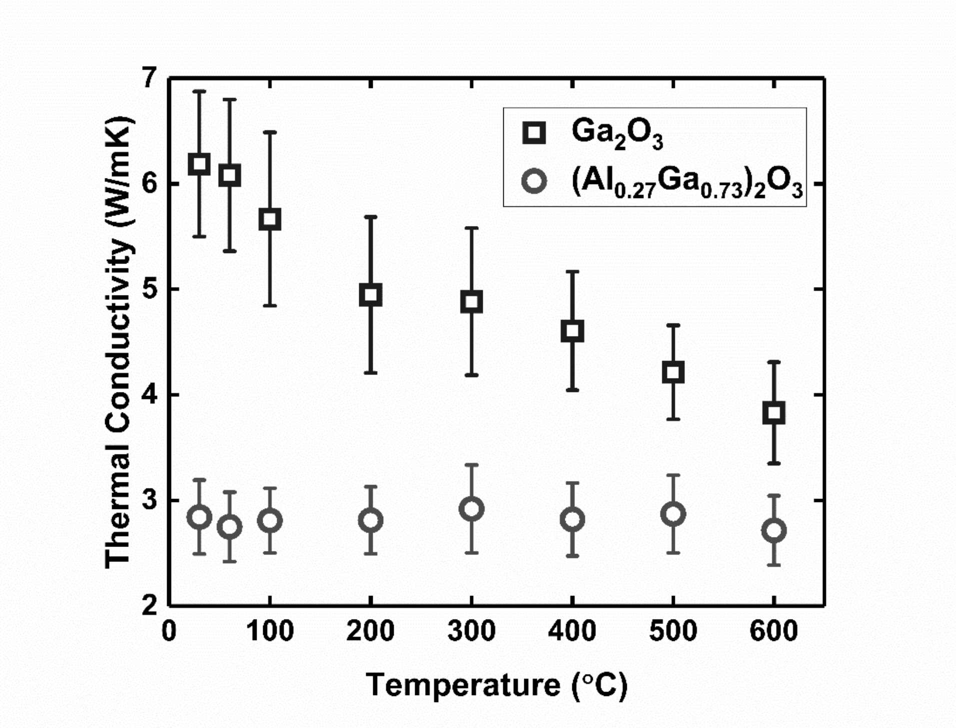

Figure 3.10: The temperature dependence of the thermal conductivity of ~500 nm thick β-Ga_2O_3 and β-$(Al_xGa_{1-x})_2O_3$ thin films.

Raman spectroscopy measurements were performed on the β-$(Al_xGa_{1-x})_2O_3$ films as a function of Al composition. **Figure 3.11** presents the Raman spectra of β-$(Al_xGa_{1-x})_2O_3$ films grown on sapphire, and the Raman spectrum of a bare sapphire substrate. Raman peaks of the Ga_2O_3 ($x = 0$) film are marked in **Figure 3.11**. The incorporation of Al atoms causes a blueshift in the Raman peak positions and reduces the peak intensity. At $x = 0.40$, the $A_g^{(3)}$ peak flattens and cannot be identified. The peak position (P [cm^{-1}]) of the $A_g^{(3)}$ Raman peak can be roughly correlated to the Al composition (x) up to 27% as $P[cm^{-1}] = 201.382 + 0.107\ x$; however, it should be noted that not only the Al composition but also the strain in the films will influence the Raman peak position.

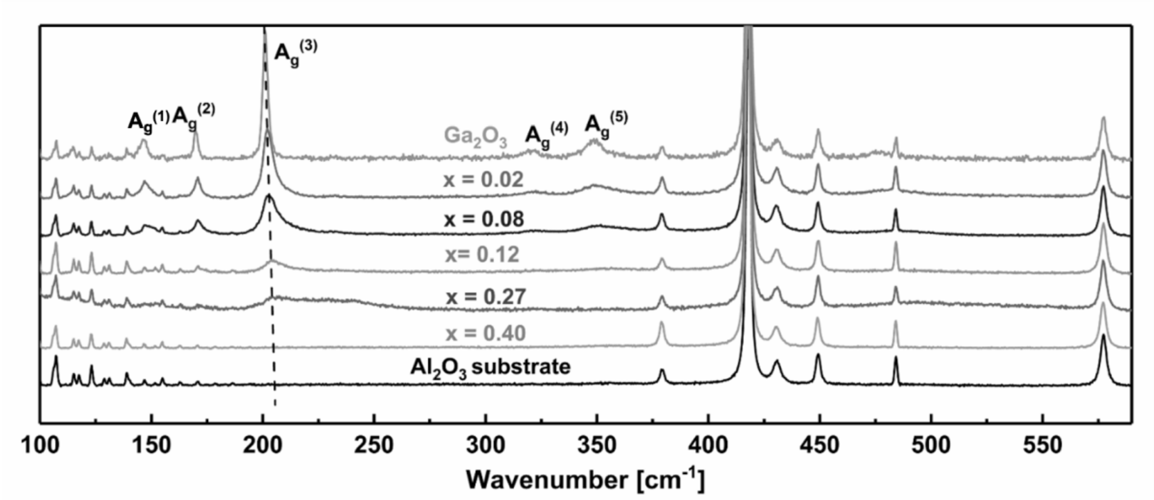

Figure 3.11: Raman spectra of the β-$(Al_xGa_{1-x})_2O_3$ films as a function of Al composition (x) and the Raman spectrum of the sapphire substrate. The dashed line qualitatively shows the blueshift of the $A_g^{(3)}$ mode as x increases. Most of the unlabeled peaks are from the substrate.

3.1.3 Conclusions

Heteroepitaxial growth of β-Ga_2O_3 via LPCVD and MOVPE has significant technological importance in terms of the mass production of optoelectronic/electronic-grade β-Ga_2O_3 and β-$(Al_xGa_{1-x})_2O_3$ thin films. This work investigated physical mechanisms that govern the thermal transport across β-Ga_2O_3 and β-$(Al_xGa_{1-x})_2O_3$ thin films grown on foreign substrates. First, a strong thickness dependence of the thermal conductivity was observed in β-Ga_2O_3 films with submicrometer thickness. The thermal conductivity monotonically increased with thickness, such that a 4,350 nm-thick film exhibited the bulk thermal conductivity. This thickness dependence was confirmed by a Debye-Callaway model, which indicates that phonon-boundary scattering is dominant over other scattering mechanisms (at room temperature), leading to the observed thickness-dependent thermal conductivity. Second, the crystallinity of the samples impacts thermal transport within the β-Ga_2O_3 films. The β-Ga_2O_3 films grown on 6° off-axis sapphire substrates exhibited a 10 – 30% higher thermal conductivity as compared to films grown on on-axis c-plane sapphire substrates with a comparable thickness. The higher thermal conductivity of films grown on offcut substrates is attributed to the higher crystalline quality of the films, confirmed by SEM, XRD, and Raman measurements. The interface quality of the films grown on the 0° and 6° off-axis sapphire substrates was evaluated using atomic scale STEM imaging. Data reveals that the interface quality of the samples grown on 6° off-axis substrates is inferior to the on-axis grown samples, which leads to a higher TBC. In addition, the thermal conductivity of MOVPE-grown β-$(Al_xGa_{1-x})_2O_3$ films with various Al compositions ($x = 0.08 – 0.43$) was measured. A significant reduction (>50%) in the thermal conductivity was observed for the β-$(Al_xGa_{1-x})_2O_3$ films as compared to β-Ga_2O_3 films with similar thicknesses. This reduction is attributed to phonon-alloy disorder scattering, which also results in weak film thickness and temperature dependence of the β-$(Al_xGa_{1-x})_2O_3$ thermal conductivity. β-$(Al_xGa_{1-x})_2O_3$ films grown on 6° off-axis sapphire substrates exhibit higher thermal conductivities than the films grown on on-axis sapphire substrates, showing that the crystallinity still impacts thermal transport within the solid solution.

The outcomes of this study highlight the key thermal design considerations for DUV optoelectronic and power electronics applications based on heteroepitaxial β-phase Ga_2O_3 and $(Al_xGa_{1-x})_2O_3$ thin films. From a thermal engineering standpoint, the thickness of the epitaxial layers should be carefully chosen to minimize the overall device thermal resistance. From the material growth perspective, heteroepitaxy on foreign substrates with an offcut angle could improve the crystalline quality, which in turn improves thermal and electrical performance. However, growing films on substrates with an offcut angle was shown to limit the interfacial thermal transport due to the formation of structural defects and extra strain at the interface. This design tradeoff between the enhancement in the thermal conductivity and reduction in the TBC by substrate offcut angle should be carefully balanced based on the application specifics. Finally, a remarkable reduction in the thermal conductivity caused by alloying should not be overlooked during device design phase of DUV optoelectronics and power electronics based on the β-Ga_2O_3.

3.1.4 Experimental Methods

Metalorganic vapor phase epitaxy (MOVPE) growth of Ga_2O_3 and $(Al_xGa_{1-x})_2O_3$ thin films

MOVPE growth of UID β-phase Ga_2O_3 and $(Al_xGa_{1-x})_2O_3$ films was performed using an Agnitron Agilis MOVPE reactor with triethyl gallium (TEGa), trimethyl aluminum (TMAl), and O_2 as precursors. MOVPE growth of β-Ga_2O_3 and β-$(Al_xGa_{1-x})_2O_3$ films was performed on on-axis and 6˚ offcut (with respect to the a-plane) c-plane sapphire wafers. The substrates were first cleaned with acetone, isopropyl alcohol, and DI water before loading into the chamber. The growth temperature for all films was kept between 800˚C – 880˚C. The typical growth conditions used for the MOVPE growth are: TEGa 22 – 105 sccm, O_2 250 – 800 sccm, and pressure 15 – 60 Torr. The growth time was varied between 30 mins – 2.5 hours to obtain films of the required thickness. Growth of β-$(Al_xGa_{1-x})_2O_3$ films was achieved by using a combination of TEGa and TMAl precursors. The Al composition was increased by increasing the [Al]/[Ga]+[Al] precursor molar ratio.

MOVPE-grown (010) β-Ga_2O_3 films with mobility close to the theoretical limit have been reported.[57] However, direct growth on other orientations ((100), ($\bar{2}01$), (001)) has led to films with lower mobility due to the higher density of structural defects.[58,59] It has been shown that high-quality (100)-oriented β-Ga_2O_3 thin films can be grown by choosing a β-Ga_2O_3 substrate with the correct offcut orientation, which suppresses the formation of structural defects.[60] Similar defects have been observed in MOVPE-grown ($\bar{2}01$) homoepitaxial β-Ga_2O_3 films.[58] Therefore, both low and high quality $(\bar{2}01)$-oriented heteroepitaxial β-Ga_2O_3 films were grown in this work using 0° and 6° off-angled c-plane sapphire substrates, respectively.

Low pressure chemical vapor deposition (LPCVD) growth of Ga_2O_3 thin films

Unintentionally-doped (UID) heteroepitaxial β-Ga_2O_3 films were grown on both on-axis and off-axis (6° towards $<11\bar{2}0>$) c-plane sapphire substrates in a custom-built LPCVD system. Details of setup for film deposition can be found in previous work[28]. β-Ga_2O_3 thin films prepared in this paper were grown at a growth temperature of 900 °C and a chamber pressure of 2 Torr.

Typical LPCVD grown UID heteroepitaxial β-Ga_2O_3 films on sapphire substrates were found to be electrically insulating due to possible compensation effects. Si-doped films grown under similar growth conditions (900 °C) have shown controllable n-type doping with a wide doping range. Typical room temperature mobilities measured from LPCVD heteroepitaxial β-Ga_2O_3 thin films ranged between 40 ~ 60 cm^2/Vs when grown on on-axis c-plane sapphire, and 60 ~ 110 cm^2/Vs when grown on 6° off-cut sapphire, for a typical doping concentration of $10^{17} cm^{-3}$ ~ 10^{18} cm^{-3}.[23,28,29]

Scanning electron microscopy (SEM)

Scanning electron microscope (SEM) images of the surface of the β-Ga_2O_3 films were collected at varying magnifications to characterize the surface morphology and grain structure. Cross-sectional images were also obtained to measure the thicknesses of the films. The samples were cleaved to obtain these cross-sectional measurements of the fracture surface. For samples that were too small to physically cleave, a cross-section was prepared by focused ion beam (FIB) with an approximately 2 μm thick carbon cap. All SEM images were collected at 5 kV in a Mira TESCAN3 system with the exception for the FIB sections, which were prepared and imaged in a FEI Scios II system at a 52° tilt (accounted for during measurements).

To confirm the film thickness of the specimens, additional SEM images were collected on a Zeiss Supra55 VP at 20 kV with an aperture size of 120 mm in high current mode. The working distance for all images was 10 mm (±0.1 mm). Copper tape was used on samples to dissipate charge, but there was still noticeable charging in some regions which limited the spatial resolution. A backscattered electron detector was used for most imaging as it made phase and z contrast more prominent. Samples were cleaved and then mounted onto a cross-sectional stub for imaging.

X-ray diffraction (XRD)

X-ray diffraction (XRD) was used to confirm the phase and orientation, and to assess the crystalline quality of the films. First, 2-Theta (2Θ) scans were obtained using a Malvern Panalytical Empyrean system with Cu $K\alpha_1$=1.54 Å radiation in the Bragg-Brentano geometry. These scans were collected over a wide range (10-70° 2Θ) to verify the phase and identify the film and substrate peaks (when applicable). Within this range, ($\bar{2}01$)-oriented β-Ga_2O_3 is anticipated to exhibit diffraction peaks at 18.964°, 38.404°, and 59.236° 2Θ corresponding to the ($\bar{2}01$), ($\bar{4}02$), and ($\bar{6}03$) symmetric reflections, respectively (ICSD 04-008-8217). The (0006) peak of the c-plane Al_2O_3 substrate is also observed at 41.680° 2Θ (ICSD 01-074-1081). Next, high-resolution scans were collected using a Malvern Materials Research Diffractometer (MRD) system in line focus mode with Cu $K\alpha_1$=1.54 Å radiation. This system is equipped with a five-axis goniometer, 2xGe (220) hybrid monochromator, and PIXcel detector with a fixed anti-scatter slit. All XRD characterization was completed at room temperature in this study.

The general procedure for collecting these scans begins by finding the coarse substrate offcut angle/tilt direction with a Laue diffractometer (for sample pieces without a flat). The sample is then loaded into the MRD system and fine calibration offsets were applied. For a c-plane Al_2O_3 substrate, the sample is initially aligned using the (0006) substrate peak. Then, a coupled ω-2Θ scan is obtained over a wide range of 10-70° 2Θ. From this scan, a film peak (e.g., $(\bar{2}01)$) is selected for an XRD rocking curve measurement. Before obtaining this measurement, the sample is aligned to the film peak by completing successive omega (ω) and chi (χ) scans over progressively narrow ranges to optimize the sample tilt by maximizing intensity. Additionally, X and Y line scans are completed to select the measurement location based on maximum intensity. Finally, to obtain the rocking curve, an ω scan was collected over a range of 6° with a 0.01° step size and dwell time of 0.1 s. In this study, rocking curves were obtained for both the $(\bar{2}01)$ and $(\bar{4}02)$ symmetric reflections. For the bulk β-Ga_2O_3 substrate a narrower range of 1.0° was utilized with a smaller step size of 0.001° to ensure a sufficient number of data points over the breadth of the peak. The full-width-at-half-maximum (FWHM) was calculated for each rocking curve, where a lower value implies superior crystalline quality.

Raman spectroscopy

β-Ga_2O_3 has 15 Raman-active phonon modes.[45] Among these, the $A_g(3)$ phonon mode near 199.7 cm^{-1} was used in this study due to its relatively large intensity. The room temperature Raman spectra were obtained using a Horiba LabRAM HR Evolution spectrometer equipped with a 532 nm laser and an 1800 grooves/mm grating. A long working distance 50× objective (NA = 0.45) was used to probe the samples. Since the laser excitation energy (2.33 eV) is smaller than the bandgap energy of β-Ga_2O_3 (4.8 eV) and the sapphire substrate (8.8 eV), the laser heating was assumed to be negligible; therefore, a high laser power of ~20 mW was used. The results were based on five repeated measurements at three random locations on each sample. According to the energy-time uncertainty principle, as the crystalline quality decreases, the linewidth of the $A_g(3)$ phonon mode will increase as a result of decreased phonon lifetime. Therefore, the linewidth was used to qualitatively compare the crystalline quality of the β-Ga_2O_3 samples.

Time-domain thermoreflectance (TDTR)

Details of the setup for TDTR measurements have been described in Chapter 2.2. The radii of the focused pump and probe beams were 7.0 μm and 4.5 μm, respectively. It should be noted that TDTR and FDTR measurements require a relatively smooth sample surface [31]; in this study, only samples with a reflected probe signal intensity greater than 40% of that for a smooth Au/Si calibration sample were included, which is expected to have a RMS surface roughness less than 30 nm. Literature values were used for the thermal conductivity of Au as well as volumetric heat capacities (C_v) of Au[61], β-Ga_2O_3[62] and α-Al_2O_3[63] where the value of C_v for β-$(Al_xGa_{1-x})_2O_3$ was approximated as a weighted average of the constitutive materials based on the alloy composition. The temperature dependent thermal properties for the Au transducer[64], sapphire substrate[65], and β-Ga_2O_3[66] were taken from literature. The thermal boundary conductance (TBC) between the metal transducer and the β-Ga_2O_3 films was fitted simultaneously with the β-Ga_2O_3 thermal conductivity. Due to the high sensitivity (as shown in **Figure 3.12**), TDTR fits the β-Ga_2O_3 thermal conductivity accurately without being affected by the assumption for the TBC between the β-Ga_2O_3 films and the substrate. The uncertainty was calculated based on 95% confidence bounds from the random spots and ±2 nm uncertainty associated with the transducer thickness.

Frequency-domain thermoreflectance (FDTR)

Details of the FDTR setup have been described in Chapter 2.3. The radii of the focused pump and probe beams were 13.4 μm and 13.1 μm, respectively. Material properties used in the FDTR fitting model were identical to those used in the TDTR model. To extract the thermal boundary conductance of the MOVPE-grown samples, the thermal conductivities of the films were adopted from the TDTR measurement results to reduce the number of fitting parameters. The FDTR has a relatively low sensitivity to the TBC between the β-Ga_2O_3 films and the substrate (G2) as shown in **Figure 3.12**; therefore, a qualitative assessment of the TBCs were made based other parameters determined by TDTR. The upper and lower bounds of G2 were determined based on the 95% confidence bounds for the thermal conductivity of β-Ga_2O_3 films and the substrates. Representative fitting for TDTR and FDTR is shown in **Figure 3.13**.

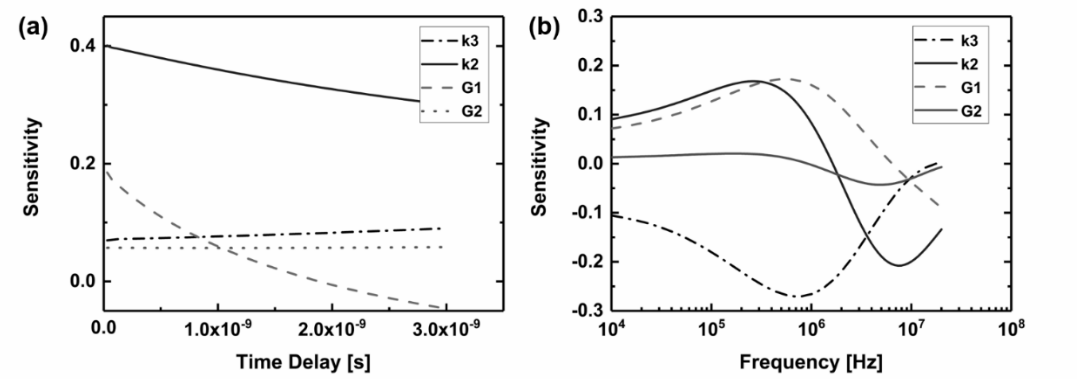

Figure 3.12: The sensitivity plot for 164 nm thick MOVPE-grown β-Ga_2O_3 film on c-plane sapphire measured by a) TDTR, and b) FDTR. In the legend, k2 is the cross-plane thermal conductivity of the β-Ga_2O_3 film. k3 is the thermal conductivity of the sapphire substrate. G1 and G2 are the thermal boundary conductance of the transducer- β-Ga_2O_3 and β-Ga_2O_3-substrate interfaces, respectively.

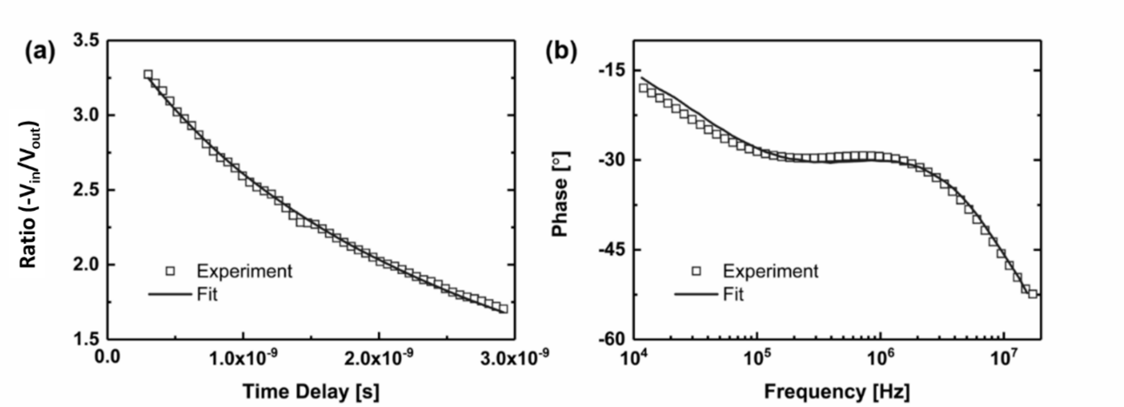

Figure 3.13: The data fitting for 164 nm thick MOVPE-grown β-Ga_2O_3 film on *c*-plane sapphire measured by a) TDTR, and b) FDTR.

Scanning transmission electron microscopy (STEM)

Cross-sectional TEM samples were prepared using a focused ion beam. To identify the crystalline quality at the atomic scale in the interface regions, thin and clean TEM foils were obtained using a low-energy (500 eV) ion milling (Fischione Nanomill). High-resolution STEM high angle annular dark filed (HAADF) imaging was performed using a probe corrected Thermo Fisher Scientific Themis Z STEM mode (Cs_3=0.002 mm, Cs_5=1.0 mm) with probe convergence half angles of 17.9 mrad at an accelerating voltage of 200 kV. Since HAADF-STEM image contrast is approximately proportional to the square of atomic number, contrast patterns resulted from the different crystal structures of the Ga_2O_3 and the Al_2O_3 were atomically differentiated.

First principles calculations

First-principles calculations of the phonon structure as well as the anharmonic phonon coupling were performed with the ShengBTE software package[67]. Density Functional Theory (DFT) total energy calculations were utilized for the computation of interatomic force constants (IFCs) using the QuantumEspresso package[68]. For anharmonic as well as harmonic force constants, single atoms were displaced in a supercell for various configurations based on the symmetry of the crystal. Total energy calculations from the various displaced supercells allow forces, and subsequently IFCs, to be computed. In this work, a 2×2×2 supercell containing 80 atoms was utilized with a 2×2×2 k-point sampling grid for subsequent self-consistent total energy calculations in computing the force-constant matrix as well as the phonon-phonon coupling matrix elements. These phonon-phonon coupling matrix elements were used to determine the scattering rates necessary for a single-mode relaxation time approximation of the phonon Boltzmann transport equation. Full details of the Boltzmann transport equation solution for thermal conductivity can be found in reference [30].

Thermal conductivity modeling

The Debye-Callaway model was applied to obtain the thickness-dependent thermal conductivity of β-Ga_2O_3 single crystals along the $\perp(\bar{2}01)$ direction.[11] The phonon-phonon Umklapp scattering, phonon-impurity scattering, and phonon-boundary scattering are included in the resistive phonon scattering processes of the model. The scattering rates of the three scattering mechanisms are expressed as

$$\left[\tau_U^j(x)\right]^{-1} = \frac{k_{\mathrm{B}}^2\gamma_j^2}{M\hbar v_j^2\theta_j}x^2T^3e^{-\frac{\theta_j}{3T}} \tag{3.1}$$

$$\left[\tau_I^j(x)\right]^{-1} = \frac{Vk_{\mathrm{B}}^4\Gamma}{4\pi\hbar^4 v_j^3}x^4T^4 \tag{3.2}$$

$$\left[\tau_B^j\right]^{-1} = \frac{v_j}{d} \tag{3.3}$$

where k_{B} is the Boltzmann constant, T is the temperature, $\hbar$ is the reduced Planck's constant, θ is the Debye temperature, v is the phonon velocity, subscript "j" denotes the branch in the phonon dispersion spectrum, and $x = \hbar\omega/k_{\mathrm{B}}T$ with ω being the angular frequency. For β-Ga_2O_3, V = 1.0587 × 10^{-29} m^3/atom and M = 6.2231 × 10^{-26} kg/atom. The Grüneisen parameters, γ_L and γ_T, are obtained by fitting the temperature-dependent thermal conductivity from 100 to 700 K to the first-principles calculations along the $\perp(\bar{2}01)$ direction of bulk β-Ga_2O_3. The parameters that were used in the model calculation are listed in **Table 3.1**. These parameters were derived from the aforementioned first principles calculations, which are in good agreement with values reported in literature[10]. Parameters associated with other crystallographic directions of β-Ga_2O_3 can be found in open literature[10,37].

Table 3.1: Zone-boundary frequencies $\boldsymbol{f_{L,T}}$ and phonon velocities $\boldsymbol{v_{L,T}}$ of longitudinal and transverse phonons for β-Ga_2O_3 along the ⊥ $(\bar{\mathbf{2}}\mathbf{01})$ direction from the first-principles calculations. $\boldsymbol{\theta_{L,T}}$ are the Debye temperatures calculated from these cutoff frequencies following $\boldsymbol{\theta = \frac{2\pi\hbar f}{k_B}}$. $\gamma_{L,T}$ are the Grüneisen parameters.

Direction	f_L (THz)	f_{T1} (THz)	f_{T2} (THz)	v_L (m s^{-1})	v_{T1} (m s^{-1})	v_{T2} (m s^{-1})	θ_L (K)	θ_{T1} (K)	θ_{T2} (K)	γ_L	γ_T
⊥ $(\bar{2}01)$	3.9	2.5	2.3	6656	3206	2385	187	120	110	1.1	0.78

AMM and DMM

The TBC for the β-Ga_2O_3/sapphire interface was analytically calculated by implementing the Landauer formalism with the acoustic mismatch (AMM) and diffusive mismatch (DMM) models. The general Landauer formula for the TBC can be expressed as follows:

$$G = \sum_p \frac{1}{2} \int_0^{\omega_d} \int_0^{\pi/2} D_1(\omega) \frac{df_{BE}}{dT} \hbar\omega v_1(\omega) \tau_{1,2}(\theta,\omega) \cos(\theta) \sin(\theta)\, d\theta d\omega \tag{3.4}$$

where D represents the phonon density of states (DOS), f_{BE} is the Bose-Einstein distribution function of phonons, $\hbar$ is the reduced Planck constant, ω represents the angular frequency, ω_d represents the cutoff frequency, v is the phonon group, $\tau_{1,2}$ is the transmission coefficient from the medium 1 to 2, θ is the angle of incidence, and the index p indicates the phonon branch. For the AMM, the transmission coefficient can be expressed as:

$$\tau_{1,2,\mathrm{AMM}}(\theta, \omega) = \frac{4\frac{Z_2}{Z_1} \cdot \frac{\cos(\theta_2)}{\cos(\theta_1)}}{\left(\frac{Z_2}{Z_1} + \frac{\cos(\theta_2)}{\cos(\theta_1)}\right)^2} \tag{3.5}$$

Alternatively, since the transmission function for DMM does not depend on the angle of incidence, the integration over θ is not needed, and the transmission coefficient adopts the following form:

$$\tau_{1,2,\mathrm{DMM}}(\omega) = \frac{\sum_p M_2(\omega)}{\sum_p M_1(\omega) + \sum_p M_2(\omega)} \tag{3.6}$$

where Z is the acoustic impedance and M is the phonon number of modes of mediums 1 and 2. The formulations of the AMM and DMM presented by Bellis et al. [49] were adopted in the present study, and the model input parameters are listed in **Table 3.2.**

Table 3.2: Parameters implemented for the calculations of the thermal boundary conductance (G) using the AMM and DMM formulations.

Medium A	**Medium B**	**Speed of sound** [m/s] v_L, v_T		**Mass density** [kg/m^3]		**GAMM**	**GDMM**
		Medium A	Medium B	Medium A	Medium B	[MWm^{-2}K^{-1}]	[MWm^{-2}K^{-1}]
β-Ga_2O_3 [$\bar{2}01$]	Sapphire c-plane	6600, 2750[10]	11260, 6467[69,70]	5880	3980	522.8069	72.65426

3.2 Thermal Management and Interface Phonon Transport

3.2.1 Introduction

Ultra-wide bandgap (UWBG) β-phase gallium oxide (Ga_2O_3), E_G~4.8 eV, is emerging as a replacement for commercially available wide bandgap (WBG) power electronics such as gallium nitride (GaN) and silicon carbide (SiC) due to its improvements in performance and manufacturing cost.[3] The lateral figure of merit (LFOM)[71] is a metric that compares the theoretically achievable power switching performance of laterally configured transistor devices. It is defined as $LFOM = V_{BR}^2/R_{ON-SP}$, where V_{BR} is the breakdown voltage and R_{ON-SP} is the specific ON-resistance. The LFOM can also be expressed as $q\mu n_s E_C^2$, where q is the electron charge, μ is the channel mobility, n_s is the sheet charge density, and E_C is the critical electric field[71]. Since E_C scales as the 2-2.5 power of the bandgap energy (E_G), the LFOM offered by Ga_2O_3 is the highest among the technologically relevant semiconductors shown in **Table 3.3**. While diamond (E_G~5.5 eV) could potentially offer a higher LFOM, key challenges associated with large area substrate availability and substitutional doping have remained unsolved over the last few decades. In contrast, high crystalline quality and potentially low cost Ga_2O_3 substrates can be manufactured using diverse melt-growth techniques (similar to the case of Si)[3], and shallow n-type doping schemes are readily available. The high LFOM offered by Ga_2O_3 gives promise to the development of lateral power switches with kV-class breakdown voltages and minimized device footprints. The enhanced power switching performance at the device-level will eventually translate into commensurate improvement in the system-level size, weight, and power (SWaP) and efficiency.

Table 3.3: Material properties and the LFOM for conventional, WBG, and UWBG semiconductors.[10,72–74]

Material	Conventional		WBG		UWBG
Property	Si	GaAs	SiC	GaN	β-Ga_2O_3
Bandgap, E_G (eV)	1.12	1.43	3.26	3.42	4.8
Relative dielectric constant, ε	11.9	13.1	10.1	9.7	10
Breakdown field, E_C (MV/cm)	0.3	0.4	3	3.3	8
Electron (channel) mobility, μ ($cm^2/V \cdot s$)	1400	8500	1020	1350(2000)	180(420)
Saturated electron velocity, v_s (cm/s)	1×10^7	2×10^7	2×10^7	2.7×10^7	1.5×10^7
Thermal conductivity, k (W/m·K)	150	46	490	130	11-27
Normalized LFOM ($q\mu n_s E_C^2$)	1	10.8	72.9	172.9	213.3

The targeted higher power handling capability (e.g., 10 W/mm) and reduced device footprint of Ga_2O_3 electronics (both enabled by the superior LFOM), translate into extremely high operational heat fluxes (>1 MW/cm^2). Moreover, the thermal conductivity of Ga_2O_3 (10.9-27 W/m·K)[10] is the lowest among the semiconductors listed in **Table 3.3**. Therefore, overheating has become a major bottleneck to the commercialization of Ga_2O_3 electronics. In fact, no reported Ga_2O_3 device has achieved the performance projected by the superior LFOM, and a thermally limited technological plateau has been reached.

Chatterjee et al.[7] demonstrated that the channel temperature of a homoepitaxial Ga_2O_3 metal-oxide-semiconductor field-effect transistor (MOSFET) would exceed 1500°C at a targeted power density of 10 W/mm. This work highlights that a composite wafer[37,75] which consists of a Ga_2O_3 layer (thinner than 10 μm) integrated with a high thermal conductivity substrate (e.g., SiC, AlN, diamond) using an integration process that results in a reasonable interfacial thermal boundary resistance (<60 $m^2 \cdot K/GW$) would reduce the device junction-to-package thermal resistance to a manageable level, which is comparable to that for commercial GaN-on-Si high electron mobility transistors (HEMTs) [76]. The importance of these thermal design parameters has also been suggested in a study aiming for Ga_2O_3/polycrystalline-SiC vertical device development.[75] In addition, an ideal and practical composite substrate should allow subsequent growth/fabrication of Ga_2O_3 lateral devices. Such composite wafers require an epi-ready surface morphology, low wafer bow, and a process that is scalable to large-diameter wafers. Another critical challenge is managing the strain induced by the difference in thermal expansion coefficients between the two materials attached with each other. The interface between the Ga_2O_3 and the heat-sinking substrate needs to be stress-engineered so that the materials stay attached from room temperature up to subsequent high temperature device processing steps. A previous study has demonstrated direct growth of Ga_2O_3 on SiC via molecular beam epitaxy (MBE).[77] In this work, a composite wafer has been constructed using a wafer bonding approach to better fulfill the aforementioned requirements.

In this work, a novel Ga_2O_3/4H-SiC composite wafer with high heat transfer performance has been developed using a fusion bonding approach.[78] The thermal conductivity of the Ga_2O_3 layer and the effective thermal boundary resistance (TBR) at the Ga_2O_3/4H-SiC interface were characterized through the combined use of time-domain thermoreflectance (TDTR), frequency-domain thermoreflectance (FDTR), and a differential steady-state thermoreflectance (SSTR) technique. The measured thin film thermal conductivity was compared with a Debye-Callaway model incorporating phononic parameters derived from first-principles calculations. Individual resistive components that comprise the effective TBR at the Ga_2O_3/4H-SiC interface were analyzed using an acoustic mismatch model (AMM) and diffusive mismatch model (DMM). Furthermore, scanning transmission electron microscopy (STEM) and energy-dispersive X-ray spectroscopy (EDX) were used to investigate the interface quality and chemistry, respectively. A Si-doped Ga_2O_3 epitaxial layer was successfully grown on the composite substrate by taking advantage of a low-temperature metalorganic vapor phase epitaxy (MOVPE) process. Finally, thermal modeling of single- and multi-finger Ga_2O_3 lateral transistors was performed to evaluate the improvement of the device thermal resistance by replacing the Ga_2O_3 substrate with the composite substrate developed in this study. The outcomes of this work suggest that the Ga_2O_3/4H-SiC composite substrate technology is an effective solution for the device-level thermal management of Ga_2O_3 electronics, promising the possibility of exploiting the full potential of the UWBG material.

3.2.2 Fabrication of a Ga_2O_3/4H-SiC Composite Substrate

A novel composite substrate to serve as a platform for subsequent epitaxial growth and device fabrication was created using a wafer integration scheme illustrated in **Figure 3.14 (a)**. The starting material was a (010)-oriented Fe-doped Ga_2O_3 wafer using the Czochralski method in an inductively heated iridium crucible. The wafers were produced by slicing 750-µm-thick disks from an ingot and polishing them to achieve an epi-ready finish.[79] This orientation was selected because it is favorable over the $(\bar{2}01)$ and (001) orientations due to the higher cross-plane thermal conductivity[10] and lower coefficient of thermal expansion (CTE) mismatch with 4H-SiC.[80] The surface of the 25 mm-diameter Ga_2O_3 wafer was processed to result in an average surface roughness of ~1 nm (RMS roughness of 2.8 nm). This surface preparation was necessary to make the wafers suitable for the subsequent low-temperature bonding process.[81] The Ga_2O_3 wafer and a 50 mm-diameter 4H-SiC wafer were each coated with 15 nm of SiN_x to prepare them for fusion bonding using a standard process[82,83] with well-characterized TBR in previous reports[84].

Wet activation was performed in a diluted SC1 cleaner (ammonium hydroxide, hydrogen peroxide and deionized water) to remove organic contaminants and particles. The Ga_2O_3 and 4H-SiC wafer surfaces were then activated in oxygen plasma, joined at room temperature to initiate fusion bonding[82,83], and the bonded wafers were cured at 215°C in a N_2 convection oven. The interface is covalently bonded, which avoids the poor interface quality associated with previously reported Ga_2O_3/diamond van der Waals interfaces.[37].The low-temperature bonding process enables bow and warp requirements to be met for potential large-diameter wafer integration (**Figure 3.14 (b)**). Finally, the Ga_2O_3 was thinned down using a series of lapping plates and a diamond abrasive (9 µm, 3 µm, and 0.25 µm diamond grit size), followed by a silica-based chemical-mechanical polishing (CMP) process to remove subsurface damage and enable subsequent epitaxial growth for device processing. A Ga_2O_3 film thickness of less than 10 µm was pursued as shown in **Figure 3.14 (c)**, to minimize the overall thermal resistance of the composite substrate, and the final thickness of the Ga_2O_3 layer was determined to be ~6.5 µm. The aforementioned integration process does not involve the introduction of implantation-induced point defects into the Ga_2O_3 layer which is accompanied by a previously reported surface-activated bonding method.[38] Therefore, the Ga_2O_3/SiC substrate developed in this work can serve as an ideal platform for subsequent device fabrication as it allows the growth of homoepitaxial layers with the highest crystalline quality, potentially without threading dislocations.

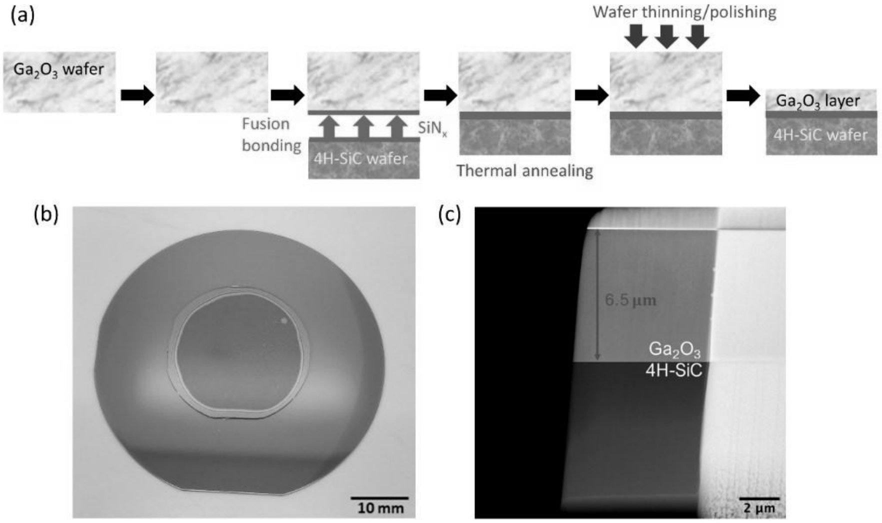

Figure 3.14: (a) The wafer bonding and thinning approach used to create the Ga_2O_3 composite substrate. (b) An image of Ga_2O_3 bonded onto 4H-SiC. The yield is nominally 100% except in the edge exclusion region. (c) Cross-sectional transmission electron microscopy (TEM) image of the Ga_2O_3-on-SiC composite wafer.

It should be noted that the stress/strain induced by the CTE mismatch of the two attached materials must be managed such that the heterointerface stays intact from room temperature up to high-temperature conditions associated with the subsequent device processing steps. Although diamond possesses a higher thermal conductivity (> 1500 W/m·K)[85] than 4H-SiC, 4H-SiC was selected due to the availability of larger diameter semi-insulating substrates, high thermal conductivity (347 W/m·K)[86], and lower CTE mismatch[80,87], that would prevent de-bonding of the Ga_2O_3 caused by unacceptable levels of thermal strain[88] under high growth temperatures, i.e., 600-1000°C for molecular beam epitaxy (MBE), metalorganic chemical vapor deposition (MOCVD), and low-pressure chemical vapor deposition (LPCVD) growth processes.[15]

3.2.3 Low-Temperature MOVPE Growth of Ga_2O_3 Epitaxial Layer

MOVPE has emerged as a promising technique that allows the growth of high-quality β-Ga_2O_3 homoepitaxial films with room-temperature electron mobility values close to the theoretical limit (~ 200 cm^2/Vs) over a wide range of growth temperatures[13,15,19,89–91]. Recently device-grade homoepitaxial films with high carrier mobility values were grown at a lowered growth temperature of 600°C using MOVPE[92]. To avoid potential de-bonding of the Ga_2O_3 layer of the composite substrate due to the thermal expansion mismatch exacerbated by high growth temperatures, the low-temperature MOVPE technique was employed. A lightly Si-doped Ga_2O_3 epitaxial film was grown in an Agnitron Agilis reactor using Tri-ethylgallium, oxygen gas, and diluted silane as the precursor gases, and argon as the carrier gas. Prior to loading into the growth reactor, the sample was cleaned using acetone, isopropyl alcohol (IPA), and DI water in a sonication bath for 2 minutes each. This was followed by a diluted HF dip for 15 minutes. The growth was performed at a temperature of 600°C, chamber pressure of 60 Torr, and a ~ 400 nm thick Ga_2O_3 epilayer was grown at a growth rate of 6.2 nm/min[13]. After growth, the electronic transport properties, and the surface morphology of the MOVPE grown film were characterized using Hall-effect measurements and atomic force microscopy (AFM), respectively. Prior to growth, the composite substrate was analyzed using AFM (Bruker Dimension Icon) as shown in **Figure 3.15(a)**. The surface of the composite substrate was extremely smooth with an RMS roughness of ~0.17 nm, which is similar to those for commercially available (010)-oriented Ga_2O_3 substrates, thus, showing the efficacy of the polishing technique. Extremely smooth films with atomically flat surfaces with sub-nanometer RMS roughness (~0.4 nm) were achieved. **Figure 3.15 (b) and (c)** show large area (5×5 μm^2) and a corresponding small area (0.5×0.5 μm^2) AFM scans of the MOVPE grown film. Smooth surface morphology could be achieved at this growth temperature due to large Ga adatom diffusion as discussed elsewhere[13]. The sample did not show any signs of wear during the entire growth/processing steps including the solvent cleaning, acid cleaning, and epilayer growth.

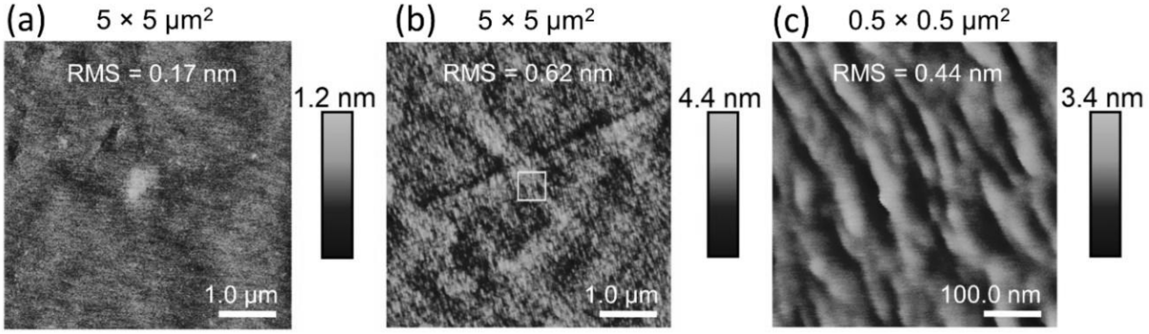

Figure 3.15: (a) AFM image of the polished Ga_2O_3/4H-SiC composite substrate after solvent cleaning. (b) Surface morphology of the MOVPE grown Si-doped film for a 5×5 μm^2 area. (c) A 0.5×0.5 μm^2 AFM scan corresponding to the yellow-boxed area shown in (b).

The electronic transport properties were analyzed using room-temperature Hall measurements (Ecopia HMS 3000). Ti/Au (50 nm/100 nm) ohmic contacts were deposited using DC sputtering on the four corners using a shadow-mask to form the Van der Pauw structure. The contacts exhibited perfectly Ohmic behavior without the need for contact annealing. A room temperature Hall mobility of 94 cm^2/Vs and a sheet charge of 1.2×10^{13} cm^{-2} were extracted corresponding to a volume charge of ~3×10^{17} cm^{-3}. This first demonstration of epilayer growth on the novel composite substrate shows the feasibility of growing smooth homoepitaxial n-type doped high-quality single crystalline epilayers using MOVPE. In other words, this demonstration highlights the compatibility of this novel composite substrate with standard solvent cleaning and acid cleaning while also proving its sturdiness at low pressures and high temperatures, that are required for epilayer growth. These initial results are extremely promising for the development of high-power Ga_2O_3-based lateral devices with potentially superior thermal performance to that of devices on Ga_2O_3 bulk substrates.

3.2.4 Results and Discussion

Figure 3.16 illustrates phonon scattering mechanisms that would govern the overall junction-to-package thermal resistance of devices grown on the Ga_2O_3/4H-SiC composite wafer. First, when the thickness of the thinned single crystal Ga_2O_3 film becomes comparable to the mean free path of the acoustic phonons, incoherent phonon-boundary scattering will reduce the thermal conductivity. Also, the wafer thinning/polishing processes may result in subsurface crystallographic imperfections causing phonon-defect scattering effects. Second, the transmission of phonons across the Ga_2O_3/4H-SiC interface will not only be governed by the acoustic/diffusive mismatch between dissimilar materials but also the low thermal conductivity of the SiN_x bonding layer.

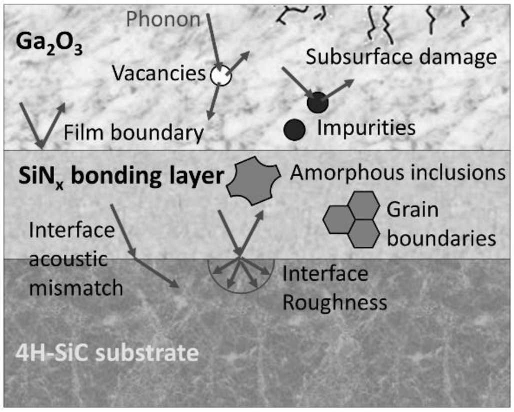

Figure 3.16: Phonon scattering within the Ga_2O_3/4H-SiC composite wafer.

Thermal Conductivity of the Thinned/Polished Ga_2O_3

Previous studies[7,37,75] suggest that a thinner Ga_2O_3 layer remaining on a composite substrate will result in a higher heat transfer performance. Therefore, in addition to measuring the thermal conductivity of the 6.5 μm-thick Ga_2O_3 layer of the composite wafer, this layer was thinned into a wedge shape and characterized. The film thickness was measured along several locations using cross-sectional scanning electron microscopy (SEM) on specimens prepared via focused ion beam (FIB) milling, as shown in **Figure 3.17 (a)**. The cross-plane thermal conductivity of the pre-integrated (010) substrate and the post-integrated Ga_2O_3 film were measured via time-domain thermoreflectance (TDTR)[47] and resulting values are shown in **Figure 3.17 (b)**. The cross-plane thermal conductivity of the (010)-oriented substrate (i.e., in the [010] direction) agrees with values reported in the literature (22.5-27.0 W/m·K) [10,11]. The TDTR measurements were performed next to each FIB region as well as in between the FIB regions where the thickness was estimated via linear interpolation. It should be noted that results for the ~1.828 μm region are not reported due to de-bonding near-edge interface which resulted from the additional polishing process. Possible root causes for the discrepancy between the thermal conductivities of the bulk and thinned Ga_2O_3

include (i) the thickness dependence of the thermal conductivity of the Ga_2O_3 films (i.e., incoherent phonon-boundary scattering) [31,32] and (ii) potential subsurface crystallographic imperfections (i.e., phonon-defect scattering) resulting from the wafer thinning/polishing processes.

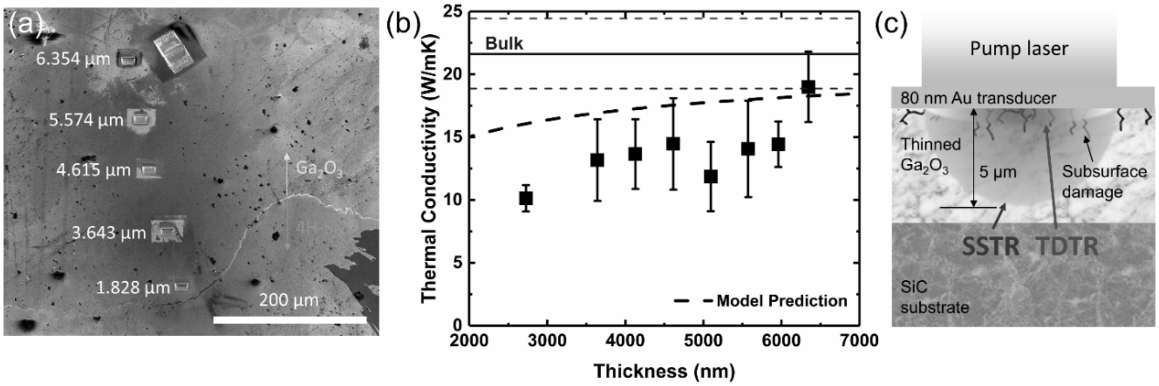

Figure 3.17: (a) Plan view 325× SEM image showing the locations of FIB milling and their corresponding thicknesses measured via cross-sectional SEM. The dark spots are holes or indentations on the surface (b) The measured thermal conductivity of the wedged Ga_2O_3 thin film and the bulk substrate. The blue dashed lines indicate the upper and lower bounds of the bulk thermal conductivity, i.e., error bars. Also shown are predictive modeling results used to estimate the thickness dependence of the Ga_2O_3 thermal conductivity in the [010] direction. (c) Probing volumes of TDTR and SSTR within the Ga_2O_3 composite wafer.

TDTR and SSTR[93] measurements were leveraged to determine whether subsurface defects are indeed present and impacting the thermal conductivity of the Ga_2O_3 layer. As shown in **Figure 3.17 (c)**, SSTR probes the through-thickness average thermal conductivity of the thinned Ga_2O_3 layer (the probing depth is 5 μm) whereas TDTR only probes the cross-plane thermal conductivity near the top surface of the films (the probing depth is 1.35 μm).[94] The directionally-averaged thermal conductivity of the pre-integrated (010) substrate and the post-integrated 6.5 μm Ga_2O_3 film were determined by SSTR to be 19.4 ± 3.03 W/m·K and 18.4 ± 3.39 W/m·K, respectively.

The difference between these results (5% reduction in the thermal conductivity) confirms the presence of phonon-boundary scattering effects, because the SSTR probes a volume that extends much deeper than the potential region with subsurface damage; otherwise, the thermal conductivities of the Ga_2O_3 bulk substrate and the film measured by SSTR should have been similar values. However, TDTR results in **Figure 3.17 (b)** show overall lower thermal conductivity values as compared to the model predictions. This suggests the presence of subsurface damage that reduces the near-surface cross-plane thermal conductivity of the thinned Ga_2O_3 layers.

The thermal conductivity accumulation function[95,96] of bulk Ga_2O_3 in the [010] direction has been derived using first-principles calculations[30]. This calculated phonon mean free path spectrum indicates that acoustic phonons with intrinsic mean free paths ranging from several nm to ~1 μm carry a significant fraction of the heat in this crystalline system. Therefore, Ga_2O_3 films with a thickness on the order of 1-10 μm would exhibit a noticeable film thickness dependence for their thermal conductivities.[97] It should be noted that a strong film thickness dependence of the thermal conductivity of single crystalline β-phase Ga_2O_3 in the [100] direction has been reported.[36] **Figure 3.17 (b)** plots the measured thermal conductivities of the Ga_2O_3 layer with variable thickness along with the Debye-Callaway model[11] predictions (black dashed line). According to the Debye-Callaway model, the phonon-boundary scattering rate is dominant over impurity and Umklapp scattering rates, leading to the decreasing trend of the thermal conductivity as the film thickness reduces. The model predictions and measurement data show reasonable agreement, which suggests that the thermal design of Ga_2O_3 composite substrates must account for the film thickness dependence of the Ga_2O_3 thermal conductivity.

TBR at the Ga_2O_3/4H-SiC Interface

A different SSTR process that uses variable thermal penetration depth to enable sensitivity to individual parameters was used to determine the effective thermal boundary resistance (TBR) at the Ga_2O_3/4H-SiC interface. First, the thermal conductivity of the 4H-SiC substrate is determined prior to wafer bonding (**Figure 3.18 (a)**). Next, probing depth of the SSTR setup is controlled by adjusting the pump laser radius to measure the thermal conductivity of the Ga_2O_3 thin film after the bonding/thinning process is complete (**Figure 3.18 (b)**). Finally, the overall thermal resistance of a probing volume that extends below the Ga_2O_3/4H-SiC interface of the composite wafer is measured using a larger pump laser radius (**Figure 3.18 (c)**). By subtracting the measured thermal resistance of the 4H-SiC substrate and the Ga_2O_3 film from the total thermal resistance, the effective TBR at the Ga_2O_3/4H-SiC interface is extracted. The directionally averaged thermal conductivities of the 6.5 μm thick Ga_2O_3 layer and the 350 μm thick 4H-SiC substrate were measured by SSTR and were determined to be 18.4 W/m·K and 306.4 W/m·K, respectively. The mean value of the measured effective thermal boundary conductance (TBC) was 21.2 MW/m^2K, which corresponds to an effective TBR of 47.1 m^2K/GW. This TBR value is comparable to effective TBRs for GaN-on-diamond composite wafers formed via similar fusion bonding techniques using SiN_x adhesive layers with a similar thickness.[78,98] However, this TBR is more than 3× higher than the reported value for a Ga_2O_3/SiC interface with a 30 nm Al_2O_3 interlayer[38], and a much lower TBR (~7 m^2K/GW) has been achieved via direct heteroepitaxial growth of Ga_2O_3 on SiC[77]. The reason for the higher TBR in this study and strategies for potential improvement are discussed in the following text.

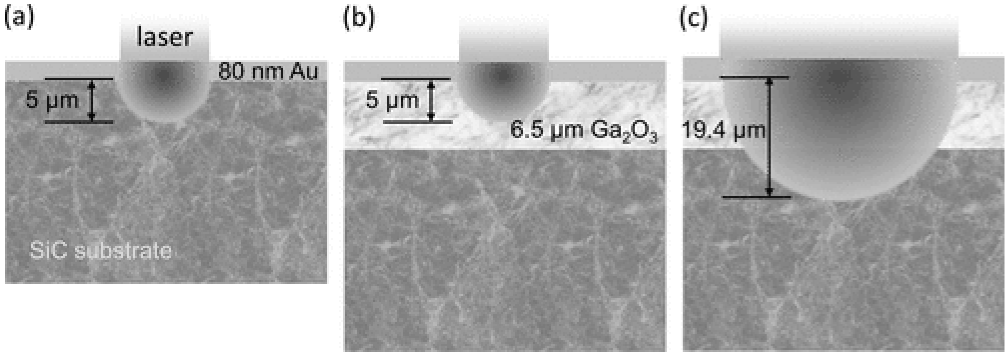

Figure 3.18: Differential SSTR process to measure (a) thermal conductivity of the 4H-SiC substrate, (b) thermal conductivity of the Ga_2O_3 layer, and (c) effective TBR at the Ga_2O_3/4H-SiC interface.

Due to the total thermal resistance in the SSTR probed volume being dominated by the 6.5 μm Ga_2O_3 film, the TBC has a relatively low measurement sensitivity (discussed later in **EXPERIMENTAL METHOD section**). The low sensitivity implies that a change in the TBC will have little impact on the measurement results. Even though the mean value for the TBC was fitted with the SSTR, the error range cannot be accurately determined. Therefore, FDTR was also performed on a thinner region of the wedged Ga_2O_3 on SiC (**Figure 3.17 (a)**) to determine the error bars of the TBC. The thickness (2.2μm) of the Ga_2O_3 layer below the FDTR probing spot (~26.4 μm in diameter) was estimated based on two adjacent FIB regions. The FDTR measured effective thermal boundary conductance (TBC) was 23.4 ± 7.6 MW/m^{2}K, which corresponds to an effective TBR of $42.8^{+20.6}_{-10.5}$ m^{2}K/GW (the error bars for TBR are derived from the upper and lower bounds of the measured TBC; therefore, the error bars are asymmetric).

It should be noted that the effective TBR at the Ga_2O_3/4H-SiC interface of the composite substrate is an aggregate of thermal resistance components arising from (i) the interfacial acoustic/diffusive mismatch between the Ga_2O_3 and the bonding layer, (ii) the low thermal conductivity bonding layer itself, and (iii) the interfacial acoustic/diffusive mismatch between the bonding layer and the 4H-SiC substrate. The theoretical TBR at the Ga_2O_3/SiN_x and SiN_x/4H-SiC interfaces were calculated using the acoustic mismatch model (AMM) and diffusive mismatch model (DMM) following the implementation presented by Bellis et al.[49]. **Figure 3.19** shows the fractional contributions of the calculated interfacial transmission of phonons, and the equivalent thermal resistance from the 30 nm thick SiN_x adhesive layer to the effective Ga_2O_3/4H-SiC TBR. The largest contribution arises from the SiN_x intermediate bonding layer due to its low thermal conductivity (~1.9 W/m·K)[99] and its comparatively large estimated thickness (30 nm).[85,100] Discussions on the SiO_x related data shown in **Figure 3.19** follows next.

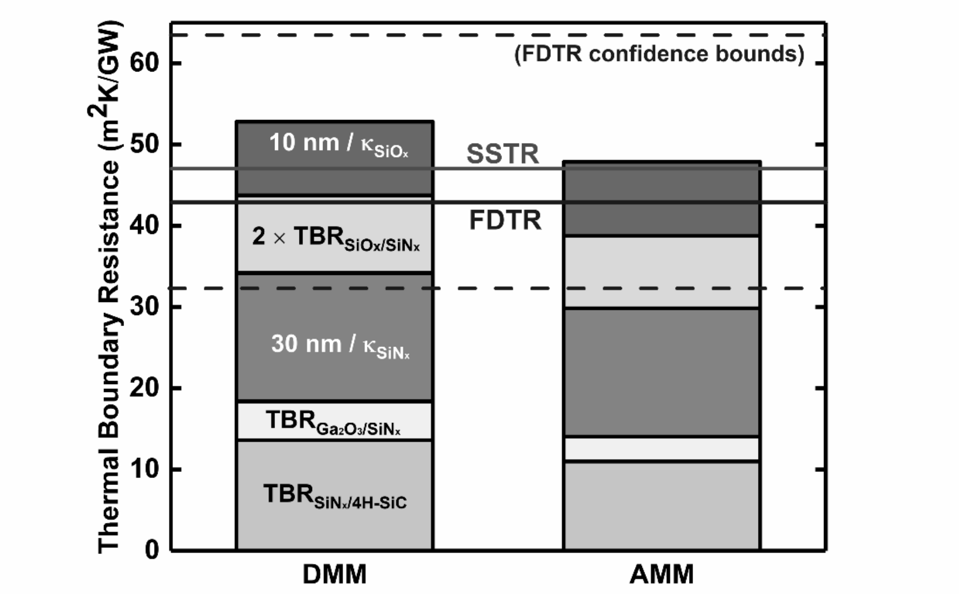

Figure 3.19: The effective TBR at the Ga_2O_3/4H-SiC interface measured by the differential SSTR process and FDTR, and the calculated sum of individual resistive components that contribute to the overall effective TBR. Also shown are the thermal resistance components arising from the unintentionally formed 10 nm SiO_x interlayer within the SiN_x bonding layer. The blue dashed lines indicate the 95% confidence bounds for the FDTR measurement result.

To determine the accurate bonding layer thickness and to evaluate the interface quality and chemistry, scanning transmission electron microscopy (STEM) imaging and energy dispersive X-ray spectroscopy (EDX) mapping were performed. **Figure 3.20** shows a 10 nm SiO_x interlayer formed between the 15 nm thick SiN_x bonding layers that were joined together via fusion bonding. This SiO_x interlayer is typical of hydrophilic fusion bonding processes and is understood to result from the reaction of interfacial water and oxygen with silicon[101]. The inset in **Figure 3.20 (a)** shows the nanodiffraction patterns from individual layers across the interface, and they confirm that the structure of the SiN_x layer remains amorphous. By considering the thermal resistance of this interlayer and the TBR at the two SiO_x/SiN_x interfaces (from AMM and DMM calculations), the experimentally determined effective TBR shows good agreement with the theoretical calculation results. The low thermal conductivity of the SiO_x layer (1.1 W/mK[102]) contributes 21% towards the total TBR determined by FDTR. Additionally, the acoustic and diffusive mismatch between the SiO_x and the SiN further increases the thermal resistance across the interface. These experimental and theoretical findings suggest that a minimum effective TBR of 20 m^2K/GW (based on the prediction by DMM) can be achieved by eliminating the formation of the SiO_x interlayer (by, optimizing the activation process) and reducing the thickness of the SiN_x bonding layer to, for example, 3 nm. Other possible avenues for improving the TBR of the bond interface are reducing the roughness of each of the two bonding surfaces, optimizing the deposition parameters of the intermediate layer, and utilizing intermediate material with a higher thermal conductivity.[103]

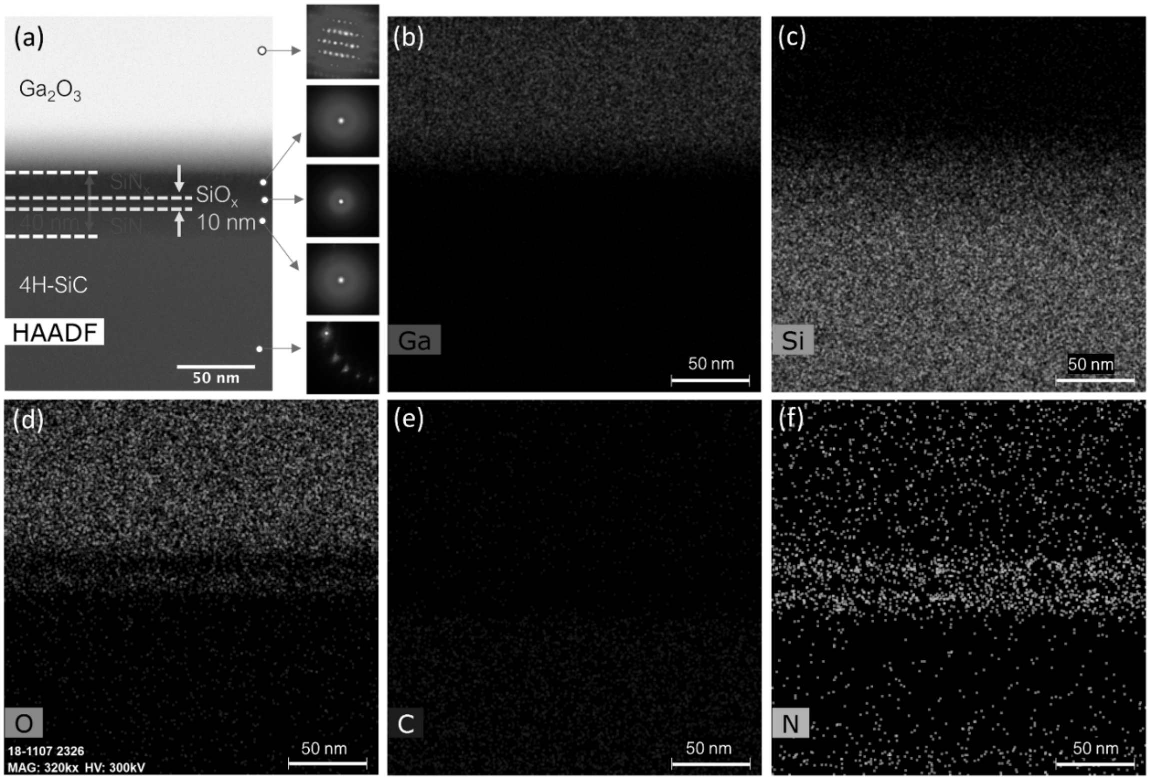

Figure 3.20: STEM-EDX for the Ga_2O_3/4H-SiC interface. (a) A high angle annular dark field (HAADF) image. The inset in (a) shows the nanodiffraction patterns from individual layers shown in the cross section. (b) Ga (c) Si (d) O (e) C and (f) N EDX profiles. The elemental mapping represents the existence of both SiN_x bonding layer and SiO_x interlayer between the Ga_2O_3 film and 4H-SiC substrate.

Implications on Device Thermal Performance

Thermal simulation was performed using COMSOL Multiphysics to estimate the improvement in the device thermal performance by incorporating the Ga_2O_3/4H-SiC composite substrate into the device design. An 85°C constant temperature boundary condition was applied on the bottom of surface of the devices, while a natural convection boundary condition (with a heat transfer coefficient, h = 5 W/mK) was applied to the remaining surfaces. To calculate temperature, a 1 μm diameter domain probe adjacent to the drain side of the gate edge (**Figure 3.21 (b), (c)**) was used to mimic the results of Raman measurements in literature[6,104]. It should also be noted that while the single channel model represented the full device geometry; in order to save computational resources, a quarter model of the 6-finger device was constructed taking into account of the four-fold symmetry. A hypothetical single channel homoepitaxial Ga_2O_3 metal-semiconductor field-effect transistor (MESFET) fabricated on a (010)-oriented Fe-doped semi-insulating Ga_2O_3 substrate is shown in **Figure 3.21 (a)**. The gate-to-source distance (L_{GS}), gate length (L_G), and gate-to-drain spacing (L_{GD}) were 1 μm, 1.5 μm, and 1.5 μm, respectively. The gate width for this device was 185 μm. More details of the thermal modeling procedure can be found in references[6,105]. To simplify the thermal analysis, the device was assumed to operate under a fully-opened channel condition, where the gate-source voltage (V_{GS}) was kept at 0 V. Therefore, the heat generation profile across the channel was assumed as a uniform heat flux distribution.[106] Temperature-dependent thermal conductivity of the Ga_2O_3 substrate was adopted from reference[10]. For comparison, a hypothetical single channel MESFET fabricated on the Ga_2O_3 (6.5 μm)/4H-SiC (350 μm) composite wafer developed in this study (**Figure 3.21 (b)**) was simulated. The anisotropic temperature-dependent thermal conductivities of the Ga_2O_3 layer and 4H-SiC substrate were adopted from references[11] and [86,107], respectively. The directionally averaged thermal conductivities at room temperature measured in these references reasonably agree with the SSTR results for the composite substrate. **Figure 3.21 (d)** shows a comparison of the simulation results for the single channel homoepitaxial device and the device integrated with the composite substrate. The temperature rise was calculated for power densities ranging from 1 W/mm to 5 W/mm. The temperatures shown in **Fi Figure 3.21 (d)** correspond to the average value within a 1 μm×1 μm area in the mid-point of the channel surface next to the drain side corner of the gate. The temperature rise (ΔT) and thus the junction-to-package device thermal resistance of the homoepitaxial device case was found to be ~4.5 times higher than that of the device fabricated on the composite substrate.

Figure 3.21 (e) compares the channel temperature rise of hypothetical 6-finger Ga_2O_3 MESFETs fabricated on a 500 µm thick (010)-oriented semi-insulating Ga_2O_3 substrate versus the Ga_2O_3/4H-SiC composite substrate. A diagram of the 6-finger MESFET's device layout can be found in **Figure 3.21 (c).** The homoepitaxial 6-finger device exhibits an extremely high device thermal resistance, which is ~2.3 times higher than that of a single finger device due to thermal crosstalk among adjacent channel regions dissipating heat.[108] However, if the composite substrate is utilized, heat dissipation is remarkably improved, and the resulting device thermal resistance is reduced from ~370 mm·K/W for the homoepitaxy case to ~42 mm·K /W, which is far lower than other Ga_2O_3 FETs reported in literature[104] and comparable to GaN-on-Si multi-finger devices[109]. These results indicate that implementing a high heat transfer performance composite substrate will be essential for cooling practical multi-finger lateral FETs or reducing the device thermal resistance to a manageable level once the device technology matures.

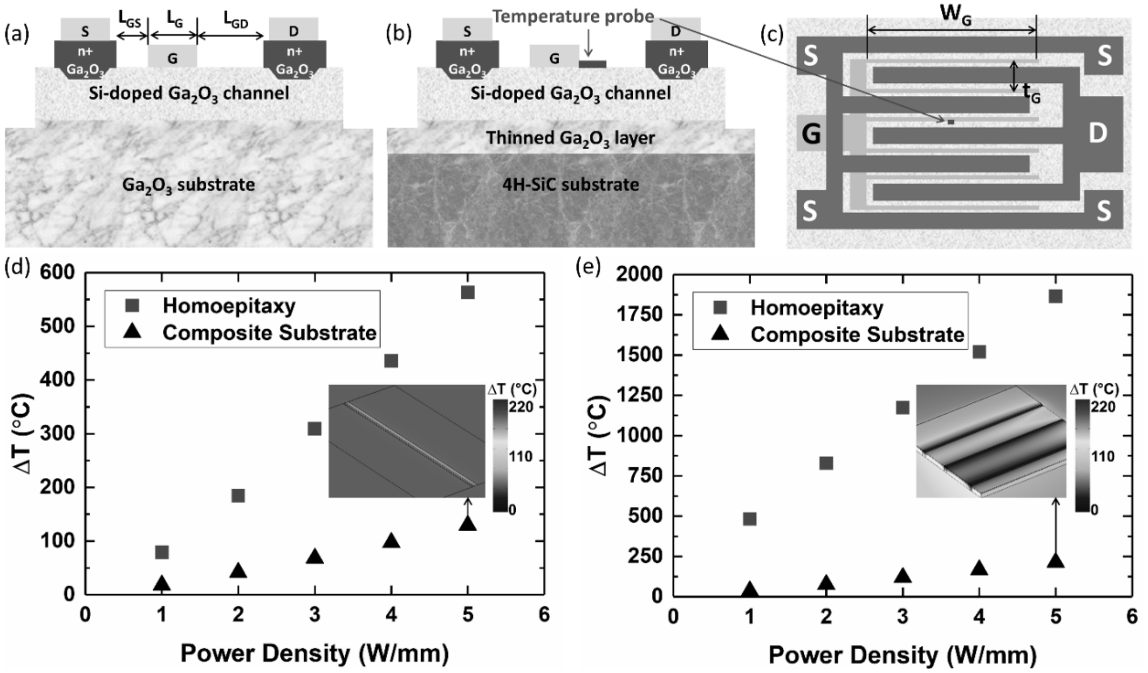

Figure 3.21: (a) Schematic of a simulated single-channel Ga_2O_3 MESFET. (b) Hypothetical MESFET fabricated over the Ga_2O_3 composite substrate. (c) The planar device layout of the hypothetical multi-finger Ga_2O_3 MESFET. (d) The simulated channel temperature rise of the single-finger homoepitaxial MESFET vs. the MESFET integrated with the Ga_2O_3/4H-SiC composite substrate. The surface temperature profile of the "Composite Substrate" case for 5 W/mm power dissipation is shown in the inset. (e) The simulated channel temperature rise of 6-finger Ga_2O_3 MESFETs employing a 500 μm thick Ga_2O_3 substrate vs. the Ga_2O_3/4H-SiC composite substrate. The surface temperature profile of the "Composite Substrate" case for 5 W/mm power dissipation is shown in the inset.

3.2.5 Conclusion

In this study, a novel Ga_2O_3/4H-SiC composite wafer with high heat transfer performance and an epi-ready surface finish was developed. The composite wafer meets the design requirement that will enable reliable thermal management for high power Ga_2O_3 lateral FETs as suggested by Chatterjee et al.[7]. Thermal characterization was performed with a combined approach of TDTR, FDTR, and SSTR. Notably, a differential-SSTR method was demonstrated to directly characterize the effective TBR at the Ga_2O_3/4H-SiC interface, which is inaccessible by TDTR and FDTR methods due to the relatively thick Ga_2O_3 layer (6.5 μm). The TBC measured by differential-SSTR (21.2 MW/m^2K) is in good agreement with the FDTR measurement (23.4 ± 7.6 MW/m^2K) performed after thinning the Ga_2O_3 layer. The TBC is mainly limited by the low thermal conductivity SiN_x bonding layer and an unintentionally formed SiO_x layer; therefore, the TBC can be further improved with optimization of the bonding process and interface. The thermal conductivity of the post-integrated/thinned (010) Ga_2O_3 layers (measured by TDTR) showed a strong film thickness dependence within a thickness ranging of 2.7 – 6.5 μm. The measured thickness-dependent thermal conductivities were overall lower than the Debye-Callaway model predictions. The discrepancy could be caused by the defects or the subsurface damages resulting from the thinning and polishing procedures. The collected thermal data highlights important thermal design considerations for developing similar composite wafers.

The Ga_2O_3/4H-SiC composite wafer enables subsequent growth of homoepitaxial Ga_2O_3 layers and device fabrication. In this study, Si-doped Ga_2O_3 was homoepitaxially grown on the composite substrate by low-temperature MOVPE and has demonstrated promising electronic transport characteristics. The low-temperature MOVPE process demonstrated the feasibility to fabricate devices on the composite wafer without damaging the Ga_2O_3/SiC interface.

The thermal performance of the composite wafer was studied via device thermal simulation. The composite substrate effectively cools a single finger MESFET to a ~4.5 times lower temperature rise as compared to a homoepitaxial device fabricated on a Ga_2O_3 substrate. Effective heat dissipation was demonstrated for a hypothetical multi-finger device where the device thermal resistance is reduced from ~370 mm·K/W to ~42 mm·K /W. The thermal simulation demonstrated the composite wafer as a reliable thermal management solution that has the potential to facilitate mass production of commercial devices. Outcomes of this work will facilitate the electro-thermal co-design[76] of next generation Ga_2O_3 power electronics with unparalleled performance, minimized form factor, and higher power density over current WBG device technologies. The new class of Ga_2O_3 electronics will reduce system-level cooling complexity and cost while increasing component lifetime. The performance gains in power switching for individual devices can lower wafer processing demands and manufacturing costs.

3.2.6 Experimental Methods

Steady-state Thermoreflectance (SSTR)

The detailed setup of the SSTR system has been described in Chapter 2.1. The pump and probe lasers were focused on the sample with the following objectives: (1) a 2.5× objective (NA = 0.08), which has pump and probe radius of 19.4 μm and 12.4 μm, respectively, (2) a 10× objective (NA = 0.25), which has pump and probe radius of 5 μm and 4.3 μm, respectively. The pump and probe radii were measured using a scanning-slit optical beam profiler to evaluate the probe-averaged temperature rise in the thermal model.[93,110] As shown in **Figure 3.22 (a)**, when the pump radius is at 5 μm, the measurement has exclusive sensitivity to the Ga_2O_3 thermal conductivity. When the pump size increases, the thermal penetration depth increases, and therefore the measurement gains sensitivity to the TBC at the heterointerface. The thermal conductivity of the 4H-SiC is measured using a pre-integrated bare substrate, and the TBC at the metal transducer/sample interface is measured with by using calibration samples and assumed to be the same for the tested materials since the metal transducers are deposited on all of these samples simultaneously. In this work, single crystal sapphire was used as a calibration sample due to its well-known thermal conductivity of 33 W/mK.[111] A representative fitting result for SSTR measurements is shown in **Figure 3.23 (a)**.

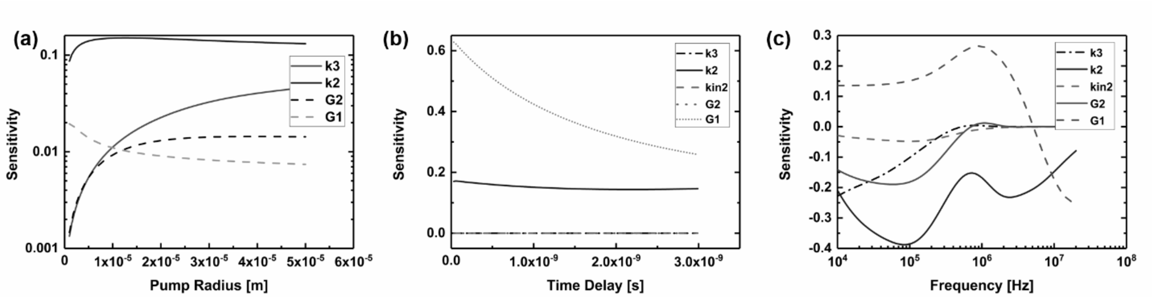

Figure 3.22: The sensitivity plot for the composite wafer for (a) SSTR on 6.5 μm-thick Ga_2O_3 on SiC, (b) TDTR on 3.6 μm-thick Ga_2O_3 on SiC, and (c) FDTR on 2.2 μm-thick Ga_2O_3 on SiC. In the legend, k2 and kin2 stand for the cross-plane and in-plane thermal conductivity of the Ga_2O_3 film, respectively. k3 stands for the thermal conductivity of the 4H-SiC substrate. G1 and G2 stand for the thermal boundary conductance at the transducer/Ga_2O_3 and Ga_2O_3/4H-SiC interfaces, respectively.

Time-domain Thermoreflectance (TDTR)

The radius of the focused pump and probe beams were characterized using a scanning-slit optical beam profiler and were 8.4 μm and 6 μm, respectively. Literature values were used for the thermal conductivity of Au as well as volumetric heat capacities (c_v) of Au[61], β-phase Ga_2O_3[62] and

4H-SiC[112]. The TBC between the metal transducer and the Ga_2O_3 films was fitted simultaneously with the Ga_2O_3 thermal conductivity. The TBC between the Ga_2O_3 films and the 4H-SiC substrate, the in-plane thermal conductivity, and the 4H-SiC substrate thermal conductivity have little impact on the fitting process due to their low measurement sensitivity, as shown in **Figure 3.22 (b)**. Measurements were performed on three locations near each FIB location to account for errors in laser focusing, pump and probe alignment, and local variation of the material. The uncertainty was calculated based on 95% confidence bounds from the multiple measurements and ±2 nm uncertainty associated with the transducer thickness. The same measurement approach was used for FDTR. A representative fitting result for TDTR measurements is shown in **Figure 3.23 (b)**.

Frequency-domain thermoreflectance (FDTR)

The radius of the focused pump and probe beams were characterized using a scanning-slit optical beam profiler and were 13.4 μm and 13.1 μm, respectively. Material properties used to post-process the FDTR raw data were identical to those used in the analytical model for TDTR experiments. As shown in **Figure 3.22 (c)**, the in-plane thermal conductivity of the Ga_2O_3 has low sensitivity. The TBC between the metal transducer and the 4H-SiC substrate and the 4H-SiC thermal conductivity were simultaneously determined (fitted) by characterizing a bare 4H-SiC substrate. A metal transducer/Ga_2O_3 TBC identical to the metal transducer/4H-SiC TBC was assumed for the wedge-shape thinned Ga_2O_3 composite substrate because an identical transducer deposition procedure was used for these samples. The 4H-SiC thermal conductivity was used as a known parameter for subsequent measurement, where the TBC between the Ga_2O_3 layer and 4H-SiC and the Ga_2O_3 thermal conductivity were simultaneously determined during the characterization of the composite wafer. A representative fitting result for FDTR measurements is shown in **Figure 3.23 (c)**.

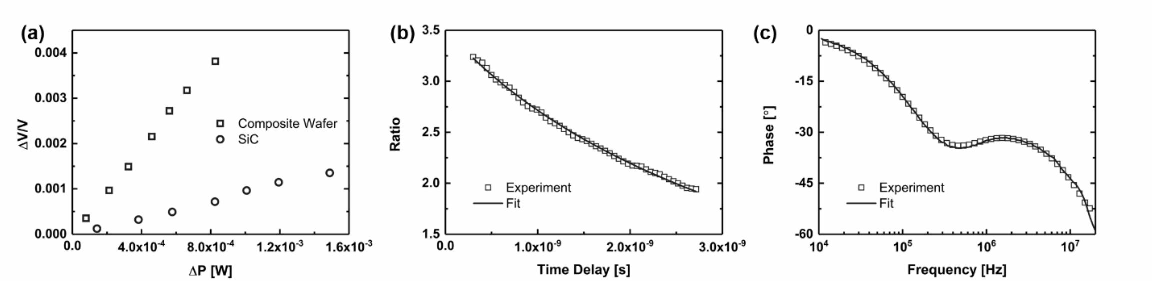

Figure 3.23: (a) SSTR measurement results for the composite wafer and 4H-SiC substrate using a 19.4 μm pump radius. The difference between the slopes for the 4H-SiC and the composite wafer data corresponds to the total thermal resistance of the 6.5 μm-thick Ga_2O_3 layer and the effective TBR. The TBR was extracted by conducting SSTR measurements on the 6.5 μm-thick Ga_2O_3 layer using a 5 μm pump radius (not shown), which allowed to perform the differential SSRT process. Representative data fitting results for (b) TDTR on a 3.6 μm-thick Ga_2O_3 layer on 4H-SiC, and (c) FDTR on a 2.2 μm-thick Ga_2O_3 layer on 4H-SiC, where the Ga_2O_3/SiC TBC and the Ga_2O_3 thermal conductivity were simultaneously fitted.

Scanning transmission electron microscopy (STEM)

Scanning Transmission Electron Microscopy (STEM) samples were prepared using focused ion beam (Thermofisher Helios Dual-beam FIB). To retain a clean and thin specimen, the surface of the STEM foils was cleaned using low energy ion milling (Fischione Nanomill) operated at 500 eV. The high angle annular dark field (HAADF) STEM imaging was performed using Thermofisher aberration-corrected Titan STEM with probe convergence half angles of 10.03 mrad at an accelerating voltage of 300 kV. The microscope is also equipped with ChemiSTEM Energy dispersive X-ray spectroscopy (EDX) system, which allows for the characterization of the composition of the cross-section STEM sample. Five chemical species (Ga, Si, O, C, and N) at the interface were analyzed by the EDX elemental mapping. The 40 nm SiN_x adhesive layer was determined at the interface region. Due to the inhomogeneity of the lattice mismatch between the Ga_2O_3 thin films and 4H-SiC substrate, the SiN_x bonding interface was marginally delaminated, resulting in the oxidation layer of 10 nm SiO_x within the SiN_x interfacial region. The elemental profile further demonstrated the distribution of O based on the cross-section STEM-EDX measurements.

Thermal Conductivity Modeling

The Debye-Callaway model was applied to obtain the thickness-dependent thermal conductivity of β-phase Ga_2O_3 single crystals along the [010] direction.[11] The phonon-phonon Umklapp scattering, phonon-impurity scattering, and phonon-boundary scattering are included in the resistive phonon scattering processes of the model. The scattering rates of the three scattering mechanisms are expressed as:

$$\left[\tau_U^j(x)\right]^{-1} = \frac{k_{\mathrm{B}}^2 \gamma_j^2}{M\hbar v_j^2 \theta_j} x^2 T^3 e^{-\frac{\theta_j}{3T}} \tag{3.7}$$

$$\left[\tau_I^j(x)\right]^{-1} = \frac{V k_{\mathrm{B}}^4 \Gamma}{4\pi\hbar^4 v_j^3} x^4 T^4 \tag{3.8}$$

$$\left[\tau_B^j\right]^{-1} = \frac{2v_j}{d} \tag{3.9}$$

where k_B is the Boltzmann constant, T is the temperature, $\hbar$ is the reduced Planck's constant, q is the Debye temperature, v is the sound velocity, subscript "j" denotes the branch in the phonon dispersion spectrum, and $x = \hbar\omega/k_BT$ with ω being the angular frequency. For β-phase Ga_2O_3, $V = 1.0587 \times 10^{-29}$ m^3/atom and $M = 6.2231 \times 10^{-26}$ kg/atom. The Grüneisen parameters, γ_L and γ_T, are treated as two fitting parameters and are obtained by fitting the temperature-dependent thermal conductivity from 80 to 400 K to the first-principles calculations along the [010] direction of bulk β-phase Ga_2O_3. The parameters that were used in the model calculation are listed in **Table 3.4**. These parameters were derived from the aforementioned first-principles calculations.[10]

Table 3.4: Zone-boundary frequencies $\boldsymbol{f_{L,T}}$ and phonon (sound) velocities $\boldsymbol{v_{L,T}}$ of longitudinal and transverse phonons for β-phase Ga_2O_3 along the [010] direction from the first-principles calculations. $\boldsymbol{\theta_{L,T}}$ are the Debye temperatures calculated from these cutoff frequencies following $\boldsymbol{\theta = \frac{2\pi\hbar f}{k_B}}$. $\gamma_{L,T}$ are the Grüneisen parameters.

Parameter	f_L	f_{T1}	f_{T2}	v_L	v_{T1}	v_{T2}	θ_L	θ_{T1}	θ_{T2}	γ_L	γ_T
Unit	(THz)	(THz)	(THz)	(m s^{-1})	(m s^{-1})	(m s^{-1})	(K)	(K)	(K)		
Value	4.6	3.0	2.4	7270	3590	1960	220	144	115	1.1	0.85

Acoustic Mismatch (AMM) and Diffusive Mismatch (DMM) Modeling

The acoustic mismatch (AMM) and diffusive mismatch (DMM) models were implemented to calculate the interfacial thermal conductance (TBC) for the β-phase Ga_2O_3/SiN_x, SiN_x/4H-SiC, and SiO_x/SiN_x interfaces. The AMM and DMM models are based on the Landauer formalism following the general Landauer formula for the TBC expressed as:

$$G = \sum_p \frac{1}{2} \int_0^{\omega_d} \int_0^{\pi/2} D_1(\omega) \frac{df_{BE}}{dT} \hbar\omega v_1(\omega) \tau_{1,2}(\theta, \omega) \cos(\theta) \sin(\theta)\, d\theta d\omega \tag{3.10}$$

The index p indicates the phonon branch, ω_d represents the cutoff frequency, D represents the phonon density of states (DOS), ω represents the angular frequency, f_{BE} is the Bose-Einstein distribution function of phonons, T is the temperature, $\hbar$ is the reduced Planck constant, v is the phonon group (or sound) velocity, $\tau_{1,2}$ is the transmission coefficient from the medium 1 to 2, and θ is the angle of incidence. The major difference in the mathematical expressions for the AMM and DMM models relies on the definition of the transmission coefficients. The transmission coefficient is defined in terms of ω for the DMM and, for the AMM, θ and ω are involved in the definition of $\tau_{1,2}$. Thus, for the AMM, the transmission coefficient can be expressed as

$$\tau_{1,2,\mathrm{AMM}}(\theta, \omega) = \frac{4 \frac{Z_2}{Z_1} \cdot \frac{\cos(\theta_2)}{\cos(\theta_1)}}{\left(\frac{Z_2}{Z_1} + \frac{\cos(\theta_2)}{\cos(\theta_1)} \right)^2} \tag{3.11}$$

where Z represents the acoustic impedance. On the other hand, the transmission function for the DMM model as a function of the frequency can be written as follows:

$$\tau_{1,2,\mathrm{DMM}}(\omega) = \frac{\sum_p M_2\,(\omega)}{\sum_p M_1\,(\omega) + \sum_p M_2\,(\omega)} \tag{3.12}$$

where M is the phonon number of modes of mediums 1 and 2. Since the transmission coefficient for the DMM model is not dependent on the incidence angle, the integration θ is not required, and the mathematical expression for the TBC can be simplified. The calculations of the TBC using the AMM and DMM models are based on the formulation presented by Bellis et al.[49], and **Table 3.5** lists the main parameters required for these calculations.

Table 3.5: Implemented parameters for the calculations of the thermal boundary conductance (*G*) using the AMM and DMM formulations.

Medium A	Medium B	Speed of sound [m/s] v_L,v_T		Mass density [kg/m^3]		G_{AMM}	G_{DMM}
		Medium A	Medium B	Medium A	Medium B	[MWm^{-2}K^{-1}]	[MWm^{-2}K^{-1}]
4H-SiC [0001]	SiN_x [111]	13200, 6900[113]	23189, 9276[114]	3210	3100	91.0991	73.6241
β-Ga_2O_3 [010]	SiN_x [111]	7800, 3550[10]	23189, 9276[114]	5880	3100	327.8500	208.8000
SiO_2 [Amorp.]	SiN_x [111]	5800, 3700[115]	23189, 9276[114]	2650	3100	224.3095	209.5125

3.3 Device-level Thermal Management

3.3.1 Introduction

β-phase gallium oxide (Ga_2O_3) is an ultra-wide bandgap (UWBG) semiconductor (E_G~4.8 eV), which promises significant improvements in the performance and manufacturing cost over today's commercial wide bandgap (WBG) power electronic devices based on GaN and SiC.[116] During the past half-decade, significant progress has been made in the Ga_2O_3 bulk material synthesis (i.e., only Ga_2O_3 offers melt-grown single crystal substrates like Si wafers, among today's WBG and UWBG semiconductors), epitaxial growth, doping, and the development of homoepitaxial device architectures.[2,116,117] UWBG Ga_2O_3 electronics give promise to allow designers to use fewer devices and smaller passive components in power electronics circuits.[118] Power conversion systems for electric vehicles and charging stations, renewable energy sources, and smart grids will benefit from the Ga_2O_3 device technologies.

However, device overheating has become one of the most critical bottlenecks to the commercialization of Ga_2O_3 device technologies.[119] In fact, no Ga_2O_3 device reported to date has achieved the performance expected by the outstanding electronic properties because a thermally limited technological plateau has been reached. Ga_2O_3 possesses a poor anisotropic thermal conductivity (11-27 W/mK)[10,11], which is an order of magnitude lower than those for GaN (~150 W/mK)[97,120] and SiC (~400 W/mK)[86,107]. It has been experimentally reported that single-finger Ga_2O_3 metal-oxide-semiconductor field effect transistors (MOSFETs)[7] and modulation-doped FETs (MODFETs)[6,121] exhibit a ~6× higher channel temperature rise than commercial GaN high electron mobility transistors (HEMTs) under identical power dissipation levels. Moreover, recent computational work[122] indicates that self-heating will be significantly aggravated in practical multi-finger devices due to the thermal cross-talk[108] among adjacent current channels. Specifically, it has been predicted that the channel temperature rise of a six-finger Ga_2O_3 MOSFET would be another 4× higher than that for a single finger Ga_2O_3 device. Such aggravated self-heating in multi-channel Ga_2O_3 FinFETs as compared to single-fin devices has been experimentally demonstrated.[123] This signifies the importance of minimizing the junction-to-package thermal resistance of Ga_2O_3 devices.

Efforts to counter the overheating at the package/system-level not only increase the system size and weight but also have proven to be ineffective in cooling ultra-high power density WBG/UWBG devices.[124] Therefore, the electro-thermal co-design of novel device architectures that can simultaneously achieve the lowest thermal resistance and highest electrical performance is essential to enable the commercialization of UWBG Ga_2O_3 device technologies.[124]

In our previous work[122], a Ga_2O_3/4H-SiC composite wafer was created by taking advantage of a fusion bonding process. The thermal conductivity of the Ga_2O_3 layer and the thermal boundary resistance at the Ga_2O_3/SiC interface were characterized via a steady-state thermoreflectance technique. Scanning transmission electron microscopy and energy dispersive X-ray spectroscopy were used to study the interface quality and chemistry. In this work, Ga_2O_3 MOSFETs were fabricated on the composite substrate using low temperature ($\leq$ 600°C) metalorganic vapor-phase epitaxy, that allowed the first realization of "homoepitaxial" Ga_2O_3 MOSFETs on a composite substrate. This growth technique is necessary to prevent interface failure of the composite substrate due to mismatch of the coefficients of thermal expansion. Electrical testing was performed to determine the device output characteristics and breakdown voltages. The enhanced device thermal impedance achieved by integration with the composite wafer was assessed by using nanoparticle-assisted Raman thermometry. A design optimization study has been conducted with an aim to reduce the device thermal impedance of Ga_2O_3 transistors below that for a commercial GaN power switch under high power and frequency switching operation. The outcomes of this work provide guidelines to surpass the ultimate thermal limit of the (laterally configured) UWBG device technology.

3.3.2 Results and Discussion

DEVICE FABRICATION

This work is based on the Ga_2O_3/4H-SiC composite substrate presented in Chapter 3.2. To maintain the structural integrity of a composite substrate, it is of critical importance to limit the maximum temperature that occurs during the multiple processing steps associated with device fabrication. For this reason, a low temperature device processing scheme was developed that keeps the maximum temperature of the entire process below 600°C. It should be noted that current growth techniques for other WBG and UWBG materials systems such as GaN, SiC, and AlGaN do not allow this.[125–127] Device fabrication began with the epitaxial growth of a Si-doped channel. The composite substrate was solvent cleaned in sonication baths of acetone, isopropyl alcohol and deionized (DI) water. Next, the substrate was dipped in a hydrofluoric acid solution for 15 minutes and then cleaned using DI water. After cleaning, the sample was loaded into a metalorganic vapor-phase epitaxy (MOVPE) reactor and a (010) oriented Si-doped Ga_2O_3 epilayer (~400 nm thick) was grown at 600°C.[13] An Agnitron Agilis vertical quartz tube MOVPE reactor was used with triethylgallium (TEGa) and O_2 as the precursor gases, argon as the carrier gas, and diluted silane for doping. From Hall measurements, the room temperature channel sheet charge and mobility were found to be 1.3×10^{13} cm^{-2} and 94 cm^2/Vs, respectively. Due to the sufficient adatom diffusion lengths at this growth condition (i.e., temperature and molar gas flow fluxes), an atomically smooth surface morphology (RMS roughness of ~0.5 ± 0.1 nm) was maintained and single crystal films with high crystalline quality and transport properties were synthesized. The low temperature MOVPE growth process helps minimize the potential risk of debonding of the composite wafer due to the thermal expansion mismatch between the Ga_2O_3 and 4H-SiC materials.[122] A cross-sectional schematic of a Ga_2O_3 metal-oxide-semiconductor field-effect transistor (MOSFET) fabricated on the composite wafer is shown in **Figure 3.24 (a)**. Device fabrication started with mesa isolation using a patterned Ni/SiO_2 hard mask and directional dry etching, i.e., inductively coupled plasma - reactive ion etching (ICP-RIE) SF_6-Ar (600W ICP, 150 RF powers – 45 nm/min etch rate for Ga_2O_3).[92,128] This was followed by source-drain region patterning using the same Ni-SiO_2 patterning process and contact region recessing using a low power ICP-RIE SF_6-Ar (150W ICP, 50 RF powers – 1.5 nm/min etch rate for Ga_2O_3).[129] After selectively wet etching Ni, the sample with the patterned SiO_2 mask was loaded into the MOVPE reactor for ohmic contact regrowth. A heavily Si-doped n+ (estimated 1.4×10^{20} cm^{-3}) Ga_2O_3 layer was grown at 600°C with an approximate thickness of 100 nm.[128] The sample was then cleaned in an HF solution and the regrowth mask including regrown Ga_2O_3 was selectively removed from all regions except the source-drain regions. This was followed by ohmic metal evaporation of Ti/Au/Ni (20/100/50 nms) on the n+ regions by photolithography and lift-off. The contacts were then annealed in a rapid thermal processing (RTP) furnace at 450°C for 1.5 mins in a N_2 ambient. A thermal atomic layer deposition (ALD) grown Al_2O_3 layer (at 250°C) with a target thickness of 25 nm was blanket deposited to form the gate insulator. Then, a Ni/Au/Ni (30/100/30 nm) metal stack was evaporated to form the gate electrode. Finally, the Al_2O_3 over the source-drain metal pad regions was removed using a photoresist mask and CF_4-O_2-N_2 ICP-RIE dry etching. It is to be noted that (apart from benefitting from the low temperature processes), the composite substrate shows strong ruggedness against standard device processing steps (such as ultrasonication in solvents, acid cleaning, wet and dry etching, and dielectric/metal deposition), as well as patterning processes. This confirms its compatibility with standard device processing methods used to fabricate homoepitaxial devices on bulk Ga_2O_3 wafers.

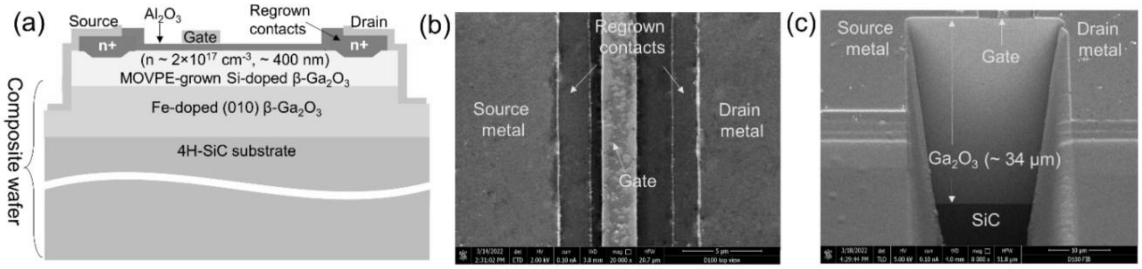

Figure 3.24: **(a)** A cross-sectional schematic of a Ga_2O_3 MOSFET fabricated on the composite substrate. **(b)** Plan-view SEM image of a final device structure. **(c)** Cross-sectional SEM image of the same device showing the thickness of Ga_2O_3 layer.

The device dimensions were verified by top-side SEM imaging (**Figure 3.24 (b)**). The L_{GS} and L_G were fixed at ~0.7 nm and ~2.1 μm, respectively, while the L_{GD} was varied from ~2.5 to 55 μm. The thickness of the Ga_2O_3 layer was determined to be ~34 μm using cross-sectional SEM imaging (**Figure 3.24 (c)**). From transfer length method (TLM) measurements, the contact resistance to the channel was ~1.6 ± 0.2 Ω.mm. **Figure 3.25 (a)** and **(b)** show the direct current (DC) output and transfer curves, respectively, for a device with L_{GD} ~ 2.5 µm. A device with L_{GD} ~ 2.5 µm exhibits a drain current of ~100 mA/mm at a drain-source voltage of 8 V and gate bias of 0 V. The ON resistance from the linear region of the output curve is ~ 65 Ω·mm. From the transfer curve, the device shows clear pinch-off characteristics, and the ON/OFF ratio is ~10^8. The device showed a large threshold voltage of -50 V, most likely due to the presence of a remnant active parasitic channel at the epilayer/Ga_2O_3 (of the composite substrate) interface. **Figure 3.25 (c)** shows the channel charge profile that is extracted from capacitance-voltage (C-V) measurements. A clear charge peak can be seen at the epilayer-substrate interface, potentially originating from the polishing step used to thin down the bonded Ga_2O_3 wafer. The magnitude of this parasitic charge was spatially nonuniform across the composite wafer. This is also revealed by the nonuniform threshold (or pinch-off) voltage of transistors fabricated on the composite substrate, which varied from -40 V to -85 V. This observation indicates a parasitic charge of 3 – 8×10^{12} cm^{-2} at the epilayer/composite substrate interface contributing to the total channel charge. Proper surface preparation of the composite substrate (e.g., chemical and plasma treatment) and development of an insulating buffer schemes will be necessary to remove the parasitic charges at the epilayer/Ga_2O_3 interface.

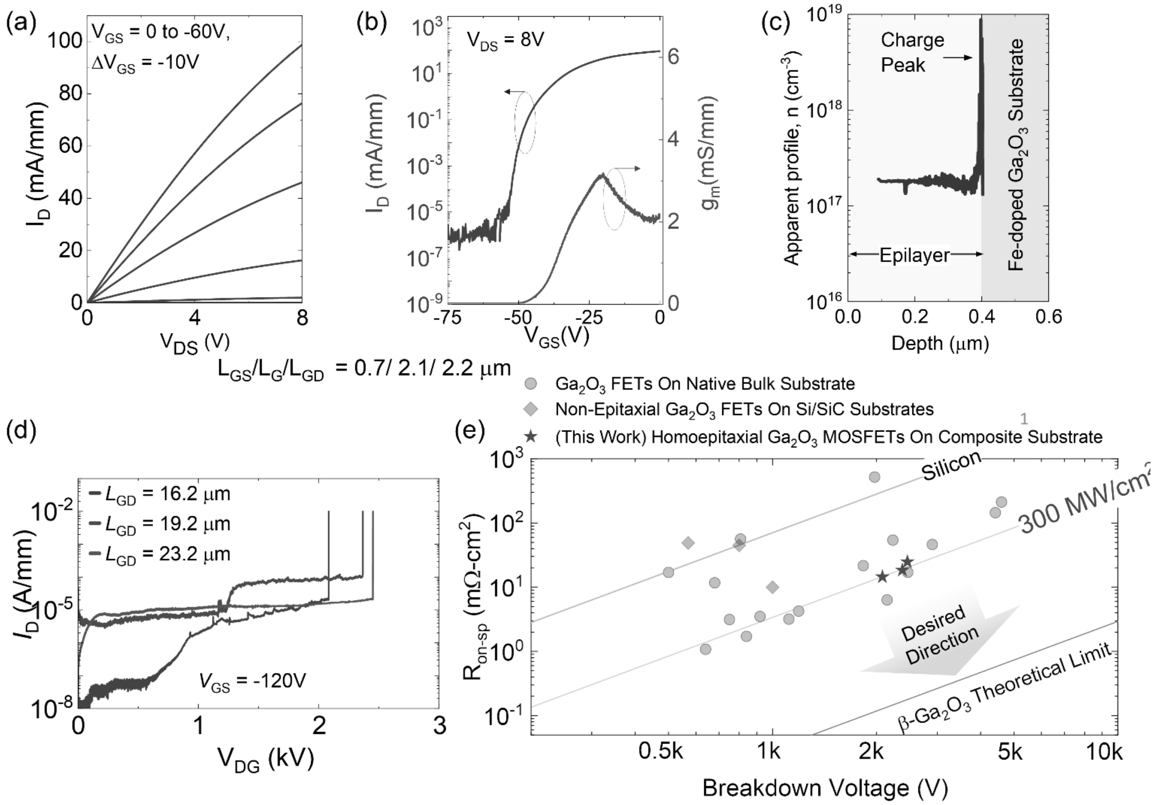

Figure 3.25: (a) DC output and (b) transfer curves of the Ga_2O_3 MOSFET fabricated on the composite substrate. (c) Channel charge profile extracted from C-V measurements. (d) Off-state breakdown characteristics of the Ga_2O_3 MOSFETs with various L_{GD} values. (e) Benchmarking of the MOSFET fabricated on the composite substrate against homoepitaxial Ga_2O_3 FETs[92,128–140] and devices fabricated on other bonded substrates[141–143] in literature.

Device breakdown measurements were performed on the large L_{GD} devices with the wafer submerged in a dielectric liquid (Fluorinert FC-40). A large negative gate bias of -120V was applied during breakdown measurements to minimize bulk-related source-to-drain leakage. The breakdown voltages (V_{BR}) increased from 2.08 kV to 2.45 kV as the L_{GD} was scaled from 16.2 μm to 23.2 μm. The average breakdown field was around ~1.3 MV/cm, which is promising given that the devices did not employ any field plates to lower the peak electric field. The specific ON resistance (R_{on-sp}; normalized with respect to the device area) values were 14.5, 18.4 and 24.8 mΩ·cm^2 for devices with L_{GD} of 16.2, 19.2 and 23.2 μm, respectively. The respective power figure of merit (PFOM[144]; $V_{BR}^2/R_{on\text{-}sp}$) of the devices were 295 MW/cm^2 (V_{BR}=2.08 kV), 303 MW/cm^2 (V_{BR}=2.37 kV) and 242 MW/cm^2 (V_{BR}=2.45 kV). These are the highest V_{BR} and PFOM values ever reported for Ga_2O_3 transistors fabricated on engineered substrates.[141–143] **Figure 3.25 (e)** benchmarks the $R_{on\text{-}sp}$-V_{BR} performance of the MOSFETs against values reported in literature. With a PFOM of ~300 MW/cm^2, these devices are better than most state-of-the-art homoepitaxial Ga_2O_3 devices fabricated on native Ga_2O_3 substrates and are significantly better than "transferred and non-epitaxial" Ga_2O_3 transistors on SiC substrates.[141–143] The electrical performance is not compromised by fabricating devices on the composite substrate when using the low temperature device processing scheme. Even though this is the first demonstration of "epitaxially grown" Ga_2O_3 MOSFETs fabricated on a composite substrate, the devices show promising OFF-state voltage blocking capabilities up to 2.45 kV suitable for power electronics applications.

Device thermal Characterization

Nano-particle assisted Raman thermometry[145,146] was used to perform *in situ* channel temperature measurement of the MOSFET structures. Anatase TiO_2 nanoparticles of 99.98% purity were deposited on the devices to serve as surface temperature probes. The Stokes Raman peak shift of the E_g phonon mode was monitored during device operation to estimate the channel temperature rise. Measurements were taken on nanoparticles close to the drain side edge of the gate, where the channel peak temperature is expected to occur due to electric field and Joule heat concentrations. Measurements were performed on devices with different dimensions (L_{GD} of ~2.2, 28, and 55 μm) fabricated on both the composite wafer and a native Ga_2O_3 substrate. **Figure 3.26** shows the steady-state temperature rise (ΔT) as a function of power density and the corresponding heat flux values.

When comparing the temperature rise for devices with different L_{GD}, it is important to consider the heat flux since the area where Joule heating occurs is changing. Therefore, a device with a larger L_{GD} will experience a lower temperature rise for a given power density. It should be noted that the devices on the composite and native substrates exhibited similar power densities for particular drain voltages (V_{ds}). Due to the enhanced heat transfer performance of the composite substrate, a significant reduction in channel temperature rise (up to a 2.4× reduction) was observed for devices (especially those with larger L_{GD}) operating under a power density of 2.63 W/mm.

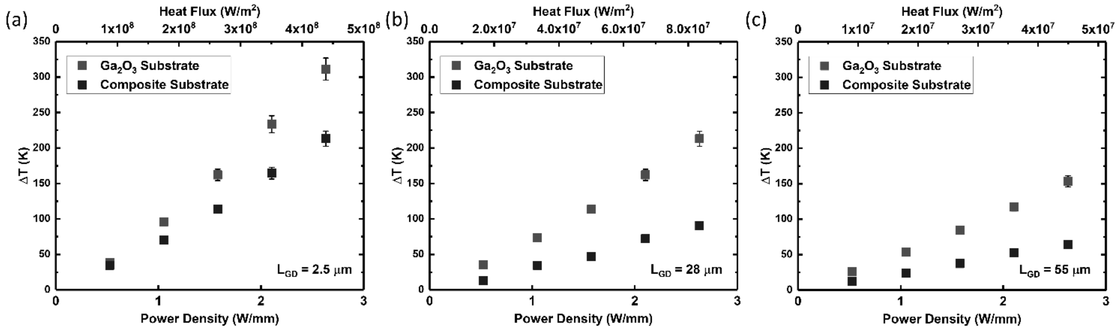

Figure 3.26: Steady-state channel temperature rise of the MOSFETs fabricated on the composite substrate and a bulk Ga_2O_3 wafer. Devices with different L_{GD} were tested. (a) L_{GD}=2.5 μm, (b) L_{GD}=28 μm, and (c) L_{GD}=55 μm.

The transient channel temperature rise of the devices was characterized to understand the cooling effectiveness of the composite substrate under high frequency switching operation. A transient Raman thermometry setup (details can be found in the experimental section) was used to monitor the channel temperature rise in response to a square electrical power pulse with a temporal resolution of 25 μs.[145,146] As shown in **Figure 3.27**, the early-stage temperature rise (<100 μs) is similar between the homoepitaxial and composite substrate; this is because of the low thermal diffusivity (or slow transient thermal response) of Ga_2O_3, causing the heating to be restricted within the ~34 μm thick Ga_2O_3 layer for both devices fabricated on the composite wafer and a native substrate. A lower temperature rise is observed for the devices on the composite wafer only after 100 μs, from which the high thermal conductivity of 4H-SiC contributes to spreading the heat away from the device active region[3]. Data in **Figure 3.27** indicate that the channel temperature of the devices on the composite substrate reaches steady-state after 200-300 μs while the temperatures of the devices on a Ga_2O_3 substrate continues to increase. In contrast to previously developed diamond integration methods for GaN high electron mobility transistors (HEMTs)[81,124,147–149], the low thermal diffusivity of Ga_2O_3 renders a more in-depth thermal design process required for the development of Ga_2O_3 devices on a composite wafer,. For our current design, the thickness of the Ga_2O_3 layer of the composite substrate is far larger than ~10 μm (recommended by Chatterjee *et al.*[7]), which is necessary to reduce the device thermal resistance less than that of a GaN-on-Si power switch. Therefore, 3D modeling was performed in the next section to further discuss the transient thermal response and its implications on design optimization.

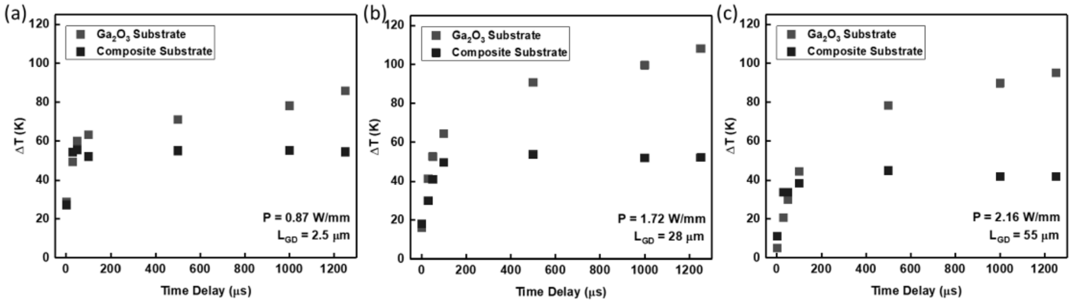

Figure 3.27: The transient channel temperature rise of MOSFETs fabricated on native (Ga_2O_3) and composite substrates. Devices with different L_{GD} were tested. (a) L_{GD}=2.5 μm, (b) L_{GD}=28 μm, and (c) L_{GD}=55 μm.

Modeling and design optimization

In order to verify the results of the nanoparticle-assisted Raman thermometry measurements, a 3D transient electro-thermal model was constructed.[7,150] The (010) Ga_2O_3 layer was modeled to be 34.6 μm based on the SEM results and a directional and temperature dependent thermal conductivity was employed from values published by Guo et al.[10] The 4H-SiC substrate layer was modeled to be 500 μm thick, and a temperature dependent thermal conductivity was adopted from Wei et al.[86] An effective TBR of 47.1 m^2K/GW[122] was applied at the Ga_2O_3/SiC interface based on SSTR measurement results. First, the device detailed in section 2.2 (L_{GD}~2.5 μm) was modeled under steady-state conditions matching the operating conditions used in the nanoparticle Raman experiments listed in **Figure3.26 (a)**. **Figure 3.28** shows the modeling results, which are in excellent agreement with the temperatures measured via the Raman thermometry experiments. The composite wafer is shown to reduce the device peak temperature during operation; however, the thermal performance can be further enhanced by reducing the Ga_2O_3 layer thickness, improving phonon transport across the interface, and using a higher thermal conductivity substrate instead of 4H-SiC. Therefore, a second model was built to assess the theoretical performance limit by using such “ideal” composite wafer. This ideal model assumes a reduced Ga_2O_3 thickness of 1 μm (which consists of 200 nm from ion-cutting[38], 300 nm from a back barrier, and 500 nm for the channel) and a single crystalline diamond substrate[151]. An effective thermal boundary resistance of 7.8 m^2K/GW was assumed between the Ga_2O_3 and the diamond substrate based on the TBC for using 10 nm Al_2O_3 as the bonding interlayer.[38] This ideal case showed a significant reduction in channel temperature rise (~10×) as compared to the current composite wafer design, suggesting the potential for further enhancement in the cooling performance with optimization.

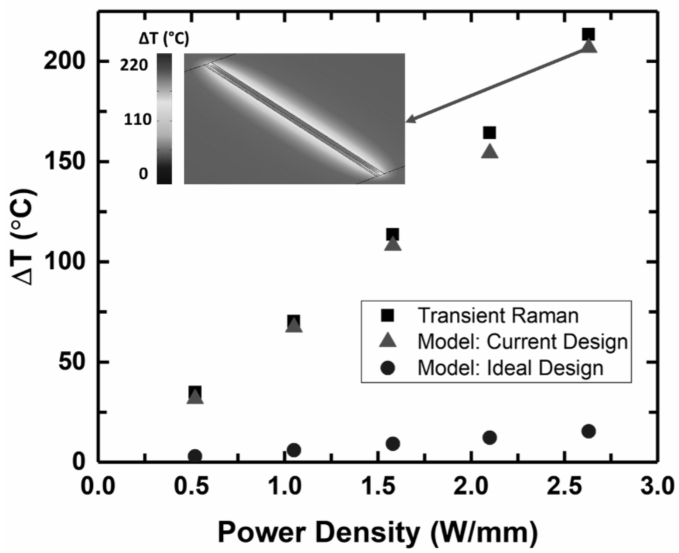

Figure 3.28: Comparison of results (channel temperature rise) from the Raman experiments and simulation for the fabricated Ga_2O_3-on-SiC MOSFET and an “ideal” device.

As previously mentioned, a composite wafer must be designed so that high cooling performance is offered under high frequency switching operation. Transient thermal models for both the current design and the ideal case were constructed, with a device ON (power) square pulse of a 1.3 ms period and a 10% duty cycle (to match the transient Raman thermometry experiments). **Figure 3.29** shows the normalized transient response for the measured and simulated responses for the current design and the ideal case. A power density of 0.87 W/mm was used in this study for both simulation and experiments. Due to the relatively large thickness (~35 μm) of the Ga_2O_3 layer, the current design took ~300 μs to reach a quasi-steady state temperature, while this took only ~4 μs for the ideal case. In other words, the current design only offers its full cooling performance for switching frequencies less than ~3 kHz, while the ideal case is effective for frequencies up to ~250 kHz. This switching frequency limit can be further increased by the implementation of top-side cooling solutions such as a diamond passivation overlayer[152] and flip-chipping.[153]

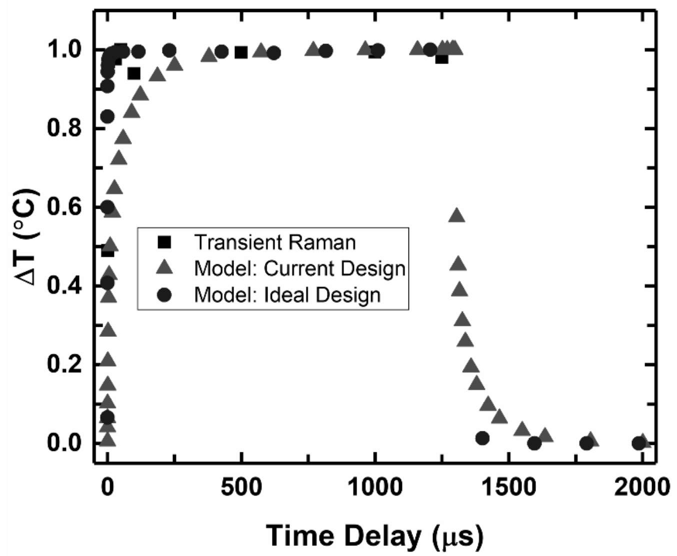

Figure 3.29: Transient thermal response for the current Ga_2O_3-on-SiC device (measured via Raman thermometry and simulated) and an "ideal" device. The temperature is normalized based on their respective quasi steady-state temperatures (~55°C for the current design and ~6°C for the ideal design).

A recent computational study[122] has predicted that practical multi-finger devices would experience significantly aggravated self-heating (a 4× higher channel temperature than single-finger Ga_2O_3 devices under identical power density conditions) due to the thermal cross-talk[108] among adjacent current channels. This trend has been experimentally confirmed by an experimental study[123] on multi-channel Ga_2O_3 FinFETs. Therefore, multi(6)-finger device structures were simulated for both the current Ga_2O_3/SiC composite wafer and an ideal case as detailed earlier. Further details of the electrically aware thermal model can be found in our previous work.[153] In **Figure 3.30**, the temperature results can be found for both aforementioned single- and multi (6)-finger Ga_2O_3 cases, in addition to that for a commercial multi-finger GaN-on-SiC device (details of the device geometry can be found in [153]). Due to the thermal cross-talk between the channels, the temperature rise is greater than that of a single channel device (by comparing with results in

Figures 3.28 and 3.30). A significant reduction in the channel temperature of ~8× is seen in the ideal multi-finger case, giving promise to lower the device thermal resistance below that for today's commercial GaN-on-SiC transistors.[153]

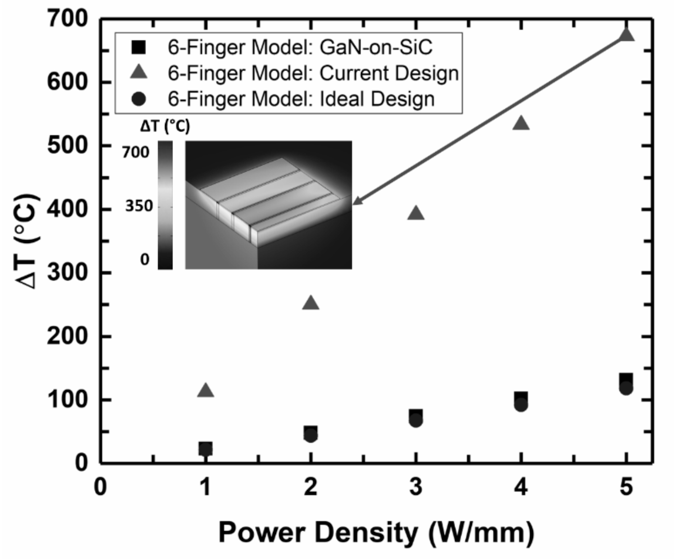

Figure 3.30: Comparison of the real and ideal 6-finger devices temperature rise.

3.3.3 Conclusion

This work reports the fabrication of ultra-wide bandgap Ga_2O_3 power MOSFETs on a Ga_2O_3/4H-SiC composite wafer with simultaneous enhancement in the electrical and thermal performance. Low temperature (≤600°C) epitaxy and device fabrication processes were developed to preserve the structural integrity of the composite substrate. This enabled the first realization of (010)-oriented "homoepitaxial" Ga_2O_3 MOSFETs fabricated on a Ga_2O_3/4H-SiC composite substrate. The epitaxial Ga_2O_3-on-SiC MOSFETs exhibit a record high V_{BR} (of up to 2.45 kV) and PFOM (~300 MW/cm^2), both of which are highest among Ga_2O_3 FETs constructed on an engineered substrate to date. Under DC operation, a significant reduction in the channel temperature was achieved for the MOSFETs fabricated on the composite wafer as compared to devices homoepitaxially grown on a native Ga_2O_3 substrate. The experimentally measured temperature rise was validated by a 3D FEA electro-thermal model. Transient thermal analysis suggests that the cooling performance of an unoptimized composite wafer will be limited under high frequency switching operation. The theoretical cooling limit of using a hypothetical Ga_2O_3/diamond composite substrate with ideal heat transfer performance was assessed by modeling. A 10× improvement in thermal performance can be achieved by reducing the Ga_2O_3 layer thickness (to ~1 μm) and lowering the TBR at the Ga_2O_3/diamond interface (~7.8 m^2K/GW). This work provides key guidelines for the fabrication and realization of high-power UWBG devices on a composite wafer that will enable to surpass the thermal limit of next-generation Ga_2O_3 power electronic.

3.3.4 Experimental Methods

FIB/Scanning Electron Microscopy

Plan view and cross-sectional scanning electron microscope (SEM) imaging was performed using a Helios NanoLab™ 650 Dual Beam system with focused ion beam (FIB) milling capabilities with samples under vacuum. For plan view imaging, the samples were imaged with the electron beam perpendicular to the sample surface at low-currents with acceleration voltages of 2 - 5 kV. For cross-sectional imaging, Ga ion current milling with a Pt protective capping layer was used to create craters up to 50 μm deep. Ion current levels of up to 1 nA were used. For charge dissipation, an Omiprobe™ probing system was used to probe the metal contacts.

Scanning Transmission Electron Microscopy

Scanning transmission electron microscopy (STEM) samples were prepared via focused ion beam (FIB) milling using a Thermofisher Helios Dual-beam FIB system. To prepare a clean and thin specimen, the surface of the STEM foil was cleaned using low energy ion milling (Fischione Nanomill) operated at 500 eV. High angle annular dark field (HAADF) STEM imaging was performed using a Thermofisher aberration-corrected Titan STEM microscope with probe convergence half angles of 10.03 mrad at an accelerating voltage of 300 kV. The microscope is also equipped with ChemiSTEM Energy dispersive X-ray spectroscopy (EDX) system, which allows for the characterization of the composition of the cross-sectional STEM sample. Five chemical species (Ga, Si, O, C, and N) at the interface were analyzed by the EDX elemental mapping. The bonding layer (including SiN_x) total thickness of 40 nm was determined at the interface region. Due to the inhomogeneity of the lattice mismatch between the Ga_2O_3 thin films and 4H-SiC substrate, the SiN_x bonding interface was marginally delaminated, resulting in the oxidation layer of 10 nm SiO_x within the SiN_x interfacial region. The elemental profile further demonstrated the distribution of O based on the cross-section STEM-EDX measurements.

Raman Thermometry:

Raman thermometry is a temperature measurement technique that uses Raman spectroscopy, which employs monochromatic photonic excitation (typically in the visible wavelength regime) to interrogate the energy or frequency of crystal lattice vibration (i.e., phonons). The temperature effect on a phonon can be observed in the Raman spectra through peak position shifts, peak broadening (or linewidth), and changes in the ratio of anti-Stokes/Stokes Raman peak intensity.[154,155] Among these three ways, the peak position-based temperature measurement offers higher measurement sensitivity with low uncertainty, and shorter measurement times. However, this method can lead to inaccuracies due to its sensitivity to both temperature and mechanical stress. Moreover, this measurement technique only provides the depth-averaged temperature information for UWBG semiconductors such as Ga_2O_3.

In this study, both steady-state and transient Raman thermometry were performed using a Horiba LabRAM HR Evolution spectrometer with a 532 nm excitation laser. A long working distance 50× objective (NA=0.45) was used in a 180° backscattering configuration. A nanoparticle-assisted Raman thermometry technique[156] was used to measure the surface temperature of the channel region of the Ga_2O_3 MOSFETs. Anatase titanium dioxide (TiO_2) nanoparticles with 99.98% purity were deposited on the device surface.[156] As the nanoparticle remains in thermal equilibrium with the device surface, the temperature dependent frequency shift of the E_g phonon mode mode was monitored to determine the device channel temperature. Since the nanoparticle can expand freely, the mechanical stress effect on the Raman peak position is negligible and does not affect temperature measurement results. The spatial resolution is determined by the size of the TiO_2 nanoparticles (~200 nm).

By augmenting the standard Raman microscope with a function generator, delay generator, trigger switch, and oscilloscope, a setup for transient temperature measurement was constructed.[157] This transient setup uses a lock-in modulation scheme in which electrical and laser pulse trains are synchronized, and the Raman signal accumulates over many periods. A full transient thermal response is constructed by controlling/sweeping the laser pulse delay time (τ_{delay}) along the entire device electrical (V_{DS}) pulse width (τ_{on}). An exemplary temporal schematic of the transient measurement is shown in **Figure 3.31**. In this example, V_{DS} ~35 V (i.e., electric pulse) is applied to achieve a power dissipation level of ~0.5 W while the device is ON. The laser pulse is active at the very end of the electrical pulse. A digital delay generator controls the time delay (τ_{delay}) between the electrical and laser pulses, in order to monitor the transient self-heating behavior of the device in response to a square electrical pulse with a 10% duty cycle. Here, the device pulse width (τ_{on}) is 1.3 ms and the laser pulse width (τ_{laser}) is 25 μs. A temporal resolution up to ~20 ns can be achieved with our experimental setup. The synchronization and operation of the transient measurements were controlled by a LabVIEW program. To maximize the signal-to-noise ratio of the Raman signals, an electron multiplying charge-coupled device (EMCCD) was used during the measurements.

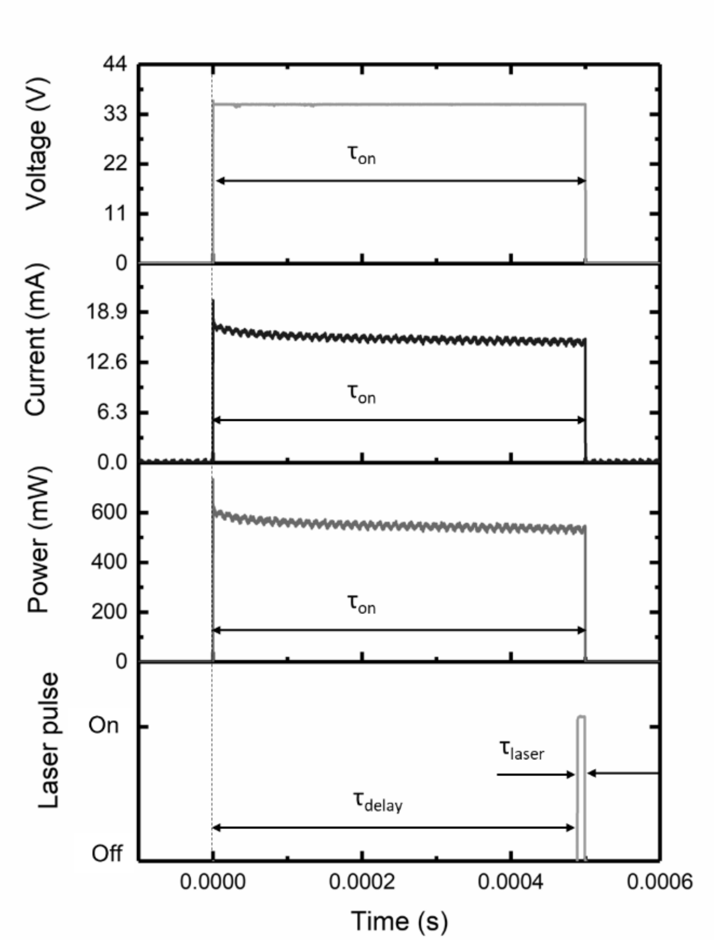

Figure 3.31: A typical synchronized pulsing scheme used during transient Raman thermometry measurements.

Device Modeling

Ga_2O_3 device models were constructed using a 3D electro-thermal modeling scheme that has been demonstrated in our previous work.[7,150] A 2D electro-hydrodynamic model that adopts carrier mobility and Ohmic contact resistance determined from experiments is created so that it reproduces the device output/transfer characteristics. This electrical model calculates the internal heat generation profile as a function of electrical bias. The 2D Joule heat distribution is projected along the channel width so that a 3D volumetric heat generation profile is obtained. This 3D heat generation profile is imported into a 3D finite element transient thermal model. The Ga_2O_3 and 4H-SiC thermal conductivities determined from experiments are employed in the thermal model. Interfacial phonon transport across the Ga_2O_3/4H-SiC interface is captured in the model by adopting the TBR values determined by experiments.

Chapter References

[1] T. Wei, D. Tsai, P. Ravadgar, J. Ke, M. Tsai, D. Lien, C. Huang, R. Horng, and J. He, "See-through Ga_2O_3 solar-blind photodetectors for use in harsh environments," IEEE J. Sel. Top. Quantum Electron. **20**(6), 112–117 (2014).

[2] M. Higashiwaki, and G.H. Jessen, "Guest Editorial: The dawn of gallium oxide microelectronics," Appl. Phys. Lett. **112**(6), 60401 (2018).

[3] S.J. Pearton, J. Yang, P.H. Cary, F. Ren, J. Kim, M.J. Tadjer, and M.A. Mastro, "A review of Ga_2O_3 materials, processing, and devices," Appl. Phys. Rev. **5**(1), 11301 (2018).

[4] S. Rafique, L. Han, and H. Zhao, "Thermal annealing effect on β-Ga_2O_3 thin film solar blind photodetector heteroepitaxially grown on sapphire substrate," Phys. Status Solidi **214**(8), 1700063 (2017).

[5] S. Krishnamoorthy, Z. Xia, C. Joishi, Y. Zhang, J. McGlone, J. Johnson, M. Brenner, A.R. Arehart, J. Hwang, S. Lodha, and S. Rajan, "Modulation-doped β-$(Al_{0.2}Ga_{0.8})_2O_3/Ga_2O_3$ field-effect transistor," Appl. Phys. Lett. **111**(2), 23502 (2017).

[6] B. Chatterjee, Y. Song, J.S.J.S. Lundh, Y. Zhang, Z. Xia, Z. Islam, J. Leach, C. McGray, P. Ranga, S. Krishnamoorthy, A. Haque, S. Rajan, and S. Choi, "Electro-thermal co-design of β-$(Al_xGa_{1-x})_2O_3/Ga_2O_3$ modulation doped field effect transistors," Appl. Phys. Lett. **117**(15), 153501 (2020).

[7] B. Chatterjee, K. Zeng, C.D. Nordquist, U. Singisetti, and S. Choi, "Device-level thermal management of gallium oxide field-effect transistors," IEEE Trans. Components, Packag. Manuf. Technol. **9**(12), 2352–2365 (2019).

[8] B. Chatterjee, A. Jayawardena, E. Heller, D.W. Snyder, S. Dhar, and S. Choi, "Thermal characterization of gallium oxide Schottky barrier diodes," Rev. Sci. Instrum. **89**(11), 114903 (2018).

[9] J.S. Lundh, T. Zhang, Y. Zhang, Z. Xia, M. Wetherington, Y. Lei, E. Kahn, S. Rajan, M. Terrones, and S. Choi, "2D materials for universal thermal imaging of micro- and nanodevices: an application to gallium oxide electronics," ACS Appl. Electron. Mater. **2**(9), 2945-2953 (2020).

[10] Z. Guo, A. Verma, X. Wu, F. Sun, A. Hickman, T. Masui, A. Kuramata, M. Higashiwaki, D. Jena, and T. Luo, "Anisotropic thermal conductivity in single crystal β-gallium oxide," Appl. Phys. Lett. **106**(11), 1–6 (2015).

[11] P. Jiang, X. Qian, X. Li, and R. Yang, "Three-dimensional anisotropic thermal conductivity tensor of single crystalline β-Ga_2O_3," Appl. Phys. Lett. **113**(23), 232105 (2018).

[12] F. Alema, B. Hertog, A. Osinsky, P. Mukhopadhyay, M. Toporkov, and W. V Schoenfeld, "Fast growth rate of epitaxial β–Ga_2O_3 by close coupled showerhead MOCVD," J. Cryst. Growth **475**, 77–82 (2017).

[13] A. Bhattacharyya, P. Ranga, S. Roy, J. Ogle, L. Whittaker-Brooks, and S. Krishnamoorthy, "Low temperature homoepitaxy of (010) -$Ga_2O_3$by metalorganic vapor phase epitaxy: Expanding the growth window," Appl. Phys. Lett. **117**(14), 142102 (2020).

[14] H. Ghadi, J.F. McGlone, C.M. Jackson, E. Farzana, Z. Feng, A.F.M.A.U. Bhuiyan, H. Zhao, A.R. Arehart, and S.A. Ringel, "Full bandgap defect state characterization of β-Ga_2O_3 grown by metal organic chemical vapor deposition," APL Mater. **8**(2), 21111 (2020).

[15] Z. Feng, A.F.M.M. Anhar Uddin Bhuiyan, M.R. Karim, and H. Zhao, "MOCVD homoepitaxy of Si-doped (010) β-Ga_2O_3 thin films with superior transport properties," Appl. Phys. Lett. **114**(25), 250601 (2019).

[16] F. Alema, Y. Zhang, A. Osinsky, N. Orishchin, N. Valente, A. Mauze, and J.S. Speck, "Low 1014 cm−3 free carrier concentration in epitaxial β-Ga_2O_3 grown by MOCVD," APL Mater. **8**(2), 21110 (2020).

[17] G. Seryogin, F. Alema, N. Valente, H. Fu, E. Steinbrunner, A.T. Neal, S. Mou, A. Fine, and A.

Osinsky, "MOCVD growth of high purity Ga_2O_3 epitaxial films using trimethylgallium precursor," Appl. Phys. Lett. **117**(26), 262101 (2020).

[18] A.F.M. Anhar Uddin Bhuiyan, Z. Feng, J.M. Johnson, Z. Chen, H.L. Huang, J. Hwang, and H. Zhao, "MOCVD epitaxy of β -$(Al_xGa_{1-x})_2O_3$ thin films on (010) Ga_2O_3 substrates and N-type doping," Appl. Phys. Lett. **115**(12), 1–6 (2019).

[19] P. Ranga, A. Rishinaramangalam, J. Varley, A. Bhattacharyya, D. Feezell, and S. Krishnamoorthy, "Si-doped β-$(Al_{0.26}Ga_{0.74})_2O_3$ thin films and heterostructures grown by metalorganic vapor-phase epitaxy," Appl. Phys. Express **12**(11), 111004 (2019).

[20] A.F.M.A.U. Bhuiyan, Z. Feng, J.M. Johnson, H.-L. Huang, J. Sarker, M. Zhu, M.R. Karim, B. Mazumder, J. Hwang, and H. Zhao, "Phase transformation in MOCVD growth of $(Al_xGa_{1-x})_2O_3$ thin films," APL Mater. **8**(3), 31104 (2020).

[21] A.F.M.A.U. Bhuiyan, Z. Feng, J.M. Johnson, H.-L. Huang, J. Hwang, and H. Zhao, "MOCVD growth of β-phase $(Al_xGa_{1-x})_2O_3$ on ($2\bar{0}1$) β-Ga_2O_3 substrates," Appl. Phys. Lett. **117**(14), 142107 (2020).

[22] A.F.M.A.U. Bhuiyan, Z. Feng, J.M. Johnson, H.-L. Huang, J. Hwang, and H. Zhao, "Band offsets of (100) β-$(Al_xGa_{1-x})_2O_3$/β-Ga_2O_3 heterointerfaces grown via MOCVD," Appl. Phys. Lett. **117**(25), 252105 (2020).

[23] S. Rafique, L. Han, A.T. Neal, S. Mou, J. Boeckl, and H. Zhao, "Towards high-mobility heteroepitaxial β-Ga_2O_3 on sapphire − dependence on the substrate off-axis angle," Phys. Status Solidi **215**(2), 1700467 (2018).

[24] S. Rafique, L. Han, A.T. Neal, S. Mou, M.J. Tadjer, R.H. French, and H. Zhao, "Heteroepitaxy of N-type β-Ga_2O_3 thin films on sapphire substrate by low pressure chemical vapor deposition," Appl. Phys. Lett. **109**(13), 132103 (2016).

[25] S. Rafique, M.R. Karim, J.M. Johnson, J. Hwang, and H. Zhao, "LPCVD homoepitaxy of Si doped β-Ga_2O_3 thin films on (010) and (001) substrates," Appl. Phys. Lett. **112**(5), 52104

(2018).

[26] S. Rafique, L. Han, M.J. Tadjer, J.A. Freitas, N.A. Mahadik, and H. Zhao, "Homoepitaxial growth of β-Ga_2O_3 thin films by low pressure chemical vapor deposition," Appl. Phys. Lett. **108**(18), 182105 (2016).

[27] S. Rafique, L. Han, and H. Zhao, "Synthesis of wide bandgap Ga_2O_3 (Eg ~ 4.6–4.7 eV) thin films on sapphire by low pressure chemical vapor deposition," Phys. Status Solidi **213**(4), 1002–1009 (2016).

[28] Z. Feng, M.R. Karim, and H. Zhao, "Low pressure chemical vapor deposition of β-Ga_2O_3 thin films: Dependence on growth parameters," APL Mater. **7**(2), 22514 (2018).

[29] Y. Zhang, Z. Feng, M.R. Karim, and H. Zhao, "High-temperature low-pressure chemical vapor deposition of β-Ga_2O_3," J. Vac. Sci. Technol. A **38**(5), 50806 (2020).

[30] M.D. Santia, N. Tandon, and J.D. Albrecht, "Lattice thermal conductivity in β-Ga_2O_3 from first principles," Appl. Phys. Lett. **107**(4), 41907 (2015).

[31] D.G. Cahill, P. V. Braun, G. Chen, D.R. Clarke, S. Fan, K.E. Goodson, P. Keblinski, W.P. King, G.D. Mahan, A. Majumdar, H.J. Maris, S.R. Phillpot, E. Pop, and L. Shi, "Nanoscale thermal transport. II. 2003-2012," Appl. Phys. Rev. **1**(1), 011305 (2014).

[32] D.G. Cahill, W.K. Ford, K.E. Goodson, G.D. Mahan, A. Majumdar, H.J. Maris, R. Merlin, and S.R. Phillpot, "Nanoscale thermal transport," J. Appl. Phys. **93**(2), 793–818 (2003).

[33] Z. Yan, and S. Kumar, "Phonon mode contributions to thermal conductivity of pristine and defective β-Ga_2O_3," Phys. Chem. Chem. Phys. **20**(46), 29236–29242 (2018).

[34] C.J. Szwejkowski, N.C. Creange, K. Sun, A. Giri, B.F. Donovan, C. Constantin, and P.E. Hopkins, "Size effects in the thermal conductivity of gallium oxide (β-Ga_2O_3) films grown via open-atmosphere annealing of gallium nitride," J. Appl. Phys. **117**(8), 084308 (2015).

[35] Z. Cheng, V.D. Wheeler, T. Bai, J. Shi, M.J. Tadjer, T. Feygelson, K.D. Hobart, M.S. Goorsky, and S. Graham, "Integration of polycrystalline Ga_2O_3 on diamond for thermal

management," Appl. Phys. Lett. **116**(6), 62105 (2020).

[36] Y. Zhang, Q. Su, J. Zhu, S. Koirala, S.J. Koester, and X. Wang, "Thickness-dependent thermal conductivity of mechanically exfoliated β-Ga_2O_3 thin films," Appl. Phys. Lett. **116**(20), 202101 (2020).

[37] Z. Cheng, L. Yates, J. Shi, M.J. Tadjer, K.D. Hobart, and S. Graham, "Thermal conductance across β-Ga_2O_3-diamond van der Waals heterogeneous interfaces," APL Mater. **7**(3), 03111 (2019).

[38] Z. Cheng, F. Mu, T. You, W. Xu, J. Shi, M.E. Liao, Y. Wang, K. Huynh, T. Suga, M.S. Goorsky, X. Ou, and S. Graham, "Thermal transport across ion-cut monocrystalline β-Ga_2O_3 thin films and bonded β-Ga_2O_3–SiC interfaces," ACS Appl. Mater. Interfaces **12**(40), 44943–44951 (2020).

[39] N. Blumenschein, M. Slomski, P.P. Paskov, F. Kaess, M.H. Breckenridge, J.F. Muth, and T. Paskova, "Thermal conductivity of bulk and thin film β-Ga_2O_3 measured by the 3ω technique," in *Proc.SPIE*, 10533 (2018).

[40] O. Ambacher, J. Smart, J.R. Shealy, N.G. Weimann, K. Chu, M. Murphy, W.J. Schaff, L.F. Eastman, R. Dimitrov, L. Wittmer, M. Stutzmann, W. Rieger, and J. Hilsenbeck, "Two-dimensional electron gases induced by spontaneous and piezoelectric polarization charges in N- and Ga-face AlGaN/GaN heterostructures," J. Appl. Phys. **85**(6), 3222 (1999).

[41] Y. Zhang, Z. Xia, J. Mcglone, W. Sun, C. Joishi, A.R. Arehart, S.A. Ringel, and S. Rajan, "Evaluation of low-temperature saturation velocity in β-$(Al_xGa_{1-x})_2O_3/Ga_2O_3$ modulation-doped field-effect transistors," IEEE Trans. Electron Devices **66**(3), 1574–1578 (2019).

[42] Y. Oshima, E.G. Víllora, and K. Shimamura, "Quasi-heteroepitaxial growth of β-Ga_2O_3 on off-angled sapphire (0001) substrates by halide vapor phase epitaxy," J. Cryst. Growth **410**, 53–58 (2015).

[43] C.-T. Zhong, and G.-Y. Zhang, "Growth of N-polar GaN on vicinal sapphire substrate by metal

organic chemical vapor deposition," Rare Met. **33**(6), 709–713 (2014).

[44] X.Q. Shen, H. Matsuhata, and H. Okumura, "Reduction of the threading dislocation density in GaN films grown on vicinal sapphire (0001) substrates," Appl. Phys. Lett. **86**(2), 21912 (2005).

[45] C. Kranert, C. Sturm, R. Schmidt-Grund, and M. Grundmann, "Raman tensor elements of β-Ga_2O_3," Sci. Rep. **6**(1), 35964 (2016).

[46] M. Kuball, "Raman spectroscopy of GaN, AlGaN and AlN for process and growth monitoring/control," Surf. Interface Anal. **31**(10), 987–999 (2001).

[47] D.G. Cahill, "Analysis of heat flow in layered structures for time-domain thermoreflectance," Rev. Sci. Instrum. **75**(12), 5119–5122 (2004).

[48] A.J. Schmidt, R. Cheaito, and M. Chiesa, "A frequency-domain thermoreflectance method for the characterization of thermal properties," Rev. Sci. Instrum. **80**(9), 94901 (2009).

[49] L. De Bellis, P.E. Phelan, and R.S. Prasher, "Variations of acoustic and diffuse mismatch models in predicting thermal-boundary resistance," J. Thermophys. Heat Transf. **14**(2), 144–150 (2000).

[50] S. Adachi, "Lattice thermal conductivity of group-IV and III–V semiconductor alloys," J. Appl. Phys. **102**(6), 63502 (2007).

[51] B. Chatterjee, J.S. Lundh, Y. Song, D. Shoemaker, A.G. Baca, R.J. Kaplar, T.E. Beechem, C. Saltonstall, A.A. Allerman, A.M. Armstrong, B.A. Klein, A. Bansal, H.R. Seyf, D. Talreja, A. Pogrebnyakov, E. Heller, V. Gopalan, A.S. Henry, J.M. Redwing, B. Foley, and S. Choi, "Interdependence of electronic and thermal transport in $Al_xGa_{1-x}N$ Channel HEMTs," IEEE Electron Device Lett., **41**(3), 461-464 (2020).

[52] Y. He, D. Donadio, and G. Galli, "Heat transport in amorphous silicon: Interplay between morphology and disorder," Appl. Phys. Lett. **98**(14), 144101 (2011).

[53] Z. Cheng, N. Tanen, C. Chang, J. Shi, J. McCandless, D. Muller, D. Jena, H.G. Xing, and S.

Graham, “Significantly reduced thermal conductivity in β-$(Al_{0.1}Ga_{0.9})_2O_3/Ga_2O_3$ superlattices,” Appl. Phys. Lett. **115**(9), 92105 (2019).

[54] Y. Song, C. Perez, G. Esteves, J.S. Lundh, C.B. Saltonstall, T.E. Beechem, J.I. Yang, K. Ferri, J.E. Brown, Z. Tang, J.-P. Maria, D.W. Snyder, R.H. Olsson, B.A. Griffin, S.E. Trolier-McKinstry, B.M. Foley, and S. Choi, “Thermal conductivity of aluminum scandium nitride for 5g mobile applications and beyond,” ACS Appl. Mater. Interfaces, 13, 19031-19041 (2021).

[55] R. Tarumi, H. Ledbetter, H. Ogi, and M. Hirao, “Low-temperature elastic constants of monocrystal corundum (α-Al_2O_3),” Philos. Mag. **93**(36), 4532–4543 (2013).

[56] H. He, M.A. Blanco, and R. Pandey, “Electronic and thermodynamic properties of β-Ga_2O_3,” Appl. Phys. Lett. **88**(26), 261904 (2006).

[57] A. Bhattacharyya, P. Ranga, S. Roy, and S. Krishnamoorthy, “High-density electron gas β-Ga_2O_3 field effect transistors with metalorganic vapor phase epitaxy-regrown ohmic contacts,” in *Device Res. Conf.*, (2020).

[58] B.A. Eisner, P. Ranga, A. Bhattacharyya, S. Krishnamoorthy, and M.A. Scarpulla, “Compensation in ($2\bar{0}1$) homoepitaxial β-Ga_2O_3 thin films grown by metalorganic vapor-phase epitaxy,” J. Appl. Phys. **128**(19), 195703 (2020).

[59] A. Fiedler, R. Schewski, M. Baldini, Z. Galazka, G. Wagner, M. Albrecht, and K. Irmscher, “Influence of incoherent twin boundaries on the electrical properties of β-Ga_2O_3 layers homoepitaxially grown by metal-organic vapor phase epitaxy,” J. Appl. Phys. **122**(16), 165701 (2017).

[60] R. Schewski, K. Lion, A. Fiedler, C. Wouters, A. Popp, S. V Levchenko, T. Schulz, M. Schmidbauer, S. Bin Anooz, R. Grüneberg, Z. Galazka, G. Wagner, K. Irmscher, M. Scheffler, C. Draxl, and M. Albrecht, “Step-flow growth in homoepitaxy of β-Ga_2O_3 (100)—The influence of the miscut direction and faceting,” APL Mater. **7**(2), 22515

(2018).

[61] Y.S. Touloukian, and E.H. Buyco, *Thermophysical Properties of Matter - the TPRC Data Series. Volume 4. Specific Heat - Metallic Elements and Alloys* (United States, 1971).

[62] G.B. Adams, and H.L. Johnston, "Low temperature heat capacities of inorganic solids. XI. the heat capacity of β-gallium oxide from 15 to 300°K.1," J. Am. Chem. Soc. **74**(19), 4788–4789 (1952).

[63] D.A. Ditmars, S. Ishihara, S.S. Chang, G. Bernstein, and E.D. West, "Enthalpy and heat-capacity standard reference material: synthetic sapphire (alpha -Al_2O_3) from 10 to 2250 K.," J. Res. Natl. Bur. Stand. (United States) **87**(2), 159–163 (1982).

[64] J.W. Arblaster, "Thermodynamic properties of gold," J. Phase Equilibria Diffus. **37**(2), 229–245 (2016).

[65] B. Schulz, "High temperature thermal conductivity of irradiated and non-irradiated α-Al_2O_3," J. Nucl. Mater. **155**–**157**, 348–351 (1988).

[66] S. Yoshioka, H. Hayashi, A. Kuwabara, F. Oba, K. Matsunaga, and I. Tanaka, "Structures and energetics of Ga_2O_3 polymorphs," J. Phys. Condens. Matter **19**(34), 346211 (2007).

[67] W. Li, J. Carrete, N. A. Katcho, and N. Mingo, "ShengBTE: A solver of the Boltzmann transport equation for phonons," Comput. Phys. Commun. **185**(6), 1747–1758 (2014).

[68] P. Giannozzi, S. Baroni, N. Bonini, M. Calandra, R. Car, C. Cavazzoni, D. Ceresoli, G.L. Chiarotti, M. Cococcioni, I. Dabo, A. Dal Corso, S. de Gironcoli, S. Fabris, G. Fratesi, R. Gebauer, U. Gerstmann, C. Gougoussis, A. Kokalj, M. Lazzeri, L. Martin-Samos, N. Marzari, F. Mauri, R. Mazzarello, S. Paolini, A. Pasquarello, L. Paulatto, C. Sbraccia, S. Scandolo, G. Sclauzero, A.P. Seitsonen, A. Smogunov, P. Umari, and R.M. Wentzcovitch, "QUANTUM ESPRESSO: a modular and open-source software project for quantum simulations of materials," J. Phys. Condens. Matter **21**(39), 395502 (2009).

[69] J.M. Winey, Y.M. Gupta, and D.E. Hare, "r-axis sound speed and elastic properties of sapphire

single crystals," J. Appl. Phys. **90**(6), 3109–3111 (2001).

[70] J. Pedrós, F. Calle, J. Grajal, R.J. Jiménez Riobóo, Y. Takagaki, K.H. Ploog, and Z. Bougrioua, "Anisotropy-induced polarization mixture of surface acoustic waves in GaN⁄c-sapphire heterostructures," Phys. Rev. B **72**(7), 75306 (2005).

[71] M.E. Coltrin, A.G. Baca, and R.J. Kaplar, "Analysis of 2D Transport and Performance Characteristics for Lateral Power Devices Based on AlGaN Alloys," ECS J. Solid State Sci. Technol. **6**(11), S3114–S3118 (2017).

[72] Y. Zhang, A. Neal, Z. Xia, C. Joishi, J.M. Johnson, Y. Zheng, S. Bajaj, M. Brenner, D. Dorsey, K. Chabak, G. Jessen, J. Hwang, S. Mou, J.P. Heremans, and S. Rajan, "Demonstration of high mobility and quantum transport in modulation-doped β-$(Al_xGa_{1-x})_2O_3/Ga_2O_3$ heterostructures," Appl. Phys. Lett. **112**(17), 173502 (2018).

[73] M. Higashiwaki, K. Sasaki, A. Kuramata, T. Masui, and S. Yamakoshi, "Gallium oxide (Ga_2O_3) metal-semiconductor field-effect transistors on single-crystal β-Ga_2O_3 (010) substrates," Appl. Phys. Lett. **100**(1), 013504 (2012).

[74] K. Ghosh, and U. Singisetti, "Electron mobility in monoclinic β-Ga_2O_3—Effect of plasmon-phonon coupling, anisotropy, and confinement," J. Mater. Res. **32**(22), 4142–4152 (2017).

[75] C.H. Lin, N. Hatta, K. Konishi, S. Watanabe, A. Kuramata, K. Yagi, and M. Higashiwaki, "Single-crystal-Ga_2O_3 /polycrystalline-SiC bonded substrate with low thermal and electrical resistances at the heterointerface," Appl. Phys. Lett. **114**(3), 1–6 (2019).

[76] A. Bar-cohen, J.J. Maurer, and A. Sivananthan, "Near-junction microfluidic thermal management of RF power amplifiers," 2015 IEEE Int. Conf. Microwaves, Commun. Antennas Electron. Syst. (November), 2–4 (2015).

[77] N. Nepal, D.S. Katzer, B.P. Downey, V.D. Wheeler, L.O. Nyakiti, D.F. Storm, M.T. Hardy, J.A. Freitas, E.N. Jin, D. Vaca, L. Yates, S. Graham, S. Kumar, and D.J. Meyer, "Heteroepitaxial growth of β-Ga_2O_3 films on SiC via molecular beam epitaxy," J. Vac. Sci.

Technol. A **38**(6), 63406 (2020).

[78] T. Liu, Y. Kong, L. Wu, H. Guo, J. Zhou, C. Kong, and T. Chen, "3-inch GaN-on-diamond HEMTs with device-first transfer technology," IEEE Electron Device Lett. **38**(10), 1417–1420 (2017).

[79] J.D. Blevins, K. Chabak, G. Jessen, D. Thomson, K. Stevens, G. Foundos, A. Lindsey, J.H. Leach, J. Rumsey, and A. Green, "Growth of 50mm beta-gallium oxide (β-Ga_2O_3) substrates," CS MANTECH 2018 - 2018 Int. Conf. Compd. Semicond. Manuf. Technol. **1**(010), 4–7 (2018).

[80] M.E. Liao, C. Li, H.M. Yu, E. Rosker, M.J. Tadjer, K.D. Hobart, and M.S. Goorsky, "Coefficients of thermal expansion of single crystalline β-Ga_2O_3 and in-plane thermal strain calculations of various materials combinations with β-Ga_2O_3," APL Mater. **7**(2), 22517 (2018).

[81] P.C. Chao, K. Chu, J. Diaz, C. Creamer, S. Sweetland, R. Kallaher, C. McGray, G.D. Via, J. Blevins, D.C. Dumka, C. Lee, H.Q. Tserng, P. Saunier, and M. Kumar, "GaN-on-diamond HEMTs with 11W/mm output power at 10GHz," MRS Adv. **1**(02), 147–155 (2016).

[82] K. Reck, C. Stergaard, E. V. Thomsen, and O. Hansen, "Fusion bonding of silicon nitride surfaces," J. Micromechanics Microengineering **21**(12), 125015 (2011).

[83] R.W. Bower, M.S. Ismail, and B.E. Roberds, "Low temperature Si_3N_4 direct bonding," Appl. Phys. Lett. **62**(26), 3485–3487 (1993).

[84] J. Cho, K.K. Chu, P.C. Chao, C. McGray, M. Asheghi, and K.E. Goodson, "Thermal conduction normal to thin silicon nitride films on diamond and GaN," Thermomechanical Phenom. Electron. Syst. -Proceedings Intersoc. Conf., 1186–1191 (2014).

[85] T.L. Bougher, L. Yates, Z. Cheng, B.A. Cola, S. Graham, R. Chaeito, A. Sood, M. Ashegi, and K.E. Goodson, "Experimental considerations of CVD diamond film measurements using time domain thermoreflectance," in *2017 16th IEEE Intersoc. Conf. Therm.*

Thermomechanical Phenom. Electron. Syst., (2017), pp. 30–38.

[86] R. Wei, S. Song, K. Yang, Y. Cui, Y. Peng, X. Chen, X. Hu, and X. Xu, "Thermal conductivity of 4H-SiC single crystals," J. Appl. Phys. **113**(5), 53503 (2013).

[87] Z. LI, and R.C. BRADT, "Thermal expansion and thermal expansion anisotropy of SiC polytypes," J. Am. Ceram. Soc. **70**(7), 445–448 (1987).

[88] G.A. Slack, and S.F. Bartram, "Thermal expansion of some diamondlike crystals," J. Appl. Phys. **46**(1), 89–98 (1975).

[89] Z. Feng, A.F.M.A.U. Bhuiyan, Z. Xia, W. Moore, Z. Chen, J.F. McGlone, D.R. Daughton, A.R. Arehart, S.A. Ringel, S. Rajan, and H. Zhao, "Probing charge transport and background doping in metal-organic chemical vapor deposition-grown (010) β-Ga_2O_3," Phys. Status Solidi – Rapid Res. Lett. **14**(8), 2000145 (2020).

[90] P. Ranga, A. Bhattacharyya, A. Chmielewski, S. Roy, R. Sun, M.A. Scarpulla, N. Alem, and S. Krishnamoorthy, "Growth and characterization of metalorganic vapor-phase epitaxy-grown β-$(Al_xGa_{1-x})_2O_3$/β-Ga_2O_3 heterostructure channels," Appl. Phys. Express **14**(2), 25501 (2021).

[91] P. Ranga, A. Bhattacharyya, A. Chmielewski, S. Roy, N. Alem, and S. Krishnamoorthy, "Delta-doped β-Ga_2O_3 films with narrow FWHM grown by metalorganic vapor-phase epitaxy," Appl. Phys. Lett. **117**(17), 172105 (2020).

[92] A. Bhattacharyya, S. Roy, P. Ranga, D. Shoemaker, Y. Song, J.S. Lundh, S. Choi, and S. Krishnamoorthy, "130 mA mm−1 β-Ga_2O_3 metal semiconductor field effect transistor with low-temperature metalorganic vapor phase epitaxy-regrown ohmic contacts," Appl. Phys. Express **14**(7), 76502 (2021).

[93] J.L. Braun, D.H. Olson, J.T. Gaskins, P.E. Hopkins, D.H. Olson, and J.T. Gaskins, "A steady-state thermoreflectance method to measure thermal conductivity," Rev. Sci. Instrum. **90**(2), 24905 (2019).

[94] J.L. Braun, and P.E. Hopkins, "Upper limit to the thermal penetration depth during modulated heating of multilayer thin films with pulsed and continuous wave lasers: A numerical study," J. Appl. Phys. **121**(17), 1–13 (2017).

[95] J.P. Freedman, J.H. Leach, E.A. Preble, Z. Sitar, R.F. Davis, and J.A. Malen, "Universal phonon mean free path spectra in crystalline semiconductors at high temperature," Sci. Rep. **3**, 2963 (2013).

[96] F. Yang, and C. Dames, "Mean free path spectra as a tool to understand thermal conductivity in bulk and nanostructures," Phys. Rev. B **87**(3), 35437 (2013).

[97] T.E. Beechem, A.E. McDonald, E.J. Fuller, A.A. Talin, C.M. Rost, J.-P. Maria, J.T. Gaskins, P.E. Hopkins, and A.A. Allerman, "Size dictated thermal conductivity of GaN," J. Appl. Phys. **120**(9), 95104 (2016).

[98] J. Cho, E. Bozorg-Grayeli, T. Kodama, D. Francis, F. Ejeckam, F. Faili, M. Asheghi, K.E. Goodson, Z. Li, E. Bozorg-Grayeli, T. Kodama, D. Francis, F. Ejeckam, F. Faili, M. Asheghi, and K.E. Goodson, "Improved thermal interfaces of gan-diamond composite substrates for HEMT applications," IEEE Trans. Components, Packag. Manuf. Technol. **3**(1), 79–85 (2013).

[99] H. Sun, R.B. Simon, J.W. Pomeroy, D. Francis, F. Faili, D.J. Twitchen, and M. Kuball, "Reducing GaN-on-diamond interfacial thermal resistance for high power transistor applications," Appl. Phys. Lett. **106**(11), 111906 (2015).

[100] J. Anaya, S. Rossi, M. Alomari, E. Kohn, L. Tóth, B. Pécz, K.D. Hobart, T.J. Anderson, T.I. Feygelson, B.B. Pate, and M. Kuball, "Control of the in-plane thermal conductivity of ultra-thin nanocrystalline diamond films through the grain and grain boundary properties," Acta Mater. **103**, 141–152 (2016).

[101] U.G. Q.-Y. Tong, *SemiConductor Wafer Bonding: Science and Technology* (1998).

[102] J.L. Braun, C.H. Baker, A. Giri, M. Elahi, K. Artyushkova, T.E. Beechem, P.M. Norris, Z.C.

Leseman, J.T. Gaskins, and P.E. Hopkins, "Size effects on the thermal conductivity of amorphous silicon thin films," Phys. Rev. B **93**(14), 1–5 (2016).

[103] E.A. Scott, J.T. Gaskins, S.W. King, and P.E. Hopkins, "Thermal conductivity and thermal boundary resistance of atomic layer deposited high-k dielectric aluminum oxide, hafnium oxide, and titanium oxide thin films on silicon," APL Mater. **6**(5), 58302 (2018).

[104] N.A. Blumenschein, N.A. Moser, E.R. Heller, N.C. Miller, A.J. Green, A. Popp, A. Crespo, K. Leedy, M. Lindquist, T. Moule, S. Dalcanale, E. Mercado, M. Singh, J.W. Pomeroy, M. Kuball, G. Wagner, T. Paskova, J.F. Muth, K.D. Chabak, and G.H. Jessen, "Self-heating characterization of β-Ga_2O_3 thin-channel MOSFETs by pulsed I–V and Raman nanothermography," IEEE Trans. Electron Devices **67**(1), 204–211 (2020).

[105] R. Pearson, B. Chatterjee, S. Kim, S. Graham, A. Rattner, and S. Choi, "Guidelines for reduced-order thermal modeling of multifinger GaN HEMTs," J. Electron. Packag. **142**(2), (2020).

[106] S. Choi, E.R. Heller, D. Dorsey, R. Vetury, and S. Graham, "The impact of bias conditions on self-heating in AlGaN/GaN HEMTs," IEEE Trans. Electron Devices **60**(1), 159–162 (2013).

[107] X. Qian, P. Jiang, and R. Yang, "Anisotropic thermal conductivity of 4H and 6H silicon carbide measured using time-domain thermoreflectance," Mater. Today Phys. **3**, 70–75 (2017).

[108] A. Manoi, J.W. Pomeroy, R. Lossy, R. Pazirandeh, J. Würfl, M.J. Uren, T. Martin, and M. Kuball, "Time-dependent thermal crosstalk in multifinger AlGaN/GaN HEMTs and implications on their electrical performance," Solid. State. Electron. **57**(1), 14–18 (2011).

[109] H. Zhang, Z. Guo, and Y. Lu, "Enhancement of hot spot cooling by capped diamond layer deposition for multifinger AlGaN/GaN HEMTs," IEEE Trans. Electron Devices **67**(1), 47–52 (2020).

[110] J.L. Braun, C.J. Szwejkowski, A. Giri, and P.E. Hopkins, "On the steady-state temperature rise during laser heating of multilayer thin films in optical pump–probe techniques," J. Heat

Transfer, **140**(5), 052801 (2018).

[111] B. Chatterjee, J.S. Lundh, J. Dallas, H. Kim, and S. Choi, "Electro-thermal reliability study of GaN high electron mobility transistors," Proc. 16th Intersoc. Conf. Therm. Thermomechanical Phenom. Electron. Syst. ITherm 2017, 1247–1252 (2017).

[112] L. Hitova, R. Yakimova, E.P. Trifonova, A. Lenchev, and E. Janzen, "Heat capacity of 4H-SiC determined by differential scanning calorimetry," J. Electrochem. Soc. **147**(9), 3546 (2000).

[113] A.T. Tarekegne, B. Zhou, K. Kaltenecker, K. Iwaszczuk, S. Clark, and P.U. Jepsen, "Terahertz time-domain spectroscopy of zone-folded acoustic phonons in 4H and 6H silicon carbide," Opt. Express **27**(3), 3618–3628 (2019).

[114] A.K. Kushwaha, and others, "Lattice dynamical, elastic properties and sound velocities of γ-Si3N4," Indian J. Pure \& Appl. Phys. **53**(9), 585–589 (2015).

[115] R.O. Pohl, X. Liu, and E. Thompson, "Low-temperature thermal conductivity and acoustic attenuation in amorphous solids," Rev. Mod. Phys. **74**(4), 991–1013 (2002).

[116] M. Higashiwaki, "β-Gallium oxide devices: progress and outlook," Phys. Status Solidi – Rapid Res. Lett. **15**(11), 2100357 (2021).

[117] A.J. Green, J. Speck, G. Xing, P. Moens, F. Allerstam, K. Gumaelius, T. Neyer, A. Arias-Purdue, V. Mehrotra, A. Kuramata, K. Sasaki, S. Watanabe, K. Koshi, J. Blevins, O. Bierwagen, S. Krishnamoorthy, K. Leedy, A.R. Arehart, A.T. Neal, S. Mou, S.A. Ringel, A. Kumar, A. Sharma, K. Ghosh, U. Singisetti, W. Li, K. Chabak, K. Liddy, A. Islam, S. Rajan, S. Graham, S. Choi, Z. Cheng, and M. Higashiwaki, "β-Gallium oxide power electronics," APL Mater. **10**(2), 29201 (2022).

[118] J.Y. Tsao, S. Chowdhury, M.A. Hollis, D. Jena, N.M. Johnson, K.A. Jones, R.J. Kaplar, S. Rajan, C.G. Van de Walle, E. Bellotti, C.L. Chua, R. Collazo, M.E. Coltrin, J.A. Cooper, K.R. Evans, S. Graham, T.A. Grotjohn, E.R. Heller, M. Higashiwaki, M.S. Islam, P.W.

Juodawlkis, M.A. Khan, A.D. Koehler, J.H. Leach, U.K. Mishra, R.J. Nemanich, R.C.N. Pilawa-Podgurski, J.B. Shealy, Z. Sitar, M.J. Tadjer, A.F. Witulski, M. Wraback, and J.A. Simmons, "Ultrawide-bandgap semiconductors: research opportunities and challenges," Adv. Electron. Mater. **4**(1), 1600501 (2018).

[119] S. Choi, S. Graham, S. Chowdhury, E.R. Heller, M.J. Tadjer, G. Moreno, and S. Narumanchi, "A perspective on the electro-thermal co-design of ultra-wide bandgap lateral devices," Appl. Phys. Lett. **119**(17), 170501 (2021).

[120] Y. Song, J.S. Lundh, W. Wang, J.H. Leach, D. Eichfeld, A. Krishnan, C. Perez, D. Ji, T. Borman, K. Ferri, J.-P. Maria, S. Chowdhury, J.-H. Ryou, B.M. Foley, and S. Choi, "The doping dependence of the thermal conductivity of bulk gallium nitride substrates," J. Electron. Packag. **142**(4), 041112 (2020).

[121] J.S. Lundh, D. Shoemaker, A.G. Birdwell, J.D. Weil, L.M. De La Cruz, P.B. Shah, K.G. Crawford, T.G. Ivanov, H.Y. Wong, and S. Choi, "Thermal performance of diamond field-effect transistors," Appl. Phys. Lett. **119**(14), 143502 (2021).

[122] Y. Song, D. Shoemaker, J.H. Leach, C. McGray, H.-L. Huang, A. Bhattacharyya, Y. Zhang, C.U. Gonzalez-Valle, T. Hess, S. Zhukovsky, K. Ferri, R.M. Lavelle, C. Perez, D.W. Snyder, J.-P. Maria, B. Ramos-Alvarado, X. Wang, S. Krishnamoorthy, J. Hwang, B.M. Foley, and S. Choi, "Ga_2O_3-on-SiC composite wafer for thermal management of ultrawide bandgap electronics," ACS Appl. Mater. Interfaces **13**(34), 40817–40829 (2021).

[123] B. Chatterjee, W. Li, K. Nomoto, H.G. Xing, and S. Choi, "Thermal design of multi-fin Ga_2O_3 vertical transistors," Appl. Phys. Lett. **119**(10), 103502 (2021).

[124] A. Bar-Cohen, J.J. Maurer, and D.H. Altman, "Embedded cooling for wide bandgap power amplifiers: a review," J. Electron. Packag. **141**(4), 040803 (2019).

[125] C.E. Reilly, N. Hatui, T.E. Mates, S. Nakamura, S.P. DenBaars, and S. Keller, "2DEGs formed in AlN/GaN HEMT structures with AlN grown at low temperature," Appl. Phys. Lett.

118(22), 222103 (2021).

[126] H. Tsuchida, I. Kamata, T. Miyazawa, M. Ito, X. Zhang, and M. Nagano, "Recent advances in 4H-SiC epitaxy for high-voltage power devices," Mater. Sci. Semicond. Process. **78**, 2–12 (2018).

[127] M. Kasu, "Diamond epitaxy: Basics and applications," Prog. Cryst. Growth Charact. Mater. **62**(2), 317–328 (2016).

[128] A. Bhattacharyya, S. Sharma, F. Alema, P. Ranga, S. Roy, C. Peterson, G. Seryogin, A. Osinsky, U. Singisetti, and S. Krishnamoorthy, "4.4 kV β-Ga_2O_3 MESFETs with power figure of merit exceeding 100 MW cm^{-2}," Appl. Phys. Express **15**(6), 61001 (2022).

[129] A. Bhattacharyya, P. Ranga, S. Roy, C. Peterson, F. Alema, G. Seryogin, A. Osinsky, and S. Krishnamoorthy, "Multi-kV class β-Ga_2O_3 MESFETs with a Lateral Figure of Merit up to 355 MW/cm^2," IEEE Electron Device Lett., 2–5 (2021).

[130] K. Tetzner, E.B. Treidel, O. Hilt, A. Popp, S. Bin Anooz, G. Wagner, A. Thies, K. Ickert, H. Gargouri, and J. Würfl, "Lateral 1.8 kV beta-Ga_2O_3 MOSFET With 155 MW/cm^2 Power Figure of Merit," IEEE Electron Device Lett. **40**(9), 1503–1506 (2019).

[131] C. Wang, H. Zhou, J. Zhang, W. Mu, J. Wei, Z. Jia, X. Zheng, X. Luo, X. Tao, and Y. Hao, "Hysteresis-free and μs-switching of D/E-modes Ga_2O_3 hetero-junction FETs with the BV2/$R_{on,sp}$ of 0.74/0.28 GW/cm^2," Appl. Phys. Lett. **120**(11), 112101 (2022).

[132] Y. Lv, H. Liu, X. Zhou, Y. Wang, X. Song, Y. Cai, Q. Yan, C. Wang, S. Liang, J. Zhang, Z. Feng, H. Zhou, S. Cai, and Y. Hao, "Lateral β-Ga_2O_3 MOSFETs with high power figure of merit of 277 MW/cm^2," IEEE Electron Device Lett. **41**(4), 537–540 (2020).

[133] C. Joishi, Y. Zhang, Z. Xia, W. Sun, A.R. Arehart, S. Ringel, S. Lodha, and S. Rajan, "Breakdown characteristics of β-$(Al_{0.22}Ga_{0.78})_2O_3/Ga_2O_3$ field-plated modulation-doped field-effect transistors," IEEE Electron Device Lett. **40**(8), 1241–1244 (2019).

[134] N.K. Kalarickal, Z. Xia, H.-L. Huang, W. Moore, Y. Liu, M. Brenner, J. Hwang, and S. Rajan,

"β-($Al_{0.18}Ga_{0.82}$)$_2O_3$/Ga_2O_3 double heterojunction transistor with average field of 5.5 MV/cm," IEEE Electron Device Lett. **42**(6), 899–902 (2021).

[135] S. Sharma, K. Zeng, S. Saha, and U. Singisetti, "Field-plated lateral Ga_2O_3 MOSFETs with polymer passivation and 8.03 kV breakdown voltage," IEEE Electron Device Lett. **41**(6), 836–839 (2020).

[136] K.D. Chabak, J.P. McCandless, N.A. Moser, A.J. Green, K. Mahalingam, A. Crespo, N. Hendricks, B.M. Howe, S.E. Tetlak, K. Leedy, R.C. Fitch, D. Wakimoto, K. Sasaki, A. Kuramata, and G.H. Jessen, "Recessed-gate enhancement-mode beta-Ga_2O_3 MOSFETs," IEEE Electron Device Lett. **39**(1), 67–70 (2018).

[137] Y. Lv, X. Zhou, S. Long, X. Song, Y. Wang, S. Liang, Z. He, T. Han, X. Tan, Z. Feng, H. Dong, X. Zhou, Y. Yu, S. Cai, and M. Liu, "Source-field-plated beta-Ga_2O_3 MOSFET with record power figure of merit of 50.4 MW/cm^2," IEEE Electron Device Lett. **40**(1), 83–86 (2019).

[138] K. Tetzner, K. Egbo, M. Klupsch, R.-S. Unger, A. Popp, T.-S. Chou, S. Bin Anooz, Z. Galazka, A. Trampert, O. Bierwagen, and J. Würfl, "SnO/β-Ga_2O_3 heterojunction field-effect transistors and vertical p–n diodes," Appl. Phys. Lett. **120**(11), 112110 (2022).

[139] N.K. Kalarickal, Z. Feng, A.F.M.A.U. Bhuiyan, Z. Xia, W. Moore, J.F. McGlone, A.R. Arehart, S.A. Ringel, H. Zhao, and S. Rajan, "Electrostatic engineering using extreme permittivity materials for ultra-wide bandgap semiconductor transistors," IEEE Trans. Electron Devices **68**(1), 29–35 (2021).

[140] C. Wang, H. Gong, W. Lei, Y. Cai, Z. Hu, S. Xu, Z. Liu, Q. Feng, H. Zhou, J. Ye, J. Zhang, R. Zhang, and Y. Hao, "Demonstration of the p-NiO_x/n-Ga_2O_3 heterojunction Gate FETs and diodes with $BV^2/R_{on,sp}$ figures of merit of 0.39 GW/cm^2 and 1.38 GW/cm^2," IEEE Electron Device Lett. **42**(4), 485–488 (2021).

[141] Y. Wang, W. Xu, T. You, F. Mu, H. Hu, Y. Liu, H. Huang, T. Suga, G. Han, X. Ou, and Y. Hao, "β-Ga_2O_3 MOSFETs on the Si substrate fabricated by the ion-cutting process," Sci. China

Physics, Mech. Astron. **63**(7), 277311 (2020).

[142] W. Xu, Y. Wang, T. You, X. Ou, G. Han, H. Hu, S. Zhang, F. Mu, T. Suga, Y. Zhang, Y. Hao, and X. Wang, "First demonstration of waferscale heterogeneous integration of Ga_2O_3 MOSFETs on SiC and Si substrates by ion-cutting process," in *2019 IEEE Int. Electron Devices Meet.*, (2019), pp. 12.5.1-12.5.4.

[143] Y. Wang, G. Han, W. Xu, T. You, H. Hu, Y. Liu, X. Zhang, H. Huang, X. Ou, X. Ma, and Y. Hao, "Recessed-Gate Ga_2O_3;-on-SiC MOSFETs demonstrating a stable power figure of merit of 100 mW/cm^2; up to 200 °C," IEEE Trans. Electron Devices **69**(4), 1945–1949 (2022).

[144] B.J. Baliga, "Power semiconductor device figure of merit for high-frequency applications," IEEE Electron Device Lett. **10**(10), 455–457 (1989).

[145] J.S. Lundh, B. Chatterjee, Y. Song, A.G. Baca, R.J. Kaplar, T.E. Beechem, A.A. Allerman, A.M. Armstrong, B.A. Klein, A. Bansal, D. Talreja, A. Pogrebnyakov, E. Heller, V. Gopalan, J.M. Redwing, B.M. Foley, and S. Choi, "Multidimensional thermal analysis of an ultrawide bandgap AlGaN channel high electron mobility transistor," Appl. Phys. Lett. **115**(15), 153503 (2019).

[146] J.W. Pomeroy, C. Middleton, M. Singh, S. Dalcanale, M.J. Uren, M.H. Wong, K. Sasaki, A. Kuramata, S. Yamakoshi, M. Higashiwaki, and M. Kuball, "Raman thermography of peak channel temperature in β-Ga_2O_3 MOSFETs," IEEE Electron Device Lett. **40**(2), 189–192 (2019).

[147] Z. Cheng, F. Mu, L. Yates, T. Suga, and S. Graham, "Interfacial thermal conductance across room-temperature-bonded GaN/Diamond interfaces for GaN-on-diamond devices," ACS Appl. Mater. Interfaces **12**(7), 8376–8384 (2020).

[148] D.E. Field, J.A. Cuenca, M. Smith, S.M. Fairclough, F.C.-P. Massabuau, J.W. Pomeroy, O. Williams, R.A. Oliver, I. Thayne, and M. Kuball, "Crystalline interlayers for reducing the

effective thermal boundary resistance in GaN-on-diamond," ACS Appl. Mater. Interfaces **12**(48), 54138–54145 (2020).

[149] M.J. Tadjer, T.J. Anderson, M.G. Ancona, P.E. Raad, P. Komarov, T. Bai, J.C. Gallagher, A.D. Koehler, M.S. Goorsky, D.A. Francis, K.D. Hobart, and F.J. Kub, "GaN-On-diamond HEMT technology with TAVG = 176°C at $P_{DC,max}$ = 56 W/mm measured by transient thermoreflectance imaging," IEEE Electron Device Lett. **40**(6), 881–884 (2019).

[150] S.H. Kim, D. Shoemaker, B. Chatterjee, A.J. Green, K.D. Chabak, E.R. Heller, K.J. Liddy, G.H. Jessen, S. Graham, and S. Choi, "Thermally-aware layout design of β-Ga_2O_3 lateral MOSFETs," IEEE Trans. Electron Devices **69**(3), 1251–1257 (2022).

[151] A. V Inyushkin, A.N. Taldenkov, V.G. Ralchenko, A.P. Bolshakov, A. V Koliadin, and A.N. Katrusha, "Thermal conductivity of high purity synthetic single crystal diamonds," Phys. Rev. B **97**(14), 144305 (2018).

[152] M. Malakoutian, Y. Song, C. Yuan, C. Ren, J.S. Lundh, R.M. Lavelle, J.E. Brown, D.W. Snyder, S. Graham, S. Choi, and S. Chowdhury, "Polycrystalline diamond growth on β-Ga_2O_3 for thermal management," Appl. Phys. Express **14**(5), 55502 (2021).

[153] D. Shoemaker, M. Malakoutian, B. Chatterjee, Y. Song, S. Kim, B.M. Foley, S. Graham, C.D. Nordquist, S. Chowdhury, and S. Choi, "Diamond-incorporated flip-chip integration for thermal management of GaN and ultra-wide bandgap rf power amplifiers," IEEE Trans. Components, Packag. Manuf. Technol. **11**(8), 1177–1186 (2021).

[154] M. Kuball, J.M. Hayes, M.J. Uren, I. Martin, J.C.H. Birbeck, R.S. Balmer, and B.T. Hughes, "Measurement of temperature in active high-power AlGaN/GaN HFETs using Raman spectroscopy," IEEE Electron Device Lett. **23**(1), 7–9 (2002).

[155] S. Choi, E.R. Heller, D. Dorsey, R. Vetury, and S. Graham, "Thermometry of AlGaN/GaN HEMTs using multispectral raman features," IEEE Trans. Electron Devices **60**(6), 1898–1904 (2013).

[156] J. Dallas, G. Pavlidis, B. Chatterjee, J.S. Lundh, M. Ji, J. Kim, T. Kao, T. Detchprohm, R.D. Dupuis, S. Shen, S. Graham, and S. Choi, “Thermal characterization of gallium nitride p-i-n diodes,” Appl. Phys. Lett. **112**(7), 73503 (2018).

[157] J.S. Lundh, Y. Song, B. Chatterjee, A.G. Baca, R.J. Kaplar, A.M. Armstrong, A.A. Allerman, B.A. Klein, D. Kendig, H. Kim, and S. Choi, “Device-level multidimensional thermal dynamics with implications for current and future wide bandgap electronics,” J. Electron. Packag. **142**(3), 031113 (2020).

Chapter 4

AlN/$Al_{1-x}Sc_xN$ MEMS

4.1 Growth-Microstructure-Thermal Property Relations in AlN Thin Films

4.1.1 Introduction

Aluminum nitride is an ultra-wide bandgap semiconductor that exhibits piezoelectricity and is utilized in optoelectronics, power electronics, and electro-acoustic applications.[1–4] For example, AlN-based deep ultraviolet (DUV) light-emitting diodes (LEDs) emitting at a wavelength of 210 nm have been demonstrated,[5] while alloying Ga (i.e., $Al_xGa_{1-x}N$) allows continuous spectral tuning to 400 nm. LED's operating in this UV-band support a wide range of applications such as water purification, UV sensors, and energy harvesting.[6] From a power electronics perspective, AlN's direct bandgap of ~6.2 eV and high breakdown field (>10 MV/cm) lead to a Baliga figure of merit (BFOM)[7] that is 34 times higher than that of GaN.[4] Electro-acoustically, AlN-based film bulk acoustic resonators (FBARs) have contributed to the performance enhancement and system size reduction of radio frequency (RF) signal processing applications[1] and telecommunication technologies[8]. A variety of AlN-based microelectromechanical systems (MEMS) such as surface acoustic wave (SAW) devices,[9] flexural plate wave (FPW) sensors,[10] micromachined ultrasonic transducers (pMUTs)[11], and contour mode resonators (CMRs)[12] have been commercialized.

To optimize the manufacturability and performance of AlN-based microsystems, several growth techniques have been employed. For DUV optoelectronic applications, large diameter high quality single crystal AlN wafers are desired. Physical vapor transport (PVT) is the most widely used approach for growing single crystal bulk AlN. Wafers with diameters up to 2-inches have been commercialized.[13,14] Several modified PVT methods have been developed to improve the crystal quality of bulk AlN.[15] For power electronic devices, including high-electron-mobility transistors (HEMTs), the growth of smooth and low defect density AlN films[16] is desired to form multilayered AlN/GaN/AlN[17] and AlN/AlGaN[18–20] heterostructures. Molecular beam epitaxy (MBE),[16,21] metalorganic chemical vapor deposition (MOCVD),[22] and hydride vapor phase epitaxy (HVPE)[23] have each been successfully used to grow high quality epitaxial AlN films on non-native substrates. AlN templates produced by these methods are also commonly used to produce epitaxial UV-C LEDs/detectors and high-power radio frequency (RF) electronic devices. These epitaxial growth methods require both high temperature growth conditions and single crystalline substrates to obtain epitaxial AlN films. For MEMS applications, growth of the piezoelectric thin film on metal electrodes is often needed and the growth temperature may be limited (<400 ˚C)[24] to be compatible with the complementary metal-oxide-semiconductor (CMOS) integrated circuit technology. Reactive sputtering is commonly used to synthesize oriented AlN thin films on a variety of growth templates at such moderate temperature ranges.[24] High quality, dense, c-axis textured AlN films have similar piezoelectric modulus (d_{33}) and elastic stiffness (C_{33}) as single crystal AlN and epitaxially grown films.[25–27] $Al_xGa_{1-x}N$-based DUV LEDs are often grown by MOCVD on high temperature-annealed sputter-deposited AlN/sapphire templates.[28]

High thermal conductivity is favored for engineering applications to mitigate device self-heating; however, the thermal conductivity of a thin film generally differs from its bulk counterpart. Bulk single crystal AlN exhibits a high thermal conductivity of ~320 W/mK at room temperature due to the strong interatomic bonding and the relatively light constituent elements.[29–31] The microstructure of a thin film is strongly affected by the substrate and the growth conditions, resulting in varying levels of crystallinity and point/extended defect densities.[24,32] For example, consider an AlN film prepared by sputter-annealing: AlN sputtered at modest temperatures typically exhibits a columnar structure with a small lateral grain size. These columnar grain domains combine and increase in size starting at 1300-1450°C. As the annealing temperature and/or time rises, the solid-state reaction continues to increase the grain size until around 1600-1750°C, where the previous columnar grain structure is transformed into a nearly grain boundary-free film. While the mechanism is not fully understood, oxygen is believed to have a significant role in the annealing process.[33] The film microstructure and finite thickness can limit heat conduction in the film due to increased levels of phonon scattering with point defects, dislocations, grain boundaries, and film boundaries. For example, Xu *et al.*[34] reported a room temperature thermal conductivity of 237 ± 6 W/mK for bulk PVT-grown AlN with O, Si, C impurities with concentrations ranging from 0.4×10^{19} to 2×10^{19} cm^{-3}, and Al vacancies with concentrations of ~2×10^{19} cm^{-3}; this is significantly lower than the value calculated for pure AlN (~320 W/mK).[31] A detailed literature survey for thermal conductivity of bulk AlN with various defect and impurity concentrations has been reported by Inyushkin *et al.*[30] Xu *et al.*[34] also reported that 50% of the phonons of AlN (at room temperature) have mean free paths (MFPs) greater than ~0.3 μm and 10% of the phonons have long MFPs over ~7 μm. Taken in aggregate, the thermal conductivity of AlN will likely vary substantially when it is incorporated within a LED (e.g., bulk single crystal), a power switching transistor (i.e., epitaxial film), and a piezoelectric MEMS device (oriented film).

Owing to these expected differences, this work investigates the correlation between the microstructure and thermal conductivity of AlN thin films synthesized by different growth techniques. The implications on the thermal management and design of relevant device applications are assessed as well. Specifically, a commercial bulk AlN single crystal grown by PVT was prepared as a reference sample. The thermal properties of this single crystal reference were then compared to several industry-grade AlN thin films prepared by reactive sputter deposition, sputter-annealing, halide vapor epitaxy (HVPE), molecular beam epitaxy (MBE), and metal organic chemical vapor deposition (MOCVD). To understand the underlying causes for the variations in thermal properties observed, field emission scanning electron microscopy (FESEM), scanning transmission electron microscopy (STEM), energy dispersive x-ray spectroscopy (EDS), Raman spectroscopy, X-ray diffraction (XRD), and secondary ion mass spectrometry (SIMS) probed the crystallinity, defects, film stress, and microstructure. Finally, a device-level finite-element thermal model was used to demonstrate the significantly different level of self-heating in FBAR structures adopting oriented vs. epitaxial AlN thin films as the active piezoelectric layer.

4.1.2 Results and Discussion

Film Characterization

The cross-plane (κ_z) and in-plane (κ_r) thermal conductivities of the AlN films were measured by routine time-domain thermoreflectance (TDTR) and beam-offset TDTR, respectively.[35–37] Complementary techniques were used to validate results when applicable. For example, frequency-domain thermoreflectance (FDTR) measurements have been performed on pulse-DC reactive sputter-deposited samples and the results agreed with TDTR κ_z data within the error bar ranges (SP-157/Si: 18.3 ± 5.2 W/mK; SP-733/Si: 58.8 ± 6.1 W/mK). Steady-state thermoreflectance (SSTR), meanwhile, confirmed the thermal conductivity of the single crystal bulk sample producing a directionally averaged thermal conductivity of 292.4 ± 61.3 W/mK, which shows good agreement with the average of κ_z (330.1 ± 28.1 W/mK) and κ_r (326.5 ± 62.0 W/mK) acquired from TDTR measurements. SSTR was also used to extract the κ_r (230 ± 52.1 W/mK) of a HVPE-grown AlN film (HVPE-1083/Al_2O_3), based on the κ_z determined by TDTR measurements. The result agrees well with κ_r determined by beam-offset TDTR measurements. Together these results highlight the difference in thermal conductivities among the films are due to material variations and are not a measurement artifact.

TABLE 4.1 Summary of the characterization results. A positive residual stress means the film is under tensile stress.

	Growth Method	Substrate	Thickness (nm)	Grain Size (nm)	XRD FWHM (deg)	Raman FWHM (cm^{-1})	κ_z (W/mK)	κ_r (W/mK)	Stress (GPa)	Sample ID
Bulk single crystal	PVT	N/A	N/A	N/A		3.3 ± 0.02	330.1 ± 28.1	326.5 ± 62.0	0	PVT-Bulk
Epitaxial films	Sputter-annealing	(0001) Al_2O_3	394	N/A	0.016	3.90 ± 0.02	50.2 ± 16.6	115.5 ± 18.6	-1.24	SA-394/Al_2O_3
	Sputter-annealing	(0001) Al_2O_3	487	N/A	0.022	4.01 ± 0.05	89.2 ± 45.7	168.6 ± 17.0	-1.24	SA-487/Al_2O_3
	HVPE	(0001) Al_2O_3	1083	N/A	0.081	4.41 ± 0.02	96.2 ± 28.6	215 ± 34.0	-0.80	HVPE-1083/Al_2O_3
	MOCVD	(0001) 4H-SiC	967	N/A	0.062	3.90 ± 0.04	122.9 ± 16.1	286.4 ± 112.6	-0.84	MOCVD-967/SiC
	MBE	(111) Si	413	N/A	0.496	7.93 ± 0.57	104 ± 46	60.9 ± 23.0	0.37	MBE-413/Si
Oriented films	Sputtering	(001) Si	157	20.03	3.702	N/A	19.4 ± 4.8	N/A	N/A	SP-157/Si
	Sputtering	(001) Si	490	37.98	1.538	10.20 ± 0.22	42.8 ± 6.9	28.7 ± 15.2	0.43	SP-490/Si
	Sputtering	(001) Si	707	34.68	1.444	9.99 ± 0.14	79.6 ± 13.7	35 ± 9.9	0.30	SP-707/Si
	Sputtering	(001) Si	733	35.34	2.108	N/A	50.5 ± 6	39.3 ± 9.5	-0.16	SP-733/Si

Table 4.1 summarizes results of the thermal and structural characterizations performed on the AlN films. Each sample listed in **Table 4.1** is named based on the growth method, AlN film thickness, and substrate material. For example, SP-490/Si refers to a film deposited by reactive sputtering with a thickness of 490 nm, on a Si substrate. The thermal conductivity data presented in **Table 4.1** were measured by TDTR; the experimental details including the pump/probe spot sizes, sensitivity analysis, and error analysis are discussed in the EXPRIMENTAL SECTION/METHODS. The measured room temperature thermal conductivity of the bulk single crystal is nearly isotropic, with $\kappa_r = 326.5 \pm 62.0$ W/mK and $\kappa_z = 330.1 \pm 28.1$ W/mK; this agrees with the previously reported data for bulk AlN within the error bar ranges.[29,30,38] The cross-plane thermal conductivities of the AlN thin films show a strong correlation with the film thickness, as shown in **Figure 4.1 (a)**. The strong thickness dependence of κ_z is due to the relatively large population of long MFP phonons in AlN. Xu *et al.* calculated that 50% of the heat in pure, defect-free AlN is carried by phonons with MFPs greater than 0.3 μm and 10% is carried by phonons with MFPs longer than 7 μm at room temperature, as shown by the continuous line of **Figure 4.1 (a)**.[34]

Freedman *et al.* measured the MFP spectra using broadband FDTR and reported that 50% of the thermal conductivity is contributed by phonons with MFPs greater than 2.5 μm at room temperature.[39] Overall, the measured κ_z values are lower than the theoretical predictions at the corresponding thicknesses due to additional phonon scattering mechanisms, which will be discussed in the following text. Nevertheless, the strong correlation between κ_z and thickness regardless of the film microstructure indicates the dominance of phonon-boundary scattering in sub-micrometer thick AlN films, as has been observed in GaN.[40]

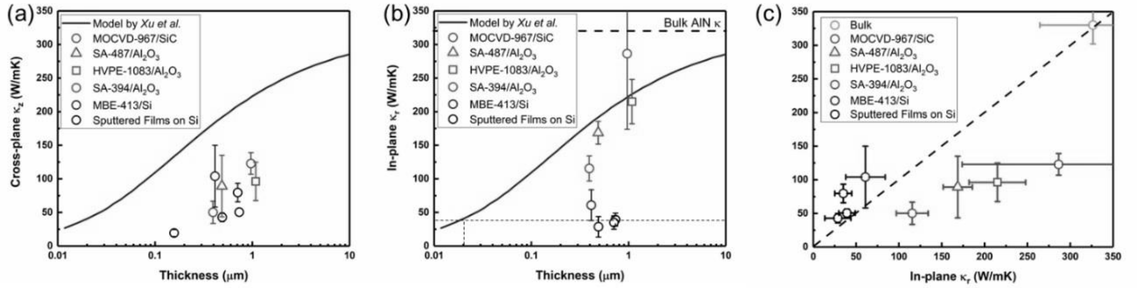

Figure 4.1. (a) The cross-plane thermal conductivity of the samples as a function of film thickness. The solid blue line plots the model predictions by Xu *et al.* for perfect single crystal AlN.[34] (b) The measured in-plane thermal conductivity of the AlN thin films. Also plotted is the bulk thermal conductivity of single crystal AlN[31] for comparison. The intersection of the blue line (cross-plane thermal conductivity calculations by Xu et al.[34]) and the gray dashed line corresponds to the thermal conductivity at a characteristic scattering length of 20 nm. (c) The cross-plane thermal conductivity versus the in-plane thermal conductivity of the AlN films and a bulk AlN substrate.

The in-plane thermal conductivities, however, do not show an apparent correlation with the film thickness; instead, they are dominated by the microstructures of the films. In other words, the anisotropy in the thermal conductivities observed in the AlN thin films results from different scattering mechanisms that dominate phonon transport in the in-plane and cross-plane directions.

Figure 4.1 (c) plots the κ_z values against the κ_r for the measured films. The dashed line is where κ_z equals to κ_r; therefore, the data points above the dashed line corresponds to films that possess a higher κ_z than κ_r, and the data below the dashed line are films with a κ_r larger than κ_z. While all the films show that κ_z is primarily limited by the finite film thickness (**Figure 4.1 (a)**), an interesting observation is that all the AlN films grown on Si have a higher κ_z than κ_r. As shown in **Figure 4.1 (b)**, the oriented films grown by pulsed-DC reactive sputtering possess a significantly lower κ_r than those for the epitaxial films. The reactive sputtering process produces c-axis textured polycrystalline films[24] that exhibit average lateral grain sizes ranging 20-40 nm as characterized by plan-view field emission scanning electron microscopy (FESEM) (**Figure 4.2 (a)**). When using the grain size (20 nm) as the characteristic scattering length, the measured κ_r agrees well with the model for a 20 nm thickness,[34] as shown by the vertical dashed line in **Figure 4.1 (b)**. Based on the observation that bulk single crystal AlN possesses an isotropic thermal conductivity, this indicates that the in-plane heat conduction in the oriented films is mainly limited by phonon-grain boundary scattering. Reactive sputtering of oriented AlN films is particularly important for fabricating CMOS compatible MEMS devices owing to the relatively low growth temperatures (<500 ˚C) and ability to grow on metal electrodes.[24] Industry-grade, dense c-axis textured AlN films possess a piezoelectric modulus (d_{33}) and elastic stiffness (C_{33}) comparable to those for epitaxial films and single crystal AlN.[25–27] Therefore, sputter-deposited films are favorable to be employed as the active piezoelectric layer of piezoelectric MEMS resonators. Recently, the electro-acoustic performance of FBAR band-pass RF filters based on physical vapor deposition (PVD)-sputtered c-axis oriented polycrystalline AlN films and MOCVD-grown epitaxial films was compared.[41] The devices based on MOCVD-grown epitaxial films were reported to have a 2.6 dB (or 18.1 W) higher power handling capability and a 0.2 dB lower insertion loss than those for RF filters based on sputter-deposited oriented films.[41] The results above suggest that the lateral heat spreading capability of the active AlN piezoelectric layer may significantly impact the power handling capability and energy loss of/within the MEMS resonators (to be discussed later in device self-heating section).

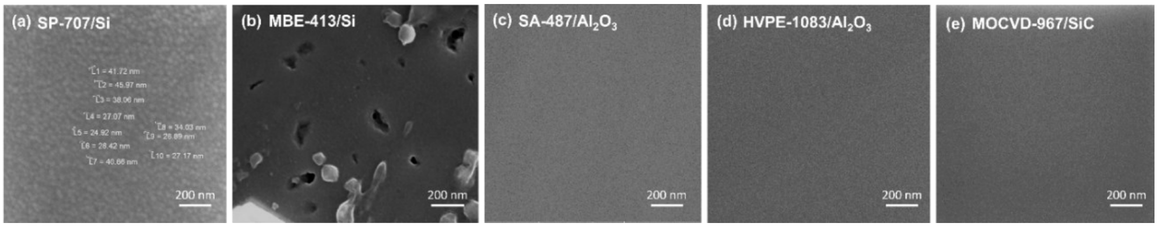

Figure 4.2. Representative plan-view FESEM images of the AlN samples. (a) Sputter-deposited oriented film on Si; *c*-axis textured grains are observed. (b) MBE-grown film on Si. (c) Sputter-annealed epitaxial film on a sapphire substrate. (d) HVPE-grown epitaxial film on sapphire. (e) Epitaxial film grown on a SiC substrate via MOCVD. The surface morphology of all epitaxial films grown on sapphire and SiC substrates (grown by sputter-annealing, HVPE, and MOCVD) were smooth and did not show the presence of pits, cracks, or large angle grain boundaries.

As discussed previously, the sputter-deposited oriented films on Si have *c*-axis oriented columnar grains with a small lateral grain size that limit the in-plane heat conduction due to phonon-grain boundary scattering. Interestingly, the MBE-grown film on Si also exhibits a relatively low κ_r, even though no lateral grain structure is observed in **Figure 4.2 (b)**. However, the scanning transmission electron microscopy (STEM) image of the MBE-grown AlN film suggests a significantly larger area density of dislocations (**Figure 4.3 (b)**, **(g)**) than that for epitaxial films grown on sapphire (HVPE and sputter-annealing) and SiC substrates (MOCVD). This is likely due to the large lattice mismatch (19%) between the AlN (0001) and Si (111).[42,43] The strain formed by this lattice mismatch can be relieved by misfit dislocations as observed in the low-angle annular dark field (LAADF) STEM image shown in **Figure 4.3 (b)**. The MBE grown film is under a relatively low tensile stress (**Table 4.1**) due to this relaxation. The coefficient of thermal expansion

(CTE) mismatch between (111) Si[44] ($2.6 \times 10^{-6} K^{-1}$ at room temperature) and AlN would also induce a tensile stress in the AlN film due to the high growth temperature of MBE (typically, ~1200 ˚C)[45]. Raghavan *et al.* calculated a 1000˚C drop from growth temperature would result in an AlN epitaxial film with a tensile stress of 0.9 GPa.[46] The high dislocation density observed in **Figure 4.3 (b), (g)** is thought to have further relaxed the strain and resulted in the relatively low tensile stress of ~0.4 GPa measured by Raman spectroscopy.

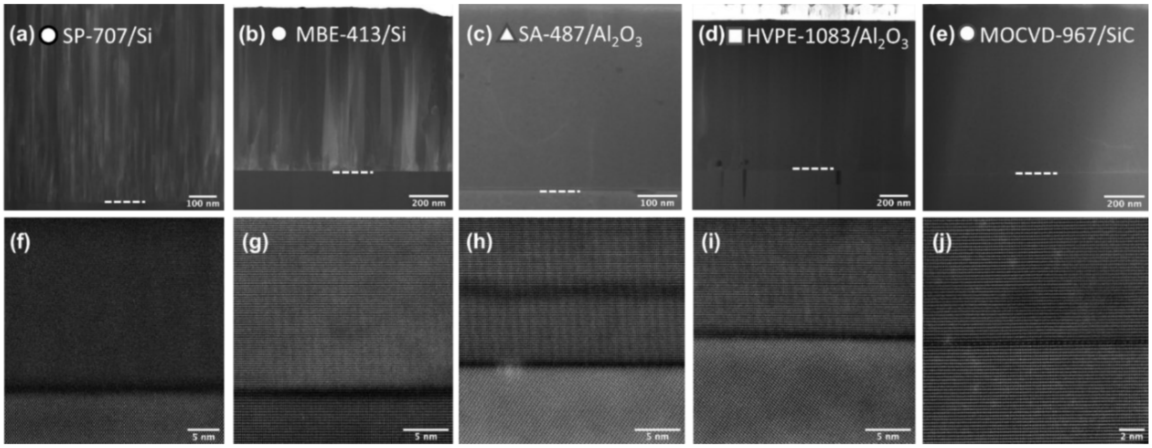

Figure 4.3. Representative LAADF-STEM images for a (a) sputter-deposited oriented film on Si, (b) MBE-grown film on Si, (c) a sputter-annealed epitaxial film on sapphire, (d) HVPE-grown epitaxial film on sapphire, and (e) the MOCVD-grown epitaxial film on SiC. Also shown are representative atomic resolution STEM images of the AlN/substrate interface for a (f) sputter-deposited oriented film on Si, (g) MBE-grown epitaxial film on Si, (h) sputter-annealed epitaxial film on sapphire, (i) HVPE-grown epitaxial film on sapphire, and (j) MOCVD-grown epitaxial film on SiC. All of the films show clear film/substrate interfaces. The color code for the sample IDs corresponds to the color code used in **Figure 4.2**.

According to **Figure 4.1 (b)**, the epitaxial films grown by sputter-annealing, HVPE, and MOCVD exhibit κ_r values that are far higher than those for the reactive sputtered and MBE-grown films. FESEM (**Figure 4.2 (c)** – **(e)**) and STEM images (**Figure 4.3 (c)** – **(e)**) show the absence of large angle grain boundaries or columnar grains in the epitaxial films. X-ray diffraction (XRD) and Raman spectroscopy were used to qualitatively compare the crystalline quality of all the samples. As shown in **Figure 4.4 (a)**, the epitaxial AlN films grown on sapphire and SiC substrates show narrower XRD full width at half maximum (FWHM) in the rocking curves than those for the films grown by reactive sputtering and MBE on Si, which indicates superior crystal quality. The MBE-grown film on a Si substrate shows a broader FWHM than the other epitaxial films, which supports the observation of a lower κ_r than those for SA-487/Al_2O_3 and SA-394/Al_2O_3 films of similar layer thicknesses (**Figure 4.1(b)**). This results in a different anisotropy in the thermal conductivity shown in **Figure 4.1 (c)** as compared to the other epitaxial AlN films. In contrast, the higher crystal quality for the epitaxial films on sapphire and SiC substrates supports the observation that κ_r is higher than κ_z of these films (**Figure 4.1 (c)**). The sputtered AlN films on Si substrates exhibit the largest FWHM, consistent with a broader distribution of the crystallite orientations. Raman spectroscopy (**Figure 4.4 (b)**) confirms the findings from XRD measurements. For Raman measurements, the narrower FWHM of the E_2(high) peak indicates better crystalline quality.

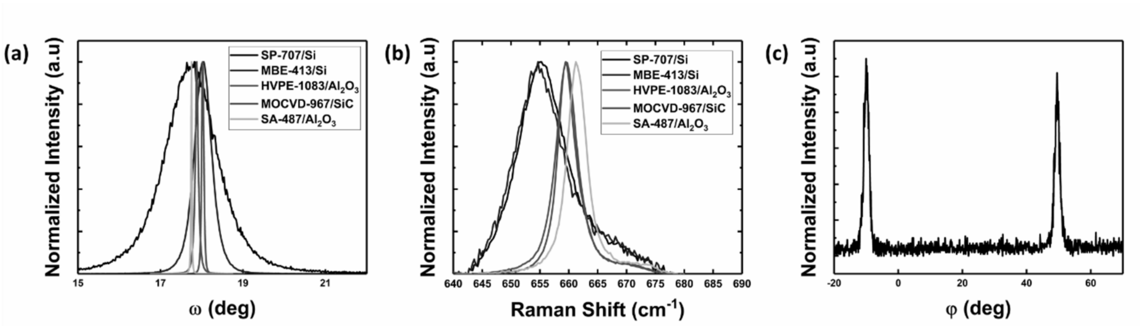

Figure 4.4. (a) XRD rocking curves showing the (002) AlN film peaks of the AlN films (b) Raman spectra of the AlN films showing the E_2(high) peak. All peaks are normalized with respect to the maximum intensity. The difference in Raman peak positions and linewidths between the two groups of the oriented films (sputtered, MBE) and epitaxial films (sputter-annealed, HVPE, MOCVD) show evidence supporting the difference in the crystalline quality and residual stress, respectively. (c) XRD φ scan for asymmetric planes of (102) of MBE-413/Si.

Among the epitaxial films, it should be noted that the MOCVD-grown film exhibits a κ_r that is comparable to a value predicted for single crystal bulk AlN (**Figure 4.1 (b)**); On the other hand, the films grown by MBE, sputter-annealing, and possess κ_r values that are considerably lower than the bulk thermal conductivity of single crystal AlN. To understand if the observed discrepancy is attributed to phonon-dislocation scattering, XRD measurements were performed on the epitaxial films to estimate their dislocation densities. The screw and edge dislocation densities of an AlN film were estimated from the full width at half maximum (FWHM) of the (002) and (102) XRD rocking curves, respectively, as shown below[47,48]:

$$\rho_e = \frac{\Delta\omega_{(102)}^2}{2\pi \ln(2)\, b_a^2} \tag{4.1}$$

$$\rho_s = \frac{\Delta\omega_{(002)}^2}{2\pi \ln(2)\, b_c^2} \tag{4.2}$$

The coefficients b_a and b_c are the magnitude of the corresponding Burger vector components; for the case of AlN they are the a and c lattice parameters, $b_a = 0.3113$ nm and $b_c = 0.49814$ nm.

The sputtered films only show the out of plane (002) peaks whereas no peak representing the (102) planes is observed in phi (φ) scans, indicating in-plane rotational disorder. Accordingly, the edge dislocation density could not be estimated. The XRD φ scan for (102) planes of the MBE-grown AlN film is shown in **Figure 4.4 (c)**. The peaks separated by a 60° interval indicate the six-fold rotational symmetry of hexagonal AlN and confirm the in-plane (c-plane) periodicity, similar to what was observed in XRD φ scans for the epitaxial films grown by sputter-annealing, HVPE, and MOCVD.

Table 4.2 is a summary of the calculation results for the screw and edge dislocation densities of the epitaxial films. The MBE-grown AlN film exhibits the highest dislocation densities. These results confirm that the relatively low κ_r of MBE-413/Si among the epitaxial films is due to the high dislocation density. It should be noted that the sputter-annealed AlN films (SA-394/Al_2O_3 and SA-487/Al_2O_3) exhibit the lowest dislocation densities among the epitaxial films. The improvement in the crystallinity of sputtered AlN films by high temperature annealing has been reported in literature.[33,49] However, their κ_r values are far lower than those for the HVPE- and MOCVD-grown films, which suggests that their in-plane heat conduction may be limited by other phonon scattering mechanisms such as phonon-point defect scattering.

Table 4.2 Dislocation densities calculated based on XRD rocking curve.

	Edge Dislocation Density (cm^{-2})	Screw Dislocation Density (cm^{-2})
SA-394/Al_2O_3	3.36×10^8	6.19×10^6
SA-487/Al_2O_3	6.83×10^8	3.38×10^6
HVPE-1083/Al_2O_3	4.88×10^9	1.65×10^8
MOCVD-967/SiC	6.43×10^8	1.36×10^8
MBE-413/Si	1.06×10^{11}	7.54×10^9

An established scattering model (similar to the approach used in Beechem *et al.*[50]) was constructed to qualitatively study the effect of dislocation density on the AlN thermal conductivity. Results are shown in **Figure 4.5 (a)**. For simplicity, a combined effect of phonon scattering with screw and edge dislocations has been evaluated. Dislocations weakly affect the thermal conductivity up to a concentration level of ~10^8 cm^{-2}. MBE-413/Si exhibits significantly higher dislocation densities than the epitaxial films grown on SiC and Al_2O_3 due to the larger lattice mismatch between AlN and Si (19%); therefore, a lower κ_r was observed in this film as compared to other epitaxial films. SA-394/Al_2O_3 and SA-487/Al_2O_3 possess lower dislocation densities than HVPE-1083/Al_2O_3, due to the improved crystallinity from the high temperature annealing process.[51] However, it is worth noting that the κ_r of MOCVD-967/SiC is the highest among the AlN films tested even with higher dislocation densities as compared to these sputter-annealed samples; again, this is likely due to the additional phonon scattering mechanisms discussed in the following text. The dislocation density of the MOCVD-967/SiC is lower than the HVPE-grown film on Al_2O_3. This is attributed to the smaller lattice mismatch (~1%) between AlN and 4H-SiC.[52]

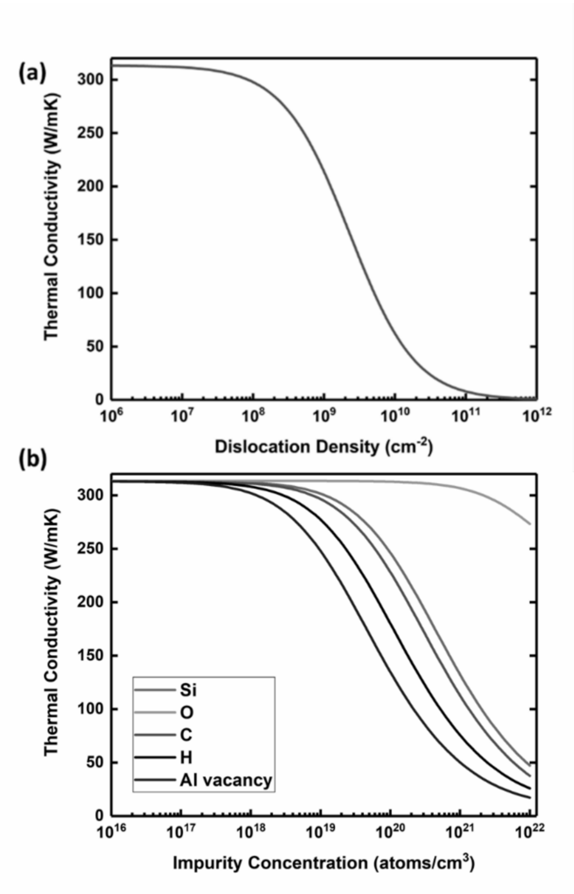

Figure 4.5. Thermal conductivity as a function of (a) the combined dislocation densities of the AlN film (b) the concentration of impurities and Al vacancies from simulation.

While the film thickness limits the cross-plane heat conduction and dislocations have a stronger effect on the in-plane thermal transport, point defects homogeneously scatter phonons traveling in all directions.[32,38,53,54] As seen in Figure 1 (a), the measured κ_z values for all of the AlN films are overall lower than the model prediction for a perfect AlN crystal with corresponding thicknesses. This suggests additional phonon-point defect scattering mechanisms may prevail. Such additional scattering events are also evidenced by the lower κ_r of all the epitaxial AlN films including MOCVD-967/SiC (286.4 ± 112.6 W/mK; with low dislocation density) as compared to that for bulk single crystal AlN (~319 W/mK)[31]. The κ_r of the sputter annealed samples are much lower than the bulk value even with the lowest estimated dislocation densities. The impurity concentrations of Si, O, C, H were characterized by secondary ion mass spectrometry (SIMS), and the thickness-averaged results are summarized in **Table 4.3**. The established scattering model[50] was further utilized to assess the impact of these impurities on phonon scattering, and hence on the AlN thermal conductivity. Results are summarized in **Figure 4.5 (b)**. It should be noted that H concentrations are higher in the oriented films; modeling results show H interstitial impurities with a concentration above ~10^{19} atoms/cm^3 can significantly reduce thermal conductivity. However, the thermal conductivities of the epitaxial films are expected to be less impacted by H impurities due to their overall lower concentrations. C and Si impurities are predicted to weakly impact the thermal conductivity below concentration levels of 10^{20} atoms/cm^3. This is because Si has a similar atomic mass and ionic radius as Al.[55,56] Also, the difference between the atomic mass and ionic radius of C and Al is much smaller than the case of H and Al. The overall low levels of C and Si impurity concentrations of the tested samples rule out the possibility for these impurities to significantly reduce the thermal conductivities. For a similar reason, the O substitutional impurities on the N site are predicted to have a relatively weak effect on the thermal conductivity due to the similar atomic masses and ionic radii.

This is not to say that O does not affect the thermal conductivity. Rather, previous studies have suggested that Al vacancies forming in response to this O substitutional process can have a strong effect on the thermal conductivity (and the piezoelectric response[57]) of AlN.[31,58] When O atoms enter the AlN lattice, it is energetically favorable for them to replace the N sites; this process leaves one Al vacancy (V_{Al}) for every three O atoms incorporated into the lattice.[54,58] The Al vacancies, in turn, create large mass and size differences with respect to the original lattice and therefore significantly reduce the thermal conductivity. Notably, the MOCVD-967/SiC and MBE-413/Si samples, which have the lowest O concentrations, also exhibit the highest cross-plane thermal conductivity for the films at comparable thickness, as shown in **Figure 4.1 (a)**. O contamination is commonly found in AlN thin films grown by various techniques because O atoms exhibit a higher affinity than N towards Al atoms.[59,60] The O impurity concentrations in the HVPE-grown sample and the sputter annealed films are observed to be four orders of magnitude higher than that for the MOCVD-grown film. This explains why these epitaxial films with comparable or even lower dislocation densities exhibit lower κ_r values than the MOCVD-grown sample. In fact, the incorporation of O is common for all the growth techniques discussed. For example, multiple sources of O contamination have been reported for the HVPE growth process. These include the quartz-made aluminum boat reacting with the AlCl precursor, the aluminum oxide that remains in the source boat after HCl activation, and the residual contamination of the source gases.[61] O impurities in PVT-grown AlN mainly come from the Al_2O which is a major gas-phase species in the growth chamber.[62] For sputter deposition, the O contamination can be caused by residual gas molecules remaining that are not completely removed from the vacuum chamber.[59,63] For this reason, Al vacancies are thought to be responsible for both the κ_r and κ_z of all samples to be lower than the calculated values for a perfect crystal (**Figure 4.1 (a)**, **(b)**).

TABLE 4.3 Impurity concentrations (atoms/cm^3) of O, H, C, and Si

	Sample ID	Substrate	O	H	C	Si
Single crystal bulk	PVT-Bulk	N/A	1.0×10^{18}	1.3×10^{17}	9.1×10^{18}	9.8×10^{19}
Epitaxial films	SA-394/Al_2O_3	(0001) Al_2O_3	2.6×10^{20}	9.6×10^{18}	1.1×10^{18}	8.5×10^{18}
	SA-487/Al_2O_3	(0001) Al_2O_3	1.3×10^{20}	2.0×10^{17}	7.8×10^{17}	7.5×10^{18}
	HVPE-1083/Al_2O_3	(0001) Al_2O_3	1.4×10^{20}	2.5×10^{17}	2.3×10^{16}	1.7×10^{18}
	MOCVD-967/SiC	SiC	5.1×10^{16}	3.4×10^{17}	2.8×10^{16}	3.0×10^{17}
Oriented films	MBE-413/Si	(111) Si	2.3×10^{17}	2.9×10^{17}	1.0×10^{16}	4.2×10^{19}
	SP-490/Si	(001) Si	3.9×10^{18}	4.0×10^{19}	3.8×10^{17}	5.6×10^{17}
	SP-707/Si	(001) Si	6.1×10^{18}	7.7×10^{18}	9.1×10^{17}	4.7×10^{17}

It should be noted that oxygen can be intentionally incorporated into AlN films for ultraviolet (UV) optoelectronic applications. As shown in **Figure 4.6 (b)**, energy dispersive x-ray spectroscopy (EDS) mapping shows an oxygen concentrated layer near the AlN/substrate interface of a sputter-annealed AlN sample (SA-394). This oxygen rich layer is also shown in the elemental maps in **Figure 4.6 (a)**. Sapphire is often used as a UV-transparent substrate for optoelectronic applications based on AlN and $Al_xGa_{1-x}N$. The aluminum oxynitride (AlON) layer near the interface improves index matching for better optical extraction from UV LEDs.[64] However, from a thermal management perspective, this AlON layer potentially hinders heat extraction through chip packaging and may result in additional device self-heating that can compromise the maximum achievable power, efficiency, and lifetime of the LEDs.[6] Therefore, it may be important to consider phonon scattering caused by the low thermal conductivity AlON layer (~10 W/mK)[65,66] when designing thermal management solutions for optoelectronic devices.

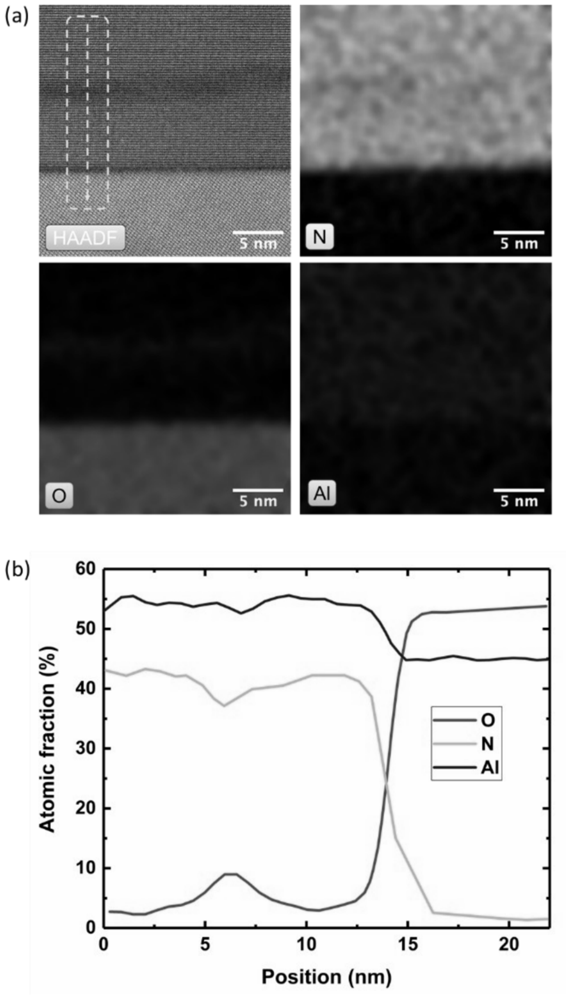

Figure 4.6. (a) STEM-EDS elemental map of the SA-394 sample from the cross-section. An oxygen rich layer was observed ~10 nm above the interface. (b) Line scan of the EDS data along the yellow dashed line shown in (a), from the AlN film towards the Al_2O_3 substrate.

Device Self-Heating

It is clear from the preceding data that that thermal conductivity is closely linked to the growth technique used to synthesize the AlN films. Here, it is shown that these changes in thermal conductivity have a practical impact on device applications. A 3-dimensional (3D) finite-element thermal model of a film bulk acoustic resonator (FBAR) was created using COMSOL

Multiphysics.[67] AlN was used as the active piezoelectric layer of two FBAR devices with identical geometry but with different thermal conductivities, corresponding to the measured values for sputter-deposited and MOCVD-grown AlN films. The film thicknesses were both assumed to be 800 nm, yielding a fundamental thickness-mode resonance frequency of ~4 GHz.[68] The active area is 85 μm × 85 μm to give a 50 Ω capacitive impedance at the resonant frequency. A square device shape was assumed to simplify calculations for the thermal performance. A mapped mesh was used with maximum element size of 5 μm for the active area. For the bulk geometry, the mesh was built by using a user-defined fixed number of elements to properly simulate the domain while managing the computational cost. A stationary, direct solver was used to calculate the device temperature rise. A power vs. device temperature study was performed for three existing and potential applications. Assuming 1 / 20 / 50 W of transmit power (for mobile, base station, and military radar applications, respectively), a filter insertion loss of 2 dB per resonator, and 8 resonators in the ladder filter, 0.046 / 0.92 / 2.3 W is dissipated per resonator. Uniform volumetric heat generation corresponding to these values was applied to the active region of the FBAR models. All the dissipated energy was assumed to convert to heat within this volume, and therefore the simulated temperatures represent the upper bound of self-heating. A schematic of the simulated FBAR cross section is shown in **Figure 4.7 (a)**. The bottom of the Si substrate was assumed to be at room temperature. Natural convection, represented by a heat transfer coefficient of 10 W/m^2K, was used as a thermal boundary condition for all other surfaces. Two case studies were performed using measured anisotropic thermal conductivity values for oriented and epitaxial AlN films with thicknesses close to 800 nm (i.e., the sputter-deposited oriented film shown in **Figure 4.7 (b)** and the MOCVD-grown epitaxial film illustrated in **Figure 4.7 (c)**). The lower thermal conductivity of the sputtered film resulted in a 50 K higher peak temperature rise (85 K) as compared to the device based on a MOCVD film (35 K) for mobile applications. The electro-acoustic performance of FBAR band-pass RF filters based on c-axis oriented polycrystalline AlN films and epitaxial

MOCVD grown-films has been reported elsewhere.[41] Filters based on MOCVD-grown epitaxial AlN films exhibited the highest reported power handling capability (46.1 dBm or 40.6 W) for bulk acoustic wave (BAW) RF filters at the mid-3 GHz frequency range. A device based on MOCVD-grown AlN exhibited a 2.6 dB or 18.1 W higher power handling capability and a 0.2 dB lower insertion loss compared to RF filters based on oriented sputtered films. Therefore, the modeling data in **Figure 4.7** suggest that the thermal conductivity of the active piezoelectric layer may significantly impact the energy loss (e.g., via Akhiezer damping[69]) and power handling capability of piezoelectric MEMS resonators.

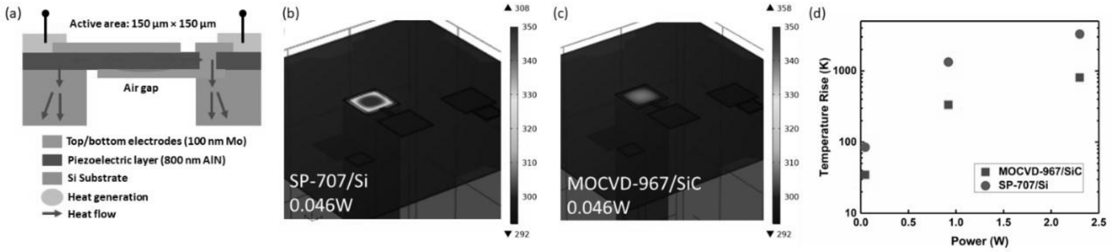

Figure 4.7. (a) Cross-sectional schematic of the simulated AlN FBARs. Device modeling results for AlN FBARs based on (b) a sputter-deposited oriented film and (c) a MOCVD-grown epitaxial film. (d) The peak temperature rises of simulated FBARs as a function of dissipated power for mobile, base station, and military radar applications.

4.1.3 Conclusion

In this study, thermal/structural characterizations on AlN thin films synthesized by different growth techniques was performed. The cross-plane heat conduction in the AlN thin films is limited by the phonon-boundary scattering due to the relatively large population of acoustic phonons with long MFP present in AlN. The lowest in-plane thermal conductivity was observed in the *c*-axis oriented sputtered AlN films. This may impose drive level limitations on the AlN piezoelectric layer in piezoelectric MEMS resonators prepared via reactive sputtering, that may limit the power handling capability. Epitaxial films grown by sputter-annealing, HVPE, and MOCVD exhibit higher in-plane thermal conductivities. The in-plane thermal conductivity of an epitaxial film is strongly affected by the dislocation density, as observed in a film grown on a Si substrate. Impurity concentrations in the films were characterized by SIMS and a thermal conductivity model suggests that Al vacancies decrease the thermal conductivity of a AlN thin film substantially. Finally, a 3D finite-element thermal model was constructed to study the self-heating behavior of FBARs based on a sputter-deposited textured AlN film and an epitaxial film. Simulation results indicate that overheating in devices based on sputter-deposited films can limit their use in high power applications. The outcomes of this work provide insight into the importance of using appropriate thermal properties for the modeling and design of AlN-based microsystems; for example, using the bulk thermal conductivity of AlN will significantly underestimate the temperature rise in relevant AlN thin film-based technologies.

4.1.4 Experimental Methods

AlN film synthesis

SP-157/Si, SP-707/Si, SP-733/Si: This series of AlN films were reactively sputtered using a SPTS Sigma 200 deposition system with an Al target. Deposition conditions are like those found in reference[70]. Sample SP-707 differs from others since it used 100% N_2 gas during deposition (others were made with an Ar/N_2 mixture) and had a pre-sputter etch before AlN deposition, which allowed the film to achieve a higher crystallographic texture.

SP-490/Si: The 490 nm of sputtered AlN was deposited directly onto Si <100> wafers using an Al target and a N_2/Ar gas mixture at a chuck temperature of 300°C.

SA-487/Al$_2$O$_3$: The sputter-annealing process has been well-described by Uesugi *et al.*[71] Aluminum was reactively sputtered in a nitrogen plasma onto the sapphire substrate at temperatures higher than 1000°C. The sputtering process forms AlN columns with relatively high levels of threading dislocations. Initial rocking curves for the (102) plane in the as-sputtered films have FWHM that generally exceed 2000 arcsec. The sputtered templates are then annealed at temperatures above 1500°C for several hours, resulting in healing of dislocations and a large reduction in the FWHM value to less than 300 arcsec.

SA-394//Al$_2$O$_3$: This sputter-annealed sample with a thickness of 394 nm was prepared using DC reactive magnetron sputtering of AlN onto a sapphire substrate using a pure Al target and sputtering in argon and nitrogen. After growth, the films were annealed for 2 hours under a nitrogen overpressure at a nominal temperature of 1650°C in order to improve its structural quality as reported in reference[71].

HVPE-1083/Al$_2$O$_3$: Aluminum nitride (AlN) was grown on a c-plane sapphire substrate by HVPE. The deposition utilized a two zone inductively heated hot-wall reactor capable of temperatures exceeding 1500°C. During the process, $AlCl_3$ gas was formed in the first zone by flowing HCL in a nitrogen carrier gas over high-purity aluminum pellets, and then the $AlCl_3$ gas mixture was introduced into a high temperature zone where it impinged on the sapphire substrate in the presence of anhydrous NH_4, forming the final AlN film. This film has a low level of dislocations, with typical FWHM values less than 400 arcsec for the (102) plane, and less than 300 arcsec for the (002) plane.

MBE-413/Si: Plasma- MBE was used for growth of AlN. Aluminum was evaporated from an effusion cell and activated nitrogen was introduced from a plasma source. A high purity 100 mm <111> orientation float-zone (FZ) Si wafer (resistance 3000 Ω·cm) was used as the substrate. More details on the epitaxial growth process are available elsewhere[72].

MOCVD-967/SiC: The MOCVD-grown AlN was deposited onto a semi-insulating 4H-SiC substrate in a single deposition step at 1250°C using trimethylaluminum (TMAl) and NH_3 precursors. The properties of this material is discussed in[41].

Scanning electron microscopy (SEM) imaging

Scanning electron microscopy (SEM) was used to characterize the film microstructure.[73] Topside imaging was performed under high vacuum in a Tescan MIRA3 SEM with an Everhart-Thornley secondary electron (SE) detector.

Scanning transmission electron microscopy (STEM)

STEM samples were prepared using FIB (Thermofisher Helios Dual-beam FIB). To retain a clean and thin specimen, the surface of the STEM foils was cleaned using low-energy ion milling (Fischione Nanomill) operated at 500 eV. Both high-angle and low-angle annular dark-field (HAADF and LAADF, respectively) STEM imaging were performed using a Thermofisher aberration-corrected Titan scanning transmission electron microscope with a probe convergence half angle of 10.03 mrad at an accelerating voltage of 300 kV. The microscope is also equipped with a ChemiSTEM EDX system, which allows for the characterization of the composition of the cross-sectional STEM sample. Three chemical species (O, Al, and N) at the interface were analyzed by the EDX elemental mapping.

X-ray diffraction (XRD)

X-ray diffraction (XRD) was used to confirm the phase and orientation as well as assess the crystalline quality of the AlN films. High-resolution scans were collected using a Malvern Panalytical Materials Research Diffractometer (MRD) system in line focus mode with Cu $K_{\alpha 1}$ radiation. 2-Theta (2Θ) scans were obtained over a wide range (10-70° 2Θ) to verify the phase and identify the film and substrate peaks. The detector (PIXcel 3D; beam mask = 10 mm; divergence slit = ¼ degree) was aligned to the (002) AlN film peak at approximately 35.796° 2Θ by collecting successive omega (ω) and chi (χ) scans over progressively narrow ranges to optimize the sample tilt by maximizing intensity. A rocking curve or ω scan was collected over a range of 2.000° with a 0.005° step size and dwell time of 0.100 s. The φ-scan for (102) planes was collected over a range of 100.00° with a 0.1° step size and a dwell time of 0.100 s. Note that the range and step size were increased for the samples with a Si substrate. The full-width-at-half-maximum (FWHM) was calculated for each rocking curve, where a lower value generally implies superior crystalline quality.

Raman Spectroscopy:

To assess the crystalline quality of the AlN epitaxial films, room temperature Raman spectra were collected using a Horiba LabRAM HR Evolution spectrometer equipped with an excitation laser of 532 nm and an 1800 grooves/mm grating. A long working distance 50× objective (NA = 0.45) was used to probe the samples. According to the energy-time uncertainty principle, as the crystalline quality decreases, the linewidth of the E_2(high) phonon mode will increase because of decreased phonon lifetime. Therefore, the E_2(high) linewidth was used to qualitatively compare the crystalline quality of the AlN samples. In addition, the film residual stress was quantitatively measured with Raman spectroscopy with recently published work.[74] The peak shift in the E_2(high) mode with respect to a stress-free phonon frequency of 656.68 cm^{-1} (measured from the bulk single crystal AlN sample in **Table 4.1**) is monitored and the difference is converted to biaxial stress using a stress coefficient of -3.8 cm^{-1}/GPa.[74] The system is initially calibrated to single crystal Si peak at 520.7 cm^{-1}. A mercury emission line at ~480 cm^{-1} was used as a reference to monitor and compensate the instrument drift from error sources such as room temperature fluctuations. A low laser power ~1 mW was used to measure films on Si substrate to avoid heating in the Si due to the lower bandgap energy as compared to the laser energy (~2.33 eV).[74] The Raman peak intensity for SP-157/Si was too low to obtain meaningful results due to the low thickness of this sample.

Time Domain Thermoreflectance (TDTR):

For the cross-plane thermal conductivities of AlN films, routine TDTR measurements were taken at a modulation frequency of 9 MHz and with a larger beam spot (a 5× objective lens for sputtered films which produces a $1/e^2$ radius of 12 μm, and a 10× objective lens for epitaxial films which yields a radius of 6 μm). A smaller beam spot size was used for the epitaxial films with Au transducers because Au has a lower thermoreflectance coefficient than Al at the 780 nm[75] wavelength and thus necessitates a smaller beam spot size and higher laser powers to improve the signal amplitudes. The powers of the pump and probe beams were carefully tuned to ensure a good signal-to-noise ratio with moderate steady-state heating for all sample stacks at room temperature. The cross-plane thermal conductivities of the samples are extracted by fitting the TDTR ratio signals ($-V_{\mathrm{in}}/V_{\mathrm{out}}$) to a heat diffusion model. For in-plane thermal conductivities, beam-offset measurements were conducted at 1.51 MHz with a 20× objective lens ($1/e^2$ radius of 3 μm) to maximize the measurement sensitivity to in-plane thermal transport.[76–78] The FWHM of the out-of-phase signal (V_{out}) at -50 ps from beam-offset measurements was compared with that predicted from the heat diffusion model to determine the in-plane thermal conductivities of AlN thin films. The values of κ_z obtained from routine TDTR served as input parameters in the data reduction of in-plane beam-offset measurements.

The error bars of the in-plane thermal conductivities (κ_r) of the AlN samples were calculated based on the sensitivity analysis of the beam-offset measurements as follows:[37,77,78]

$$S_\alpha = \frac{\partial \ln(\mathrm{FWHM})}{\partial \ln(\alpha)} \tag{4.3}$$

$$\frac{\delta\kappa_\mathrm{r}}{\kappa_\mathrm{r}} = \sqrt{\sum_\alpha \left(\frac{S_\alpha}{S_{\kappa_\mathrm{r}}}\frac{\delta\alpha}{\alpha}\right)^2} \tag{4.4}$$

where FWHM is the full width at half maximum of the out-of-phase signal from the beam-offset measurements. α stands for certain parameters in the thermal model that also act as individual error sources, including the beam spot size (w_0), thicknesses (h_tran, h_AlN), heat capacities (C_tran, C_AlN, C_sub), interfacial thermal conductance (G_1 at the transducer/AlN interface and G_2 at the AlN/substrate interface), and thermal conductivities (κ_tran, through-plane κ_z of AlN, in-plane κ_r of AlN, κ_sub). Errors from parameters other than κ_r will propagate into the total uncertainty of κ_r. Representative examples for modeling parameters and their percent errors are summarized in **Table 4.4**; it should be noted that the transducers used for MOCVD-967/SiC (Al) and HVEP-1083/Al_2O_3 (Au) are different and therefore the corresponding errors in the properties vary. The sensitivity of each modeling parameter is plotted in **Figure 4.8**. The uncertainties of each modeling parameter can propagate into the fitting results for the thermal conductivity based on their corresponding sensitivity. For example, the larger in-plane thermal conductivity uncertainty of the MOCVD-967/SiC can be attributed to the larger sensitivities of the other parameters that propagates error into the fitting.

The pump laser spot sizes were large enough to capture the impacts of different scattering mechanisms for each film. For instance, the heating area is similar to the pump size (3-12 μm for TDTR), which is orders of magnitude larger than the averaged grain size (20-40 nm). At this pump radius, the impacts of dislocations are also sufficiently captured as their densities are on the order of $10^8 – 10^{11}$/cm^2.

Table 4.4: Summary of individual parameters with error sources (%) for MOCVD-967/SiC and HVPE-1083/Al$_2$O$_3$.

Sample ID	h_{tran} (nm)	h_{AlN}	C_{tran} (MJ/m^{3}K)	C_{AlN}	C_{sub}	G_1 (MW/m^{2}K)	G_2	κ_{tran} (W/mK)	κ_z of AlN	κ_{sub} (W/mK)	w_0 (μm)
MOCVD-967/SiC	71 (3%)	967.2 (3%)	2.42 (3%)	2.38 (3%)	2.21 (3%)	38 (5.6%)	200 (20%)	89.5 (3%)	122.9 (13%)	324.8 (10%)	≈3 (2%)
HVPE-1083/Al$_2$O$_3$	81.3 (1.2%)	1083 (3%)	2.46 (1.2%)	2.38 (3%)	3.03 (3%)	22 (5.4%)	400 (20%)	200 (1.2%)	96.2 (29.7%)	32.1 (12%)	≈3 (2%)

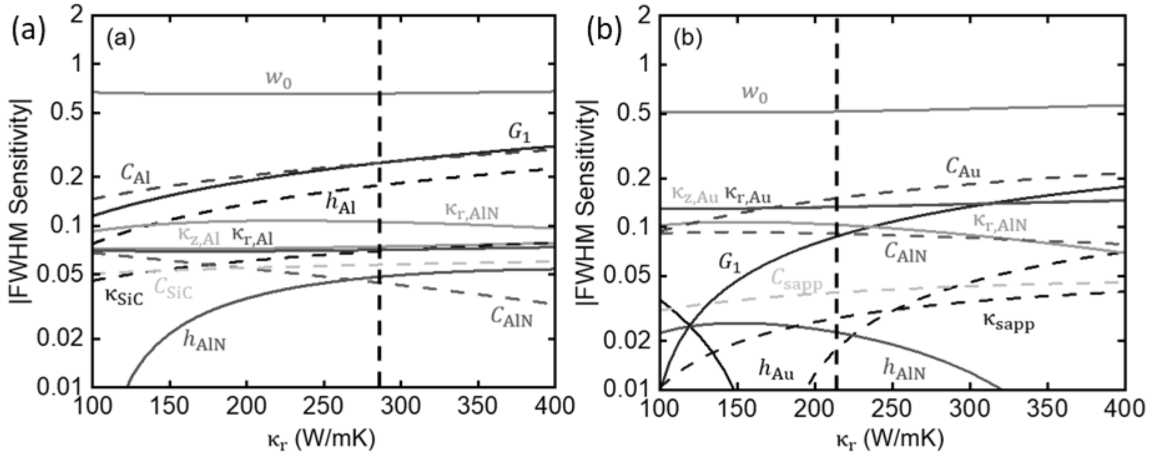

Figure 4.8. Sensitivity analyses of the beam-offset measurements to individual parameters for (a) MOCVD-967/SiC and (b) HVPE-1083/Al$_2$O$_3$.

Thermal Conductivity Measurements (FDTR):

The detailed setup of the FDTR used in this study has been described Chapter 2.2. The radius of the focused pump and probe beams were 13.4 μm and 13.1 μm, respectively. Material properties used in the FDTR fitting model were identical to those used in the TDTR model.

Thermal Conductivity Measurements (SSTR):

The detailed setup of the SSTR used in this study has been described Chapter 2.1. The radius of the focused pump and probe beams were 19.9 μm and 12.4 μm, respectively. Single crystal Si (135 W/mK) and sapphire (31 W/mK) were used as calibration samples with known thermal conductivities. SSTR is well suited for measuring the directionally averaged thermal conductivity of bulk materials and was used to characterize a single crystal bulk AlN substrate in this work. It is also possible to extract the in-plane thermal conductivity of a thin-film when the film has a much higher thermal conductivity than the substrate material, as recently demonstrated by Hoque et al.[38] A similar approach was used to extract the in-plane thermal conductivity of HVPE-1083/Al_2O_3, where the cross-plane thermal conductivity measured by TDTR was used as a known fitting parameter in the model used to extract the in-plane thermal conductivity. Measurements were performed on 3 random spots on the sample and were averaged over 30 data points at each power level.

Secondary Ion Mass Spectrometry (SIMS):

Secondary ion mass spectrometry measurements were performed using a commercial vendor (Evans Analytical Group).

THEORETICAL CALCULATIONS

The thermal conductivity is calculated via the approach described by Beechem et al.[50] The thermal conductivity is calculated with[50]:

$$\kappa = \frac{1}{6\pi^2}\sum_s \int_0^{q_{m,s}} \frac{\hbar^2\omega^2(q)}{\kappa_B T^2} \frac{\exp\left(\frac{\hbar\omega(q)}{\kappa_B T}\right)}{\left[\exp\left(\frac{\hbar\omega(q)}{\kappa_B T}\right)-1\right]^2} \nu^2(q)\tau_s(q)q^2 dq \tag{4.5}$$

where q is the wavevector, ħ is the modified Planck's constant, ω is the phonon frequency, κ_B is the Boltzmann constant, ν is the group velocity, and τ is the scattering time. All phonon branches were summed over for the Γ-A direction, representing the cross-plane thermal conductivity. The scattering term τ includes Umklapp scattering τ_U, boundary scattering, τ_B, and impurity scattering, τ_I. The impurity scattering τ_I discussed in this study is calculated based on the mass and size difference of the impurity atoms as compared to the original lattice. The mass difference for the vacancies are accounted for by assuming the mass to be double that of the missing atom.[79] The Pauling ionic radii of oxygen and aluminum were used to calculate the strain induced by oxygen substitutional defects at nitrogen sites, due to the size difference between these atoms. For other impurities, their covalent radii were used in the calculations, as the bonding characteristics of these impurities are more covalent, determined by their electronegativity. The method is adopted from reference.[56]

4.2 Thermal Conductivity of Aluminum Scandium Nitride for 5G Mobile Applications and Beyond

4.2.1 Introduction

To meet the ultra-wide bandwidth requirements for fifth-generation (5G) mobile phones,[1,80] manufacturers have recently adopted scandium aluminum nitride ($Al_{1-x}Sc_xN$; x is the Sc composition), a wurtzite-structured solid solution, as the piezoelectric in film bulk acoustic wave resonators (FBARs). The interest in replacing aluminum nitride (AlN) FBARs (used in some 4G mobile phone radio frequency (RF) duplexers) with $Al_{1-x}Sc_xN$ FBARs, originates from the enhancement of electromechanical coupling (k_t^2), which scales indirectly with the piezoelectric coefficient d_{33}. The d_{33} of $Al_{1-x}Sc_xN$ has been predicted to reach a value five times larger than that for AlN at x=0.43.[81] This dramatic enhancement of d_{33} and the CMOS process-compatibility facilitates the development of 5G mobile phone duplexers[80,82–84] with wide bandwidth[85–87] and low insertion loss[85,86]. These intrinsic advantages are, in turn, motivating significant research aimed at achieving high k_t^2 and quality factor (Q), simultaneously.

However, for an FBAR to handle the high operational frequencies of the 5G mobile network, its physical dimensions typically decrease, and higher RF input powers are required to counter signal attenuation. Higher power and smaller size translate into an increased operational heat flux. This higher heat flux, meanwhile, occurs within a solid solution ($Al_{1-x}Sc_xN$) that will have a greatly reduced thermal conductivity relative to the AlN material that it replaces. Furthermore, the FBAR structure itself is prone to overheating because the piezoelectric film is typically released from the substrate, which severely limits the thermal pathway for heat dissipation. $Al_{1-x}Sc_xN$ resonators exhibit a 50% larger resonant frequency drift with temperature rise[88] than their AlN counterparts.[89,90] Self-heating in $Al_{1-x}Sc_xN$ FBARs can, in principle, constrain the maximum transmission rate, and if allowed to proceed unchecked, may cause thermal failure.[85,90,91] Despite the thermal implications on performance, fundamental investigations of the thermal transport processes that govern heat dissipation in $Al_{1-x}Sc_xN$ remain lacking.

In response, this work reports how changes in the alloy composition, thickness, and microstructure influence the thermal conductivity of $Al_{1-x}Sc_xN$. Specifically, we measure the variation in $Al_{1-x}Sc_xN$ thermal conductivity for films synthesized via reactive sputter deposition, as a function of Sc composition, film thickness, temperature, and the concentration of abnormally oriented grains. Through this examination, the design trade-offs associated with this material, in terms of attempting to optimize both the device acousto-electric performance and the ability to dissipate heat, are identified. In particular, it is shown that several phonon scattering mechanisms associated with solid solution (i.e., phonon-alloy/disorder scattering), grain boundaries, and film surfaces drive a substantial thermal conductivity reduction relative to AlN. Device engineers must therefore grapple with the necessity of designing cooling solutions enabling the use of a low thermal conductivity material (<10 W m^{-1} K^{-1}) operating within the envelope of 5G requirements.

4.2.2 Results and Discussion

AlN and $Al_{1-x}Sc_xN$ Film Description

Polycrystalline AlN and $Al_{1-x}Sc_xN$ films with compositions of $x = 0$, 0.125, and 0.20 were deposited via reactive sputter deposition on 6” Si <100> substrates using pulsed-DC magnetron sputtering, following previous reports.[24] Deposition conditions for the $Al_{1-x}Sc_xN$ films were 5 kW of power on the single-alloy target, an Ar/N_2 gas flow of 25/125 sccm, and a platen temperature of 375°C. For AlN growth, a platen temperature of 350°C and an Ar/N_2 gas flow of 20/80 sccm were employed. The film stress was controlled using substrate bias, which applies RF power to the substrate during deposition to increase the compressive stress of the film.[92,93] The film thickness range used in this study was 50-1000 nm, while the stress ranged from −1700 MPa to −5.7 MPa. These stress values were determined via wafer curvature measurements.[94] As reported elsewhere, the density of abnormally oriented grains (AOGs) tended to be lower in films with higher substrate bias.[95]

Figure 4.9 shows representative transmission microscopy (TEM) and scanning electron microscopy images. As shown in **Figure 4.9 (b)**, the columnar grain size of the c-axis textured AlN and $Al_{1-x}Sc_xN$ films were approximately 35 nm across in all samples. The AOGs observed in the $Al_{1-x}Sc_xN$ films had lateral sizes of 50-250 nm. The degree of c-axis orientation was characterized with X-ray diffraction (XRD) by measuring the rocking curve of the {0002} reflection of the $Al_{1-x}Sc_xN$ film. Correlation between the rocking curve measurement of various AlN films and the electromechanical coupling coefficient (k_t^2) has shown that films with smaller rocking curve linewidths (full width at half-maximum, FWHM) exhibit high k_t^2.[96] Therefore, $Al_{1-x}Sc_xN$ films with rocking curve measurements $\leq 2°$ should be used to achieve high k_t^2.[97] In this study, films with a thickness greater than 400 nm showed a FWHM less than 2°.

The presence of abnormally oriented grains (AOGs) lowers the crystallographic texture of $Al_{1-x}Sc_xN$ films. **Figure 4.9 (c)** illustrates AOGs on $Al_{0.8}Sc_{0.2}N$ film that protrude out of the c-axis oriented matrix. As shown in the electron backscattering diffraction (EBSD) data (**Figure 4.9 (e)**) of **Figure 4.9 (d)**, for an $Al_{0.8}Sc_{0.2}N$ film with a high density of AOGs, there is no preferred orientation for the AOGs.

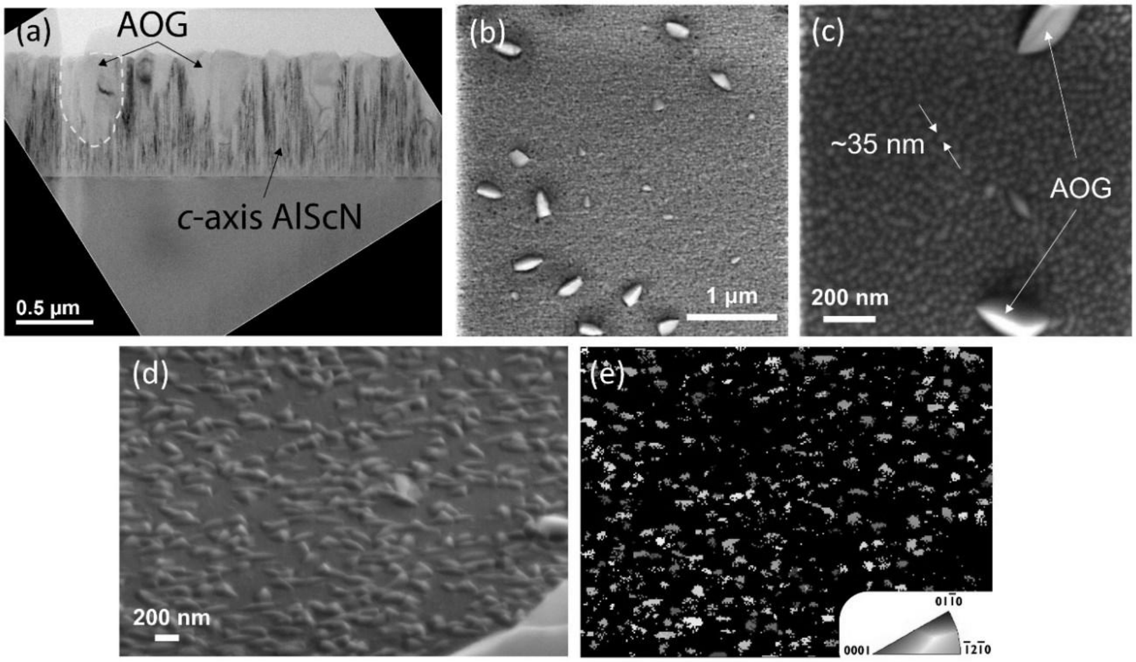

Figure 4.9. (a) TEM cross-section of an $Al_{0.875}Sc_{0.125}N$ film showing AOGs and their propagation through the film thickness. (b) 75k× and (c) 200 k× plan-view SEM images of an $Al_{0.8}Sc_{0.2}N$ film showing the primary c-axis oriented grain structure as well as AOGs. (d) A 750-nm thick $Al_{0.8}Sc_{0.2}N$ film with a high density of AOGs, and (e) an inverse-pole figure, gathered from EBSD, that maps the orientation of AOGs from the film normal direction (Z-direction). EBSD results show no strong preferred orientation for the AOGs.

Raman spectroscopy was employed to qualitatively assess changes in the phonon energies and scattering rates that were induced with the incorporation of scandium. Using this approach, **Figure 4.10 (a)** presents the difference Raman spectra between the Si wafer coated with $Al_{1-x}Sc_xN$ and the bare Si substrate where modes associated with the E_2 (high) (635-660 cm^{-1}) and A_1(LO) (825-850 cm^{-1}) of $Al_{1-x}Sc_xN$ are clearly observed. The incorporation of scandium causes a redshift and broadening of the Raman modes indicating a softening of the lattice and an increased scattering rate of the optical phonons. Each change is associated with a reduction in thermal conductivity. Softening, for example, is seen in the redshift of the E_2 (high) and A_1 (LO) mode peak positions to lower wavenumbers with additional Sc content (**Figure 4.10 (a)**). **Figure 4.10 (b) and (c)** quantify the concentration dependent shift, which is similar to those reported previously by Deng et al,[98] and Mock et al.[99] Phenomenologically, Sc incorporation promotes softening because the average atomic mass of the oscillators increases and the bond covalency drops.[98] Both effects reduce thermal conductivity.

The scattering rate of the optical modes increases with Sc-content as well, as is indicated by the broadening of the Raman modes in **Figure 4.10 (a)** with additional scandium. Quantitatively, as shown in **Table 4.5**, the linewidth of the E_2 (high) mode increases with increasing Sc content from 15.6 cm^{-1} for AlN to 61.5 cm^{-1} for $Al_{0.8}Sc_{0.2}N$. This suggests much more disruption in the period potential due to solid solution. Owing to the time-uncertainty relation[100], in which scattering time is inversely proportional to FWHM, this implies a reduction of the scattering time of the optical phonon modes by a factor of nearly 4. Reductions in the scattering time of phonons, in turn, imply a lessening in the thermal conductivity.

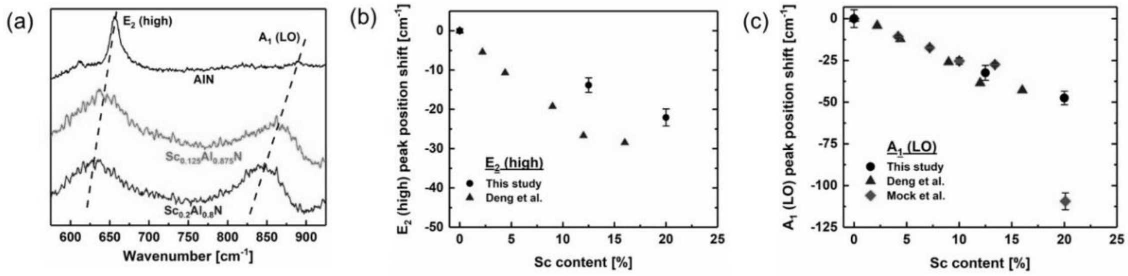

Figure 4.10. (a) Background subtracted Raman spectra of AlN, $Sc_{0.125}Al_{0.875}N$, and $Sc_{0.2}Al_{0.8}N$ films. The dashed lines qualitatively show the redshift of the E_2 (high) and A_1 (LO) modes as the Sc content in the films is increased. (b) Shift of the E_2 (high) phonon frequency (peak position) as a function of Sc content from this study and Deng et al.[98] (c) Shift of the A_1 (LO) phonon frequency as a function of Sc content from this study, Deng et al.,[98] and Mock et al.[99]

Table 4.5. Peak position and linewidth (FWHM) of the E_2 (high) phonon mode of $Al_{1-x}Sc_xN$ films with ~730-820 nm thicknesses. Data reported in this study[a)] were based on an average of 100 measurements.

Sc content [%]	0 (AlN)	12.5	20
Peak position [cm^{-1}]	657.1 ± 0.4[a)] 658[b)] 657[c)]	643.2 ± 1.8[a)] 628.9[b)]	635 ± 2.1[a)] 611.4[b)]
FWHM [cm^{-1}]	15.6[a)]	52.3[a)]	61.5[a)]

[a)] This study

[b)] Calculated using linear fit parameters reported by Deng et al[98]

[c)] Value reported for unstrained AlN at 300 K[101]

Thermal Characterization Results

Thermal conductivity measurements of c-axis textured AlN and $Al_{1-x}Sc_xN$ films with various Sc compositions (x=0.125, 0.2) and two different thicknesses (~110 nm and ~760 nm) were performed using time-domain thermoreflectance (TDTR)[35] and frequency-domain thermoreflectance (FDTR) techniques[102]. This cross-validation was conducted to rule out potential sources of error and reduce uncertainty due to the complementary sensitivities of the two techniques.[103]

As shown in **Figure 4.11**, for $Al_{1-x}Sc_xN$ with x=0.125 and 0.2 and a film thickness of ~760 nm, the measured cross-plane thermal conductivities (κ) were ~7.4 $W\,m^{-1}\,K^{-1}$ and ~4.8 $W\,m^{-1}\,K^{-1}$, respectively (the actual thicknesses for the AlN, $Al_{0.875}Sc_{0.125}N$, $Al_{0.8}Sc_{0.2}N$ films are 733 nm, 765 nm, and 816 nm, respectively, as measured by spectroscopic ellipsometry). These values are an order of magnitude lower than that for the AlN film with a similar thickness and microstructure (~51 $W\,m^{-1}\,K^{-1}$), and two orders of magnitude lower than a single-crystal epitaxial film of AlN (~320 $W\,m^{-1}\,K^{-1}$)[29]. It should be noted that the average columnar (lateral) grain size resulting from the reactive sputter deposition process[95,104] was consistent (~35 nm; **Figure 4.9 (c)**) among all the AlN and $Al_{1-x}Sc_xN$ films investigated in this work. Consequently, from a practical perspective, the reduction in thermal conductivity underscores the intrinsic trade-off between piezoelectric and thermal performance in the $Al_{1-x}Sc_xN$ solid solution.

This large reduction in κ in moving from AlN to $Al_{1-x}Sc_xN$ films is attributed to increased phonon scattering that is primarily due to phonon-alloy disorder scattering[105]. The significantly increased phonon scattering rate is also manifested by the broadening of the linewidth of the Raman active phonon modes of the $Al_{0.875}Sc_{0.125}N$ and $Al_{0.8}Sc_{0.2}N$ films compared to those for AlN as shown in **Figure 4.10** and **Table 4.5**.[101,106]

Alloying has an acute effect on the κ of $Al_{1-x}Sc_xN$ because of the lattice disruption associated with alloying AlN (wurtzite) with ScN (rocksalt). To quantify, the κ of $Al_{0.8}Sc_{0.2}N$ (~4.8 W m^{-1} K^{-1}) is ~36% lower than $Al_{0.875}Sc_{0.125}N$ (~7.4 W m^{-1} K^{-1}) for films with a thickness of ~760 nm. In contrast, previous work examining the wurtzite phase isostructural alloy $Al_{1-x}Ga_xN$ with identical characterization methods found that a similar reduction in κ (35%) required a much larger variation in composition from x~0.1 to ~0.5.[107] Mechanistically, the large reduction in the κ of $Al_{1-x}Sc_xN$ as compared to $Al_{1-x}Ga_xN$ can be attributed to the evolution in bond characteristics[108] of the solid solution with increasing x. Increasing x in $Al_{1-x}Sc_xN$ solid solutions results in an increased displacement of the Al/Sc atoms along the c-axis.[108] This results in a reduction of the elastic stiffness constant C_{33} and a nonlinear enhancement of the piezoelectric stress constant e_{33}.[82,109] Accordingly, as Sc content approaches the critical concentration x_c at which phase separation occurs, significant increases are observed in both the piezoelectric modulus d_{33} ($\sim e_{33}/C_{33}$) and the electromechanical coupling coefficient k_t^2 ($= e_{33}^2/[(C_{33} + e_{33}^2/\varepsilon_{33})\varepsilon_{33}]$.[82] The lattice softening[89] with increasing x lowers the group velocities of the acoustic phonons that dominate κ. Thus, it is anticipated that $Al_{1-x}Sc_xN$ (in the wurtzite phase) will continue to exhibit a nonlinear reduction in κ as x approaches x_c, whereas d_{33} is maximized.

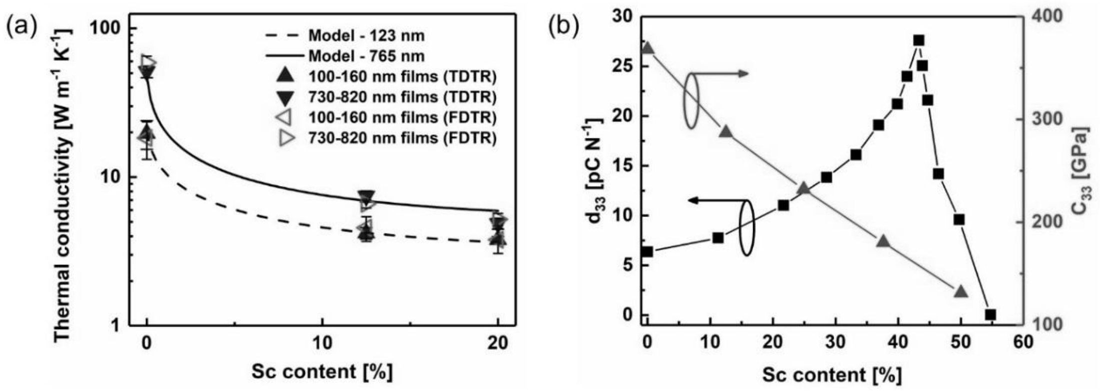

Figure 4.11. (a) The compositional dependence of $Al_{1-x}Sc_xN$ thermal conductivity obtained from time/frequency domain thermoreflectance (TDTR/FDTR) measurements and virtual crystal approximation (VCA) simulation (to be discussed in the "Thermal Modeling Results" section). (b) The evolution of the piezoelectric modulus d_{33} (from reference[110]) and elastic stiffness constant C_{33} (from reference[109]).

Despite being dominated by alloy scattering, size effects are also evident in the thermal response of the $Al_{1-x}Sc_xN$. In **Figure 4.11 (a)**, κ is observed to decrease over all Sc compositions as the thickness of the films decreases from ~760 nm to ~110 nm (the actual thicknesses for the AlN, $Al_{0.875}Sc_{0.125}N$, $Al_{0.8}Sc_{0.2}N$ films are 157 nm, 107 nm, and 105 nm, respectively). When the film thickness of a crystallites becomes comparable to the mean free path of phonons, incoherent phonon-boundary scattering will impact κ.[111,112] Since these are sputtered films, it is also speculated that the first 20-50 nm of the film where the c-axis growth has not completely taken over may be partly responsible for the observed thickness-dependence of the κ.

Recognizing that film thickness is a main design parameter that determines the resonant frequency of FBARs,[113,114] the film thickness effect[111,112] on the thermal conductivity of $Al_{1-x}Sc_xN$ was investigated in more detail via TDTR measurements to better understand the trends observed in **Figure 4.11 (a)**. For this reason, a series of $Al_{1-x}Sc_xN$ films with a thickness range of 50 –1,000 nm at a fixed composition ($x = 0.2$) and consistent lateral grain size (~35 nm) were synthesized. **Figure 4.12 (a)** shows a noticeable thickness dependence of the cross-plane κ for these $Al_{0.8}Sc_{0.2}N$ films; specifically, κ plateaus for film thicknesses > 400 nm and decreases with decreasing thicknesses < 400 nm. The turnover in κ near 400 nm in **Figure 4.12 (a)** implies that there is an appreciable amount of heat being carried by phonons with mean free paths on this order.[115] As the thickness of the films drops below 400 nm, these phonons begin to scatter at the boundaries with increasing frequency, leading to a continuing reduction in κ as the thickness decreases further. On the other hand, the compositional disorder and grain boundaries reduce κ via scattering of shorter wavelength phonons. Thermal management strategies will therefore be necessary when sub-micron thickness films are integrated into FBAR structures to realize GHz-range resonators.[116]

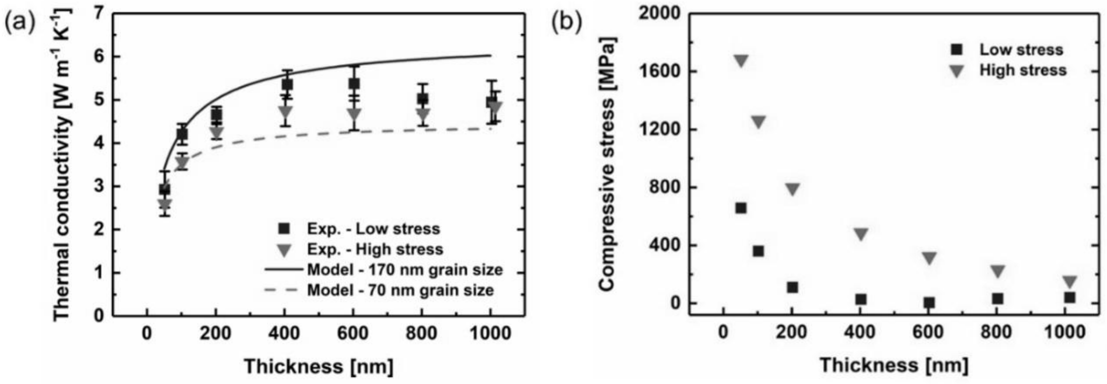

Figure 4.12. (a) The thickness dependence of the thermal conductivity of $Al_{0.8}Sc_{0.2}N$ films. (b) The residual stress in the two series of the $Al_{0.8}Sc_{0.2}N$ films (low stress vs. high stress), as a function of layer thickness (to be discussed in the "Thermal Modeling Results" section).

The implicit nature of thermal effects is further underscored by examining the temperature dependent thermal conductivity of the thicker $Al_{0.875}Sc_{0.125}N$, and $Al_{0.8}Sc_{0.2}N$ films (765 nm and 816 nm thick, respectively) over an ambient temperature range of 100 – 450 K, along with data from 300 – 450 K for the 733 nm AlN film (**Figure 4.13**). Like most crystalline solids, as the temperature is increased beyond 300 K, the thermal conductivity of AlN monotonically decreases because more frequent Umklapp scattering processes[117] cause the phonon mean free paths, and thus the thermal conductivity, to decrease. In contrast, a negligible reduction in κ with increasing temperature is observed for the $Al_{0.875}Sc_{0.125}N$ and $Al_{0.8}Sc_{0.2}N$ films, as shown in TDTR measurement results listed in **Figure 4.13.** A similar trend was found in previous work on $Al_{1-x}Ga_xN$ films with $x = 0.3$ and 0.7.[107]

Given that these temperatures are well below the Debye temperatures of the two constitutive materials,[118,119] the saturation of κ indicates that the increase in heat capacity is balanced – but not overwhelmed by increases in scattering – with temperature. This, in turn, suggests that heat transport is not being dominated by phonon-phonon (i.e., Umklapp) scattering but instead other scattering mechanisms including those discussed so far (grain boundary, film surface, alloy-disorder scattering, etc.).

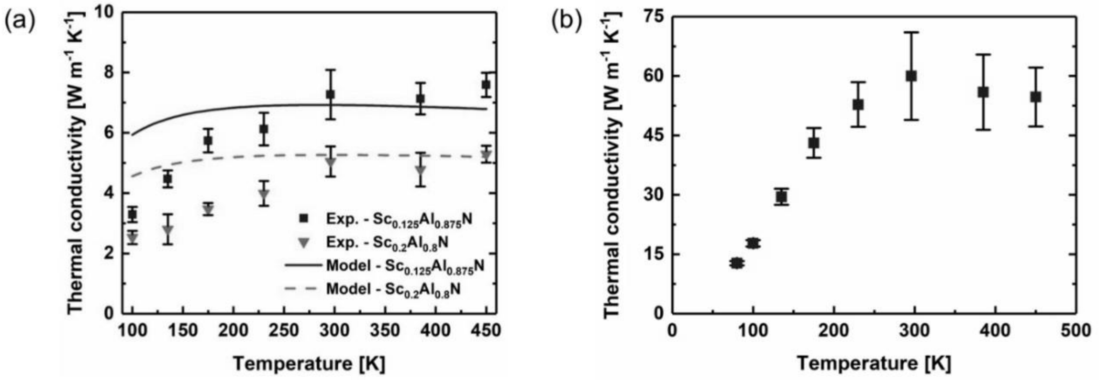

Figure 4.13. (a) The temperature dependent thermal conductivity of the ~760 nm thick $Al_{1-x}Sc_xN$ ($x = 0.125$ and 0.2) films. (b) Also shown is the AlN film thermal conductivity as a function of temperature.

Finally, thermal conductivity was examined as the $Al_{1-x}Sc_xN$ microstructure was purposely varied by intentionally varying abnormally oriented grain (AOG)[120] densities for films having a fixed composition (x=0.2) and thickness (~760 nm). Control of AOG density was realized through incomplete conditioning of the target and chamber combined with incomplete purging of the deposition chamber and load lock. This process keeps the reactive sputter deposition[121] conditions constant while varying the AOG density.[95,108,110] The inclusion of AOGs in $Al_xSc_{1-x}N$ films can dramatically increase the surface roughness in $Al_xSc_{1-x}N$ materials with high Sc content, thus potentially lowering the Q factor of RF MEMS resonators. Recent reports in literature demonstrate the significance of the microstructural quality of the base $Al_{1-x}Sc_xN$ film. For example, BAW resonators realized in nearly AOG-free $Al_{0.72}Sc_{0.28}N$ films have exhibited an effective k_t^2 of 16% and a Q_{max} of 1070 at 3.5 GHz.[122]

The effect of the AOG's is minimal, however, from a thermal perspective. The cross-plane κ is only minimally impacted by the density of AOG's as shown in **Figure 4.14**. The κ of $Al_{0.8}Sc_{0.2}N$ films with varying levels of AOGs were measured using TDTR at room temperature. The qualitative number density of the AOGs is shown in the scanning electron microscopy (SEM) images (insets) in **Figure 4.14**. Despite the fact that the characteristic size of the individual AOGs is on the order of hundreds of nanometers, their density within the majority of the $Al_{1-x}Sc_xN$ matrix remains relatively low. As a result, the rate at which phonons scatter with these AOG interfaces does not impede the total flow of heat carriers to a greater extent than the other scattering mechanisms present. That is, the overall cross-plane κ of the $Al_{1-x}Sc_xN$ films is relatively invariant to the AOG number density. Consequently, while the presence of AOGs in $Al_{1-x}Sc_xN$ is critical for optimizing the electro-acoustic performance of RF MEMS resonators, their impact on thermal transport is observed to be minimal for AOG densities that are low enough to allow the films to be piezoelectrically functional. Scattering mechanisms associated with alloying[105] and the fine crystallite structures (lateral grains; ~35 nm)[32,123] of the c-axis textured films dominate (i.e., restrict) the κ. To this end, reduction of the abnormally oriented grain density should not be expected to improve the material's thermal conductivity. However, lower insertion loss associated with minimizing AOG density will result in lower power dissipation within the resonator. Therefore, films with low AOG density will be still beneficial in terms of enhancing the device thermal performance.

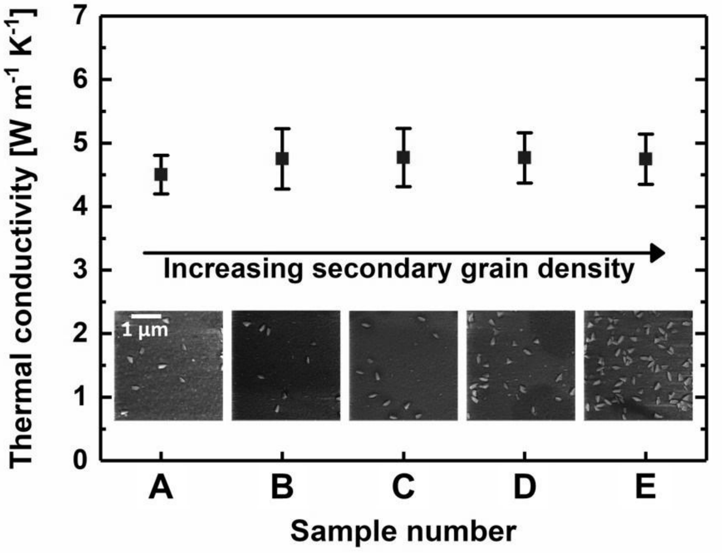

Figure 4.14. The thermal conductivity of $Al_{0.8}Sc_{0.2}N$ films with varying levels of AOG density. The insets are 75k× SEM images that qualitatively show the increasing AOG density as moving to the right of the x-axis.

A computational study was performed to understand the physical mechanisms driving the FBAR design trade-offs, as they relate to thermal transport, recognizing that composition[105], film thickness[111,112], and the fine lateral grain size[32] each contribute to the reduction in the thermal conductivity of $Al_{1-x}Sc_xN$ with respect to the base AlN ($x = 0$) and ScN ($x = 1$) crystals. Ultimately, it was found that the transport mechanisms in these textured (one-dimensionally oriented) films differ from other epitaxial (i.e., 3-dimensionally oriented) isostructural wide bandgap alloys such as $Al_xGa_{1-x}N$ films.[107] This is because the sputter growth conditions employed lead to close-packed vertically aligned columnar grains which play a significant role in the behavior of phonons and in turn thickness, temperature, and composition trends of the measured thermal conductivity.

In the previous section, thermal conductivity measurements were performed as a function of ScN composition, film thickness, temperature, and AOG density. These results were analyzed under the paradigm of the phonon gas model leveraging the virtual crystal approximation (VCA)[124,125], to assess the comparative importance of the relevant scattering effects on the thermal conductivity of $Al_{1-x}Sc_xN$. The model is in no way prescriptive as the phonon gas model is itself questionable when examining solid solutions.[126] However, it is used here to compare various effects owing to its ease of implementation in a way consistent with decades of previous research.[127]

Practically, the thermal conductivity was modeled using the k-space phonon gas model,

$$\mathrm{\kappa} = \sum_j \int_0^{\frac{\pi}{a_{\mathrm{eff}}}} \frac{\hbar \omega_j(k)}{6\pi^2} \frac{df(\omega_j(k), T)}{dT} \tau(\omega_j(k), T) v_j^2(k) k^2 dk \tag{4.6}$$

where ω is the angular frequency, k is the wave vector, a_{eff} is Debye lattice constant, $\hbar$ is the Planck's constant divided by 2π, k_B is the Boltzmann constant, T is the temperature, v is the group velocity, df/dT is the temperature derivative of the Bose-Einstein distribution and the summation is over the j-dispersion branches. The effective lattice constant, a_{eff}, was calculated by assuming a spherical unit cell where the volume of the sphere is equal to the volume of the real unit cell. Since the measured cross-plane κ is dominated by energy transport along the c-axis, a_{eff} was assumed to be equal to the c lattice constant (0.498 nm). The total scattering rate, $1/\tau$, was calculated using Matthiessen's rule to sum the contributions from Umklapp scattering, $\frac{1}{\tau_U} = B\omega^2 \exp(-C/T)$, intrinsic impurity scattering, $\frac{1}{\tau_I} = A_0\omega^4$, alloy scattering, $\frac{1}{\tau_A} = x(1-x)A\omega^4$, boundary scattering, $\frac{1}{\tau_B} = \frac{v}{d_{\mathrm{film}}}$, and grain boundary scattering, $\frac{1}{\tau_G} = \frac{v}{d_{grain}}$, where x is the ScN fraction, $\mathrm{d_{film}}$ is the film thickness and d_{grain} is the effective grain size. Deduced scattering rate coefficients are presented in Table 2.

This model assumes that the dispersion, thermal conductivity, and grain geometries are isotropic. The impact of these assumptions will be discussed in more detail later. Previous studies have shown that dispersion assumptions can have significant effects on thermal predictions.[128,129] Therefore, a full dispersion was used in the model.[130] However, since AlN and ScN possess different crystal structures, wurtzite and rocksalt, it is not possible to average the dispersions in examining the solid solution. Instead, AlN was assumed to act as a host material for Sc impurities. This approximation has shown to be valid when modeling $Al_{1-x}Sc_xN$ optical properties up to $Al_{0.8}Sc_{0.2}N$.[99] However, the elastic constant, C_{33}, significantly softens with alloying, as shown in **Figure 4.11**, leading to significant changes in the maximum phonon frequency and sound speed. This was accounted for by scaling the dispersion, and in turn the velocities, using the ratio of longitudinal velocities predicted from the elastic constants plotted in **Figure 4.11**,

$$\frac{v_L(x)}{v_L(0)} = \sqrt{\frac{C_{33}(x)\rho(0)}{C_{33}(0)\rho(x)}} \tag{4.7}$$

where, $v_L(x)$ and $\rho(x)$ are the composition-dependent longitudinal velocity and density, respectively. The mass density $\rho(x)$ of $Al_{1-x}Sc_xN$ was calculated based on the unit cell volume (V) and the molecular weight (M) as a function of the Sc composition, x. The lattice parameters of the wurtzite $Al_{1-x}Sc_xN$ have been reported in reference[131] and the corresponding a and c values for x = 0, 0.125, and 0.2 were extracted via linear interpolation to calculate the unit cell volume. The molecular weight of $Al_{1-x}Sc_xN$ is calculated as $M = xM_{ScN} + (1-x)M_{AlN}$. Finally, the density is calculated using:

$$\rho(x) = \frac{\mathrm{Z}\mathrm{M}(x)}{\mathrm{N}V} \tag{4.8}$$

where Z is the number of molecules per unit cell, and N is Avogadro's number. The calculated mass density of $Al_{1-x}Sc_xN$ were 3.24, 3.28, 3.31, and 4.24 g/cm^3 for x=0, 0.125, 0.2, and 1, respectively. It should be noted that experimentally determined ρ_{AlN} and ρ_{ScN} are 3.23 g/cm^3 [132] and 4.25 g/cm^3[133], respectively.

Umklapp and intrinsic impurity scattering coefficients were determined by fitting the model to previously reported temperature dependent AlN thermal conductivity.[31] The AlN films investigated in this work are composed of vertically oriented columnar nano-grains as shown in **Figure 4.9 (a)-(c)**. The grain boundaries significantly increase scattering, causing these films to exhibit a much lower thermal conductivity than epitaxial AlN[31]. The effective grain size was, therefore, deduced by adjusting the model to fit experimental measurements of this work. This resulted in an effective grain diameter of 70-170 nm, which is much larger than the measured 35 nm. However, the overprediction is consistent since the grains are columnar with a 35 nm diameter and lengths equal to the film thickness (50-1000 nm) and Equation (1) assumes isotropic/spherical grains, making the effective grain size larger than the grain diameter. The alloy scattering coefficient was then determined by fitting to the composition-dependent data. The alloy scattering term was forced to be constant between both the thickness and composition series of the $Al_{1-x}Sc_xN$ films. The impact of AOG scattering was neglected since no AOG density dependence was found as shown in **Figure 4.14**.

Table 4.6. The scattering coefficients obtained by fitting the VCA model with experimental data.

Scattering coefficient	Value	Units
B	1.22×10^{-19}	s
C	290	K
A_0	4×10^{-47}	s^3
A	5.5×10^{-42}	s^3

Figure 4.11 (a) plots the composition-dependent model for two film thicknesses (d_{film}= ~125 and ~750 nm) along with experimental results. It was not possible to fit the composition trend of both thicknesses simultaneously. This is because the effective grain size is not constant with film thickness. As the thickness of the films increases, so does the height of the columnar grains (not the lateral grain diameter), leading to an increase in the effective isotropic grain diameter, d_{grain} (it should be noted that the TDTR and FDTR experiments probed the cross-plane κ values). Therefore, the model predictions shown are for two different grain sizes (d_{grain} = 70 and 170 nm) in the thin (d_{film}=125 nm) and thick (d_{film}=750 nm) composition series which fit the experimental results well.

The effect of changing isotropic grain size with film thickness is observed in the thickness-dependent data. **Figure 4.12 (a)** plots the film thickness dependence of the κ of $Al_{0.8}Sc_{0.2}N$ films. Below 400 nm thickness, the κ rapidly rises due to boundary scattering of the finite thickness film. Above 400 nm, the conductivity plateaus and becomes thickness independent. It should be noted that for epitaxial GaN films, the thickness dependence was shown to extend into tens of micron thicknesses where the film becomes bulk.[40] The low thickness plateau in this case originates from the grain boundaries taking over as the dominant scattering mechanism for long wavelength, long mean free path phonons (i.e., Debye like acoustic modes).

The model is plotted for the two grain sizes (d_{grain} = 70 and 170 nm) used in the composition data to show the impact of grain boundary scattering (**Figure 4.12 (a)**). The two grain sizes plotted bound the data above 100 nm thickness since the low film thicknesses have small effective grains. However, as the film thickness increases the grain length and effective size increases and approaches the 170 nm limit. This hypothesis is further supported since the 50 nm thick films fall below the bound indicating the effective grain sizes in this case are smaller than 70 nm.

Additionally, **Figure 4.12 (a)** suggests that the effective grain sizes of the anomalous composition data point, thick $Al_{0.8}Sc_{0.2}N$ in **Figure 4.11**, is smaller than the rest of that series. The thickness-dependent plot is for the 20% ScN composition, which was shown in **Figure 4.11** to not be predicted by the composition trend. Many of the films with thicknesses near 750 nm fall between the 70 and 170 nm bound in **Figure 4.12 (a)** indicating a true effective grain size closer to 115 nm. This may suggest that grain size has some composition dependence therefore 115 nm grain size was used in the temperature plot of the $Al_{0.8}Sc_{0.2}N$ in **Figure 4.13**.

In addition to the thickness dependence, two sets of data are plotted in **Figure 4.12 (a)** to show the effect of residual film stress. The two sets were grown with different substrate bias leading to a film set with high levels of compressive stress, and a film set with lower levels of compressive stress (**Figure 4.12 (b)**). It should be noted that a higher substrate bias leads to films with higher levels of compressive residual stress. These stress values were determined via wafer curvature measurements.[94] Consistently, the films with lower stress have a higher κ. Currently, it is unclear by what mechanism stress impacts thermal conductivity. There are multiple potential ways in which there could be coupling between the average stress state of the film and thermal conductivity. These will be discussed in more detail in a follow-on publication but are introduced briefly here. First, a compressive biaxial in-plane stress could lead to either a change in the N–Al–N bond angle and/or increased out-of-plane (cross-plane) bond length.[134] These factors, in turn, reduce group velocities and increase anharmonicities, resulting in a reduced cross-plane thermal conductivity. Second, changes in stress are often accompanied by changes in the film microstructure. This in turn affects the contribution of grain scattering to the effective phonon mean free path. Third, under energetic bombardment conditions associated with sputter growth (especially with a biased substrate), atomic peening can induce densification of grain boundaries, embed sputter gas atoms, and induce point defects.[135] The latter two would be expected to degrade crystallinity and hence thermal conductivity. Furthermore, if the deposition rate is altered by the factors that influenced the stress state, it should be noted that as the growth rate rises, the concentration of defects also tends to increase. Fourth, it is possible that differences in growth conditions change the propensity for chemical segregation of Al and Sc, which would also modulate the thermal conductivity.

Lastly, the temperature-dependent thermal conductivity for two alloy compositions is plotted in **Figure 4.13**. The thermal conductivity has positive temperature trends until 300 K for both compositions. The VCA model (based on the phonon gas model) on the other hand predicts a temperature-independent trend above 150 K. First, it should be noted that the experiments were performed under a temperature range below the Debye temperature of $Al_{0.8}Sc_{0.2}N$.[118,119] Therefore, the competing effects of the increase in both heat capacity and Umklapp scattering rate with temperature are influencing the thermal conductivity. Second, this might indicate a strong thermal conductivity contribution from highly localized modes as has been predicted for $In_xGa_{1-x}As$.[126] Third, this trend can be influenced by the grain structure. The films studied in this work are not epitaxial (three-dimensionally oriented) but rather textured (one-dimensionally oriented). We speculate that our model does not properly account for phonon dispersion and scattering associated with the one-dimensional nature[95,128,136,137] of the columnar grains since we assumed an isotropic dispersion, thermal conductivity, and grain geometry.

In summary, the thermal conductivity of $Al_{1-x}Sc_xN$ films can be reasonably predicted by the phonon gas model with the typical alloy, boundary, and phonon-phonon scattering terms. However, its anisotropic grain structure changes with thickness and possibly stress, among other factors, complicating the phonon physics. Therefore, a more rigorous model for these films needs to be developed, in order to properly describe the anisotropic phonon transport and accurately predict thermal conductivity.

4.2.3 Conclusion

This work investigated the physics of thermal transport that governs the thermal conductivity of $Al_{1-x}Sc_xN$, a fundamental building block for 5G RF microelectromechanical systems (MEMS). The thermal conductivities of c-axis textured $Al_{1-x}Sc_xN$ films were found to be one order of magnitude lower than similarly textured polycrystalline AlN films and two orders of magnitude lower than single crystal and/or bulk AlN. This abrupt reduction of thermal conductivity with the incorporation of Sc atoms into the AlN crystal can be understood in terms of phonon-alloy/disorder scattering, in the context of the phonon gas theory. Increasing the Sc composition results in a further decrease in the thermal conductivity due to structural frustration and lattice softening, which is an effect absent in isomorphs such as $Al_{1-x}Ga_xN$. A relatively strong film thickness dependence of the thermal conductivity was observed for the $Al_{1-x}Sc_xN$ films. The $Al_{1-x}Sc_xN$ exhibited a weak temperature dependence beyond room temperature and 450 K. The impact of abnormally oriented grains on the cross-plane thermal conductivity was found to be negligible for the piezoelectrically functional $Al_{1-x}Sc_xN$ films tested in this work.

Outcomes of this work support the necessity of electro-thermo-mechanical co-design of 5G $Al_{1-x}Sc_xN$-based RF acoustic filters. From a thermal standpoint, for $Al_{1-x}Sc_xN$-based bulk acoustic wave (BAW) filters, the solidly mounted resonator (SAW) configuration would be preferred over the FBAR (free-standing membrane) configuration due to the poor thermal conductivity of $Al_{1-x}Sc_xN$. The thermal property data set generated in this work reveals design trade-offs for (i) increasing the Sc composition of $Al_{1-x}Sc_xN$ to maximize the electromechanical coupling factor, (ii) decreasing the film thickness to achieve higher GHz-range resonance frequencies, (iii) higher operating temperatures resulting from higher integration density and RF input powers. The thermal conductivity data will allow the construction of multi-physics device models that will enable the design and development of $Al_{1-x}Sc_xN$ RF filter technologies with enhanced device performance and improved lifetime.

4.2.4 Experimental Methods

Film thickness measurement:

Spectroscopic ellipsometry (Woollam M-2000F Focused Beam) was used to measure the thickness of the $Al_{1-x}Sc_xN$ thin films grown on n-type Si (100) substrates. The data were collected in the form of Psi (Ψ) and Delta (Δ) functions versus wavelength at a fixed angle of incidence of 65°. The three models were used for each $Al_{1-x}Sc_xN$/native SiO_2/Si structured layers, respectively. The ellipsometry measurements were performed in air at room temperature using a wavelength range of 300 nm to 1000 nm.

Scanning electron microscopy imaging:

Scanning electron microscopy (SEM) was used to characterize the film microstructure.[73] Imaging was done in a MIRA3 (TESCAN USA Inc.) at a working distance of 3 mm and an accelerating voltage of 3 kV to reduce charging. The secondary electrons were collected by the Everhart-Thornley detector. The images were taken at several magnifications, providing a field of view on the sample ranging from 1 to 4 microns. Within these ranges the microstructure of $Al_{1-x}Sc_xN$ became visible, revealing an oriented grain structure. These grains were measured to be approximately 35 nm across all samples. Some misoriented grains (AOGs) were observed, with lateral sizes of 50-250 nm.

Raman Spectroscopy:

Raman spectroscopy was used to characterize changes optical phonon energies and scattering times with scandium content. All measurements were performed at room temperature using an alpha300R WiTec Raman system employing a 488 nm laser that was focused to a diffraction limited spot by a 100X/0.95 NA laser in a $z(x-)\bar{z}$ scattering geometry. Raman scattered light was dispersed on a 2400 gr/mm grating resulting that provided a spectral accuracy <0.5 cm^{-1}. To minimize laser heating of the Si substrate, a laser power of 2 mW was used and representative sampling achieved by taking 100 separate spectra evenly spaced over a 100 μm linescan. No significant variation across the film surface was observed. Spectra provided are the composite average of the ensemble of all acquisitions.

Thermal Conductivity Measurements (TDTR):

Gold (Au) thin films were deposited as transducers via electron-beam evaporation, and the thickness of the film (81.25 nm) was confirmed via x-ray reflection (XRR) measurements on an Al_2O_3 witness sample. The diameters of the focused pump and probe beams were characterized using a scanning-slit optical beam profiler (Thorlabs BP209-VIS) and were 14 μm and 9 μm, respectively. Note that these beam sizes are much larger than any lateral variations in the films due to texturing or the presence of AOG's. Literature values were used for the thermal conductivity of Au and Si,[138] as well as volumetric heat capacities (C_V) of Au[139], AlN[140], ScN[119], and Si[141], where the value of C_V for a particular alloy composition was approximated as a weighted average of the constitutive materials. Fitting of the thermal boundary conductance (TBC) (between the metal transducer and the $Al_{1-x}Sc_xN$ film) and the $Al_{1-x}Sc_xN$ thermal conductivity was performed simultaneously for all samples. As shown in **Figure 4.15**, the TBC between the $Al_{1-x}Sc_xN$ film and the Si substrate has little impact on the resulting $Al_{1-x}Sc_xN$ thermal conductivity due to the low measurement sensitivity to this parameter. Measurements were performed on at least three different locations for each sample to account for errors associated with the laser focusing, pump and probe alignment, and potential local variation of the material. The uncertainty was calculated based on 95% confidence bounds for the measurements and a ±2 nm uncertainty in the metal transducer thickness. An identical approach for measurement, fitting, and uncertainty analysis was used in the FDTR experiments described below.

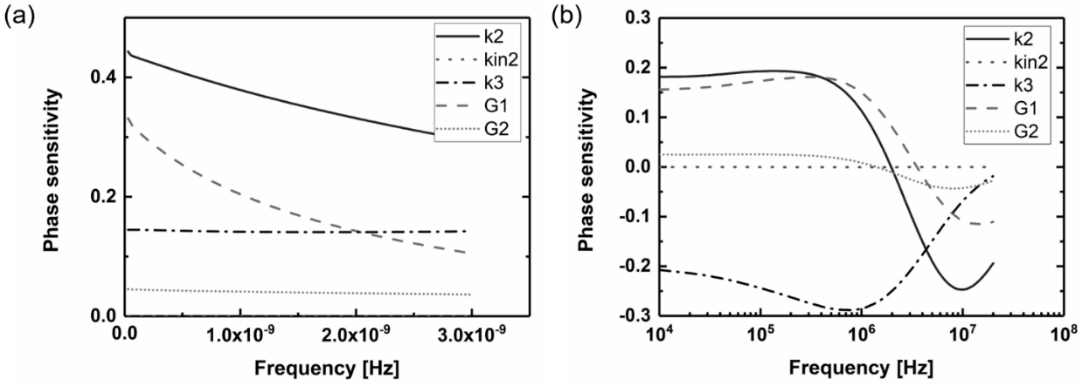

Figure 4.15. The sensitivity plot for a ~110 nm thick $Al_{0.875}Sc_{0.125}N$ film measured by (a) TDTR and (b) FDTR. In the legend, *k2* and *kin2* are the cross-plane and in-plane thermal conductivities of the $Al_{1-x}Sc_xN$ film, respectively. *k3* is the thermal conductivity of the Si substrate. *G1* and *G2* are the TBCs of the transducer/$Al_{1-x}Sc_xN$ and $Al_{1-x}Sc_xN$/Si interfaces, respectively.

Thermal Conductivity Measurements (FDTR):

Frequency-domain thermoreflectance (FDTR) measurements of the thermo-physical properties were done following deposition of an 80 nm gold (Au) transducer onto the sample surface.[102] The FDTR system uses a pump laser (λ = 405 nm) operating with a 50% duty cycle square wave to heat the Au transducer/sample while its temperature response is captured from the thermoreflectance signal of a probe laser (λ = 532 nm). The probing wavelength was specifically chosen to maximize the thermoreflectance coefficient of the Au transducer for improved measurement sensitivity. The diameters of the focused pump and probe beams were characterized using a scanning-slit optical beam profiler (Thorlabs BP209-VIS) and were 15.5 μm and 12.4 μm, respectively. To minimize the uncertainty in the analysis of the FDTR data, the Au transducer thickness was measured by x-ray reflectometry (XRR). The $Al_{1-x}Sc_xN$ film thicknesses were determined by using variable angle spectroscopic ellipsometry (VASE) and cross-sectional scanning electron microscopy (SEM). Representative raw data and fitting results for TDTR and FDTR experiments are shown in Figure 8.

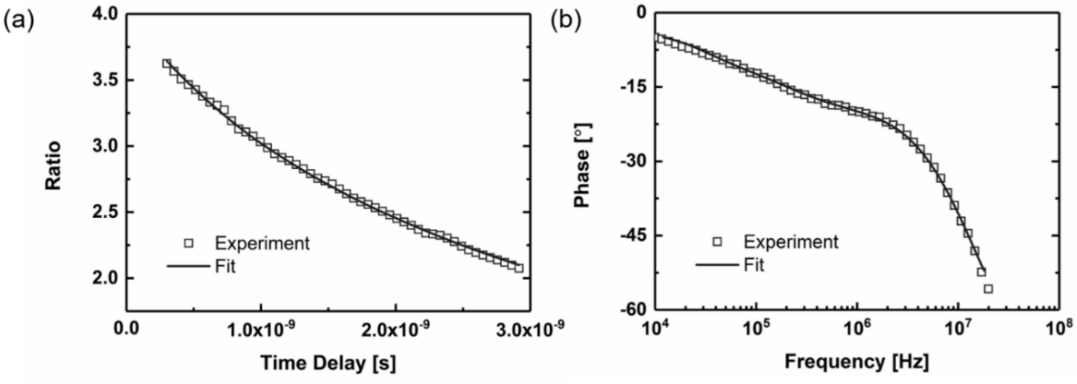

Figure 4.16. Raw data and fitting results for a ~110 nm thick $Al_{0.875}Sc_{0.125}N$ film measured by (a) TDTR and (b) FDTR.

Chapter References

[1] G. Piazza, V. Felmetsger, P. Muralt, R.H. Olsson III, and R. Ruby, “Piezoelectric aluminum nitride thin films for microelectromechanical systems,” MRS Bull. **37**(11), 1051–1061 (2012).

[2] E. Iborra, J. Olivares, M. Clement, L. Vergara, A. Sanz-Hervás, and J. Sangrador, “Piezoelectric properties and residual stress of sputtered AlN thin films for MEMS applications,” Sensors Actuators, A Phys. **115**(2-3 SPEC. ISS.), 501–507 (2004).

[3] P. Nicolay, O. Elmazria, B. Assouar, F. Sarry, and L. Lebrizoual, “Theoretical and experimental study of the differential thermal expansion effect on the TCD of layered SAW temperature sensors. Application to aluminum nitride based layered structures,” Proc. - IEEE Ultrason. Symp. (1), 272–275 (2007).

[4] J.Y. Tsao, S. Chowdhury, M.A. Hollis, D. Jena, N.M. Johnson, K.A. Jones, R.J. Kaplar, S. Rajan, C.G. Van de Walle, E. Bellotti, C.L. Chua, R. Collazo, M.E. Coltrin, J.A. Cooper, K.R. Evans, S. Graham, T.A. Grotjohn, E.R. Heller, M. Higashiwaki, M.S. Islam, P.W. Juodawlkis, M.A. Khan, A.D. Koehler, J.H. Leach, U.K. Mishra, R.J. Nemanich, R.C.N. Pilawa-Podgurski, J.B. Shealy, Z. Sitar, M.J. Tadjer, A.F. Witulski, M. Wraback, and J.A. Simmons, “Ultrawide-bandgap semiconductors: research opportunities and challenges,” Adv. Electron. Mater. **4**(1), 1600501 (2018).

[5] Y. Taniyasu, M. Kasu, and T. Makimoto, “An aluminium nitride light-emitting diode with a wavelength of 210 nanometres,” Nature **441**(7091), 325–328 (2006).

[6] M. Kneissl, T.-Y. Seong, J. Han, and H. Amano, “The emergence and prospects of deep-ultraviolet light-emitting diode technologies,” Nat. Photonics **13**(4), 233–244 (2019).

[7] B.J. Baliga, “Semiconductors for high-voltage, vertical channel field-effect transistors,” J. Appl. Phys. **53**(3), 1759–1764 (1982).

[8] G. Piazza, V. Felmetsger, P. Muralt, R.H. Olsson, and R. Ruby, "Piezoelectric aluminum nitride thin films for microelectromechanical systems," MRS Bull. **37**(11), 1051–1061 (2012).

[9] C. Li, X. Liu, L. Shu, and Y. Li, "ALN-based surface acoustic wave resonators for temperature sensing applications," Mater. Express **5**(4), 367–370 (2015).

[10] M. Reusch, K. Holc, L. Kirste, P. Katus, L. Reindl, O. Ambacher, and V. Lebedev, "Piezoelectric AlN films for FPW sensors with improved device performance," Procedia Eng. **168**, 1040–1043 (2016).

[11] J. Jung, W. Lee, W. Kang, E. Shin, J. Ryu, and H. Choi, "Review of piezoelectric micromachined ultrasonic transducers and their applications," J. Micromechanics Microengineering **27**(11), 113001 (2017).

[12] G. Piazza, P.J. Stephanou, and A.P. Pisano, "Piezoelectric aluminum nitride vibrating contour-mode MEMS resonators," J. Microelectromechanical Syst. **15**(6), 1406–1418 (2006).

[13] T.Y. Chemekova, O. V Avdeev, I.S. Barash, E.N. Mokhov, S.S. Nagalyuk, A.D. Roenkov, A.S. Segal, Y.N. Makarov, M.G. Ramm, S. Davis, G. Huminic, and H. Helava, "Sublimation growth of 2 inch diameter bulk AlN crystals," Phys. Status Solidi C **5**(6), 1612–1614 (2008).

[14] S.B. Schujman, L.J. Schowalter, R.T. Bondokov, K.E. Morgan, W. Liu, J.A. Smart, and T. Bettles, "Structural and surface characterization of large diameter, crystalline AlN substrates for device fabrication," J. Cryst. Growth **310**(5), 887–890 (2008).

[15] W.-H. Chen, Z.-Y. Qin, X.-Y. Tian, X.-H. Zhong, Z.-H. Sun, B.-K. Li, R.-S. Zheng, Y. Guo, and H.-L. Wu, "The physical vapor transport method for bulk AlN crystal growth," Molecules **24**(8), 1562 (2019).

[16] S. Tanaka, R.S. Kern, and R.F. Davis, "Initial stage of aluminum nitride film growth on 6H-silicon carbide by plasma-assisted, gas-source molecular beam epitaxy," Appl. Phys. Lett. **66**(1), 37–39 (1995).

[17] A. Hickman, R. Chaudhuri, S.J. Bader, K. Nomoto, K. Lee, H.G. Xing, and D. Jena, "High breakdown voltage in RF AlN/GaN/AlN quantum well HEMTs," IEEE Electron Device Lett. **40**(8), 1293–1296 (2019).

[18] A.G. Baca, A.M. Armstrong, A.A. Allerman, E.A. Douglas, C.A. Sanchez, M.P. King, M.E. Coltrin, T.R. Fortune, and R.J. Kaplar, "An AlN/$Al_{0.85}Ga_{0.15}N$ high electron mobility transistor," Appl. Phys. Lett. **109**(3), 033509 (2016).

[19] H. Tokuda, M. Hatano, N. Yafune, S. Hashimoto, K. Akita, Y. Yamamoto, and M. Kuzuhara, "High Al composition AlGaN-Channel high-electron-mobility transistor on AlN substrate," Appl. Phys. Express **3**(12), 121003 (2010).

[20] N. Yafune, S. Hashimoto, K. Akita, Y. Yamamoto, H. Tokuda, and M. Kuzuhara, "AlN/AlGaN HEMTs on AlN substrate for stable high-temperature operation," Electron. Lett. **50**(3), 211–212 (2014).

[21] R. Dargis, A. Clark, A. Ansari, Z. Hao, M. Park, D. Kim, R. Yanka, R. Hammond, M. Debnath, and R. Pelzel, "Single-crystal multilayer nitride, metal, and oxide structures on engineered silicon for new-generation radio frequency filter applications," Phys. Status Solidi **217**(7), 1900813 (2020).

[22] C.-P. Huang, K. Gupta, C.-H. Wang, C.-P. Liu, and K.-Y. Lai, "High-quality AlN grown with a single substrate temperature below 1200 °C," Sci. Rep. **7**(1), 7135 (2017).

[23] M. Pons, J. Su, M. Chubarov, R. Boichot, F. Mercier, E. Blanquet, G. Giusti, and D. Pique, "HVPE of aluminum nitride, film evaluation and multiscale modeling of the growth process," J. Cryst. Growth **468**, 235–240 (2017).

[24] M.-A. Dubois, and P. Muralt, "Stress and piezoelectric properties of aluminum nitride thin films deposited onto metal electrodes by pulsed direct current reactive sputtering," J. Appl. Phys. **89**(11), 6389–6395 (2001).

[25] P. Muralt, "AlN thin film processing and basic properties bt - piezoelectric MEMS resonators,"

edited by H. Bhugra and G. Piazza, (Springer International Publishing, Cham, 2017), pp. 3–37.

[26] P. Muralt, R.G. Polcawich, and S. Trolier-McKinstry, "Piezoelectric thin films for sensors, actuators, and energy harvesting," MRS Bull. **34**(9), 658–664 (2009).

[27] S. Trolier-McKinstry, and P. Muralt, "Thin film piezoelectrics for MEMS," J. Electroceramics **12**(1), 7–17 (2004).

[28] N. Susilo, S. Hagedorn, D. Jaeger, H. Miyake, U. Zeimer, C. Reich, B. Neuschulz, L. Sulmoni, M. Guttmann, F. Mehnke, C. Kuhn, T. Wernicke, M. Weyers, and M. Kneissl, "AlGaN-based deep UV LEDs grown on sputtered and high temperature annealed AlN/sapphire," Appl. Phys. Lett. **112**(4), 41110 (2018).

[29] Y.R. Koh, Z. Cheng, A. Mamun, M.S. Bin Hoque, Z. Liu, T. Bai, K. Hussain, M.E. Liao, R. Li, J.T. Gaskins, A. Giri, J. Tomko, J.L. Braun, M. Gaevski, E. Lee, L. Yates, M.S. Goorsky, T. Luo, A. Khan, S. Graham, and P.E. Hopkins, "Bulk-like intrinsic phonon thermal conductivity of micrometer-thick AlN films," ACS Appl. Mater. Interfaces **12**(26), 29443–29450 (2020).

[30] A. V Inyushkin, A.N. Taldenkov, D.A. Chernodubov, E.N. Mokhov, S.S. Nagalyuk, V.G. Ralchenko, and A.A. Khomich, "On the thermal conductivity of single crystal AlN," J. Appl. Phys. **127**(20), 205109 (2020).

[31] G.A. Slack, R.A. Tanzilli, R.O. Pohl, and J.W. Vandersande, "The intrinsic thermal conductivity of AlN," J. Phys. Chem. Solids **48**(7), 641–647 (1987).

[32] C. Duquenne, M.-P.P. Besland, P.Y. Tessier, E. Gautron, Y. Scudeller, and D. Averty, "Thermal conductivity of aluminium nitride thin films prepared by reactive magnetron sputtering," J. Phys. D. Appl. Phys. **45**(1), 15301 (2012).

[33] S. Xiao, R. Suzuki, H. Miyake, S. Harada, and T. Ujihara, "Improvement mechanism of sputtered AlN films by high-temperature annealing," J. Cryst. Growth **502**, 41–44 (2018).

[34] R.L. Xu, M. Muñoz Rojo, S.M. Islam, A. Sood, B. Vareskic, A. Katre, N. Mingo, K.E. Goodson, H.G. Xing, D. Jena, and E. Pop, "Thermal conductivity of crystalline AlN and the influence of atomic-scale defects," J. Appl. Phys. **126**(18), 185105 (2019).

[35] D.G. Cahill, "Analysis of heat flow in layered structures for time-domain thermoreflectance," Rev. Sci. Instrum. **75**(12), 5119–5122 (2004).

[36] J. Zhu, X. Wu, D.M. Lattery, W. Zheng, and X. Wang, "The ultrafast laser pump-probe technique for thermal characterization of materials with micro/nanostructures," Nanoscale Microscale Thermophys. Eng. **21**(3), 177–198 (2017).

[37] J. Zhu, H. Park, J.-Y. Chen, X. Gu, H. Zhang, S. Karthikeyan, N. Wendel, S.A. Campbell, M. Dawber, X. Du, M. Li, J.-P. Wang, R. Yang, and X. Wang, "Revealing the origins of 3D anisotropic thermal conductivities of black phosphorus," Adv. Electron. Mater. **2**(5), 1600040 (2016).

[38] M.S. Bin Hoque, Y.R. Koh, J.L. Braun, A. Mamun, Z. Liu, K. Huynh, M.E. Liao, K. Hussain, Z. Cheng, E.R. Hoglund, D.H. Olson, J.A. Tomko, K. Aryana, R. Galib, J.T. Gaskins, M.M.M. Elahi, Z.C. Leseman, J.M. Howe, T. Luo, S. Graham, M.S. Goorsky, A. Khan, and P.E. Hopkins, "High in-plane thermal conductivity of aluminum nitride thin films," ACS Nano **15**(6), 9588–9599 (2021).

[39] J.P. Freedman, J.H. Leach, E.A. Preble, Z. Sitar, R.F. Davis, and J.A. Malen, "Universal phonon mean free path spectra in crystalline semiconductors at high temperature," Sci. Rep. **3**, 2963 (2013).

[40] T.E. Beechem, A.E. McDonald, E.J. Fuller, A.A. Talin, C.M. Rost, J.-P. Maria, J.T. Gaskins, P.E. Hopkins, and A.A. Allerman, "Size dictated thermal conductivity of GaN," J. Appl. Phys. **120**(9), 95104 (2016).

[41] Y. Shen, R. Zhang, R. Vetury, and J. Shealy, "40.6 Watt, high power 3.55 GHz single crystal XBAW RF filters for 5G infrastructure applications," in *2020 IEEE Int. Ultrason. Symp.*,

(2020), pp. 1–3.

[42] R. Liu, F.A. Ponce, A. Dadgar, and A. Krost, "Atomic arrangement at the AlN/Si (111) interface," Appl. Phys. Lett. **83**(5), 860–862 (2003).

[43] O. Ambacher, "Growth and applications of Group III-nitrides," J. Phys. D. Appl. Phys. **31**(20), 2653–2710 (1998).

[44] H. Watanabe, N. Yamada, and M. Okaji, "Linear thermal expansion coefficient of silicon from 293 to 1000 K," Int. J. Thermophys. **25**(1), 221–236 (2004).

[45] S. Tamariz, D. Martin, and N. Grandjean, "AlN grown on Si(111) by ammonia-molecular beam epitaxy in the 900–1200°C temperature range," J. Cryst. Growth **476**, 58–63 (2017).

[46] S. Raghavan, and J.M. Redwing, "In situ stress measurements during the MOCVD growth of AlN buffer layers on (111) Si substrates," J. Cryst. Growth **261**(2), 294–300 (2004).

[47] S.R. Lee, A.M. West, A.A. Allerman, K.E. Waldrip, D.M. Follstaedt, P.P. Provencio, D.D. Koleske, and C.R. Abernathy, "Effect of threading dislocations on the Bragg peakwidths of GaN, AlGaN, and AlN heterolayers," Appl. Phys. Lett. **86**(24), 241904 (2005).

[48] T. Metzger, R. Höpler, E. Born, O. Ambacher, M. Stutzmann, R. Stömmer, M. Schuster, H. Göbel, S. Christiansen, M. Albrecht, and H.P. Strunk, "Defect structure of epitaxial GaN films determined by transmission electron microscopy and triple-axis X-ray diffractometry," Philos. Mag. A **77**(4), 1013–1025 (1998).

[49] D. Wang, K. Uesugi, S. Xiao, K. Norimatsu, and H. Miyake, "Low dislocation density AlN on sapphire prepared by double sputtering and annealing," Appl. Phys. Express **13**(9), 95501 (2020).

[50] J.A. Phys, T.E. Beechem, A.E. Mcdonald, E.J. Fuller, A.A. Talin, C.M. Rost, J.T. Gaskins, P.E. Hopkins, A.A. Allerman, T.E. Beechem, A.E. Mcdonald, E.J. Fuller, A.A. Talin, C.M. Rost, J. Maria, J.T. Gaskins, P.E. Hopkins, and A.A. Allerman, "Size dictated thermal conductivity of GaN Size dictated thermal conductivity of GaN," **120**, 095104 (April

2016), (2017).

[51] H. Miyake, C.-H. Lin, K. Tokoro, and K. Hiramatsu, “Preparation of high-quality AlN on sapphire by high-temperature face-to-face annealing,” J. Cryst. Growth **456**, 155–159 (2016).

[52] N. Onojima, J. Suda, T. Kimoto, and H. Matsunami, “4H-polytype AlN grown on 4H-SiC$(11\bar{2}0)$ substrate by polytype replication,” Appl. Phys. Lett. **83**(25), 5208–5210 (2003).

[53] R. Rounds, B. Sarkar, A. Klump, C. Hartmann, T. Nagashima, R. Kirste, A. Franke, M. Bickermann, Y. Kumagai, Z. Sitar, and R. Collazo, “Thermal conductivity of single-crystalline AlN,” Appl. Phys. Express **11**(7), 71001 (2018).

[54] A. Franco Júnior, and D.J. Shanafield, “Thermal conductivity of polycrystalline aluminum nitride (AlN) ceramics,” Cerâmica **50**(315), 247–253 (2004).

[55] P. Bogusławski, and J. Bernholc, “Doping properties of C, Si, and Ge impurities in GaN and AlN,” Phys. Rev. B **56**(15), 9496–9505 (1997).

[56] J. Zou, D. Kotchetkov, A.A. Balandin, D.I. Florescu, and F.H. Pollak, “Thermal conductivity of GaN films: Effects of impurities and dislocations,” J. Appl. Phys. **92**(5), 2534 (2002).

[57] M. Akiyama, T. Kamohara, K. Kano, A. Teshigahara, and N. Kawahara, “Influence of oxygen concentration in sputtering gas on piezoelectric response of aluminum nitride thin films,” Appl. Phys. Lett. **93**(2), 21903 (2008).

[58] G.A. Slack, L.J. Schowalter, D. Morelli, and J.A. Freitas, “Some effects of oxygen impurities on AlN and GaN,” J. Cryst. Growth **246**(3), 287–298 (2002).

[59] M.A. Signore, A. Taurino, D. Valerini, A. Rizzo, I. Farella, M. Catalano, F. Quaranta, and P. Siciliano, “Role of oxygen contaminant on the physical properties of sputtered AlN thin films,” J. Alloys Compd. **649**, 1267–1272 (2015).

[60] J.W. Lee, J.J. Cuomo, Y.S. Cho, and R.L. Keusseyan, “Aluminum nitride thin films on an LTCC substrate,” J. Am. Ceram. Soc. **88**(7), 1977–1980 (2005).

[61] S. Fleischmann, E. Richter, A. Mogilatenko, M. Weyers, and B. Sapphire, "Influence of quartz on silicon incorporation in HVPE grown AlN," J. Cryst. Growth **507**(November 2018), 295–298 (2019).

[62] D. Fu, Q. Wang, G. Zhang, R. Zhu, H. Liu, Z. Li, and L. Wu, "Modelling and simulation of oxygen transport during AlN crystal growth by the PVT method," J. Cryst. Growth **551**, 125902 (2020).

[63] Y.-C. Yang, C.-T. Chang, Y.-C. Hsiao, J.-W. Lee, and B.-S. Lou, "Influence of high power impulse magnetron sputtering pulse parameters on the properties of aluminum nitride coatings," Surf. Coatings Technol. **259**, 219–231 (2014).

[64] C.H. Park, J.G. Kim, S.-G. Jung, D.J. Lee, Y.W. Park, and B.-K. Ju, "Optical characteristics of refractive-index-matching diffusion layer in organic light-emitting diodes," Sci. Rep. **9**(1), 8690 (2019).

[65] F.Y.C. Boey, X.L. Song, Z.Y. Gu, and A. Tok, "AlON phase formation in a tape-cast Al_2O_3/AlN composite," J. Mater. Process. Technol. **89**–**90**, 478–480 (1999).

[66] C.T. Warner, T.M. Hartnett, D. Fisher, and W. Sunne, "Characterization of ALON optical ceramic," in *Proc.SPIE*, **5786** (2005).

[67] Y. Zheng, M. Park, A. Ansari, C. Yuan, and S. Graham, "Self-heating and quality factor: thermal challenges in aluminum scandium nitride bulk acoustic wave resonators," in *2021 21st Int. Conf. Solid-State Sensors, Actuators Microsystems*, (2021), pp. 321–324.

[68] J. Wang, Y. Zheng, and A. Ansari, "Ferroelectric aluminum scandium nitride thin film bulk acoustic resonators with polarization-dependent operating states," Phys. Status Solidi – Rapid Res. Lett. **15**(5), 2100034 (2021).

[69] S.S. Iyer, and R.N. Candler, "Mode- and direction-dependent mechanical energy dissipation in single-crystal resonators due to anharmonic phonon-phonon scattering," Phys. Rev. Appl. **5**(3), 34002 (2016).

[70] Y. Song, C. Perez, G. Esteves, J.S. Lundh, C.B. Saltonstall, T.E. Beechem, J.I. Yang, K. Ferri, J.E. Brown, Z. Tang, J.-P. Maria, D.W. Snyder, R.H. Olsson, B.A. Griffin, S.E. Trolier-McKinstry, B.M. Foley, and S. Choi, "Thermal conductivity of aluminum scandium nitride for 5G mobile applications and beyond," ACS Appl. Mater. Interfaces, **13**(16), 19031-19041 (2021).

[71] K. Uesugi, Y. Hayashi, K. Shojiki, and H. Miyake, "Reduction of threading dislocation density and suppression of cracking in sputter-deposited AlN templates annealed at high temperatures," Appl. Phys. Express **12**(6), 65501 (2019).

[72] Z. Hao, M. Park, D.G. Kim, A. Clark, R. Dargis, H. Zhu, A. Ansari, and N.A. Nw, "Single crystalline scaln surface acoustic wave resonators with large figure of merit ($Q \times k_t^2$)," 2019 IEEE MTT-S Int. Microw. Symp., 786–789 (2019).

[73] W. Zhou, R. Apkarian, Z.L. Wang, and D. Joy, "Fundamentals of scanning electron microscopy (SEM) BT - scanning microscopy for nanotechnology: techniques and applications," edited by W. Zhou and Z.L. Wang, (Springer New York, New York, NY, 2007), pp. 1–40.

[74] J.S. Lundh, K. Coleman, Y. Song, B.A. Griffin, G. Esteves, E.A. Douglas, A. Edstrand, S.C. Badescu, E.A. Moore, J.H. Leach, B. Moody, S. Trolier-McKinstry, and S. Choi, "Residual stress analysis of aluminum nitride piezoelectric micromachined ultrasonic transducers using Raman spectroscopy," J. Appl. Phys. **130**(4), 44501 (2021).

[75] Y. Wang, J.Y. Park, Y.K. Koh, and D.G. Cahill, "Thermoreflectance of metal transducers for time-domain thermoreflectance," J. Appl. Phys. **108**(4), 43507 (2010).

[76] J. Zhu, H. Park, J.-Y. Chen, X. Gu, H. Zhang, S. Karthikeyan, N. Wendel, S.A. Campbell, M. Dawber, X. Du, M. Li, J.-P. Wang, R. Yang, and X. Wang, "Black phosphorus: revealing the origins of 3D anisotropic thermal conductivities of black phosphorus," Adv. Electron. Mater. **2**(5), 1600040 (2016).

[77] J. Zhu, T. Feng, S. Mills, P. Wang, X. Wu, L. Zhang, S.T. Pantelides, X. Du, and X. Wang,

"Record-low and anisotropic thermal conductivity of a quasi-one-dimensional bulk $ZrTe_5$ single crystal," ACS Appl. Mater. Interfaces **10**(47), 40740–40747 (2018).

[78] T. Feng, X. Wu, X. Yang, P. Wang, L. Zhang, X. Du, X. Wang, and S.T. Pantelides, "Thermal conductivity of $HfTe_5$: a critical revisit," Adv. Funct. Mater. **30**(5), 1907286 (2020).

[79] C.A. Ratsifaritana, and P.G. Klemens, "Scattering of phonons by vacancies," Int. J. Thermophys. **8**(6), 737–750 (1987).

[80] T. Nishihara, T. Yokoyama, T. Miyashita, and Y. Satoh, "High performance and miniature thin film bulk acoustic wave filters for 5 GHz," Proc. IEEE Ultrason. Symp. **1**(c), 969–972 (2002).

[81] M. Akiyama, T. Kamohara, K. Kano, A. Teshigahara, Y. Takeuchi, and N. Kawahara, "Enhancement of piezoelectric response in scandium aluminum nitride alloy thin films prepared by dual reactive cosputtering," Adv. Mater. **21**(5), 593–596 (2009).

[82] G. Wingqvist, F. Tasnádi, A. Zukauskaite, J. Birch, H. Arwin, and L. Hultman, "Increased electromechanical coupling in w−$Sc_xAl_{1-x}N$," Appl. Phys. Lett. **97**(11), 112902 (2010).

[83] S. Trolier-McKinstry, S. Zhang, A.J. Bell, and X. Tan, "High-performance piezoelectric crystals, ceramics, and films," Annu. Rev. Mater. Res. **48**(1), 191–217 (2018).

[84] M. Moreira, J. Bjurström, I. Katardjev, and V. Yantchev, "Aluminum scandium nitride thin-film bulk acoustic resonators for wide band applications," Vacuum **86**(1), 23–26 (2011).

[85] R.C. Ruby, P. Bradley, Y. Oshmyansky, A. Chien, and J.D. Larson, "Thin film bulk wave acoustic resonators (FBAR) for wireless applications," in *2001 IEEE Ultrason. Symp. Proceedings. An Int. Symp. (Cat. No.01CH37263)*, (2001), pp. 813–821 vol.1.

[86] Y. Kumar, K. Rangra, and R. Agarwal, "Design and simulation of FBAR for quality factor enhancement," MAPAN **32**(2), 113–119 (2017).

[87] B.A. Griffin, M.D. Henry, R.W. Reger, and B. Heinz, "$Sc_xAl_{1-x}N$ film evaluation using contour mode resonators," in *2017 IEEE Int. Ultrason. Symp.*, (2017), pp. 1–4.

[88] R. Lu, and S. Gong, "Study of thermal nonlinearity in lithium niobate-based MEMS resonators," in *2015 Transducers - 2015 18th Int. Conf. Solid-State Sensors, Actuators Microsystems*, (2015), pp. 1993–1996.

[89] K. Umeda, H. Kawai, A. Honda, M. Akiyama, T. Kato, and T. Fukura, "Piezoelectric properties of ScAlN thin films for piezo-MEMS devices," Proc. IEEE Int. Conf. Micro Electro Mech. Syst., 733–736 (2013).

[90] R.-. Fillit, B. Ivira, J. Boussey, R. Fortunier, and P. Ancey, "Structural and thermal investigation for FBAR reliability in wireless applications," in *2005 IEEE Int. Reliab. Phys. Symp. 2005. Proceedings. 43rd Annu.*, (2005), pp. 342–346.

[91] J.D. Larson, J.D. Ruby, R.C. Bradley, J. Wen, S.-L. Kok, and A. Chien, "Power handling and temperature coefficient studies in FBAR duplexers for the 1900 MHz PCS band," in *2000 IEEE Ultrason. Symp. Proceedings. An Int. Symp. (Cat. No.00CH37121)*, (2000), pp. 869–874 vol.1.

[92] H. Mehner, S. Leopold, and M. Hoffmann, "Variation of the intrinsic stress gradient in thin aluminum nitride films," J. Micromechanics Microengineering **23**(9), 95030 (2013).

[93] H.-C. Lee, J.-Y. Lee, and H.-J. Ahn, "Effect of the substrate bias voltage on the crystallographic orientation of reactively sputtered AlN thin films," Thin Solid Films **251**(2), 136–140 (1994).

[94] F. Knöbber, V. Zürbig, N. Heidrich, J. Hees, R.E. Sah, M. Baeumler, S. Leopold, D. Pätz, O. Ambacher, and V. Lebedev, "Static and dynamic characterization of AlN and nanocrystalline diamond membranes," Phys. Status Solidi Appl. Mater. Sci. **209**(10), 1835–1842 (2012).

[95] M.D. Henry, T.R. Young, E.A. Douglas, and B.A. Griffin, "Reactive sputter deposition of piezoelectric Sc0.12Al0.88N for contour mode resonators," J. Vac. Sci. Technol. B **36**(3), 03E104 (2018).

[96] H.P. Loebl, M. Klee, C. Metzmacher, W. Brand, R. Milsom, and P. Lok, "Piezoelectric thin AlN films for bulk acoustic wave (BAW) resonators," Mater. Chem. Phys. **79**(2), 143–146 (2003).

[97] H. Bhugra, and G. Piazza, *Piezoelectric MEMS Resonators* (Springer, 2017).

[98] R. Deng, K. Jiang, and D. Gall, "Optical phonon modes in $Al_{1-x}Sc_xN$," J. Appl. Phys. **115**(1), 13506 (2014).

[99] A.L. Mock, A.G. Jacobs, E.N. Jin, M.T. Hardy, and M.J. Tadjer, "Long-wavelength dielectric properties and infrared active optical phonon modes of molecular beam epitaxy $Sc_xAl_{1-x}N$ determined by infrared spectroscopic ellipsometry," Appl. Phys. Lett. **117**(23), 232107 (2020).

[100] T. Beechem, and S. Graham, "Temperature and doping dependence of phonon lifetimes and decay pathways in GaN," J. Appl. Phys. **103**(9), 93507 (2008).

[101] M. Kuball, "Raman spectroscopy of GaN, AlGaN and AlN for process and growth monitoring/control," Surf. Interface Anal. **31**(10), 987–999 (2001).

[102] A.J. Schmidt, R. Cheaito, and M. Chiesa, "A frequency-domain thermoreflectance method for the characterization of thermal properties," Rev. Sci. Instrum. **80**(9), 94901 (2009).

[103] J.L. Braun, and P.E. Hopkins, "Upper limit to the thermal penetration depth during modulated heating of multilayer thin films with pulsed and continuous wave lasers: A numerical study," J. Appl. Phys. **121**(17), 1–13 (2017).

[104] M. David Henry, T.R. Young, and B. Griffin, "ScAlN etch mask for highly selective silicon etching," J. Vac. Sci. Technol. B, Nanotechnol. Microelectron. Mater. Process. Meas. Phenom. **35**(5), 052001 (2017).

[105] S. Adachi, "Lattice thermal conductivity of group-IV and III–V semiconductor alloys," J. Appl. Phys. **102**(6), 63502 (2007).

[106] T. Beechem, A. Christensen, S. Graham, and D. Green, "Micro-Raman thermometry in the

presence of complex stresses in GaN devices," J. Appl. Phys. **103**(12), 124501 (2008).

[107] B. Chatterjee, J.S. Lundh, Y. Song, D. Shoemaker, A.G. Baca, R.J. Kaplar, T.E. Beechem, C. Saltonstall, A.A. Allerman, A.M. Armstrong, B.A. Klein, A. Bansal, H.R. Seyf, D. Talreja, A. Pogrebnyakov, E. Heller, V. Gopalan, A.S. Henry, J.M. Redwing, B. Foley, and S. Choi, "Interdependence of electronic and thermal transport in $Al_xGa_{1-x}N$ channel HEMTs," IEEE Electron Device Lett., **41**(3), 461-464 (2020).

[108] K.R. Talley, S.L. Millican, J. Mangum, S. Siol, C.B. Musgrave, B. Gorman, A.M. Holder, A. Zakutayev, and G.L. Brennecka, "Implications of heterostructural alloying for enhanced piezoelectric performance of (Al,Sc)N," Phys. Rev. Mater. **2**(6), 63802 (2018).

[109] F. Tasnádi, B. Alling, C. Höglund, G. Wingqvist, J. Birch, L. Hultman, and I.A. Abrikosov, "Origin of the anomalous piezoelectric response in wurtzite $Sc_xAl_{1-x}N$ alloys," Phys. Rev. Lett. **104**(13), 137601 (2010).

[110] M. Akiyama, K. Kano, and A. Teshigahara, "Influence of growth temperature and scandium concentration on piezoelectric response of scandium aluminum nitride alloy thin films," Appl. Phys. Lett. **95**(16), 1–4 (2009).

[111] D.G. Cahill, W.K. Ford, K.E. Goodson, G.D. Mahan, A. Majumdar, H.J. Maris, R. Merlin, and S.R. Phillpot, "Nanoscale thermal transport," J. Appl. Phys. **93**(2), 793–818 (2003).

[112] A. Majumdar, "Microscale heat conduction in dielectric thin films," J. Heat Transfer **115**(1), 7–16 (1993).

[113] M. Park, Z. Hao, D.G. Kim, A. Clark, R. Dargis, and A. Ansari, "A 10 GHz single-crystalline scandium-doped aluminum nitride lamb-wave resonator," in *2019 20th Int. Conf. Solid-State Sensors, Actuators Microsystems Eurosensors XXXIII (TRANSDUCERS EUROSENSORS XXXIII)*, (2019), pp. 450–453.

[114] N.I.M. Nor, N. Ahmad, N. Khalid, M.M. Isa, S.S.M. Isa, M.M. Ramli, and S.R. Kasjoo, "The influence of design parameters on the performance of FBAR in 15–19 GHz," AIP Conf.

Proc. **2045**(1), 20088 (2018).

[115] K.T. Regner, J.P. Freedman, and J.A. Malen, "Advances in studying phonon mean free path dependent contributions to thermal conductivity," Nanoscale Microscale Thermophys. Eng. **19**(3), 183–205 (2015).

[116] M. Park, J. Wang, R. Dargis, A. Clark, and A. Ansari, "Super high-frequency scandium aluminum nitride crystalline film bulk acoustic resonators," in *2019 IEEE Int. Ultrason. Symp.*, (2019), pp. 1689–1692.

[117] W. Lv, and A. Henry, "Non-negligible contributions to thermal conductivity from localized modes in amorphous silicon dioxide," Sci. Rep. **6**(October), 4–11 (2016).

[118] J. Wang, M. Zhao, S.F. Jin, D.D. Li, J.W. Yang, W.J. Hu, and W.J. Wang, "Debye temperature of wurtzite AlN determined by X-ray powder diffraction," Powder Diffr. **29**(4), 352–355 (2014).

[119] B. Saha, J. Acharya, T.D. Sands, and U. V. Waghmare, "Electronic structure, phonons, and thermal properties of ScN, ZrN, and HfN: A first-principles study," J. Appl. Phys. **107**(3), 33715 (2010).

[120] S. Fichtner, N. Wolff, G. Krishnamurthy, A. Petraru, S. Bohse, F. Lofink, S. Chemnitz, H. Kohlstedt, L. Kienle, and B. Wagner, "Identifying and overcoming the interface originating c-axis instability in highly Sc enhanced AlN for piezoelectric micro-electromechanical systems," J. Appl. Phys. **122**(3), 35301 (2017).

[121] D. Wang, J. Zheng, Z. Tang, M. D'Agati, V. Roebisch, P.S.M. Gharavi, X. Liu, M.-G. Han, K. Kisslinger, M. Kratzer, B. Heinz, D. Jariwala, E. Stach, and R.H. Olsson III, "Ferroelectric c-axis textured aluminum scandium nitride thin films of 100 nm thickness," in *Jt. Conf. IEEE Int. Freq. Cntrl. Symp. IEEE Int. Symp. Appl. Ferroelectr.*, (2020), pp. 1–4.

[122] C. Moe, R.H. Olsson III, P. Patel, Z. Tang, M. D'Agati, M. Winters, R. Vetury, and J.B. Shealy, "Highly doped AlScN 3.5 GHz XBAW resonators with 16% k_{2eff} for 5G RF filter

applications," in *Proc. 2020 IEEE Ultrason. Symp.*, (2020), pp. 1–4.

[123] T.S. Pan, Y. Zhang, J. Huang, B. Zeng, D.H. Hong, S.L. Wang, H.Z. Zeng, M. Gao, W. Huang, and Y. Lin, "Enhanced thermal conductivity of polycrystalline aluminum nitride thin films by optimizing the interface structure," J. Appl. Phys. **112**(4), 044905 (2012).

[124] J.S. Reid, "Phonon gas," Phys. Educ. **11**(5), 348–353 (1976).

[125] L. Nordheim, "Zur elektronentheorie der metalle. I," Ann. Phys. **401**(5), 607–640 (1931).

[126] H.R. Seyf, L. Yates, T.L. Bougher, S. Graham, B.A. Cola, T. Detchprohm, M.H. Ji, J. Kim, R. Dupuis, W. Lv, and A. Henry, "Rethinking phonons: The issue of disorder," Npj Comput. Mater. **3**(1), 49 (2017).

[127] G. Chen, *Nanoscale energy transport and conversion: a parallel treatment of electrons, molecules, phonons, and photons* (Oxford university press, New York, NY, 2005).

[128] N. Mingo, "Calculation of Si nanowire thermal conductivity using complete phonon dispersion relations," Phys. Rev. B **68**(11), 113308 (2003).

[129] J.D. Chung, A.J.H. McGaughey, and M. Kaviany, "Role of phonon dispersion in lattice thermal conductivity modeling ," J. Heat Transfer **126**(3), 376–380 (2004).

[130] C. Bungaro, K. Rapcewicz, and J. Bernholc, "Ab initio phonon dispersions of wurtzite AlN, GaN, and InN," Phys. Rev. B **61**(10), 6720–6725 (2000).

[131] S. Zhang, D. Holec, W.Y. Fu, C.J. Humphreys, and M.A. Moram, "Tunable optoelectronic and ferroelectric properties in Sc-based III-nitrides," J. Appl. Phys. **114**(13), 133510 (2013).

[132] K.M. Taylor, and C. Lenie, "Some properties of aluminum nitride," J. Electrochem. Soc. **107**(4), 308 (1960).

[133] R. Niewa, D.A. Zherebtsov, M. Kirchner, M. Schmidt, and W. Schnelle, "New ways to high-quality bulk scandium nitride," Chem. Mater. **16**(25), 5445–5451 (2004).

[134] J. Wagner, and F. Bechstedt, "Properties of strained wurtzite GaN and AlN : Ab initio studies," 1–20 (2002).

[135] G. Abadias, E. Chason, J. Keckes, M. Sebastiani, G.B. Thompson, E. Barthel, G.L. Doll, C.E. Murray, C.H. Stoessel, and L. Martinu, “Review article: stress in thin films and coatings: current status, challenges, and prospects,” J. Vac. Sci. Technol. A **36**(2), 20801 (2018).

[136] G. Xie, Y. Guo, B. Li, L. Yang, K. Zhang, M. Tang, and G. Zhang, “Phonon surface scattering controlled length dependence of thermal conductivity of silicon nanowires,” Phys. Chem. Chem. Phys. **15**(35), 14647–14652 (2013).

[137] N. Mingo, L. Yang, D. Li, and A. Majumdar, “Predicting the thermal conductivity of Si and Ge nanowires,” Nano Lett. **3**(12), 1713–1716 (2003).

[138] C.Y. Ho, R.W. Powell, and P.E. Liley, “Thermal conductivity of the elements,” J. Phys. Chem. Ref. Data **1**(2), 279–421 (1972).

[139] Y.S. Touloukian, and E.H. Buyco, *Thermophysical Properties of Matter - the TPRC Data Series. Volume 4. Specific Heat - Metallic Elements and Alloys* (United States, 1971).

[140] A.D. Mah, W.W. Weller, and A.U. Christensen, *Thermodynamic Properties of Aluminum Nitride* (US Department of the Interior, Bureau of Mines, 1961).

[141] Y.S. Touloukian, and E.H. Buyco, *Thermophysical Properties of Matter - the TPRC Data Series. Volume 5. Specific Heat - Nonmetallic Solids. (Reannouncement). Data Book.* (IFI/Plenum, 1970).

Chapter 5

Substrate Dependence of the Self-heating in Lead Zirconate Titanate (PZT) MEMS Actuators

5.1 Introduction

Lead zirconate titanate (PZT) is a ferroelectric material that exhibits a higher piezoelectric coefficient (d_{33}) and larger electromechanical coupling factor than those for $BaTiO_3$ and $K_{1-x}Na_xNbO_3$. PZT-based devices are utilized in a wide range of technologies, enabling precise and responsive actuation, sensing, and energy harvesting applications.[1–4] However, self-heating in PZT can degrade the device reliability, especially in applications with large electric-field excitation or high-power operation. For example, excessive operational temperature rise can lead to reduced efficiency, drift in piezoelectric properties[5], material degradation due to thermal stress[6], and shift in the resonance frequencies of sensors and resonators[7,8]. Typically, actuators are intentionally limited to self-heating up to 20˚C above ambient temperature, in order to avoid changes in the domain structure.[9] Heat generation mechanisms in bulk PZT ceramics have been discussed in the literature.[9–11] Notably, heat generation was found to be caused by hysteresis loss due to domain wall motion. Domain walls act as boundaries that separate regions with different polarization orientations; their motion under applied electric fields leads to localized frictional heating. While self-heating in bulk PZT materials is well-understood, studies on the self-heating in PZT thin film-based MEMS structures are lacking.

PZT thin films in microelectromechanical systems (MEMS) can generate large motions; when the domain states are properly stabilized, they can also show low hysteresis, and high energy densities.[12] PZT thin films can be deposited on a variety of substrates such as Si[13], glass[14,15], metals[16,17], and $SrTiO_3$[18], which allows a range of mechanical and electrical performance in the elastic layer for piezoelectric MEMS devices.

The self-heating behavior in PZT thin films differs from that in PZT bulk ceramics in several aspects. First, PZT thin films often have restricted domain wall motion due to small grain size, high residual stress imposed by the substrate, and/or a high concentration of point and line defects.[19] Second, heat extraction from the film depends on the thermal conductivity of the substrate material and the structure of the device. Lundh et al. reported considerable self-heating in released PZT MEMS actuators under various driving conditions including multiple combinations of frequencies, AC amplitudes, and DC offsets.[20] Fragkiadakis et al. combined simulations and measurements of self-heating in PZT MEMS actuator arrays; they observed a temperature rise exceeding 100°C when closely spaced actuators operated simultaneously.[21] Both studies show the impact of driving conditions on self-heating in commercial PZT MEMS with released structures. This work aims to understand how substrate and device structure influences self-heating behavior in PZT film-based MEMS. Therefore, in this study, clamped PZT films were fabricated on Si and glass substrates and thermal excursions as a function of electrical excitation were examined using nanoparticle-assisted Raman thermometry. Additionally, a released structure was prepared. Results were validated and interpreted using device thermal modeling.

5.2 Device Fabrication

To investigate the heat dissipation on various substrates, PZT test structures were fabricated on Si and glass substrates, as shown in Fig. 1(a). In addition, released structures were prepared.

For PZT film on glass, a stack of 30 nm Ti and 100 nm Pt was deposited on 400 μm thick Corning Eagle glass. A commercial 114/52/48/2 solution of $PbZr_{0.52}Ti_{0.48}O_3$ from Mitsubishi

Materials Corporation was used for PZT film deposition. The solution was spun on at 2750 RPM for 30 seconds. The film was pyrolyzed at 100°C for 2 minutes and then at 300°C for 8 minutes. The film underwent crystallization processes, first at 520°C for 1 minute followed by ramping to 650°C at a rate of 3°C/second (a slow ramp rate was used to prevent the glass wafer from deforming or shattering); subsequently, the film was held at 650°C for 2 minutes. The crystallization processes were performed with a 2 sccm O_2 flow in a lead-rich rapid thermal annealer.[22] The process was repeated until a total PZT thickness of 0.98 μm was achieved. Subsequently, the top electrodes (3 nm of Ti and 100 nm of Pt) were deposited at room temperature via DC magnetron sputter deposition without breaking the vacuum. These were then patterned into circular shaped electrodes using the lift-off process. A schematic of the completed structure on glass substrate is shown in **Figure 5.1 (b)**.

The detailed deposition process for PZT on Si used in this study has been described elsewhere.[23] The PZT film on Si and the released structure were fabricated on the same 4-inch Si wafer. The PZT film was deposited on a commercial platinized Si wafer with 1 μm of SiO_2 thermal oxide. 20 nm Ti and 150 nm Pt were deposited as the bottom electrode. The solution and spinning conditions used were similar to those previously described. The film was pyrolyzed at 100 °C for 1 minute and at 300 °C for 4 minutes, followed by crystallization at 700°C thermal annealing with 2 sccm O_2 flow for 1 minute. The process was repeated until a total PZT thickness of 1.08 μm was achieved. Then, the top electrode was deposited and patterned through a lift-off process similar to that of the glass substrate sample.

Following this, an Al_2O_3 insulator pad was deposited using thermal atomic layer deposition on a commercial Kurt-Lesker ALD 150LE (Kurt J. Lesker, Pennsylvania, USA) system at 150°C, employing tetramethylammonium hydroxide (TMAH) and H_2O as precursors. The Al_2O_3 thin film underwent lithographic patterning and was wet-etched (using a TMAH-based developer and CD-26) into a rectangular insulating pad. The contact pad, consisting of 3 nm of Ti and 100 nm of Pt, was deposited and patterned using a process similar to that of the top electrode. The metal pad was positioned on top of an Al_2O_3 pad to insulate it from the PZT thin film. Finally, the Pt bottom electrode was exposed by wet etching the PZT thin film into a rectangular shape using a mixed solution of hydrochloric acid, 6:1 buffered oxide etchant, and deionized water. A schematic of the completed structure on Si is shown in **Figure 5.1 (c).**

To prepare a released PZT film, SiO_2 was removed on the back side by submerging the sample in a 6:1 buffered oxide etch (BOE) solution at room temperature, while the front side was protected with a blanket photoresist. After etching, the sample was cleaned in acetone, isopropyl alcohol, and deionized water. Then, the front side was coated with ProTEK B3 as a protective layer. Deep reactive ion etching (DRIE) was performed in a DSi-V Deep Silicon Etch system (SPTS, Newport, USA) using the Bosch process at 3°C; thick AZ4620 photoresist was utilized as a soft mask. For the release process, the sample was etched until the trench reached the buried SiO_2 layer. It is important to note that the diaphragm is delicate due to the low thickness and the choice not to use a passive elastic support. Fully removing the Si without breaking the diaphragm proved challenging. Thus, residual Si on the trench edges at the backside of the diaphragm can be seen in some devices, as depicted in **Figure 5.1 (d)**. **Figure 5.1 (e)** shows scanning electron microscopy (SEM) images of the cross-section of the released structure. The residual Si thickness on this structure measured 170 nm. It is noted that the remaining Si thickness varied along the radius of the wafer.

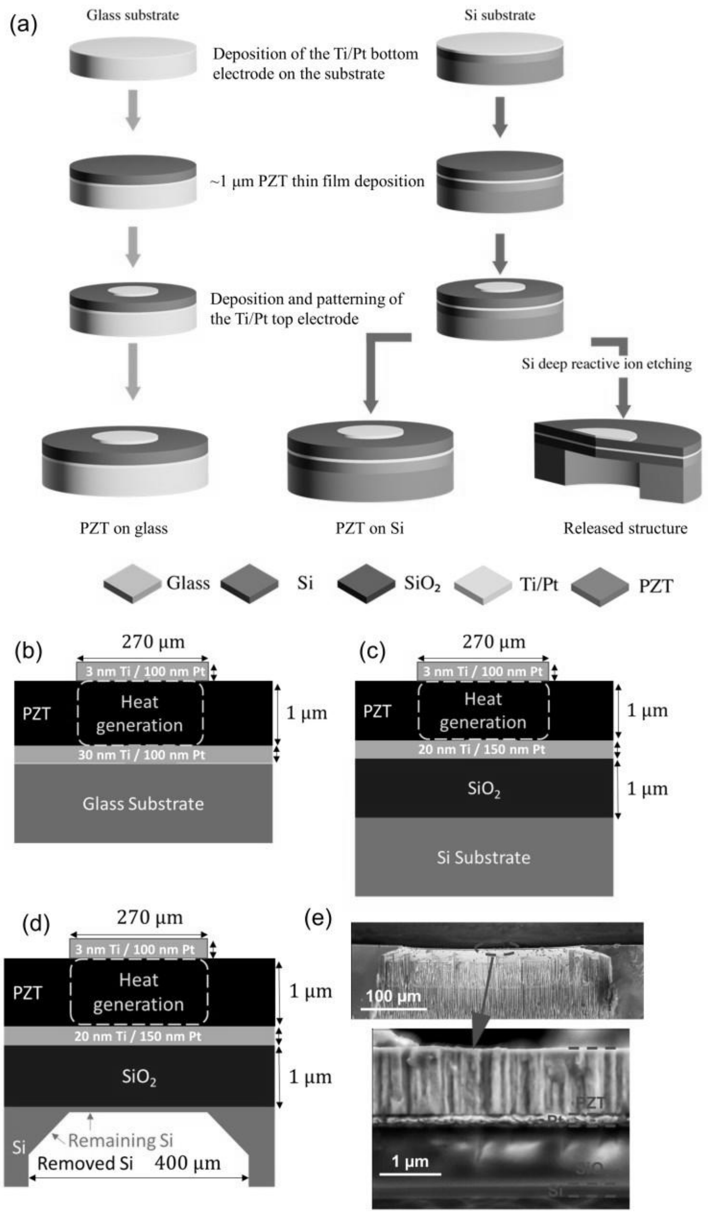

Figure 5.1: (a) The device fabrication process that illustrates preparation of the bottom electrode on a substrate, deposition of a blanket PZT thin film, and lift-off/patterning of the top electrode. The deposition and patterning of the Al_2O_3 insulator and Ti/Pt contact pads are not shown in this figure. Schematics of PZT on (b) glass, (c) Si, and (d) a released structure (not to scale). (e) Cross-sectional SEM images of the PZT film released from a Si substrate.

5.3 Thermal Characterization

Raman thermometry allows *in situ* characterization of device self-heating with a sub-micrometer resolution by monitoring changes in the optical phonon energy (or frequency) using a monochromatic laser excitation source.[24–26] In practice, the lattice temperature rise is estimated based on the spectral features of the Raman peaks including peak position, line width, and anti-Stokes/Stokes Raman intensity ratio. Standard Raman thermometry has been demonstrated for the thermal characterization of microelectronics based on materials with well-defined Raman peaks such as Si[27] and GaN[25,28]. However, the characteristic Raman peaks of PZT are too broad to track the small changes in peak position and linewidth essential to estimate the temperature rise, as shown in **Figure 5.2 (a)**. In addition, the crystal's phonon energy is a function of temperature and film stress, which change periodically under AC driving conditions; moreover, the top electrode blocked visual access to the film. Therefore, nanoparticle-assisted Raman thermometry [29,30] was used. Anatase titanium dioxide (TiO_2) nanoparticles (with 99.98% purity and ~200 nm individual size) were deposited on the surface of the top electrodes, serving as a temperature probe. As shown in **Figure 5.2 (b)**, TiO_2 nanoparticles exhibit a well-defined Raman peak (i.e., the E_g phonon mode with a frequency of ~143 cm^{-1} at room temperature) that are highly sensitive to changes in temperature[30]. This allowed precise temperature measurements. Notably, temperature values deduced from the use of TiO_2 nanoparticles are free from thermoelastic stress effects because the thermal expansion of the nanoparticles is not restricted by the underlying surface.[31]

Details of the Raman setup and experimental procedures have been previously reported by Lundh[31]; a concise summary is provided here for reference. A LabRAM HR Evolution spectrometer (Horiba, New Jersey, USA) equipped with a 532 nm laser source and 1800 grooves/mm grating, and a 50× long working distance objective (NA=0.45) was used for Raman thermometry experiments. To prevent laser-induced heating of both the TiO_2 nanoparticles and the underlying top electrode, a laser power of ~1 mW was used. A reference mercury emission line at approximately 546 nm was continuously monitored to account for instrument drift (i.e., systematic errors/offsets in the measured Raman spectra) attributed to room temperature fluctuations. To apply an AC electric field to the device, a DS345 (Stanford Research Systems, California, USA) function generator was used to control the operational frequency and DC offset of an AT Techron 7228 amplifier (AE Techron, Indiana, USA) that managed the output voltage amplitude.

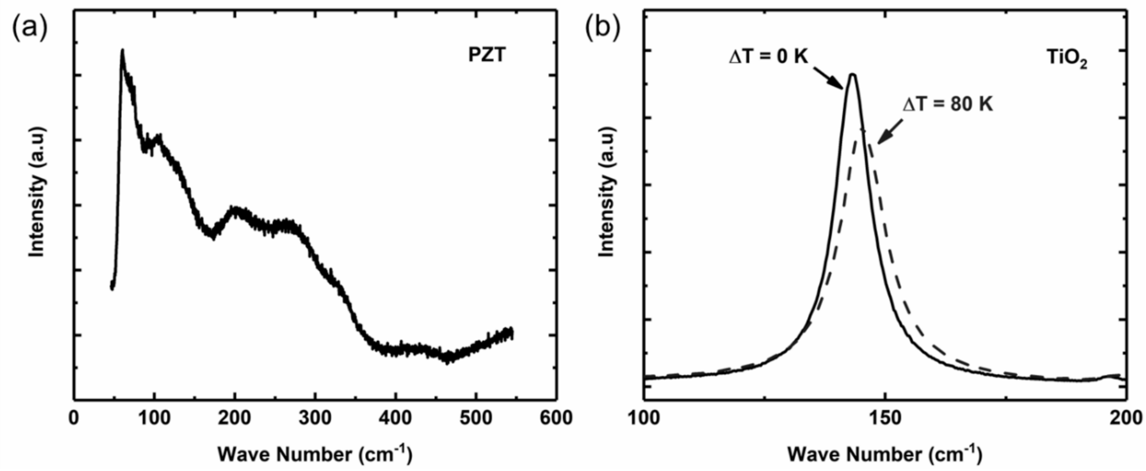

Figure 5.2: (a) Raman spectra of PZT, (b) The Raman peaks of the E_g phonon mode of TiO_2 nanoparticles at different temperatures.

5.4 Electrical Characterization and Device Modeling

3D finite element analysis (FEA) thermal modeling of the PZT MEMS devices was performed using COMSOL Multiphysics to account for heat dissipation through the device structure. Room temperature thermal conductivity values were used in the simulation due to the relatively small amount of self-heating (< 20 K).

Heat generation in PZT is known to be mainly caused by hysteresis loss due to domain wall motion.[9,10] Therefore, the volumetric heat generation per cycle was experimentally determined from the area enclosed by the polarization-electric field (P-E) loops. The power density (Q) was determined by multiplying the frequency by the heat generation per cycle.[21]

$$Q = f \times \int E \, dP \tag{5.1}$$

where f is the frequency, E is the electric field, and P is the polarization. The films underwent a large number of cycles (~3 million cycles) due to the high frequency and long acquisition time required to perform the NP Raman measurement. Thus, the magnitude of hysteresis loss may change during the cycles due to fatigue.[32] Therefore, P-E loops of both fresh films and films after cycling were measured. Self-heating was calculated using both values to account for the possible temperature range at different points in the fatigue cycle. Representative P-E loops for fresh and fatigued films driven by a 10 kHz sinusoidal waveform with an amplitude of 250 kV/cm for PZT on glass, Si, and the released structure are shown in **Figure 5.3 (a), (b), and (c)**, respectively. It should be noted that the films were prone to failure under large fields and high frequencies; therefore, the maximum field used for thermal study was limited to a relatively low magnitude of 150 kV/cm. A summary of the test conditions and their corresponding heat generation rates is shown in **Table 5.1**.

Since the devices had a circular top electrode, rotational axial symmetry was applied to the model to mitigate computational costs. An isothermal boundary condition was imposed at the bottom of the substrate (to mimic the experimental setup where the devices were placed on a temperature-controlled stage), and natural convection was applied to all other surfaces. A mesh convergence study was performed to confirm that the results did not change at higher mesh densities.

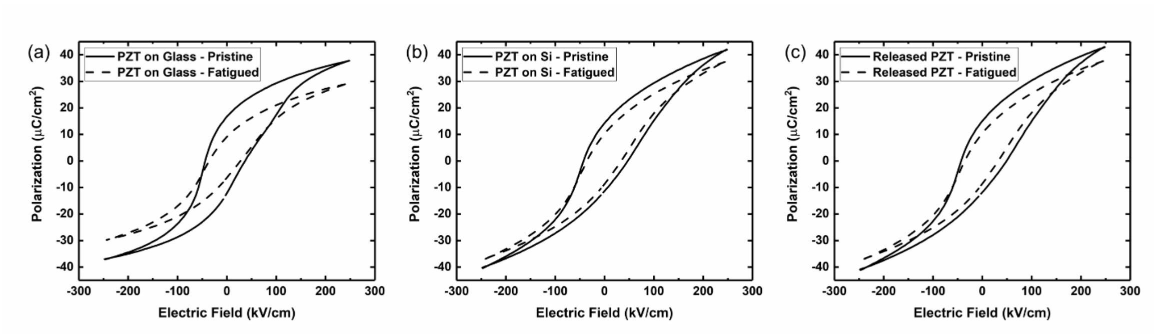

Figure 5.3: The P-E loop characterization results at a frequency of 10 kHz (sinusoidal waveform) of the PZT films on (a) a glass substrate, (b) a Si substrate, and (c) a released structure. The pristine loops were measured before cycling and the fatigued loops were measured after 1×10^6 cycles.

Table 5.1: The calculated power densities (GW/m^3) from fatigued P-E loops at 10 kHz

	50 kV/cm	100 kV/cm	150 kV/cm
PZT on glass	1.3	8.3	16.9
PZT on Si	1.4	8.5	19.2
PZT fully released	1.4	8.4	19.6

5.5 Results and Discussion

Figure 5.4 compares the temperature rise of PZT films on glass and Si substrates and two fully released films when operated under a 10 kHz bipolar AC electric field. Measurement data acquired from nanoparticle-assisted Raman thermometry was in good agreement with the FEA thermal modeling results. While no significant temperature rise occurred in the PZT films on a Si substrate, clear evidence of device self-heating was observed for the PZT films on a glass substrate. Notably, the measured power densities of the PZT films on Si and on glass substrates are comparable, especially prior to the fatigue cycles. The discrepancy in device self-heating was caused by the different thermal conductivity of the Si (~130 W/mK at room temperature) and glass

(~1 W/mK) substrates. While a similar amount of heat (19.2 GW/m^3 and 16.9 GW/m^3) was generated in both cases, the Si substrate effectively removed heat from the active region and acted as an effective heat sink, resulting in a negligible device temperature rise.

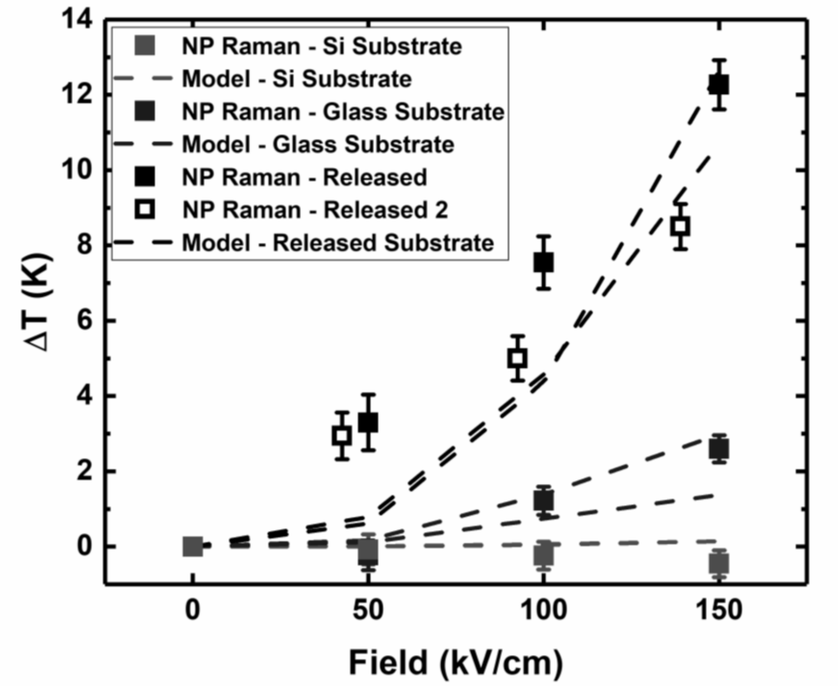

Figure 5.4: The temperature rise of PZT on Si, PZT on glass, and two fully released PZT devices operated with a 10 kHz bipolar field. The modeling results are bounded by two dashed lines: the upper and lower lines correspond to results based on the P-E loops (i.e., measured heat generation rates) of fresh and fatigued devices, respectively. The self-heating in PZT on Si is negligible. The negative temperature results (~ -0.5 K) are attributed to room temperature fluctuation.

No significant changes were observed in the P-E loop between the released film and the film on Si, indicating negligible change in the global stress state. Upon fully release of the PZT film from the Si substrate, the heat dissipation became markedly less effective, leading to more intense device self-heating. As illustrated in **Figure 5.4**, a much larger increase in temperature was observed in the fully released films as compared to the films on solid substrates. Two fully released structures were tested to account for random errors caused by room temperature fluctuations and local variations in the film quality. While the measured temperatures and the modeling results agree well under high field conditions, a notable difference is observed under low field operation. This discrepancy may have resulted from additional heating mechanisms such as Joule heating in the electrode. The effect of such heating mechanisms would become more noticeable under low field operation because of the relatively low hysteresis loss that is manifested by the small P-E loop area. Conversely, under higher field operation (e.g., 150 kV/cm), the hysteresis loss is the dominant heat generation mechanism, resulting in a closer agreement between the measured temperature rise and the modeling results (that are purely based on the hysteresis loss). Simulation results suggest that the peak temperature rise of a fully released device will be 6.8× higher (under 150 kV/cm operation) than that of a film on a glass substrate. Therefore, fully released piezoelectric MEMS structures will be prone to thermal reliability issues and more exacerbated self-heating is expected to occur in actuator arrays as reported by Fragkiadakis *et. al.*[21].

As discussed in the fabrication section, the DRIE process produces non-uniform etching across the wafer. Because there is no hard etch stop, there is some residual Si underneath the released diaphragm; the thickness of the remaining Si layer varied depending on the location. The exact thickness of the remaining Si was measured using cross-sectional SEM on multiple devices across the wafer. Near the center of the wafer where the etch rate was slower, the Si thickness was a few hundred nanometers thicker.

Therefore, it is crucial to understand the impact of the remaining Si thickness on device thermal performance. Additional NP Raman measurement and modeling were performed on a device with 170 nm of Si remaining. A higher field (200 kV/cm) and a higher frequency (20 kHz) were used. A temperature rise of 12.2 ± 1.6 K was detected using Raman thermometry.

A parametric sweep of the remaining Si thickness was performed (using the device thermal model) to evaluate its effect on device self-heating. As depicted in **Figure 5.5**, when Si is completely removed, the temperature rise in the PZT film exceeds 25°C under 200 kV/cm bipolar AC electric field operation at a frequency of 20 kHz. This produced an experimental power density of 91.8 GW/m^3. The film's thermal response was highly sensitive to the remaining Si thickness. This was attributed to the lower thermal conductance of the PZT film as compared to Si; that is, the remaining Si layer transferred heat away from the device active region more effectively. Consequently, the device temperature rise was substantially smaller, even with a thin layer of Si remaining. For example, 200 nm thick residual Si reduced the temperature rise by over 50% as compared to a fully released case. This suggests that the Si layer utilized in most SOI-based piezoelectric MEMS is critical for effective thermal management. It is important to note that this study is based on a single device. In the case of actuator arrays, such as in the case of a piezoelectric inkjet print head, the temperature rise is amplified due to thermal crosstalk.[21] For such applications, inclusion of a high thermal conductivity passive elastic layer behind the active piezoelectric film may significantly improve the thermal performance at both device- and system-levels.

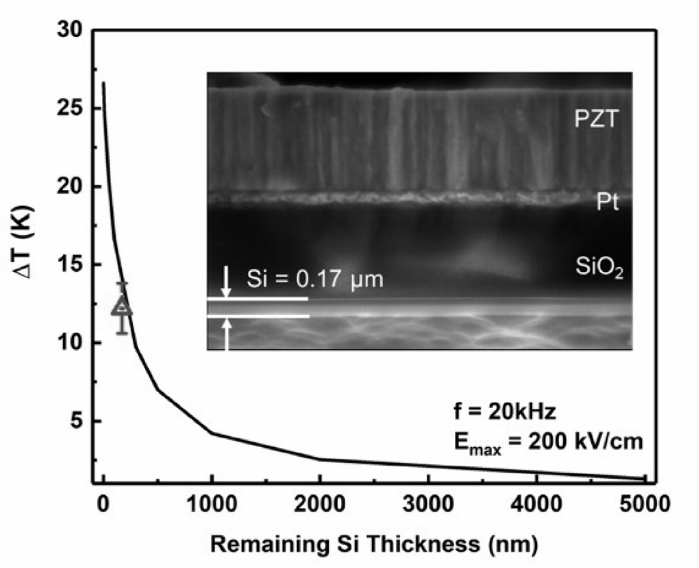

Figure 5.5: The device temperature rises as a function of the remaining Si thickness. The image insert shows a device structure with 170 nm of Si remaining below the PZT film. This device was tested via Raman thermometry and the red marker shows the measurement results (12.2 ± 1.6 K).

5.6 Conclusion

The self-heating behavior of lead zirconate titanate (PZT) thin films fabricated on glass and Si substrates as well as a released structure were measured using nanoparticle-assisted Raman thermometry. The results show that PZT thin films on a Si substrate exhibit a minimal temperature rise, attributed to the high thermal conductivity of the substrate material. In contrast, PZT thin films on a glass substrate exhibit notable self-heating due to the two orders of magnitude lower thermal conductivity of glass limiting vertical heat extraction from the device active region. When the PZT film is fully released from a Si substrate, the device temperature rise exceeds that of a PZT film on glass by 6.8× under the highest electric field test condition (150 kV/cm). Both experimental and simulation results suggest that a residual Si layer underneath the PZT film can significantly reduce the film temperature rise caused by device self-heating. These findings highlight that the choice of the passive elastic layer of PZT MEMS actuator arrays (in terms of the thermal conductivity and thickness of the layer) strongly influences effective thermal management at both device- and system-levels.

Chapter References

[1] S. Priya, “Criterion for material selection in design of bulk piezoelectric energy harvesters,” IEEE Trans Ultrason Ferroelectr Freq Control **57**(12), 2610–2612 (2010).

[2] P. Janphuang, R. Lockhart, N. Uffer, D. Briand, and N.F. de Rooij, “Vibrational piezoelectric energy harvesters based on thinned bulk PZT sheets fabricated at the wafer level,” Sens Actuators A Phys **210**, 1–9 (2014).

[3] Y. Qiu, J. V Gigliotti, M. Wallace, F. Griggio, C.E.M. Demore, S. Cochran, and S. Trolier-McKinstry, “Piezoelectric micromachined ultrasound transducer (PMUT) arrays for integrated sensing, actuation and imaging,” Sensors **15**(4), 8020–8041 (2015).

[4] P. Muralt, R.G. Polcawich, and S. Trolier-McKinstry, “piezoelectric thin films for sensors, actuators, and energy harvesting,” MRS Bull **34**(9), 658–664 (2009).

[5] M H Lente, J A Eiras, M.H. Lente, and J.A. Eiras, “Interrelationship between self-heating and ferroelectric properties in PZT ceramics during polarization reorientation,” Journal of Physics: Condensed Matter **12**(27), 5939 (2000).

[6] M. Stewart, and M.G. Cain, “Measurement and modelling of self-heating in piezoelectric materials and devices,” in Characterisation of Ferroelectric Bulk Materials and Think Films edited by M.G. Cain (Springer Netherlands, Dordrecht, 2014), pp. 147–189.

[7] S. Yan, C. Sun, Q. Cui, M. He, Willhandy, R. Wang, J. Hao, and X. Chu, “Dielectric, piezoelectric and dc bias characteristics of Bi-doped PZT multilayer ceramic actuator,” Mater Chem Phys **255**, 123605 (2020).

[8] Z. Wu, and S. Cochran, “Loss effects on adhesively-bonded multilayer ultrasonic transducers by self-heating,” Ultrasonics **50**(4), 508–511 (2010).

[9] K. Uchino, J.H. Zheng, Y.H. Chen, X.H. Du, J. Ryu, Y. Gao, S. Ural, S. Priya, and S. Hirose, “Loss mechanisms and high power piezoelectrics,” J Mater Sci **41**(1), 217–228 (2006).

[10] J. Zheng, S. Takahashi, S. Yoshikawa, K. Uchino, and J.W.C. Vries, "Heat generation in multilayer piezoelectric actuators," Journal of the American Ceramic Society **79**(12), 3193–3198 (2018).

[11] M.S. Senousy, R.K.N.D. Rajapakse, D. Mumford, and M.S. Gadala, "Self-heat generation in piezoelectric stack actuators used in fuel injectors," Smart Mater Struct **18**(4), 45008 (2009).

[12] S. Trolier-McKinstry, and P. Muralt, "Thin film piezoelectrics for MEMS," J Electroceram **12**(1), 7–17 (2004).

[13] A. Dangi, C.Y. Cheng, S. Agrawal, S. Tiwari, G.R. Datta, R.R. Benoit, R. Pratap, S. Trolier-McKinstry, and S.-R. Kothapalli, "A photoacoustic imaging device using piezoelectric micromachined ultrasound transducers (PMUTs)," IEEE Trans Ultrason Ferroelectr Freq Control **67**(4), 801–809 (2020).

[14] R.H.T. Wilke, S. Trolier-McKinstry, P.B. Reid, and D.A. Schwartz, in *Proc. SPIE* (2010), p. 78030O.

[15] R.H.T. Wilke, R.L. Johnson-Wilke, V. Cotroneo, W.N. Davis, P.B. Reid, D.A. Schwartz, and S. Trolier-McKinstry, "Sputter deposition of PZT piezoelectric films on thin glass substrates for adjustable x-ray optics," Appl Opt **52**(14), 3412–3419 (2013).

[16] T. Peters, C. Cheng, G.A. Rossetti Jr, and S. Trolier-McKinstry, "Thermal stress accommodation in dip cast lead zirconate-titanate ferroelectric films on flexible substrates," Journal of the American Ceramic Society **105**(6), 4058–4070 (2022).

[17] D. Wang, S. Dursun, L. Gao, C.S. Morandi, C.A. Randall, and S. Trolier-McKinstry, "Fabrication of bimorph lead zirconate titanate thick films on metal substrates via the cold sintering-assisted process," Acta Mater **195**, 482–490 (2020).

[18] K. Gotoh, H. Tamura, H. Takauchi, and A. Yoshida, "Pt/PZT/n-$SrTiO_3$ Ferroelectric Memory Diode," Jpn J Appl Phys **35**(1R), 39 (1996).

[19] N. Bassiri-Gharb, I. Fujii, E. Hong, S. Trolier-McKinstry, D. V Taylor, and D. Damjanovic, "Domain wall contributions to the properties of piezoelectric thin films," J Electroceram **19**(1), 49–67 (2007).

[20] J.S. Lundh, W. Zhu, Y. Song, S.W. Ko, C. Fragkiadakis, P. Mardilovich, S. Trolier-McKinstry, and S. Choi, "Local measurements of domain wall-induced self-heating in released $PbZr_{0.52}Ti_{0.48}O_3$ films," J Appl Phys **128**(21), 214102 (2020).

[21] C. Fragkiadakis, S. Sivaramakrishnan, T. Schmitz-Kempen, P. Mardilovich, and S. Trolier-McKinstry, "Heat generation in PZT MEMS actuator arrays," Appl Phys Lett **121**(16), 162906 (2022).

[22] M. Wallace, "Performance of PZT based MEMS devices with integrated ZnO electronics," Ph.D. thesis, the Pennsylvania State University, United States, Pennsylvania, (2016), pp. 17–21.

[23] C. Cheng, "Piezoelectric micromachined ultrasound transducers using lead zirconate titanate films," Ph.D. thesis, the Pennsylvania State University, December, (2021), pp. 30–32.

[24] J.S. Lundh, Y. Song, B. Chatterjee, A.G. Baca, R.J. Kaplar, A.M. Armstrong, A.A. Allerman, B.A. Klein, D. Kendig, H. Kim, and S. Choi, "Device-level multidimensional thermal dynamics with implications for current and future wide bandgap electronics," J Electron Packag **142**(3), 031113 (2020).

[25] S. Choi, E.R. Heller, D. Dorsey, R. Vetury, and S. Graham, "Thermometry of AlGaN/GaN HEMTs using multispectral Raman features," IEEE Trans Electron Devices **60**(6), 1898–1904 (2013).

[26] T. Beechem, A. Christensen, S. Graham, and D. Green, "Micro-Raman thermometry in the presence of complex stresses in GaN devices," J Appl Phys **103**(12), 124501 (2008).

[27] J.R. Serrano, L.M. Phinney, and S.P. Kearney, "Micro-Raman thermometry of thermal flexure actuators," Journal of Micromechanics and Microengineering **16**(7), 1128 (2006).

[28] S.K. Oh, J.S. Lundh, S. Shervin, B. Chatterjee, D.K. Lee, S. Choi, J.S. Kwak, and J.-H. Ryou, "Thermal management and characterization of high-power wide-bandgap semiconductor electronic and photonic devices in automotive applications," J Electron Packag **141**(2), 020801 (2019).

[29] Y. Song, A. Bhattacharyya, A. Karim, D. Shoemaker, H.-L. Huang, S. Roy, C. McGray, J.H. Leach, J. Hwang, S. Krishnamoorthy, and S. Choi, "ultra-wide band gap Ga_2O_3-on-SiC MOSFETs," ACS Appl Mater Interfaces **15**(5), 7137–7147 (2023).

[30] J. Dallas, G. Pavlidis, B. Chatterjee, J.S. Lundh, M. Ji, J. Kim, T. Kao, T. Detchprohm, R.D. Dupuis, S. Shen, S. Graham, and S. Choi, "Thermal characterization of gallium nitride p-i-n diodes," Appl Phys Lett **112**(7), 73503 (2018).

[31] J.S. Lundh, "Thermomechanical analysis of emerging microsystems using Raman spectroscopy," Ph.D. thesis, the Pennsylvania State University, December, (2021), pp. 19-39.

[32] M. Ozgul, S. Trolier-McKinstry, and C.A. Randall, "Fatigue induced effects on bipolar strain loops in PZN-PT piezoelectric single crystals," J Electroceram **20**(3), 133–138 (2008).

Chapter 6

Summary and Future Work

6.1 Summary

This dissertation addresses the thermal challenges of modern microsystem technologies based on β-Ga_2O_3, β-$(Al_xGa_{1-x})_2O_3$, AlN, $Al_{1-x}Sc_xN$, and PZT. Material-level thermal property measurements were conducted using FDTR, TDTR, and SSTR techniques, with the obtained values serving as inputs for finite element analysis (FEA) thermal modeling. Furthermore, device-level thermal characterization was carried out using Raman thermometry to validate the FEA model. The calibrated FEA models were then utilized to propose, evaluate, and optimize the performance of thermal management solutions.

Thermal conductivity of β-Ga_2O_3 and β-$(Al_xGa_{1-x})_2O_3$ heteroepitaxial thin films was found to be a strong function of film thickness and quality. Growing films on offcut sapphire substrates enhances their crystallinity and thermal conductivity; however, the thermal boundary conductance at the Ga_2O_3/sapphire heterointerface is reduced compared to growing films on an on-axis c-plane sapphire. Phonon-alloy disorder scattering dominates to the reduction in the thermal conductivity of $(Al_xGa_{1-x})_2O_3$, as evidenced by the weak temperature dependence observed in the thermal conductivity of $(Al_xGa_{1-x})_2O_3$ films.

A novel Ga_2O_3/SiC composite wafer was manufactured as a thermal management solution for Ga_2O_3-based electronics. The thermal boundary conductance at the bonding interface was characterized using a newly developed approach based on differential SSTR and was further validated by FDTR. It was discovered that the primary performance limitation of the current design stems from the relatively thick SiN_x bonding layer and the unintentionally formed SiO_x.

Nevertheless, thermal simulations demonstrated a significant enhancement in thermal performance with the composite wafer design.

Ga_2O_3 MOSFETs were then fabricated on the composite wafer. Raman thermometry was used to characterize their self-heating, revealing a 56% reduction in channel temperature compared to devices on native Ga_2O_3 substrate. Simulations suggested that further improvement in cooling performance could be achieved by reducing the thickness of Ga_2O_3, employing higher thermal conductivity diamond substrates, and optimizing the bonding interface.

Thermal conductivity and the microstructure of AlN films fabricated with various growth methods were characterized. The cross-plane thermal conductivity is primarily restricted by the film thickness, whereas the in-plane thermal conductivity is limited by the presence of grain boundaries and dislocations. A scattering model was employed to investigate the impact of impurity concentration on the thermal conductivity. Based on the acquired data, thermal simulations suggested that the self-heating on an FBAR can vary drastically depending on the AlN growth method.

Thermal transport in $Al_{1-x}Sc_xN$ was thoroughly investigated. Phonon-alloy disorder scattering causes an order of magnitude reduction in thermal conductivity of $Al_{1-x}Sc_xN$ compared to AlN with similar crystal structures. The results of thickness-dependent thermal conductivity suggest a phonon mean-free path on the order of 400 nm. Temperature-dependent thermal conductivity results suggested the heat transport in $Al_{1-x}Sc_xN$ is not dominated by Umklapp scattering. Furthermore, abnormally oriented grains were shown to have minimal effect from a thermal perspective. There results were supported by a theoretical calculation based on virtual crystal approximation.

Finally, device-level thermal characterization was conducted on PZT piezoMEMS. High thermal conductivity Si substrate was found to minimize the temperature rise due to self-heating. Conversely, low thermal conductivity materials such as glass limited heat extraction from the device's active region. When the PZT film was fully released from a substrate, the device's temperature rose drastically. However, both experimental and modeling results suggested that a residual Si layer underneath the released film could effectively reduce the device's temperature rise. This study highlights the potential of strategically choosing a passive elastic layer as a thermal management solution.

6.2 Future Work

6.2.1 Device-level Thermal Characterization of $Al_{1-x}Sc_xN$ FBARs

The thermal conductivity of $Al_{1-x}Sc_xN$ films, characterized in this study, is below 8 W/mK, which is an order of magnitude lower than that of AlN films. Therefore, $Al_{1-x}Sc_xN$ RF filters are prone to overheating, which can restrict maximum data transmission, decrease device lifespan, and cause frequency drift.[1–4] While $Al_{1-x}Sc_xN$ resonators show potential for technological improvement, the impact of self-heating on their electro-acoustic performance has yet to be addressed by industry and academic researchers. Limited discussion on self-heating in $Al_{1-x}Sc_xN$ resonators is solely based on modeling work. In this modeling work, *Zheng et al.*[5] assumed a volumetric heat density for $Al_{1-x}Sc_xN$ FBAR based on its AlN counterpart. However, due to the loss mechanisms closely related to the intrinsic material properties, heat generation in the two material systems can vary. Therefore, direct experimental measurements of self-heating during operation can provide a more accurate thermal assessment.

Previous, infrared (IR) thermometry has been used to study the self-heating of AlN FBAR.[4] Our initial attempt using IR thermometry to measure $Al_{1-x}Sc_xN$ FBAR revealed the room temperature emissivity (ε) of the active area is below the minimal requirement to obtain accurate results. The base temperature needs to be elevated to 65 ˚C for the emissivity to be useable as shown in **Figure 6.1 (a)**. Preliminary thermal imaging results for a $Al_{0.8}Sc_{0.2}N$ FBAR operated at resonance frequency of 6.06 GHz and 16.6 dBm RF power showed a temperature rise of 35 K as shown in **Figure 6.1 (b)**. While the FBAR is designed to operate within an ambient temperature of 85°C, the additional temperature increase resulting from self-heating may push the device beyond its intended operational limits. Consequently, the resonance frequency may shift and deviate from the condition used in the test. Temperature-dependent electro-mechanical characterizations should be performed to address this issue.

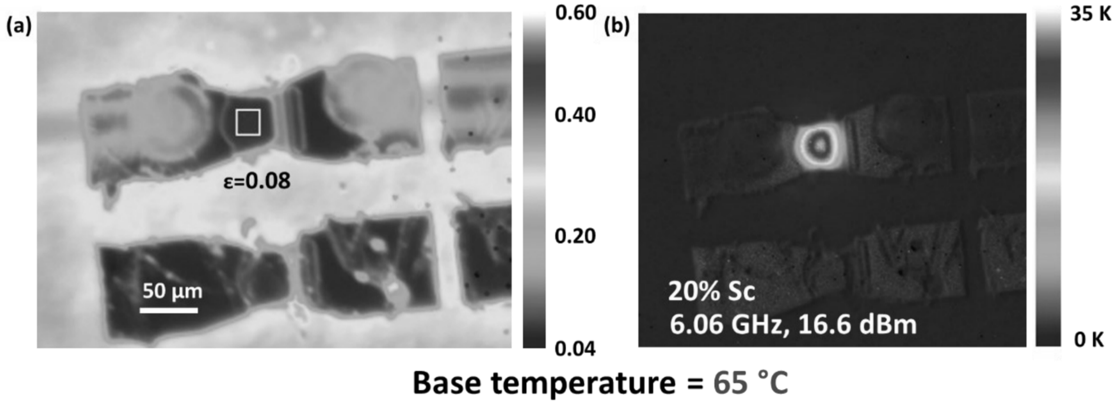

Figure 6.1: (a) emissivity map of the FBAR, and (b) IR temperature map of the FBAR at elevated base temperature of 65 ˚C.

It is also important to consider that IR thermometry tends to underestimate peak temperatures due to its relatively low spatial resolution (~3-10 µm).[6] Additionally, the emissivity calibration and the thermal imaging procedure in IR thermography may not be suitable for characterizing a device in motion, which can lead to motion-induced artifacts.[7] Therefore, a 2D material-assisted Raman thermography[8] technique is suggested to characterize the FBAR structures. This technique utilizes a monolayer MoS_2 film that conforms to the FBAR surface as a temperature transducer, which does not induce mass loading and is compatible with devices in motion.

This study aims to compare the self-heating of $Al_{1-x}Sc_xN$ FBARs with different Sc composition. Comprehensive material characterizations will accurately determine the film thickness, composition, and microstructures. Thermal characterization will utilize both IR and 2D material-assisted Raman thermography to accurately measure device self-heating. Using a COMSOL multi-physics device model, the heat generation in the FBARs can be calculated by correlating the measured temperatures. As heat generation results from losses in the FBAR, the quality factor Q can be compared among FBARs with varying Sc composition. The findings of this study will identify thermal constraints and offer crucial insights into the ideal alloy composition and film structure for 5G RF filters utilizing $Al_{1-x}Sc_xN$.

6.2.2 Thermal Characterization of Diamond-on-Ga_2O_3 Top-side Cooling

This dissertation demonstrated bottom-side composite wafer as a thermal management solution for β-Ga_2O_3 devices. While such solution is effective, keeping the native β-Ga_2O_3 substrates benefits cost-effective manufacturing. Shoemaker et al. demonstrated a potential cooling solution for UWBG materials using a top-side diamond layer and a flip-chip design.[9] Typically, diamond nanoparticles are used as seeding layers for subsequent growth. The size and coverage of the diamond nanoparticles can affect the thermal boundary resistance and the quality of the polycrystalline diamond.[10,11] While the thermal properties of CVD diamond have been previously reported,[12–14] device-level characterizations were only performed via modeling due to the challenges in device fabrication. Recently, Malakoutian et al. from Stanford University demonstrated a low-temperature (300-400°C) CVD method for growing polycrystalline diamond, which facilitates device-first fabrication and enhances the feasibility of top-side diamond cooling.[15] Material- and device-level thermal characterization are needed to provide important insight to optimize cooling performance using top-side diamond approach.

Due to the large bandgap energy of diamond and β-Ga_2O_3, optical thermal imaging techniques such as Raman thermometry and IR are unsuitable for device-level thermal characterization because these materials are transparent to the probe wavelength. Nanoparticle-assisted Raman thermometry is also limited to measuring the temperature at the diamond surface rather than the actual channel temperature. Consequently, accurately measuring the peak temperature in UWBG material-based devices with top-side diamond requires extra consideration. One method to measure the channel temperature is using confocal Raman thermometry, which enables ~1 μm vertical resolution at the focal plane to minimize depth averaging.[16] The depth temperature profile also has the merit of validating FEA modeling. Typically, only the lateral profile is matched between the model and experiments.[17,18] The vertical temperature profile is crucial for validating the thermal boundary conditions used in the FEA model. This is particularly important for high-power, large-size devices, such as multi-finger devices, because heat can propagate through the thickness of the wafer into the testing stage, which can invalidate the isothermal boundary condition typically used at the bottom surface of the substrate.[19] Thus, enabling such measurement capabilities is highly beneficial for characterizing UWBG materials.

Previously, directionally-averaged thermal conductivity of CVD diamond grown on β-Ga_2O_3 was studied by our group.[14] However, CVD diamond exhibits a columnar grain structure that typically varies along the growth direction, as illustrated in **Figure 6.2 (a).** Consequently, the thermal conductivity of CVD diamond can be both inhomogeneous along its thickness and anisotropic in in-plane and cross-plane directions. With the newly enabled capabilities of the TDTR system at Penn State, it is now possible to achieve separate sensitivity to the in-plane and cross-plane thermal conductivities of diamond on β-Ga_2O_3 with different combination of spot sizes and modulation frequencies, as illustrated in **Figure 6.2 (b)**. The material- and device-level assessment of top-side diamond cooling performance will provide valuable data for the design optimization.

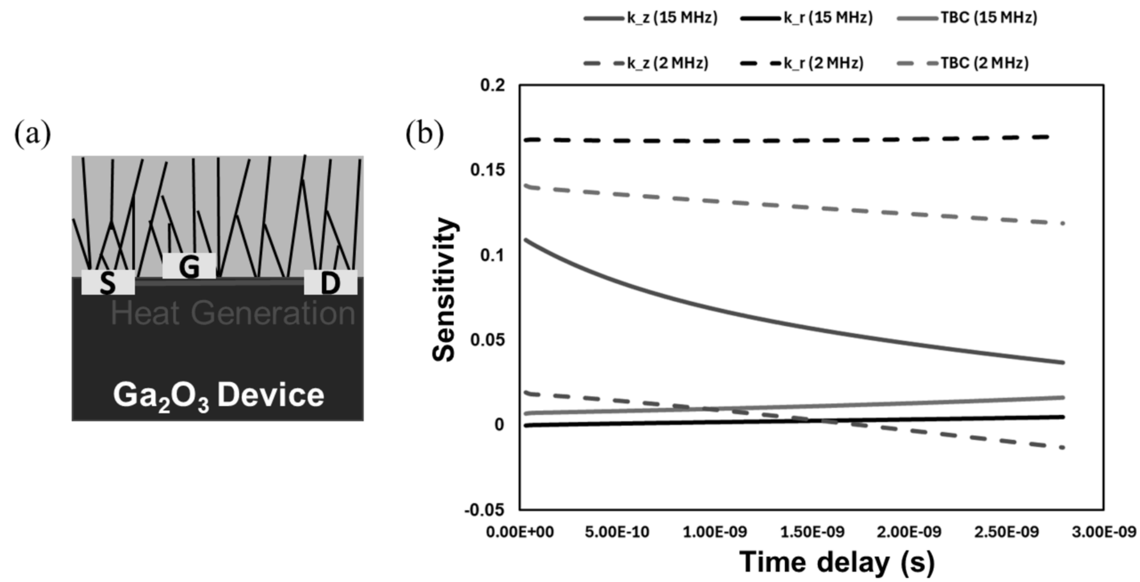

Figure 6.2: (a) Schematic of polycrystalline diamond grown on β-Ga_2O_3 device, and (b) TDTR sensitivity for cross-plane thermal conductivity (k_z), in-plane thermal conductivity (k_r), and thermal boundary conductance (TBC) at high (15 MHz) and low (2 MHz) modulation frequencies.

6.2.3 Thermal Property Measurement using Raman Thermometry

In this dissertation, it is demonstrated that accurate characterization of thermal properties is crucial for modern material systems. Techniques such as TDTR, FDTR, and SSTR, which are custom-built systems, are generally inaccessible to most research institutions. Therefore, there is a need to enable the measurement of thermal properties using common technique in material research. This section proposes several potential approaches to utilize Raman spectroscopy for extracting material thermal properties.

The first approach is using circular electrical heaters on the material surface and measure the temperature along the radial direction as demonstrated in **Figure 6.3 (a)**. The circular heater can be modeled as 2D axisymmetric heat flux and therefore simplify the analysis. The actual heat flux from the heater is unnecessary for the analysis, as the measurement and thermal model can be normalized. The thermal conductivity can then be extracted from the normalized profile of the temperature distribution, as illustrated in **Figure 6.3 (b)**. The advantage of this approach is that it allows Fourier's law of heat transfer to be solved in radial coordinates, enabling the creation of a universal analytical model without the need for FEA capabilities. Some considerations with this approach include: 1) the need for nanoparticles or other surface transducers for temperature measurement to ensure surface temperature accuracy and avoid depth averaging due to optical absorption into the material, 2) ensuring the circular heater produces a uniform heat flux, and 3) generating a significant temperature increase (approximately 20 K) by the heater to account for uncertainties in the Raman measurement.

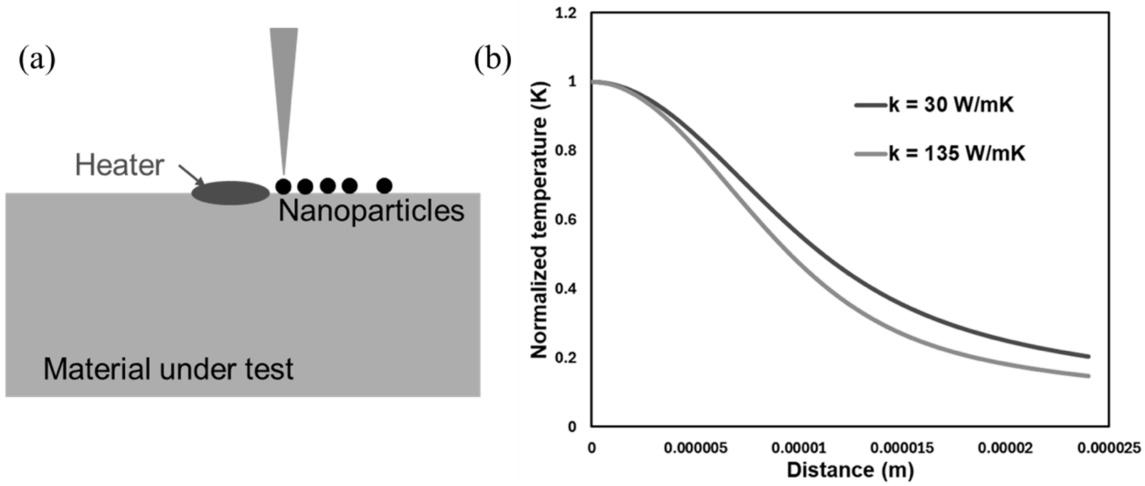

Figure 6.3: (a) schematic of measuring thermal conductivity using Raman and electrical heater, and (b) normalized temperature profile of materials with high (135 W/mK) and low (30 W/mK) thermal conductivities.

The second approach is using optical heater (pump laser) instead of electric heater. A secondary laser, typically used as optical tweezers, is often available with commercial Raman systems. Since WBG/UWBG materials are often transparent to the pump laser, a surface transducer is required to absorb the pump and produce surface heat flux. Even for materials with lower bandgap energy than the laser, using a transducer is desirable to limit the heat flux to the surface. This approach simplifies the analysis by eliminating the need to consider absorption depth into the material. Nanoparticles or other surface temperature probe (2D materials) need to be deposited on top of the transducer to enable temperature measurement. Then, the thermal properties can be extracted similarly to the electrical heater method by fitting the radial temperature profile. The advantage of this method compared to the electrical heater is that it does not require lithography to fabricate the heater, which can be challenging to achieve on small samples. However, because the temperature is measured on the surface of the transducer, the thermal properties of the transducer and the TBR between the transducer and the material must be included in the analytical model, which complicates the analysis.

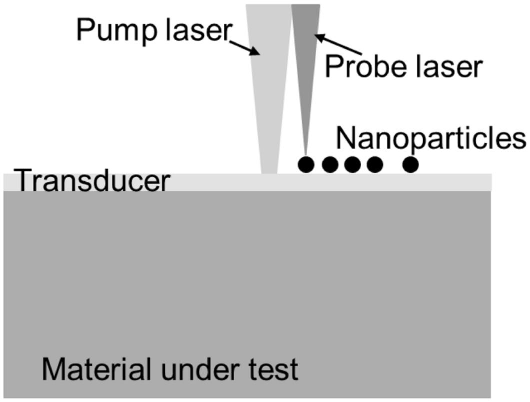

Figure 6.4: Schematic of measuring thermal conductivity using Raman and optical heater.

The third approach is to measure the temperature rise using transmission line measurement (TLM) structures. TLMs are often used to measure the ohmic contact resistance,[20] and they produce uniform heat flux between the source and drain that can be modeled using the FEA method.[19,21] By fitting the measured temperature in the TLM channel to FEA model, the thermal conductivity can be estimated. TLM structures can be incorporated into the device fabrication process, allowing for material-level and device-level characterization on the same die. However, it is not suitable for bare materials as the fabrication of TLMs requires doping to achieve ohmic contact. Due to the doped regions and often complex material stacks in TLM structures, similar to a functional device, the varying contributions of thermal resistance can lead to larger errors in the estimated thermal conductivity.

6.3 Chapter References

[1] J.D. Larson, J.D. Ruby, R.C. Bradley, J. Wen, S.-L. Kok, and A. Chien, “Power handling and temperature coefficient studies in FBAR duplexers for the 1900 MHz PCS band,” in *2000 IEEE Ultrason. Symp. Proceedings. An Int. Symp. (Cat. No.00CH37121)*, (2000), pp. 869–874 vol.1.

[2] S. Setoodeh, U. Kemiktarak, F. Bayatpur, S. Fouladi, and D. Feld, “A high power circuit model of an fbar resonator for use in filter design,” in *2019 IEEE Int. Ultrason. Symp.*, (2019), pp. 2169–2173.

[3] A. Tazzoli, M. Rinaldi, and G. Piazza, “Experimental investigation of thermally induced nonlinearities in aluminum nitride contour-mode MEMS resonators,” IEEE Electron Device Lett. **33**(5), 724–726 (2012).

[4] B. Ivira, R.-Y. Fillit, F. Ndagijimana, P. Benech, G. Parat, and P. Ancey, “Self-heating study of bulk acoustic wave resonators under high RF power,” IEEE Trans. Ultrason. Ferroelectr. Freq. Control **55**(1), 139–147 (2008).

[5] Y. Zheng, M. Park, A. Ansari, C. Yuan, and S. Graham, “Self-heating and quality factor: thermal challenges in aluminum scandium nitride bulk acoustic wave resonators,” in *2021 21st Int. Conf. Solid-State Sensors, Actuators Microsystems*, (2021), pp. 321–324.

[6] D.C. Shoemaker, A. Karim, D. Kendig, H. Kim, and S. Choi, “Deep-ultraviolet thermoreflectance thermal imaging of gan high electron mobility transistors,” in *2022 21st IEEE Intersoc. Conf. Therm. Thermomechanical Phenom. Electron. Syst.*, (2022), pp. 1–5.

[7] J.S. Lundh, W. Zhu, Y. Song, S.W. Ko, C. Fragkiadakis, P. Mardilovich, S. Trolier-McKinstry, and S. Choi, "Local measurements of domain wall-induced self-heating in released $PbZr_{0.52}Ti_{0.48}O_3$ films," J. Appl. Phys. **128**(21), 214102 (2020).

[8] J.S. Lundh, T. Zhang, Y. Zhang, Z. Xia, M. Wetherington, Y. Lei, E. Kahn, S. Rajan, M. Terrones, and S. Choi, "2D materials for universal thermal imaging of micro- and nanodevices: an application to gallium oxide electronics," ACS Appl. Electron. Mater. **2**(9), 2945-2953(2020).

[9] D. Shoemaker, M. Malakoutian, B. Chatterjee, Y. Song, S. Kim, B.M. Foley, S. Graham, C.D. Nordquist, S. Chowdhury, and S. Choi, "Diamond-incorporated flip-chip integration for thermal management of gan and ultra-wide bandgap rf power amplifiers," IEEE Trans. Components, Packag. Manuf. Technol. **11**(8), 1177–1186 (2021).

[10] M. Malakoutian, D.E. Field, N.J. Hines, S. Pasayat, S. Graham, M. Kuball, and S. Chowdhury, "Record-low thermal boundary resistance between diamond and GaN-on-SiC for enabling radiofrequency device cooling," ACS Appl. Mater. Interfaces **13**(50), 60553–60560 (2021).

[11] E.J.W. Smith, A.H. Piracha, D. Field, J.W. Pomeroy, G.R. Mackenzie, Z. Abdallah, F.C.-P. Massabuau, A.M. Hinz, D.J. Wallis, R.A. Oliver, M. Kuball, and P.W. May, "Mixed-size diamond seeding for low-thermal-barrier growth of CVD diamond onto GaN and AlN," Carbon N. Y. **167**, 620–626 (2020).

[12] J. Cho, Z. Li, E. Bozorg-Grayeli, T. Kodama, D. Francis, F. Ejeckam, F. Faili, M. Asheghi, and K.E. Goodson, "Improved Thermal Interfaces of GaN–Diamond Composite Substrates for HEMT Applications," IEEE Trans. Components, Packag. Manuf. Technol. **3**(1), 79–85 (2013).

[13] A. Sood, J. Cho, K.D. Hobart, T.I. Feygelson, B.B. Pate, M. Asheghi, D.G. Cahill, and K.E. Goodson, "Anisotropic and inhomogeneous thermal conduction in suspended thin-film polycrystalline diamond," J. Appl. Phys. **119**(17), 175103 (2016).

[14] M. Malakoutian, Y. Song, C. Yuan, C. Ren, J.S. Lundh, R.M. Lavelle, J.E. Brown, D.W. Snyder, S. Graham, S. Choi, and S. Chowdhury, "Polycrystalline diamond growth on β-Ga_2O_3 for thermal management," Appl. Phys. Express **14**(5), 55502 (2021).

[15] M. Malakoutian, R. Soman, K. Woo, and S. Chowdhury, "Development of 300–400 °C grown diamond for semiconductor devices thermal management," MRS Adv. **9**(1), 7–11 (2024).

[16] H. Ji, M. Kuball, A. Sarua, J. Das, W. Ruythooren, M. Germain, and G. Borghs, "Three-dimensional thermal analysis of a flip-chip mounted AlGaN/GaN HFET using confocal micro-Raman spectroscopy," IEEE Trans. Electron Devices **53**(10), 2658–2661 (2006).

[17] J.S. Lundh, Y. Song, B. Chatterjee, A.G. Baca, R.J. Kaplar, A.M. Armstrong, A.A. Allerman, H. Kim, and S. Choi, "Integrated optical probing of the thermal dynamics of wide bandgap power electronics," Proceedings of the ASME 2019 International Technical Conference and Exhibition on Packaging and Integration of Electronic and Photonic Microsystems. Anaheim, California, USA. October 7–9, 2019. V001T06A014. ASME.

[18] J.S. Lundh, B. Chatterjee, J. Dallas, H. Kim, and S. Choi, "Integrated temperature mapping of lateral gallium nitride electronics," in *2017 16th IEEE Intersoc. Conf. Therm. Thermomechanical Phenom. Electron. Syst.*, (2017), pp. 320–327.

[19] D.C. Shoemaker, Y. Song, K. Kang, M.L. Schuette, J.S. Tweedie, S.T. Sheppard, N.S. McIlwaine, J.-P. Maria, and S. Choi, "Implications of interfacial thermal transport on the self-heating of gan-on-sic high electron mobility transistors," IEEE Trans. Electron Devices **70**(10), 5036–5043 (2023).

[20] F. Alema, C. Peterson, A. Bhattacharyya, S. Roy, S. Krishnamoorthy, and A. Osinsky, “Low Resistance Ohmic Contact on Epitaxial MOVPE Grown β-Ga_2O_3 and β-$(Al_xGa_{1-x})_2O_3$ Films,” IEEE Electron Device Lett. **43**(10), 1649–1652 (2022).

[21] J.S. Lundh, D. Shoemaker, A.G. Birdwell, J.D. Weil, L.M. De La Cruz, P.B. Shah, K.G. Crawford, T.G. Ivanov, H.Y. Wong, and S. Choi, “Thermal performance of diamond field-effect transistors,” Appl. Phys. Lett. **119**(14), 143502 (2021).

VITA

Yiwen Song

- Doctor of Philosophy, Department of Mechanical Engineering, The Pennsylvania State University, University Park, PA, USA (2019-2024)
- Bachelor of Science, Department of Mechanical Engineering, The Pennsylvania State University, University Park, PA, USA (2015-2018)